RELATIONSHIPS BETWEEN METAMORPHISM, DEFORMATION, AND PLUTONISM AS CONSTRAINED BY GARNET GEOCHRONOLOGY FROM THE CENTRAL COAST MOUNTAINS, BRITISH COLUMBIA

A Dissertation

Presented to the Faculty of the Graduate School

of Cornell University

In Partial Fulfillment of the Requirements for the Degree of

Doctor of Philosophy

by

David Eny Wolf

May 2011

RELATIONSHIPS BETWEEN METAMORPHISM, DEFORMATION, AND PLUTONISM AS CONSTRAINED BY GARNET GEOCHRONOLOGY FROM THE CENTRAL COAST MOUNTAINS, BRITISH COLUMBIA

David Eny Wolf, Ph. D.

Cornell University 2011

Metamorphism, deformation, and plutonism are the processes that are responsible for the generation of the continental crust and the tectonic evolution of plate margins. Understanding the interactions of these processes is hampered by our ability to directly date rock forming minerals. Lu-Hf geochronology of garnet is a powerful technique that provides the ability to date the growth of garnet that can be directly tied to metamorphism and deformation.

This study utilized Lu-Hf geochronology in combination with structural and metamorphic analysis of two metamorphic belts in coastal British Columbia. This work showed that direct dating of garnet contradicts prior results derived from U-Pb dating of cross-cutting relationships. The new results require revision of the tectonic history of the Canadian Cordillera and have important implications for the entire North American Cordillera.

Profound crustal thickening across thrust faults and transpressive shear zones characterizes the structure of the Prince Rupert area. Newly obtained Lu–Hf garnet ages date metamorphism, deformation, and the development of a regionally inverted metamorphic sequence. Prior work had previously inferred that the emplacement of the 90 Ma Ecstall pluton was synchronous with regional metamorphism and

deformation. The garnet ages show that the Ecstall pluton was emplaced 10 to 15 m.y. after metamorphism and deformation. This result demonstrates that discordant paleomagnetic poles for the Ecstall pluton cannot be the result of deformation of the pluton and instead are consistent with the pluton being displaced from more southerly latitudes.

To the east, within the central gneiss complex (CGC), Lu-Hf ages date the inception of granulite facies metamorphism and document strain partitioning. Cross-cutting relationships observed in the field require deformation to have progressed temporally between adjacent domains; however, the garnet ages require that deformation was synchronous between domains requiring strain partitioning during dextral transpression. This contrasts with theoretical models for transpression that predict distributed deformation within a single oblique slip shear zone.

In both studies, the Lu-Hf system resolves the age of garnet growth despite metamorphic conditions in the upper-amphibolite- to granulite-facies. This indicates that the Lu-Hf system in garnet is an extremely robust tool for deciphering metamorphic and deformation ages despite complex thermal histories.

BIOGRAPHICAL SKETCH

David Eny Wolf was born and raised in Greenbelt, Maryland, by Elizabeth Rose Eny and Glenn Jeffery Wolf. He has one younger sister, Laura Eny Wolf, who lives and works in Washington, D.C.. He completed a B.S. in Geology with an Economics minor at Allegheny College in Meadville, Pennsylvania. His senior thesis with Dr. Ron Cole investigated the use of deformed mudcrack polygons from the Appalachian Plateau as a macro-scale strain marker to quantify layer-parallel shortening. During college, Dave spent his summers as a geologist for an aggregates mining company back home in Maryland and working as a guide in the wilderness of northern Minnesota and southern Ontario. He went on for a M.S. in Geology at Washington State University, where he worked with Dr. Jeff Vervoort on the structure and geochronology of Archean shear zones in Ontario.

Since arriving at Cornell in the fall of 2006, Dave spent two summers as an intern for Shell Petroleum, working in site development and potential fields research. Dave served with the Cayuga Heights Fire Department since arriving in Ithaca; as a firefighter, lieutenant, and assistant chief. During this time, he also served as a fire instructor for Tompkins County, teaching other firefighters how to do their job, and stay safe. Volunteering with the fire department has provided Dave with the opportunity to serve his community, work with a dedicated group of individuals, and helped him to maintain a sense of balance while working towards his Ph.D..

Dave married a fellow Cornell EAS student, Danielle Glasgow, in September of 2009. They have two Labrador retrievers named Tanner and Cricket, whom they adopted from local animal shelters. Dave has accepted a research position as a structural geologist with Shell International Exploration & Production. The Wolf family currently resides in Houston, Texas.

Dedicated to my wife, Danielle.

ACKNOWLEDGEMENTS

Many people were instrumental in helping me make it to Cornell, succeed while I was there, and ensuring I would have a future after I finished. First and foremost, I want to thank Danielle for putting up with everything necessary to see this through. She always knew when to push and when to give, was always willing to sacrifice when she thought it would help, and to put up with me when I was at my most pleasant. I could not have done this without her support.

I would like to thank my family, who has always encouraged me to do my best. My parents, Glenn Wolf and Elizabeth Eny, and sister, Laura Wolf, have always been there to make sure I have given 110%. I continue to follow two key pieces of advice I've been reminded of through the years: 1) Keep all options open as long as possible, and 2) "Try not to suck."

I could not have asked for a better advisor than Chris Andronicos. Not only does Chris have an immense knowledge of the subject in which he works, but he also has an astounding passion for science and furthering others' knowledge. Academia could use more people like Chris, who strives to be the best in both teaching and research. Chris' love of British Columbia is contagious, and I've caught it. I owe Chris much thanks for the many opportunities to travel all over the world and to learn as much as I can. I deeply appreciate his sticking with me through the tough times, and pushing me to be the best geologist (and person) that I can be.

Jason Phipps-Morgan and Paul Dawson provided useful feedback on drafts of this dissertation, and excellent discussion to help me clarify my ideas and present the relevance of this work.

I would not have come to Cornell if it were not for Rick Allmendinger. His stature in the structural geology community drew me to Cornell in the first place,

despite my love of soft-squishy rocks from much deeper in the Earth. Rather than just dismiss me and suggest I try another university, Rick was a huge proponent of his peer, and encouraged me to stay and meet Chris. It has been a lot of fun working with Rick at a TA, and I've enjoyed every opportunity to learn from him.

Jeff Vervoort, Ashley Tefft, and Garrett Hart at Washington State University were instrumental in helping me complete the geochronology aspect of this project. Jeff went out of his way to help me work in his lab on numerous occasions, consuming beakers, acids, and his time. This project is much improved because of this help, and I appreciate the opportunity to continue to learn more from him after leaving WSU. I could not have asked for more from Ashley, who was always willing to set me straight in the lab, trade chores, and keep the columns dripping. She made the time at WSU go much more smoothly, and made me feel like part of the gang. Garrett again offered his time and expertise to keep the Neptune humming, despite my frequent attempts to take if offline. Without his help, I would still be sitting in that clean lab today.

While the academic standing of Cornell University should have been more than enough to entice me, some of the credit has to go to Matt Abbinanti for getting me to Ithaca. I didn't expect that we would get to serve in the fire department together after Meadville, but there we were. Some of my best memories will be hanging out around the station, or sharing command on fires or crashes, working as a team to get the job done.

I can't thank George Tamborelle enough for taking a chance on another one from West Mead #2. It was an honor to serve in his organization, and a privilege to serve as an officer. It was a unique challenge to balance the fire department with graduate school. CHFD is an amazing group with immense talent, and the people they serve are fortunate to have George at the helm. He made me feel like part of the family, and I'll miss it more than he knows.

This work was supported by: the Geological Society of America Student Research Fund to Wolf; National Science Foundation grant EAR- 0738827 to Andronicos; and National Science Foundation grants EAR-0609856 and EAR-0711326 to Vervoort.

TABLE OF CONTENTS

ABSTRACT..... i

BIOGRAPHICAL SKETCH..... iii

DEDICATION..... iv

ACKNOWLEDGEMENTS..... v

TABLE OF CONTENTS..... ix

LIST OF FIGURES..... xii

LIST OF TABLES..... xiv

CHAPTER 1: INTRODUCTION

1. Research Question..... 1

2. Why British Columbia?..... 3

3. Dissertation Outline..... 6

4. Dissertation Conclusions..... 8

References..... 13

CHAPTER 2: APPLICATION OF LU-HF GARNET DATING TO UNRAVEL THE RELATIONSHIPS BETWEEN DEFORMATION, METAMORPHISM AND PLUTONISM: AN EXAMPLE FROM THE PRINCE RUPERT AREA, BRITISH COLUMBIA, CANADA

Abstract..... 20

1. Introduction..... 22

2. Regional Geology..... 24

3. Geochemical Methods..... 26

4. Sample descriptions, petrology and results

4.1 Kumealon Inlet..... 27

4.2. Ridley Island..... 41

4.3. Minerva Lake..... 50

5. Discussion..... 52

6. Conclusions..... 57

7. Chapter-specific acknowledgements..... 60

References..... 62

CHAPTER 3: PARTITIONED STRAIN IN THE MIDDLE CRUST OF THE COAST MOUNTIANS, BRITISH COLUMBIA, CONSTRAINTED BY GARNET GEOCHRONOLOGY

Abstract..... 74

1. Introduction..... 76

2. Regional Geology..... 79

3. Analytical Methods..... 85

4. Deformational Fabrics..... 87

5. Sample descriptions, petrology, and geochronology

5.1 GMO - Head Waters Kwinitsa Creek..... 95

5.2 Kwinitsa Quarry.....110

5.3 Recumbent Peak (96-056) 119

5.4 East Ridge Tonalite (09B-34) 125

5.5 Sample 09B-24.....127

5.6 Petrologists' Ridge (09B-15) 128

5.7 Sample 09B-06.....136

5.8 Cooper Peak (97-107) 141

6. Discussion

6.1 Thermobarometry..... 142

6.2 Geochronology..... 145

6.3 Deformational History..... 149

6.4 Regional Context..... 151

7. Conclusions..... 151

8. Chapter-specific acknowledgements..... 153

References..... 154

LIST OF FIGURES

CHAPTER 1:

Figure 1. Simplified geologic map of the Coast Mountains.....4

Figure 2. Isotopic ages plotted with respect to the Coast shear zone.....10

Figure 3. Concept of strain partitioning…….....11

CHAPTER 2:

Figure 4. Simplified geologic map of the Coast Mountains.....23

Figure 5. Photomicrographs and sketches of samples.....30

Figure 6: X-ray intensity maps and compositional line scan for G16D.....32

Figure 7: Isochemical phase diagram for G16D.....36

Figure 8: Isochron plots of geochemical data.....39

Figure 9: X-ray intensity maps and compositional line scan for 98-114.....43

Figure 10: Isochemical phase diagram for 98–114.....46

Figure 11: Isotopic ages plotted with respect to the Coast shear zone.....53

Figure 12: Tectonic map of the North American Cordillera.....59

CHAPTER 3:

Figure 13: Simplified geologic map of the Coast Mountains..... 78

Figure 14: Geologic map of the central gneiss complex..... 81

Figure 15: Detailed geologic map of the Spinel Peak area..... 82

Figure 16: Geochronology of the central gneiss complex..... 88

Figure 17: Foliation trajectory map of the central gneiss complex.....89

Figure 18: Field photographs A-D from the central gneiss complex.....92

Figure 19: Field photographs E-H from the central gneiss complex.....93

Figure 20: X-ray intensity maps and compositional line scan for GMO..... 96
Figure 21: Isochemical phase diagram for GMO..... 99
Figure 22: Trace element data of central gneiss complex samples.....106
Figure 23: Isochron plots of geochemical data.....108
Figure 24: Isochemical phase diagram for Kwinitsa.....112
Figure 25: X-ray intensity maps and compositional line scan for 96-056.....118
Figure 26: Isochemical phase diagram for 96-056.....121
Figure 27: X-ray intensity maps and compositional line scan for 09B-15.....127
Figure 28: Isochemical phase diagram for 09B-15.....129
Figure 29: X-ray intensity maps and compositional line scan for 09B-06A.....135
Figure 30: Pressure-Temperature diagram for 09B-06A.....137
Figure 31: Pressure-temperature-time path of central gneiss samples.....140
Figure 32: Lu-Hf garnet ages plotted as weighted average…….....143
Figure 33: Ages vs. distance from Coast shear zone.....144

LIST OF TABLES

CHAPTER 2:

Table 1: Microprobe analyses for G-16..... 34

Table 2: Mineral abbreviations used in phase diagrams..... 37

Table 3: Changes in mineral assemblages for phase diagram of G-16A..... 38

Table 4: Lu-Hf data for garnets in western metamorphic belt..... 40

Table 5: Microprobe analyses for 98-114..... 45

Table 6: Changes in mineral assemblages for phase diagram of 98-114..... 47

CHAPTER 3:

Table 7: Sample mineralogy for central gneiss complex..... 94

Table 8: Microprobe analyses for GMO.....97

Table 9: Changes in mineral assemblages for phase diagram of GMO.....100

Table 10: Trace element data for samples from the central gneiss complex.....107

Table 11: Lu-Hf data for analyzed garnet samples.....109

Table 12: Sm-Nd data for analyzed garnet samples.....110

Table 13: Changes in mineral assemblages for phase diagram of Kwinitsa.....113

Table 14: Microprobe analyses for 96-056.....119

Table 15: Changes in mineral assemblages for phase diagram of 96-056.....122

Table 16: Microprobe analyses for 09B-15.....128

Table 17: Changes in mineral assemblages for phase diagram of 09B-15.....130

Table 18: Microprobe analyses for 09B-06A.....138

INTRODUCTION

1. Research Question

Understanding the generation of continental crust and the tectonic evolution of plate margins is critically dependent on correctly understanding the interrelationships between the processes of metamorphism, deformation, and plutonism (Karlstrom and Williams, 1995). Orogeny, by definition, is accompanied by crustal thickening as a result of plate convergence. At depth, this deformation is accommodated by ductile deformation and accompanying changes in texture, bulk composition, and mineralogy that accompany metamorphism and crustal anatexis. Continental margin arcs are defined by calc-alkaline plutons that are derived from mixing of crustal and mantle derived melts. The understanding the temporal and spatial evolution of deformation, metamorphism and plutonism in an orogen can provide key information about the tectonic evolution of a region. Key to deciphering the relationships between regional tectonics and orogeny is determining the both the relative and absolute timing of these interrelated events. These relationships can further be used to decipher questions about plate boundary geometries and structural styles, or can be used to decipher mechanical and chemical processes responsible for pluton emplacement or crustal thickening.

In order to address these questions, the timing of the deformational events must be established independently and precisely. Geochronologic tools have long been utilized for different isotopic systems to address parts of the story. U-Pb zircon ages precisely and accurately date the crystallization of zircon and are interpreted to be the same as the time the melt passed through the solidus (Compston et al. 1982). U-Pb sphene, Ar-Ar hornblende, and Ar-Ar biotite analyses can give meaningful dates on when the mineral cooled below the systems' isotopic closure temperatures, at 600°, 500° and 350° C respectively (Spear 1995). Although these techniques do constrain

timing of crystallization of magmas and the cooling of rocks from high temperatures, it is much more difficult to infer the timing of prograde metamorphic events because there are few isotopic systems appropriate to date the formation of index minerals common in metamorphic rocks.

Garnet is an important metamorphic index mineral which is often used in the calculation of metamorphic P-T paths, and can be tied to deformation through the study of microstructures. The Lu-Hf isotopic system provides a potential method to date garnet growth giving insight into both deformation and metamorphic events. The isotopic system is based on the decay of ^{176}Lu to ^{176}Hf (Faure and Mensing 2005). The decay constant (λ) for ^{176}Lu is 1.867 x 10^{-11} yr^{-1}, and represents a half-life of 3.70 billion years (Scherer et al. 2001; Söderlund et al. 2004). Lu is preferentially fractionated into garnets' crystal structure, while non-radiogenic hafnium is excluded. The mobility of Lu and Hf is very low, minimizing the impact of thermal perturbations or fluids on the isotopic system. These characteristics make the Lu-Hf system in garnet extremely robust, and produces a useful geochronologic tool for deciphering metamorphic ages.

The focus of this dissertation is to constrain the timing of metamorphism within the Coast Mountains of British Columbia in order to understand its relationship to deformation and plutonism. This is accomplished by utilizing garnet geochronology to directly date prograde metamorphism. Kinematic indicators within garnet are utilized to discern the relative timing of deformation, which was often synchronous in the field area (and therefore dated by garnet ages). When these ages are combined with metamorphic petrology and geothermobarometry, the pressure-temperature-time history of the region can be determined.

2. Why British Columbia?

The Coast Mountains in British Columbia are an ideal setting to study orogeny. The Coast Mountains include bi-vergent fold-and-thrust belts that bound a high-grade metamorphic core, and an extensive calc-alkaline batholith intruded during orogeny (Hutchinson 1982; Crawford and Hollister 1982; Crawford et al. 1987; Crawford et al. 2000). This orogen has experienced terrane accretion, plutonism, and subsequent orogenic collapse. Further, the rocks of the middle crust are now exposed at the surface, allowing for a more thorough study of what may be happening at depth during mountain building events. The central gneiss complex is a well-exposed granulite terrane; with observable relationships to plutonic bodies and ample garnet for dating of metamorphism (Hutchinson 1982; Woodsworth et al. 1983; Hollister 1982; Armstrong 1988; van der Heyden 1992).

Coastal British Columbia, between the towns of Prince Rupert and Terrace, along the Skeena River provides an excellent transect of the features necessary to address the timing of metamorphism (Figure 1). The tectonic history of the Prince Rupert area is marked by profound crustal thickening from thrusting that produced inverted metamorphic field gradients (Crawford and Hollister 1982; Crawford et al. 1987; Crawford et al. 2000) and is segmented by transpressive shear zones (Chardon et al. 1999; Chardon 2003). Country rocks of the western metamorphic belt contain syn-tectonic garnet, the dating of which provides the timing of deformation (Wolf et al. 2010). The central Coast Mountains in the vicinity of Prince Rupert are composed of greenschist to upper amphibolite facies rocks (Hutchinson 1982) that have been correlated with the Alexander, Yukon–Tanana, and Taku terranes (Gehrels and Berg 1994), as well as rocks of the Gravina basin (Gehrels et al. 1987; Rubin and Saleeby 1992; Crawford et al. 2000). This assemblage of rocks is referred to as the western metamorphic belt (WMB) (Brew and Ford 1978; Stowell and Hooper 1990; Crawford

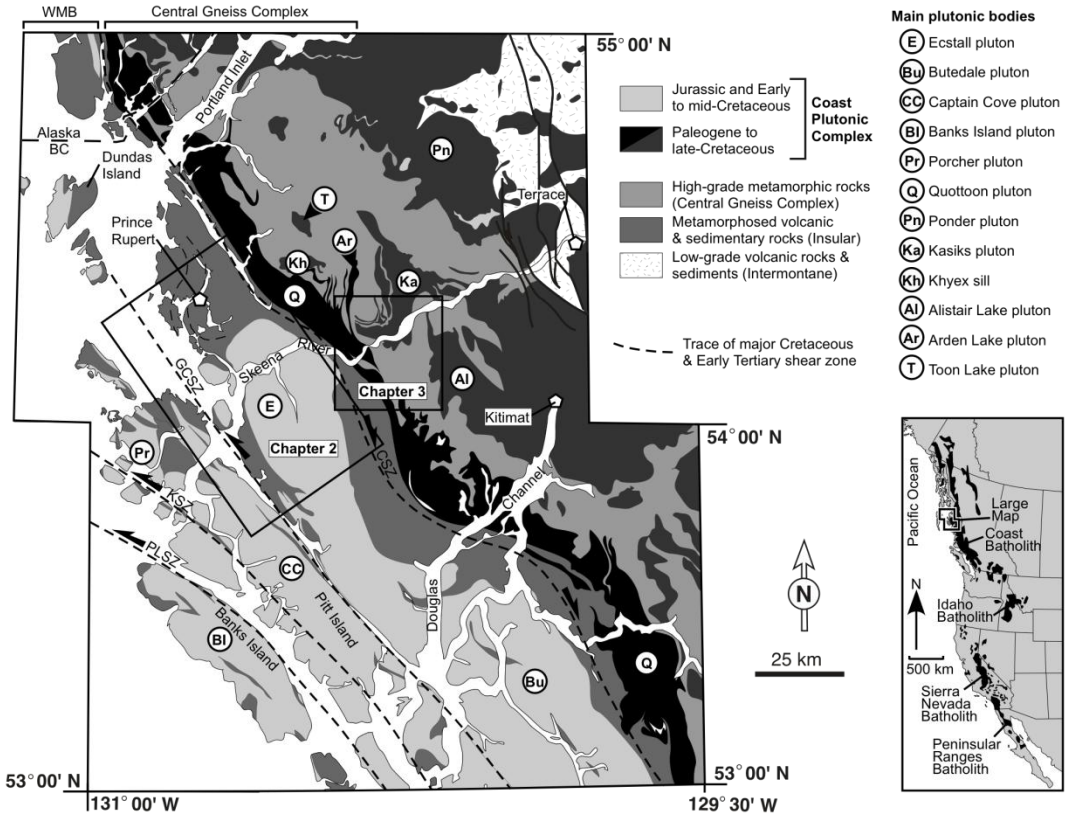

Figure 1. Simplified geologic map of the Coast Mountains between 53° and 55° N latitude, modified from Chardon et al. 1999. CSZ - Coast shear zone, GCSZ - Grenville Channel shear zone, KSZ - Kitkatla shear zone, PLSZ - Principe Laredo shear zone. Western metamorphic belt (WMB) is defined as metamorphic host rocks west of the Coast shear zone, and the central gneiss complex (CGC) are the high-grade rocks east of the CSZ, exclusive of the Stikine Terrane. Inset map shows location of field area in the western North America cordillera with Cretaceous batholiths in black modified from Driver et al. (2000). Lithologies in the large map compiled from: Roddick 1970, Crawford and Hollister 1982, Hutchinson 1982, van der Heyden 1989, Gareau 1991, Cook and Crawford 1994, Andronicos et al. 1999, Chardon et al. 1999, Rusmore et al. 2001 and Mansfield 2004; this dissertation.

et al. 2000). These rocks are intruded by plutons of Jurassic to Cretaceous age and are separated from the late Cretaceous to Paleogene high-grade core of the orogen by the Coast shear zone (Brew and Ford 1978; Crawford and Hollister 1982; Hutchinson 1982; Crawford et al. 1987; Ingram and Hutton 1994; Klepeis et al. 1998; Andronicos et al. 1999). The timing of deformation and peak metamorphism near Prince Rupert had previously been inferred to be synchronous with emplacement of the Ecstall pluton based on plutonic U-Pb zircon ages and K-Ar and ^{40}Ar-^{39}Ar cooling ages from hornblende and biotite (van der Heyden 1989; Gehrels et al. 2009; Crawford et al. 2000; Butler et al. 2002; Butler et al. 2006), but is now thought to be synchronous with emplacement of the Captain Cove Pluton and predate the Ecstall by 10-15 million years, based on Lu-Hf garnet ages (Wolf et al. 2010).

The western Canadian Cordillera and Coast Mountains of British Columbia were assembled through terrane accretion during the Jurassic and Cretaceous, but the source of those terranes and mechanics of emplacement are still widely debated. Two end-member models for the paleogeography of the Canadian Cordillera based on paleomagnetic and geological data have been put forward. One argues for large-scale coast-parallel translation and is referred to as the Baja B.C. hypothesis (Irving 1985; Umhoefer 1987; Cowan et al. 1997; Enkin 2006). Alternatively, shallow paleomagnetic inclinations in Cretaceous rocks are interpreted to indicate in-situ deformation resulting in tilting (Butler et al., 2001).

To the east of the Coast shear zone, a domain of upper amphibolite to granulite facies rocks occurs and is referred to as the central gneiss complex (CGC). These rocks represent the exhumed middle crust of a continental magmatic arc. The western boundary of the CGC is the Coast shear zone, a crustal-scale structure that separates high pressure (0.8-0.9 GPa) amphibolite facies metamorphic rocks in the west from lower pressure, higher temperature metamorphic rocks to the east (Crawford et al.

1987). Rocks of the western belt have been intruded by Jurassic to mid-Cretaceous plutons (Crawford and Hollister 1982; Crawford et al. 1987; Crawford et al. 2000). Plutons with ages ranging from Cretaceous to Eocene intrude across the central gneiss complex indicating the Coast shear zone represents a major boundary separating distinct parts of the Coast orogen (Armstrong 1988; van der Heyden 1992; Hollister and Andronicos 1997; Gehrels et al. 2009). The Coast shear zone is a near vertical shear zone that has a minimum length of 800 km and experienced a polyphase deformational history of transpression, contraction and oblique extension (Stowell and Hopper 1990; McClelland et al. 1992; Ingram and Hutton 1994; Hollister and Andronicos 1997; Andronicos et al. 1999; Andronicos et al. 2003).

Previous geochronologic work has been done in the region to constrain the timing of deformation, metamorphism and plutonism, predominately relying on U-Pb zircon ages of igneous rocks and Ar geochronology of hornblende, biotite and muscovite. U-Pb Ages from zircons are generally interpreted to provide the age of crystallization of igneous rocks and therefore track major thermal perturbations. However, zircon ages are unable to directly date the age of metamorphism and deformation directly, and instead are used in concert with cross-cutting and geological relationships to interpret the absolute timing of events. New ages on the growth of metamorphic minerals can provide a more precise understanding of the tectonic history of the metamorphic terranes. Here I use Lu/Hf ages of garnet to constrain the timing of deformation and metamorphism in the Coast Mountains, and these ages are shown to have important implications for the entire North American Cordillera.

3. Dissertation Outline

Chapters two and three are written as stand-alone manuscripts, though they are related in focus and scope. In both studies, Lu-Hf garnet geochronology is combined

with structural and metamorphic analysis to understand the tectonic evolution of coastal British Columbia. Both study sites experienced oblique convergence that resulted in partitioning between zones of crustal thickening and strike-slip displacement (Hutchinson 1982; Woodsworth et al. 1983). The use of Lu-Hf geochronology on garnet samples from these sites enabled direct dating of the deformational fabrics that resulted in dates that contrast with prior results derived from U-Pb dating of cross-cutting igneous bodies. Deformation and metamorphism in the two field areas were temporally unique, with major foliation development within the western metamorphic belt in the Cretaceous (~110-105 Ma) preceding peak metamorphic conditions in the central gneiss complex, which occurred during the late Cretaceous to early Paleogene (67 to 54 Ma).

Chapter 2 is titled, "Application of Lu-Hf garnet dating to unravel the relationships between deformation, metamorphism and plutonism: An example from the Prince Rupert Area, British Columbia." This manuscript has previously been published in Tectonophysics (2010, v. 485, n. 1-4). In this chapter, Lu-Hf garnet ages are presented from within the western metamorphic belt of the Coast Mountains in British Columbia. These data show that amphibolite facies metamorphism and deformation within the western metamorphic belt (WMB) occurs at 105 Ma and predates the emplacement of the Ecstall pluton (Wolf et al. 2010). These results accurately constrain the timing of structures in the Prince Rupert area, while K-Ar and Ar-Ar ages constrain the timing of cooling or reheating of the WMB from peak temperatures (van der Heyden 1989; Butler et al. 2002; Chardon et al. 1999; Chardon 2003). The Lu-Hf ages are consistent with regional deformation, metamorphism and plutonism throughout the entire North American Cordillera in the time period between 110 and 85 Ma (Driver et al. 2000; Evenchick 1991 and 2001; Gehrels et al. 1992; McClelland et al. 1992; Crawford et al. 1987; Chardon et al. 1999; Chardon 2003;

Brandon et al. 1988; Brown 1987; McClelland et al. 2000; Wyld and Wright 2001; Giorgis et al. 2008; DeCelles and Coogan 2006; Pickett and Saleeby 1994; Tikoff and de Saint Blanquat 1997; Johnston et al. 1999). A reversal in kinematics in the northern and southern cordillera within a coeval magmatic belt is also identified as a first-order feature of the Cordillera during the Cretaceous.

Chapter 3 is titled, "Partitioned strain in the middle crust of the Coast Mountains, British Columbia, constrained by garnet geochronology." In this section, new Lu-Hf garnet ages date the initiation of granulite-facies metamorphism within the central gneiss complex, which occurred during regional transpression between 70-63 Ma. Field-observed cross-cutting relationships require a temporal progression that is not supported by the overlap in garnet ages. This space-time relationship can only be produced by partitioning of strike-parallel and strike-normal strain within the middle crust, contradicting theoretical models for distributed deformation within a single oblique slip shear zone. A new Sm-Nd garnet age, combined with previously published U-Pb and Ar-Ar data, show that rocks of the CGC experienced upper-amphibolite to granulite facies metamorphism for at least 18 million years. The end of metamorphism coincided with regionally distributed transtensional deformation and metamorphic core complex exhumation between 51 and 48 Ma (Andronicos et al. 2003). Gently dipping isotherms and isobars across the core of the central gneiss complex indicate a significant vertical component of shortening within the mylonite zone.

4. Dissertation Conclusions

The addition of new Lu/Hf garnet ages from the central Coast Mountains constrained the timing of metamorphism in both the western metamorphic belt and the central gneiss complex. Estimates of the timing of prograde metamorphism had been

previously inferred from cross-cutting relationships, but these are the first dates of the metamorphic index minerals that track prograde metamorphism. In both localities, prograde metamorphism was synchronous with deformation, as was identified by porphyroblast matrix relationships. Deformation in both examples predated plutonism by >10 million years (Figure 2). Plutonism was followed by a complex thermal history in the west, where the Ecstall was reheated during Quottoon emplacement at 59 Ma (Hollister et al., 200X). The new ages show that rocks east of the Coast shear zone experienced prograde metamorphism between 70-65 Ma, then underwent rapid exhumation and cooling during the Eocene at 52 Ma.

Both field areas experienced strain partitioning, the timing of which was better constrained by the new garnet ages. When a convergent force is applied obliquely, the resulting slip vector can be simply resolved onto a single plane (e.g. Figure 3a), or broken down into components (e.g. Figure 3b) (Fitch 1972; McCaffrey 1992; Teyssier et al. 1995; Teyssier et al. 2002; Tikoff et al. 2002). If the crust were generally weak with no mechanical heterogeneities, then all strain can be theoretically accommodated within a single tabular shear zone (Figure 3a). When partitioning of a strain occurs, multiple structures are utilized to accommodate the deformation, with the slip partitioned into distinct shear zones (e.g. Figure 3c). These structures may record slip normal and parallel to the heterogeneity, producing dip-slip and strike-slip structures (i.e. Figure 3c), or partition into separate strike-slip faults with opposing kinematics, similar to the San Andreas and Garlock Fault systems (e.g. McCaffrey 1992; Teyssier and Tikoff 1998). The presence of strain partitioning indicates that the crust is both strong enough to transfer strain through the rigid body to a zone of weakness and that there is not a complete detachment along the zones of weakness.

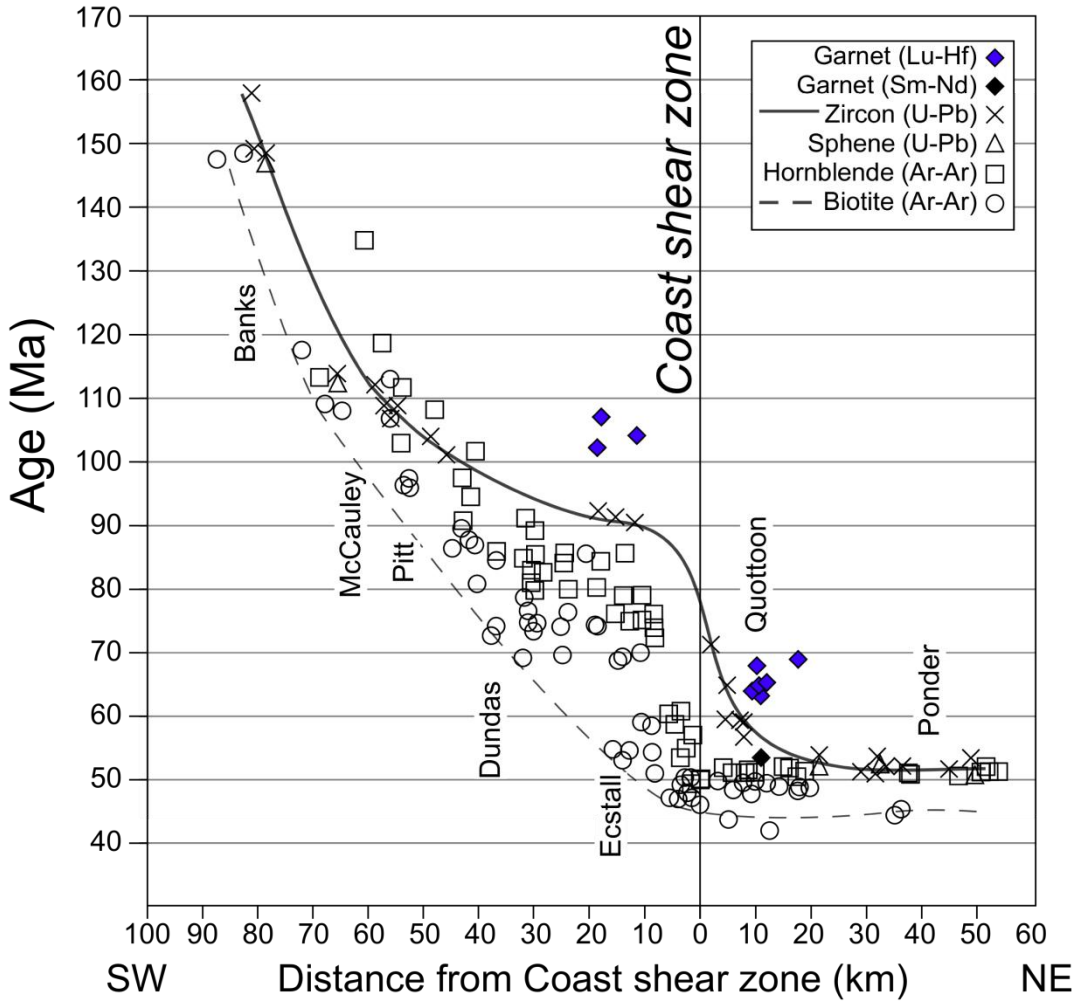

Figure 2. Isotopic ages plotted with respect to the Coast shear zone (0 km), modified from Butler et al. (2002). U–Pb zircon and titanite data are from Gehrels et al. (1991) Butler et al. (2006), and K–Ar and Ar–Ar hornblende and biotite data are from Butler et al. (2006) and Hollister et al. (2004). The solid line represents the oldest U-Pb zircon ages across the region, and the dashed line are the youngest Ar-Ar biotite ages. Zircon ages are interpreted to represent crystallization ages of igneous rocks, and are marked with "X". The blue diamonds show the ages of garnet samples dated in this study.

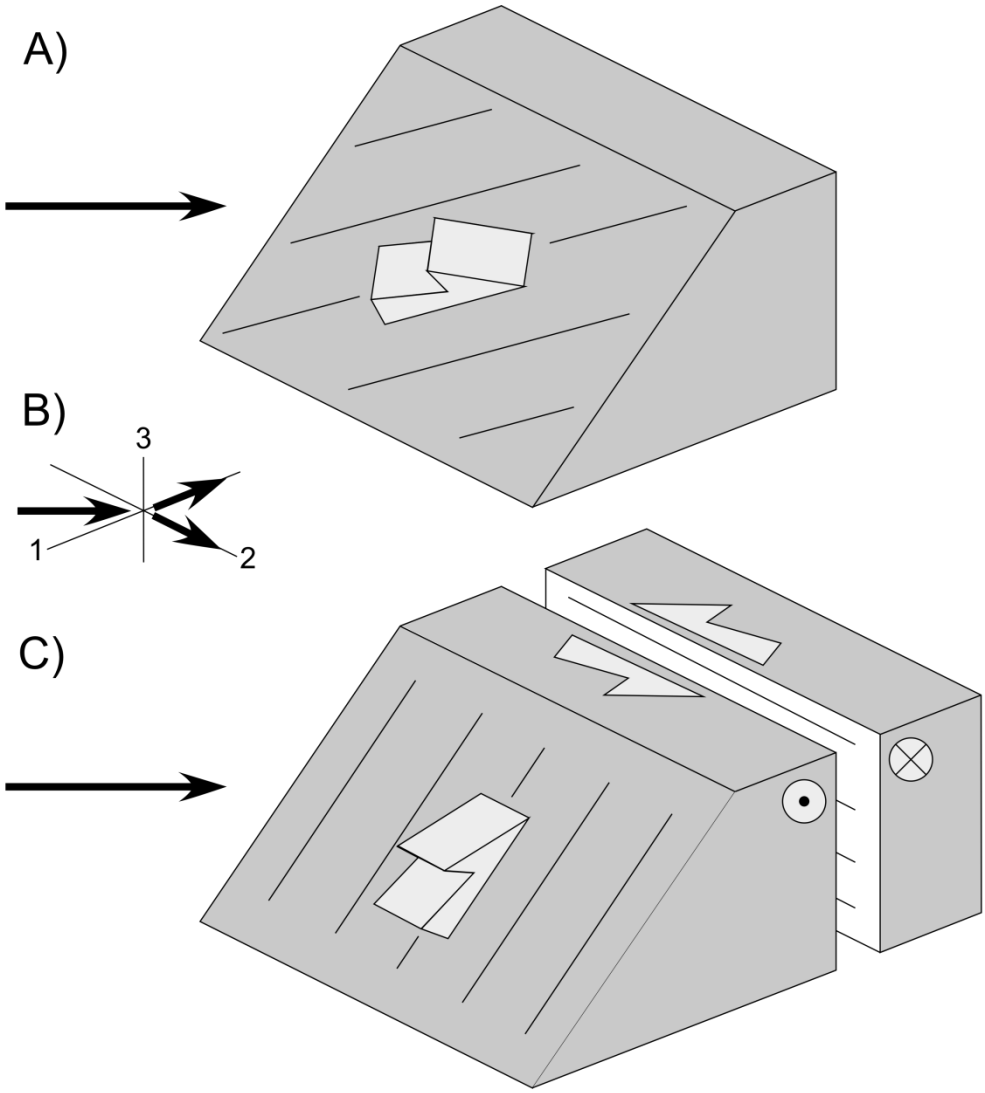

Figure 3. Concept of strain partitioning. In all Figures, shortening is applied from the left. In (A), the plane is oblique to the convergence, and all strain is resolved into a single slip vector. If the plane were a shear zone, the kinematics would be sinistral transpression (thrust). In (B), shortening oriented within the 1-2 plane is resolved into orthogonal slip directions parallel to the 1-2 axes in map view. In (C), the same convergence is partitioned into a dip-slip motion (thrust), and the strike-slip component of strain is accommodated on a new structure. The slip lineations occur at a high angle between the two zones, and total motion sums to equal the original convergence vector. After Fitch (1972).

This dissertation also demonstrates how Lu-Hf garnet ages can effectively determine the timing of prograde metamorphism, and at times, the direct dating of deformational fabric development. The Lu/Hf system can remain closed, despite thermal perturbations in excess of 750° C, and can preserve the age of prograde garnet growth despite peak metamorphic conditions in the granulite facies. Combined with field observations of structural domains, relative timing of fabrics can be interpreted with more confidence than by using cross-cutting relationships alone. This confirms that the Lu-Hf system in garnet is an extremely robust and useful geochronologic tool for deciphering metamorphic ages despite long lived and high temperature thermal histories, with potential applications for improving our understanding of many of the world's orogens.

REFERENCES

Andronicos, C.L., Hollister, L.S., Davidson, C., Chardon, D.H., 1999. Kinematics and tectonic significance of transpressive structures within the Coast Plutonic Complex, British Columbia. Journal of Structural Geology 21, 229–243.

Andronicos, C.L., Chardon, D.H., Hollister, L.S., Gehrels, G.E., Woodsworth, G.J., 2003. Strain partitioning in an obliquely convergent orogen, plutonism, and synorogenic collapse: Coast Mountains Batholith, British Columbia, Canada. Tectonics 22, 1012–1035.

Armstrong, R.L., 1988. Mesozoic and Early Cenozoic magmatic evolution of the Canadian Cordillera. Geological Society of America Special Paper 218, 55-91.

Brandon, M.T., Cowan, D.S., Vance, J.A., 1988. The late Cretaceous San Juan thrust system, San Juan Islands, Washington: Geological Society of America Special Paper 221. 81 pp.

Brew, D.A., Ford, A.B., 1978. Megalineament in southeastern Alaska marks southwest edge of Coast Range batholithic complex. Canadian Journal of Earth Sciences 15, 1763.

Brown, E.H., 1987. Structural geology and accretionary history of the Northwest Cascades system, Washington and British Columbia. Geological Society of America Bulletin 99, 201–214.

Butler, R.F., Gehrels, G.E., Baldwin, S.L., Davidson, C., 2002. Paleomagnetism and geochronology of the Ecstall pluton in the Coast Mountains of British Columbia; Evidence for local deformation rather than large-scale transport. Journal of Geophysical Research 107, 3–13. DOI:10.1029/2001JB000270.

Butler, R.F., Gehrels, G.E., Hart, W., Davidson, C., Crawford, M.L., 2006. Paleomagnetism of Late Jurassic to mid-Cretaceous plutons near Prince Rupert,

British Columbia. *In:* Haggart, J.W., Enkin, R.J., Monger, J.W.H. (Eds.), Paleogeography of the North American Cordillera: Evidence for and Against Large-scale Displacements: Geological Association of Canada Special Paper, vol. 46, pp. 171–200.

Chardon, D., Andronicos, C.L., Hollister, L.S., 1999. Large-scale transpressive shear zone patterns and displacements within magmatic arcs: the Coast Plutonic Complex, British Columbia. Tectonics 18, 278–292.

Chardon, D., 2003. Strain partitioning and batholith emplacement at the root of a transpressive magmatic arc. Journal of Structural Geology 25, 91–97.

Compston, W., Williams, I.S., and Meyer, C., 1982, U-Pb ages within single zircons using a sensitive high mass-resolution ion microprobe: Annual Conference for American Society of Mass Spectrometry 30, 593-595.

Cook, R.D., Crawford, M.L., 1994. Exhumation and tilting of the western metamorphic belt of the Coast orogen in southern southeastern Alaska. Tectonics 13, 528–537.

Cowan, D.S., Brandon, M.R., Garver, J.I., 1997. Geologic tests of hypotheses for large coastwise displacements — a critique illustrated by the Baja British Columbia controversy. American Journal of Science 297, 117–173.

Crawford, M.L., Hollister, L.S., 1982. Contrast of metamorphic and structural histories across the Work channel lineament. Coast Plutonic Complex, British Columbia. Journal of Geophysical Research 87, 3849–3860.

Crawford, M.L., Hollister, L.S., Woodsworth, G.J., 1987. Crustal deformation and regional metamorphism across a terrain boundary, Coast Plutonic Complex, British Columbia. Tectonics 6, 343–361.

Crawford, M.L., Crawford, W.A., Gehrels, G.E., 2000. Terrane assembly and structural relationships in the eastern Prince Rupert quadrangle, British Columbia.

In: Stowell, H.H., McClelland, W.C. (Eds.), Tectonics of the Coast Mountains, Southeastern Alaska and British Columbia: Geological Society of America, Special Paper 343, pp. 1–21.

DeCelles, P.G., Coogan, J.C., 2006. Regional structure and kinematic history of the Sevier fold-and-thrust belt, Central Utah. Geological Society of America Bulletin 118 (7–8), 841–864.

Driver, L.A., Creaser, R.A., Chacko, T., Erdmer, P., 2000. Petrogenesis of the Cretaceous Cassiar batholith, Yukon–British Columbia, Canada: implications for magmatism in the North American Cordilleran Interior. Geological Society of America Bulletin 112 (7), 1119–1133.

Enkin, R.J., 2006. Paleomagnetism and the case for Baja British Columbia. *In:* Haggart, J.W., Enkin, R.J., Monger, J.W.H. (Eds.), Paleogeography of the North American Cordillera: Evidence For and Against Large-Scale Displacements. Geological Association of Canada, Special Paper 46, 233–253.

Evenchick, C.A., 1991. Geometry, evolution, and tectonic framework of the Skeena fold belt, north central British Columbia. Tectonics 10 (3), 527–546.

Evenchick, C.A., 2001. Northeast-trending folds in the western Skeena fold belt, northern Canadian Cordillera: a record of early Cretaceous sinistral plate convergence. Journal of Structural Geology 23, 1123–1140.

Faure, G., and Mensing, T.M., 2005, Isotopes: Principles and Applications, Third Edition: Printed by John Wiley & Sons, Inc, Hoboken, New Jersey. 897 p.

Fitch, T.J., 1972. Plate convergence, transcurrent faults, and internal deformation adjacent to southeast Asia and the western Pacific. Journal of Geophysical Research 77 (23), 4432-4460.

Foster, D.A., Schafer, C., Fanning, C.M., Hyndman, D.W., 2001, Relationships between crustal partial melting, plutonism, orogeny, and exhumation; Idaho-

Bitterroot batholiths: Tectonophysics 342 (3), 313-350.

Gareau, S.A., 1991. The Scotia–Quaal metamorphic belt: a distinct assemblage with pre- early Cretaceous deformational and metamorphic history, Coast Plutonic complex, British Columbia. Canadian Journal of Earth Sciences 28, 870–880.

Gehrels, G.E., Saleeby, J.B., and Berg, H.C., 1987, Geology of Annette, Gravina, and Duke Islands, southeastern Alaska: Canadian Journal of Earth Sciences 24, 866-881.

Gehrels, G.E., McClelland, W.C., Samson, S.D., Patchett, P.J., Orchard, M.J., 1992. Geology of the western flank of the Coast Mountains between Cape Fanshaw and Taku Inlet, southeastern Alaska. Tectonics 11, 567–585.

Gehrels, G.E., and Bergh, H.C., 1994, Geology of southeastern Alaska, *In:* Plafker, G., and Berg, H.C. (Eds.), The geology of Alaska: Boulder, Colorado, Geological Society of America, Geology of North America G-1, 451-467.

Gehrels, G.E., Rusmore, M., Woodsworth, G., Crawford, M., Andronicos, C., Hollister, L., Patchett, J., Ducea, M., Butler, R., Klepeis, K., Davidson, C., Friedman, R., Haggart, J., Mahoney, B. Crawford, W., Pearson, D., and Girardi, J., 2009, U-Th-Pb geochronology of the Coast Mountains batholith in north-coastal British Columbia: Constraints on age and tectonic evolution. Geological Society of America Bulletin 121, 1341-1361, DOI: 10.1130/B26404.1.

Giorgis, S., McClelland, W., Fayon, A., Singer, B.S., Tikoff, B., 2008. Timing of deformation and exhumation in the western Idaho shear zone, McCall, Idaho. Geological Society of America Bulletin 120 (9–10), 1119–1133.

Hollister, L.S., 1982. Metamorphic evidence for rapid (2 mm/yr) uplift of a portion of the central gneiss complex, Coast Mountains, B.C. Canadian Mineralogist 20, 319-332.

Hollister, L.S., Andronicos, C.L., 1997. A candidate for the Baja British Columbia

fault system in the Coast Plutonic Complex. GSA Today 7 (11), 1–7.

Hutchinson, W.W., 1982, Geology of the Prince Rupert – Skeena Map Area, British Columbia: Geological Survey of Canada, Memoir 394.

Ingram, G.M., and Hutton, D.H.W., 1994. The Great Tonalite Sill: Emplacement into a contractional shear zone and implications for Late Cretaceous to early Eocene tectonics in southwest Alaska and British Columbia. Geological Society of America Bulletin 106, 715-728.

Irving, E., 1985, Whence British Columbia?: Nature 314, 673-674.

Johnston, S.E., Tate, M.C., Fanning, C.M., 1999. New geologic mapping and SHRIMP U–Pb zircon data in the Peninsular Ranges batholith, Baja California, Mexico: evidence for a suture? Geology 27 (8), 743–746.

Karlstrom, K.E., and Williams, M.L., 1995, The case for synchronous deformation, metamorphism, and plutonism in the Crazy Basin area, central Arizona. Journal of Structural Geology 17, 59-81.

Klepeis, K.A., Crawford, M.L., Gehrels, G.E., 1998. Structural history of the crustal-scale Coast shear zone north of Portland Canal, southeast Alaska and British Columbia. Journal of Structural Geology 20, 883–904.

Mansfield, M.R., 2004. Thermal and structural evolution of the Grenville Channel shear zone, Coast plutonic complex, British Columbia: M.S. thesis, University of Texas, El Paso.

McCaffrey, R., 1992. Oblique plate convergence, slip vectors, and forearc deformation. Journal of Geophysical Research 97 (11).

McClelland, W.C., Gehrels, G.E., Samson, S.D., Patchett, P.J., 1992. Structural and geochronologic relations along the western flank of the Coast Mountains batholith; Stikine River to Cape Fanshaw, central southeastern Alaska: Journal of Structural Geology 14, 475–489.

McClelland, W.C., Tikoff, B., Manduca, C.A., 2000. Two-phase evolution of accretionary margins; examples from the North American Cordillera. Tectonophysics 326, 37–55.

Pickett, D.A., Saleeby, J.B., 1994. Nd, Sr and Pb isotopic characteristics of Cretaceous intrusive rocks from deep levels of the Sierra Nevada batholith, Tehachapi Mountains, California. Contributions in Mineralogy and Petrology 118, 198–205.

Roddick, J.A., 1970. Douglas Channel — Hecate Strait Map Area. British Columbia Geological Survey of Canada, Paper 70-41.

Rubin, C.M., Saleeby, J.B., 1992. Tectonic history of the eastern edge of the Alexander Terrane, southeast Alaska. Tectonics 11, 586–602.

Rusmore, M.E., Gehrels, G., Woodsworth, G.J., 2001. Southern continuation of the Coast shear zone and Paleocene strain partitioning in British Columbia–southeast Alaska. GSA Bulletin 113, 961–975.

Spear, F.S., 1995, Metamorphic phase equilibria and pressure-temperature-time paths: Mineralogical Society of America, Washington, D.C.. 799 p.

Stowell, H.H., Hooper, R.J., 1990. Structural development of the western metamorphic belt adjacent to the Coast Plutonic Complex, southeastern Alaska: evidence from Holkham Bay. Tectonics 9, 391–408.

Teyssier, C., Tikoff, B. and Markley, M. 1995. Oblique plate motion and continental tectonics. Geology 23, 447-450.

Teyssier, C. and Tikoff, B. 1998. Strike-slip partitioned transpression of the San Andreas fault system: a lithospheric scale approach. *In:* Holdsworth, R.E., Strachan, R.A. and Dewey, J.F. (Eds.), Continental Transpression and Transtension Tectonics. Geological Society, London, Special Publications 135, 143–158.

Tikoff, B., de Saint Blanquat, M., 1997. Transpressional shearing and strike-slip partitioning in the Late Cretaceous Sierra Nevada magmatic arc, California. Tectonics 16, 442–459.

Tikoff, B., Teyssier, C., and Waters, C., 2002. Clutch tectonics and the partial attachment of lithospheric layers. *In:* Bertotti, G., Schulmann, K. and Cloetnch, S. (Eds.) Continental Collision and the Tecton-sedimentary evolution of Forelands. European Geophysical Society, Special Publications 1, 119-144.

Umhoefer, P. J., 1987. Northward translation of "Baja British Columbia" along the Late Cretaceous to Paleocene margin of western North America: Tectonics 6, 377–394.

van der Heyden, P., 1989. U–Pb and K–Ar geochronometry of the Coast Plutonic Complex, 53° N–54° N, and implication for the Insular–Intermontane superterrane boundary, British Columbia: Ph.D. thesis, University of British Columbia.

van der Heyden, P., 1992. A Middle Jurassic to Early Tertiary Andean-Sierran arc model for the Coast Belt of British Columbia. Tectonics 11, 82-97.

Wolf, D.E., Andronicos, C.L., Vervoort, J.D., Mansfield, M.R., Chardon, D., 2010. Application of Lu-Hf garnet dating to unravel the relationships between deformation, metamorphism and plutonism: An example from the Prince Rupert area, British Columbia. Tectonophysics 485, 62-77. DOI: 10.1016/j.tecto.2009.11.020.

Wyld, S.J., Wright, J.E., 2001. New evidence for Cretaceous strike-slip faulting in the United States cordillera and implications for terrane-displacement, deformation patterns, and plutonism. American Journal of Science 301, 150–181.

CHAPTER 2

APPLICATION OF LU-HF GARNET DATING TO UNRAVEL THE RELATIONSHIPS BETWEEN DEFORMATION, METAMORPHISM AND PLUTONISM: AN EXAMPLE FROM THE PRINCE RUPERT AREA, BRITISH COLUMBIA, CANADA*

Abstract

The tectonic history of the Prince Rupert area is marked by profound crustal thickening from thrusting that produced inverted metamorphic field gradients and transpression in crustal-scale shear zones. Syn-tectonic garnet in the Prince Rupert area has Lu–Hf ages of 102.6 ± 3.7 Ma and 108.3 ± 4.1 Ma (2σ). Porphyroblast–matrix relationships in these samples, and samples from the same outcrops, indicate syn-tectonic garnet growth. These relationships imply that the garnet ages directly date the development of the metamorphic foliations. A third sample of migmatitic garnet amphibolite from the contact aureole of the 94–90 Ma Ecstall pluton had complex isotope systematics interpreted to indicate a garnet growth episode ~105 Ma, similar to the ages obtained from the other samples and a growth or equilibration event at ~94 Ma during pluton emplacement. The data show that the older Lu–Hf garnet ages date prograde metamorphism during foliation development and modification during pluton emplacement. The Ecstall pluton was emplaced 10 to 15 m.y. after regional metamorphism and thrust stacking in the Prince Rupert area.

In order to place our samples in a regional tectonic context we compare our results to patterns of regional deformation, metamorphism and plutonism throughout the North American Cordillera in the time period between 110 and 85 Ma. Contractional and transpressional deformation occurred throughout much of the North

American Cordillera at this time, from southeastern Alaska to the Baja Peninsula in Mexico. Left-lateral transpression dominated the Canadian Cordillera, whereas, right-lateral transpression affected areas south of the Idaho–Salmon River suture zone, including the Sierra Nevada batholith. This reversal in kinematics in the northern and southern cordillera within coeval magmatic belts appears to be a first-order feature of the geology of the North American Cordillera during the Cretaceous.

* Reprinted from Tectonophysics, v. 485, Wolf, D.E., Andronicos, C.L., Vervoort, J.D., Mansfield, M.R., and Chardon, D., Application of Lu-Hf garnet dating to unravel the relationships between deformation, metamorphism and plutonism: An example from the Prince Rupert area, British Columbia, © 2010, DOI: 10.1016/j.tecto.2009.11.020, with permission from Elsevier.

1. Introduction

Several distinct scenarios have been proposed for the tectonics of the Coast Mountains; each makes unique predictions about the timing of deformation and plutonism. These hypotheses can be tested using precision geochronology, especially when focusing on syn-tectonic metamorphic minerals that provide the opportunity to directly constrain the timing of deformation, metamorphism, and plutonism. Garnet geochronology has previously been utilized as a method to date prograde metamorphism and thermal events, using both Sm–Nd (Burton and O'Nions 1991; Getty et al. 1993; Stowell and Goldberg 1997) and Lu–Hf isotopic systems (Scherer et al. 2000; Lapen et al. 2003; Anczkiewicz et al. 2004).

Here we present Lu–Hf garnet ages from three samples of schist and gneiss that occupy distinct positions within the western flank of the Coast Mountains in British Columbia near 54° N latitude. One sample was collected from between Ecstall pluton and the Grenville Channel shear zone, a second is from the strain gradient between Grenville Channel and Prince Rupert Harbour, and a third was collected from the aureole of the Ecstall Pluton within 500 m of the pluton at its most northeastern corner (Figure 4). Our new data show that amphibolite facies metamorphism and deformation within the western metamorphic belt (WMB) predated emplacement of the Ecstall pluton. Complex Lu–Hf systematics from a garnet amphibolite near the margin of the Ecstall pluton document deformation in the WMB and contact metamorphism during pluton emplacement. These results better constrain the timing of structures in the Prince Rupert area, where K/Ar and Ar/Ar ages constrain the timing of cooling of the WMB from peak temperatures.

Our new ages are consistent with models that indicate deformation was synchronous with left-lateral transpression within the Canadian Cordillera (Chardon et al. 1999; Chardon 2003), widespread deformation and magmatism within the Sierra

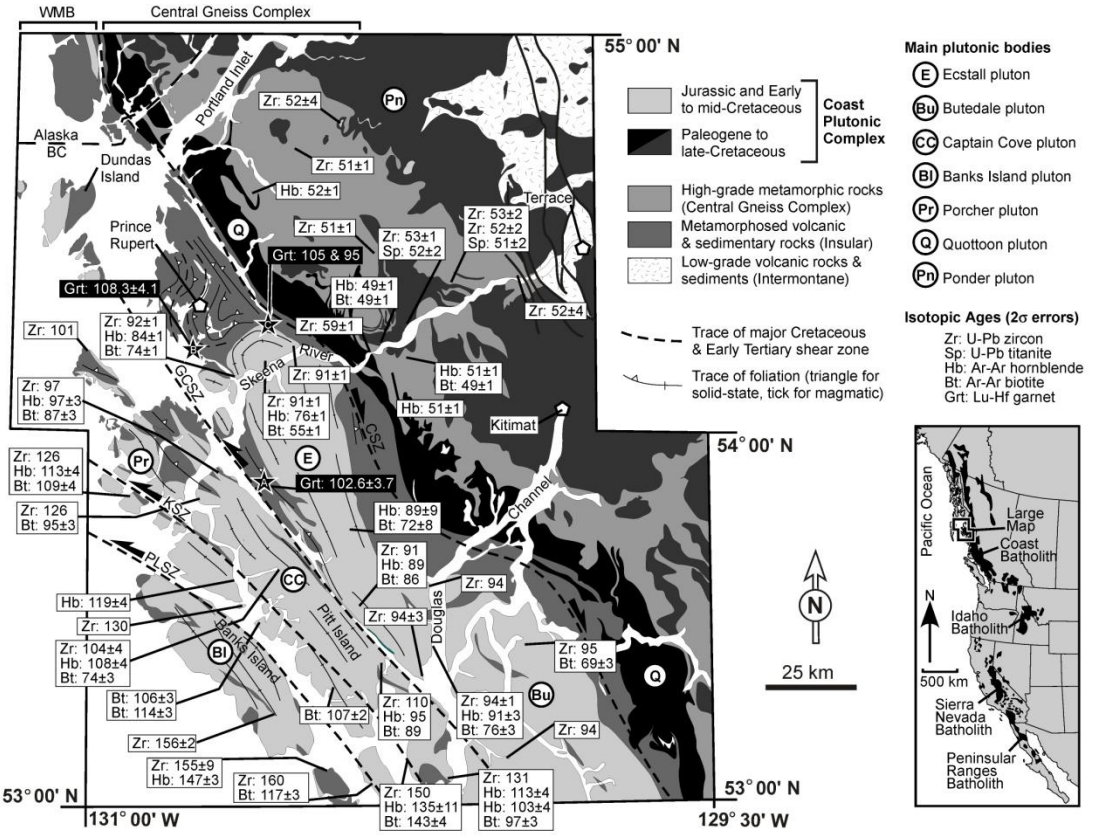

Figure 4. Simplified geologic map of the Coast Mountains between 53° and 55° N latitude (modified from Chardon et al. 1999). Foliations are representative of average trends for solid-state fabrics in metamorphic rocks and magmatic fabrics in plutonic bodies. CSZ — Coast shear zone, GCSZ — Grenville Channel shear zone, KSZ — Kitkatla shear zone, PLSZ — Principe Laredo shear zone. Sample locations from this study marked by stars with corresponding ages in black boxes: A is Kumealon Inlet (G-16), B is Ridley Island (98–114) and C is Minerva Lake (06B-57). Age on Banks Island is an average of five zircon ages ranging from 153 ± 1 to 157 ± 1 Ma. Inset map shows location of field area in the western North America cordillera with Cretaceous batholiths in black modified from Driver et al. (2000). Lithologies, foliations and structures compiled from: Roddick 1970, Crawford and Hollister 1982, Hutchinson 1982, van der Heyden 1989, Gareau 1991, Cook and Crawford 1994, Andronicos et al. 1999, Chardon et al. 1999, Rusmore et al. 2001 and Mansfield 2004; this study. Reported ages are 2σ error, compiled from: van der Heyden 1989, Butler et al. 2002, Chardon 2003 and Andronicos et al. 2003; this study.

Nevada (Busby-Spera and Saleeby 1990; Ducea 2001), and contraction and plutonism within the Idaho suture zone (McClelland et al. 2000; McClelland and Oldow 2007; Giorgis et al. 2008). Plate-scale transpressional deformation is also observed throughout the North American Cordillera between 110 and 90 Ma (Hurlow 1993; Monger et al. 1994; Chardon et al. 1999; Wyld and Wright 2001; Umhoefer 2003). Various plutonic bodies in the Coast Mountains of British Columbia were emplaced during this time period, but their exact relationship to transpressional structures has only been recognized within the last ten years (Chardon et al. 1999). Use of Lu–Hf dating of garnet enables us to directly date prograde metamorphism and development of deformational fabrics and better constrain the timing of transpressional deformation with respect to plutonism.

2. Regional Geology

The western Canadian Cordillera and Coast Mountains of British Columbia were assembled through terrane accretion during the Jurassic and Cretaceous, but the source of those terranes and mechanics of emplacement are still widely debated. Two end-member models for the paleogeography of the Canadian Cordillera based on paleomagnetic and geological data have been put forward (Cowan et al. 1997). The first interprets shallow paleomagnetic inclinations to result from a variety of processes including tilting, shallowing of inclination during sediment compaction, and in situ deformation (e.g. Butler et al. 2006). Alternatively, analysis of paleomagnetic data for which tilting, inclination shallowing and in situ deformation can be evaluated has been interpreted to indicate large-scale translations of terranes from southern latitudes (Enkin 2006). Further complicating the issue is the fact that plate reconstructions from this period are limited by either the lack of preserved magnetic reversals during the Cretaceous Supernormal from 124 to 84 Ma (Engebretson et al. 1985) or the lack of

sea floor magnetic anomalies in the Pacific basin (Lonsdale 1995). Therefore, high-quality geochronology that constrains deformation events within the continental margin is an even more critical ingredient in deciphering the paleogeography of North America.

The tectonic history of the western flank of the Coast Mountains in British Columbia is marked by phases of contractional and transpressive deformation that include the development of crustal-scale thrust slices with inverted metamorphic gradients (Crawford and Hollister 1982; Crawford et al. 1987; Crawford et al. 2000) segmented by transpressive shear zones (Chardon et al. 1999; Chardon 2003). The central Coast Mountains in the vicinity of Prince Rupert are composed of greenschist to upper amphibolite facies rocks (Hutchinson 1982) that have been correlated with the Alexander, Yukon–Tanana, and Taku terranes, as well as rocks of the Gravina basin (Crawford et al. 2000). This assemblage of rocks has been referred to as the western metamorphic belt (WMB) (Brew and Ford 1978; Stowell and Hooper 1990; Crawford et al. 2000). These rocks are intruded by plutons of Jurassic to Cretaceous age and are separated from the late Cretaceous to Paleogene high-grade core of the orogen by the Coast shear zone (Crawford and Hollister 1982; Hutchinson 1982; Klepeis et al. 1998; Andronicos et al. 1999). West of the Coast shear zone and southwest of Prince Rupert, three left-lateral transpressive shear zones cut the western metamorphic belt. From west to east these are the: Principe Laredo, Kitkatla, and Grenville Channel shear zones (Chardon et al. 1999). To the northwest of Prince Rupert and extending into southeast Alaska, east-dipping crustal-scale thrust shear zones are associated with inverted metamorphic field gradients (Crawford and Hollister 1982; Rubin and Saleeby 1992; Klepeis et al. 1998). The thrusts are interpreted from wide-angle seismic refraction to extend to middle and lower crustal depths where they are truncated by the Coast shear zone (Morozov et al. 1998;

Hollister and Andronicos 2006).

The timing of deformation and peak metamorphism near Prince Rupert has been inferred to be synchronous with emplacement of the Ecstall pluton based on plutonic U/Pb zircon ages and K/Ar and $^{40}Ar/^{39}Ar$ cooling ages from hornblende and biotite (van der Heyden 1989; Crawford et al. 2000; Butler et al. 2002). Butler et al. (2002) published zircon crystallization ages from the northern part of the Ecstall pluton that indicated this part of the pluton crystallized between 91.5 ± 1.0 Ma and 90.5 ± 1.0 Ma. K–Ar and $^{40}Ar/^{39}Ar$ ages in hornblende range from 84 ± 3 in the west to 76 ± 3 in the east, and in biotite range from 74 ± 3 to 55 ± 3, and have been interpreted to indicate the pluton was emplaced synchronously with regional metamorphism (van der Heyden 1989; Crawford et al. 2000). Emplacement of the pluton occurred at depths of 25 km (800 ± 50 MPa) and was followed by a clockwise P–T paths of decreasing pressure and temperature (Crawford et al. 2000; Mansfield 2004). Hollister et al. (2004) combined cooling ages with thermal models to show that the eastern part of the western metamorphic belt was reheated during emplacement of the Quottoon pluton at 59 Ma (Gehrels et al. 1991).

3. Geochemical Methods

All isotopic work was performed in the radiogenic isotope laboratory at Washington State University. Rock samples were ground with a mortar and pestle to sand-sized grains and handpicked into ~ 250 mg garnet and garnet-free 'whole-rock' fractions. Garnet fractions were dissolved in Savillex© beakers on hot plates, while whole-rock fractions were dissolved using both Savillex© vials and Teflon© capsules in steel pressure vessels. Both methods used a 10:1 mixture of concentrated HF and HNO3 for the primary dissolution. Samples were spiked with mixed $^{176}Lu/^{180}Hf$ tracers for the accurate determination of Lu–Hf ratios necessary for geochronology.

Separation of Lu and Hf followed established chromatographic techniques and has been described elsewhere (Münker et al. 2001; Vervoort et al. 2004; Cheng et al. 2008). Isotopic ratios of the purified elements were measured on a ThermoFinnigin© Neptune multi-collector inductively coupled plasma-mass spectrometer (MC-ICP-MS). Analytical details including data reduction methods are provided in Vervoort et al. (2004) and Cheng et al. (2008). Garnet Lu–Hf ages were calculated using $\lambda\ ^{176}Lu = 1.867 \times 10^{-11}\ y^{-1}$ (Scherer et al. 2001; Söderlund et al. 2004) and using Isoplot 3.61 (Ludwig 2003). Initial $^{176}Hf/^{177}Hf$ and ε_{Hf} values were calculated using $^{176}Hf/^{177}Hf = 0.282785$ and $^{176}Lu/^{177}Hf = 0.0336$ for CHUR (Bouvier et al. 2008). The three samples dated were: G-16A from Kumealon Inlet, on the western edge of the Ecstall pluton, proximal to the Grenville Channel Shear Zone; 98–114A from the west shore of Ridley Island to the northeast of the Grenville Channel Shear Zone; and 06B-57 from the northeast margin of the Ecstall Pluton near Minerva Lake (Figure 4).

Electron microprobe analyses for thermobarometry were completed at the University of Texas at El Paso on a Cameca SX 50 and at Cornell University on a JEOL 8900. Qualitative wavelength dispersive scanning (WDS) X-ray maps were collected by moving the stage beneath a fixed beam with a beam current of 100 or 250 ηa and a beam size 5 or 10μm, depending on the image size. Operating conditions for quantitative WDS analysis were 20 KeV and 20 ηa, using a 2 μm beam for most minerals and a 10 μm beam for micas to prevent alkali loss. Whole-rock chemical analysis for phase diagram calculations was determined by X-ray fluorescence at Washington State University's GeoAnalytical Lab.

4. Sample descriptions, petrology and results

4.1 Kumealon Inlet

Kumealon Inlet (Figure 4, Locality "A") is a narrow inlet on the eastern side of

Grenville Channel and sits between the Ecstall Pluton and the Grenville Channel shear zone (GCSZ). At the map scale, foliations strike to the northwest and dip steeply towards the Ecstall pluton. Lineations are shallowly plunging parallel to the strike of the foliations, consistent with a large strike-slip component to the deformation. In the outcrop containing the dated sample G-16A, the average outcrop-scale foliation strikes 330° and dips 61° SW, sub-parallel to the GCSZ. This foliation becomes steeper through the inlet as Grenville Channel is approached, tracking the strain gradient into the shear zone (Mansfield 2004). Aligned hornblende, biotite and elongate plagioclase grains define mineral lineations. Granodiorite dikes that crosscut the schist and orthogneiss are folded into upright, open folds with axial surfaces sub-parallel to the GCSZ.

The outcrop from which sample G-16 was collected is composed of schist with inter-beds of orthogneiss and amphibolite on the north shore of Kumealon Inlet, west of the Ecstall Pluton (Figure 4). The mineral assemblage for the dated sample is garnet–muscovite–quartz–plagioclase–microcline–biotite with trace chlorite, magnetite and ilmenite. Garnets are <1 mm in diameter (Figure 5A). The chlorite appears to be retrograde based on its presence parallel to cleavage planes of both muscovite and biotite, and as undeformed clots adjacent to a few of the garnets. The garnets have poikilitic cores containing muscovite, quartz and fine-grained ilmenite and magnetite. The foliation is differentiated into quartz and mica-rich domains. Plagioclase is asymmetrically deformed into sigma-type porphyroclasts between mica-rich domains, and indicates a left-lateral sense of shear when viewed parallel to the lineation and perpendicular to the foliation.

Garnet inclusion–matrix relationships were studied in several samples with different bulk compositions from the same outcrop. Within the dated sample, the garnet has thin inclusion poor rims, surrounding inclusion rich cores. The matrix

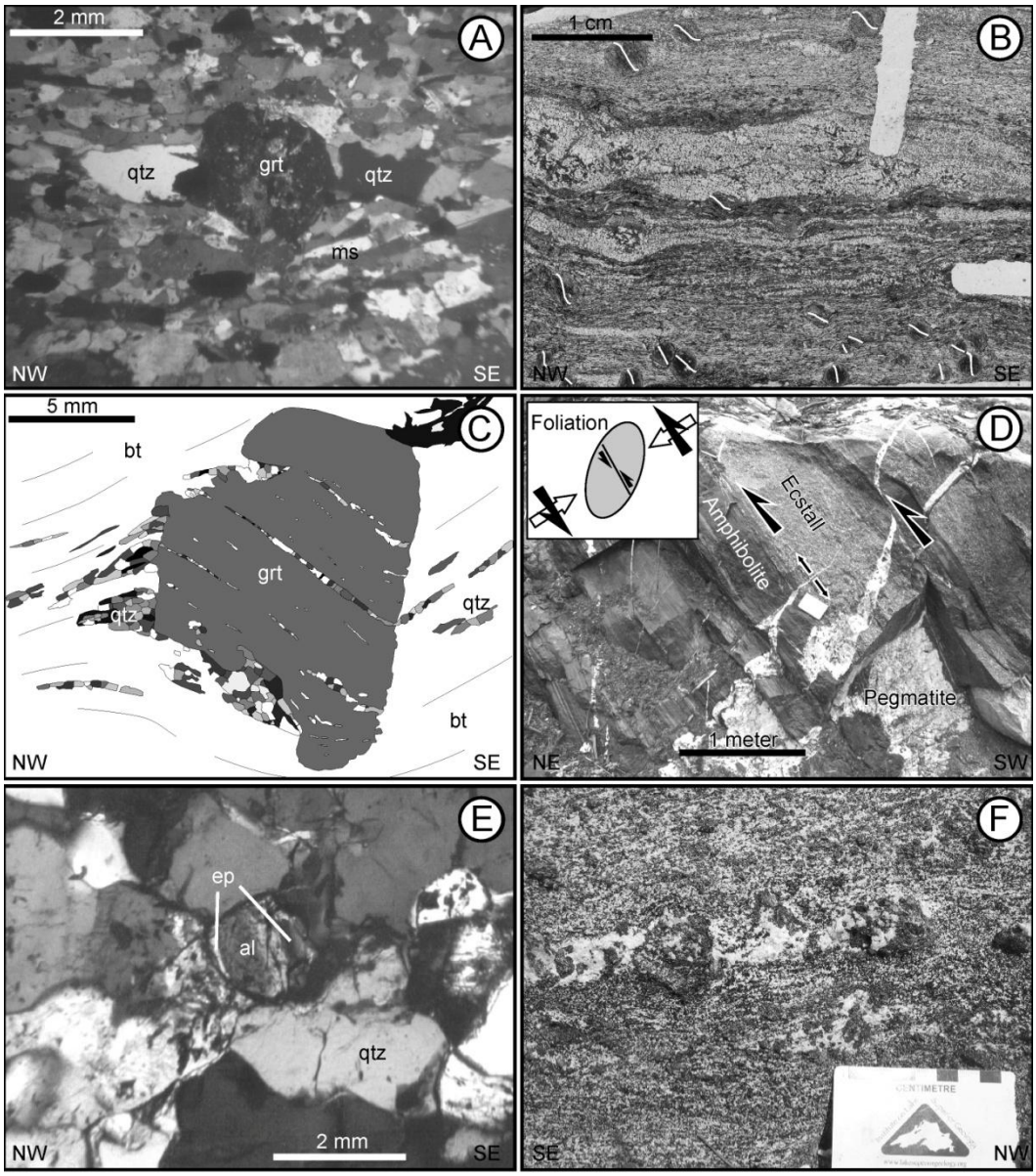

Figure 5. Caption on following page.

Figure 5. Photomicrographs and sketches of samples. A: Garnet from Kumealon Inlet, G-16, with symmetrical quartz tails forming a theta-type porphyroclast, consistent with flattening across the foliation. B: Scan of a thin section of G-16D. White lines across the garnets show the orientations of inclusion trails within the garnets. The variations observed between garnet grains appear to define a fold only preserved within the inclusion trails that has been transposed in the matrix. C: Garnet from Ridley Island, sample 98–114. Note curved inclusion trails consistent with early tectonic garnet growth. D: Field photograph from Minerva Lake showing intrusive contact between Ecstall pluton and host amphibolite. The magmatic foliation in the Ecstall is concordant with the contact. Pegmatite dikes occur as Mode-I fracture, opening perpendicular to the foliation. Melt-filled fractures are consistent with pluton-side-up deformation as the pluton is emplaced. E: Sample from Minerva Lake, 06B-57, with allanite core rimmed by epidote. Note the epidote forms wings on the allanite consistent with epidote growth during deformation. The presence of allanite rimmed by epidote is consistent with migmatization at mid-crustal levels in a thickened crust, in the stability field of magmatic epidote (Schmidt and Poli 2004), during contact metamorphism as the Ecstall pluton was emplaced. F: Outcrop photo of garnets concentrated in leucosomes from Minerva Lake, 06B-57, consistent with garnet growth during migmatization as the Ecstall pluton was emplaced.

foliation wraps around the garnet. Slightly asymmetrical tails of quartz are present on a few of the garnets indicating a left-lateral sense of shear (Figure 5A). In more biotite- rich lithologies, the cores of the garnet are extremely rich in fine-grained inclusions of ilmenite, whereas the rims are inclusion poor, similar to the dated sample. Inclusions in the garnet cores in the biotite-rich samples are up to 60° oblique to the matrix foliation and curve smoothly into the matrix foliation, although the curvature occurs entirely within the rims. The garnet inclusions are not parallel from grain to grain, but they do have a systematic pattern at the scale of the thin section. This inclusion pattern appears to define a fold that has been completely transposed within in the matrix of the sample and is only recorded by the variation in inclusion trails within the garnet cores (Figure 5B). Kinematic indicators including strain shadows around garnet, shear bands, and asymmetric folds, all consistently indicate left-lateral strike-slip shear. Taken together, the porphyroblast matrix relationships, map patterns, and kinematic indicators indicate garnet growth during shortening and left- lateral strike-slip shearing, consistent with transpressional deformation during garnet growth.

A garnet-bearing sample from the outcrop of G-16 (sample G-16D) was analyzed by electron microprobe. The mineral assemblage in this sample is garnet–biotite–muscovite–quartz–sillimanite–ilmenite. This mineral assemblage may have developed by a reaction such as staurolite + muscovite = garnet + sillimanite + biotite (Spear and Cheney 1989). Staurolite was not observed within the outcrop of the studied sample, but is a common mineral in other portions of the WMB farther to the north. WDS X-ray images and quantitative WDS analysis show that the garnets do not vary in composition from core to rim (Figure 6A). The garnets are almandine rich, with a slight gradient in Fe concentration across the garnets (e.g., Figure 6A). The side of the garnet with the lower concentration of Fe is adjacent to another garnet, whereas

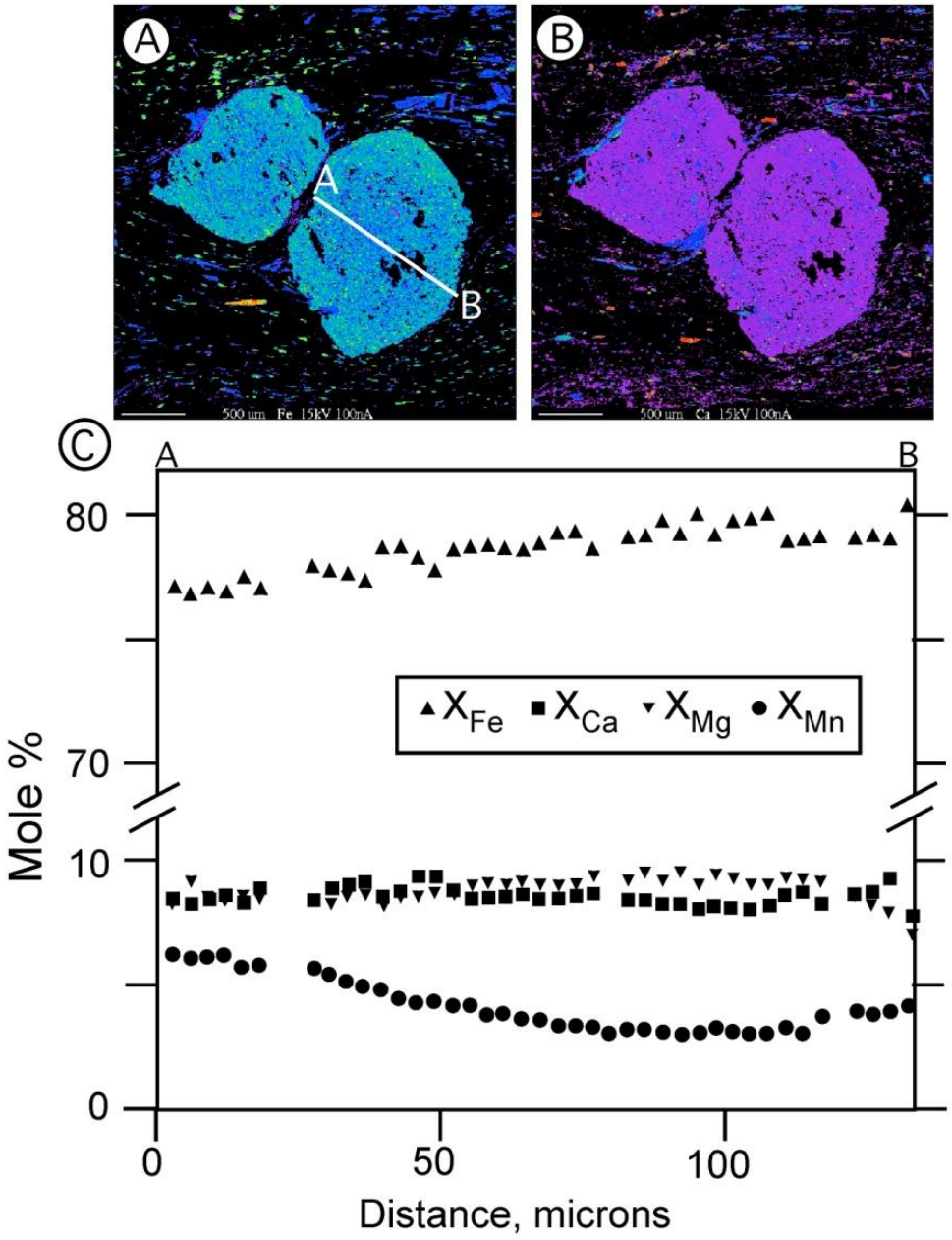

Figure 6. X-ray intensity maps and compositional line scan collected for sample G16D. A) X-ray intensity map for Fe Kα Line marked A–B is location of line scan shown in (C). B) X-ray intensity map for Ca Kα. Note that neither Fe nor Ca show significant zoning at the resolution of the X-ray maps. In both X-ray maps blues and purples are low concentrations and reds and yellows are higher concentrations. C) Compositional line scan collected by quantitative wavelength dispersive scanning analysis.

the other is in contact with the matrix of the sample, suggesting that this side may have affected by diffusion. Mn contents are slightly lower in the core of the garnet and increase towards the rims. Ca and Mg are nearly constant in composition and both show a small decrease in concentration on the rim adjacent to the matrix, whereas the rim next the other garnet appears to have a nearly constant composition. These relatively flat profiles across the garnets are likely a result of diffusion at high temperature (Tracey et al. 1976; Woodsworth 1977). The garnets do not appear to be substantially resorbed as they have euhedral to subhedral crystal form and there are no changes in texture or mineralogy of the matrix phases near the garnets.

P–T calculations were made using the computer program WinTWQ 2.10 (Berman 1991, 2007). Calculations were made using the thermo- dynamic database of Berman (1988). Non-ideal mixing corrections for K–Na exchange in muscovite were made using the model of Chatterjee and Froese (1975). Corrections for non-ideal mixing in garnet were made using the model of Berman, (1991) and for biotite using the model of McMullin et al. (1991). The resultant P–T estimates is 326 MPa and 557 °C based on the intersection of the linearly independent reactions almandine + muscovite = sillimanite + quartz + annite and phlogopite + almandine = annite + pyrope (Table 1). We have not formally estimated the error on our P–T estimates, but assume an arbitrary error of ± 50 °C and ± 100 MPa. As discussed below this result falls to lower and pressures and temperatures than that derived from a calculated isochemical phase diagram for sample G-16A, the dated sample. This is likely due to the retrograde replacement of biotite by chlorite as well as modification of the garnet composition by diffusion resulting in the mineral compositions not recording peak equilibrium conditions.

In order to provide better constraints on the P–T conditions recorded within Kumealon Inlet, an isochemical phase diagram for the dated sample (G-16A) was

Table 1. Representative microprobe mineral analyses* for sample G16 from Kumealon Inlet

Weight % Oxides

Oxides	Garnet	Biotite	Muscovite	Ilmenite
SiO_2	35.12	32.54	45.25	0.25
TiO_2	0.00	1.70	0.70	49.41
Al_2O_3	21.20	18.74	35.54	0.21
FeO	36.10	24.32	1.97	47.89
MnO	1.81	0.04	0.01	1.57
MgO	1.79	8.40	0.71	0.01
CaO	3.03	0.10	0.00	0.07
Na_2O	0.05	0.38	0.38	0.03
K_2O	0.02	9.81	9.81	0.01
Total	99.12	96.03	94.37	99.45

Ions in Formula†

Element	Garnet	Biotite	Muscovite	Ilmenite
Si	2.898	2.550	3.040	0.004
Ti	0.000	0.100	0.035	0.637
Al	2.062	1.730	2.814	0.004
Fe^{2+}	2.491	1.594	0.111	0.686
Mn	0.127	0.003	0.001	0.023
Mg	0.220	0.981	0.071	0.000
Ca	0.268	0.008	0.000	0.001
Na	0.008	0.058	0.050	0.001
K	0.002	0.981	0.841	0.000
Total	8.076	8.004	6.962	1.357

* Representative analyses were chosen for plagioclase, garnet interior and rim, and ilmenite inclusion. Biotite, muscovite and chlorite numbers were produced from averaging multiple analyses.
† Stoichiometric ratios of elements based on 12 oxygen for garnet, 11 for biotite, 11 for muscovite, 8 for plagioclase, 2 for ilmenite, 10 for chlorite.

made using the Theriak–Domino software version 150508 (http://titan.minpet.unibas.ch/minpet/theriak/theruser.html), based on the Gibbs free energy minimization algorithm of de Capitani and Brown (1987). Phase diagram calculations used the thermodynamic database of Berman (1988 and 1991), and are internally consistent with calculations made using WinTWQ. Mn was excluded from the phase diagram calculation as it only accounts for 0.29% of the bulk rock composition. Water was assumed to be a pure phase and fluid pressure was assumed to equal total pressure. The resultant phase diagram (Figure 7) reproduces the mineral assemblage of the dated sample well and suggests P–T conditions between 640° and 720° C and pressures between 360 and 810 MPa. Although this is a rather wide range in P–T conditions, this result is likely a better estimate of P–T then obtained by using WinTWQ because diffusion at high temperature altered the garnet composition from the peak equilibrium compositions and the evidence that biotite has retrogressed to chlorite.

Lu–Hf dating of garnet from this sample produced a robust isochron at 102.6 ± 3.7Ma (2σ error), with an MSWD=1.5 (Figure 8A). This isochron is defined by three whole-rock and seven garnet fractions. Fractions were picked under a microscope from a crushed bulk sample. The 176Lu/177Hf ratios for the garnet fractions ranged from 0.09 to 0.14 (Table 4). Attention was paid to remove Hf-rich ilmenite inclusions from the garnet fractions, so variation in the $^{176}Lu/^{177}Hf$ and $^{176}Hf/^{177}Hf$ values between different fractions could be attributed to zone partitioning of Lu into the garnet (Lapen et al. 2003; Lapen et al. 2005; Kohn 2009). The low $^{176}Lu/^{177}Hf$ ratios in all of the garnet fractions, however, indicate that significant amounts of fine-grained ilmenite likely still remained in the garnet fractions. The initial $^{176}Hf/^{177}Hf$ for the Kumealon Inlet sample G-16 was 0.282877 ± 9 with an initial ε_{Hf} =+3.3 ± 0.3.

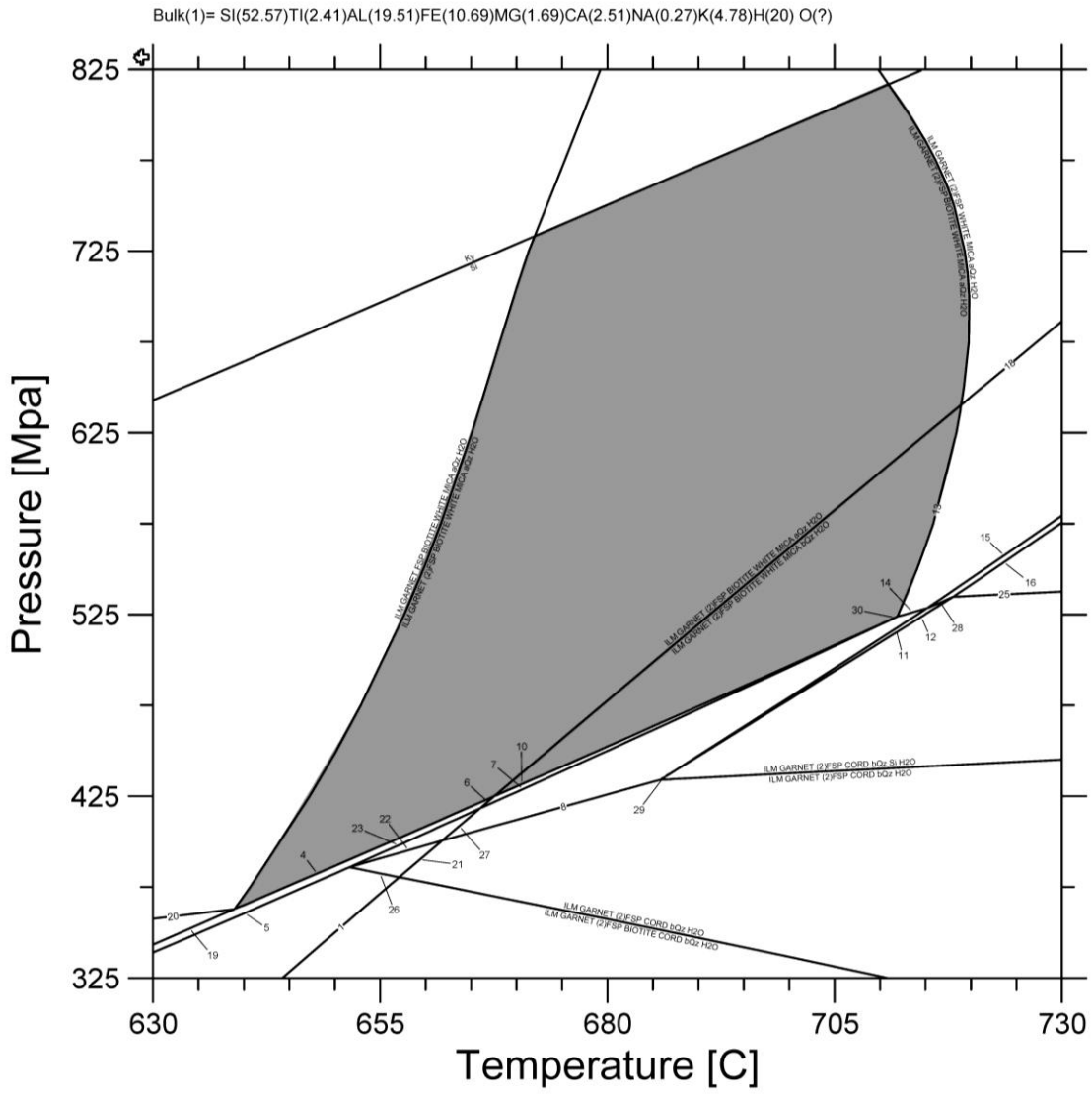

Figure 7. Isochemical phase diagram calculated using Theriak–Domino software. Gray shaded region shows estimated stability field for the mineral assemblage observed in sample G16A, which was dated. Rock bulk chemistry is shown across top of Figure. Note that the kyanite–sillimanite boundary was not produced as a result of the phase diagram calculation. However, sillimanite occurs in the outcrop from which the dated sample was collected, so the kyanite–sillimanite boundary is used as an additional constraint on *P–T* conditions. Table 2 gives definitions of mineral abbreviations shown on the phase diagram. A complete list of reactions on the phase diagram is given in Table 3.

Table 2. Definitions of mineral abbreviations shown on phase diagrams

Abbreviation	Mineral
aQz	Alpha quartz
Alm	Almandine
An	Anorthite
Ann	Annite
bQz	Beta quartz
CHL	Chlorite
CORD	Cordierite
CTOID	Chloritoid
FSP	Plagioclase or K-feldspar
FSP(2)	Both plagioclase and K-feldspar
Gr	Grossular
H2O	Water
ILM	Ilmenite
Ky	Kyanite
Ms	Muscovite
Phl	Phlogopite
Py	Pyrope
Si	Sillimanite
STAU	Staurolite

Table 3. Changes in mineral assemblages for phase diagram of sample G16A

Reaction number	Mineral assemblage, reactants	Mineral assemblage, products
1	ILM GARNET (2)FSP BIOTITE CORD aQz H2O	ILM GARNET (2)FSP BIOTITE CORD bQz H2O
2	ILM GARNET (2)FSP BIOTITE CORD bQz H2O	ILM GARNET (2)FSP CORD bQz H2O
3	ILM GARNET FSP BIOTITE WHITE MICA aQz H2O	ILM GARNET (2)FSP BIOTITE WHITE MICA aQz H2O
4	ILM GARNET (2)FSP BIOTITE WHITE MICA aQz H2O	ILM GARNET (2)FSP BIOTITE WHITE MICA CORD aQz H2O
5	ILM GARNET (2)FSP BIOTITE WHITE MICA CORD aQz H2O	ILM GARNET (2)FSP BIOTITE CORD aQz H2O
6	ILM GARNET (2)FSP BIOTITE WHITE MICA CORD aQz H2O	ILM GARNET (2)FSP BIOTITE WHITE MICA CORD bQz H2O
7	ILM GARNET (2)FSP BIOTITE WHITE MICA CORD bQz H2O	ILM GARNET (2)FSP WHITE MICA CORD bQz H2O
8	ILM GARNET (2)FSP WHITE MICA CORD bQz H2O	ILM GARNET (2)FSP CORD bQz H2O
9	ILM GARNET (2)FSP BIOTITE WHITE MICA aQz H2O	ILM GARNET (2)FSP BIOTITE WHITE MICA bQz H2O
10	ILM GARNET (2)FSP BIOTITE WHITE MICA bQz H2O	ILM GARNET (2)FSP BIOTITE WHITE MICA CORD bQz H2O
11	ILM GARNET (2)FSP WHITE MICA CORD bQz H2O	ILM GARNET (2)FSP WHITE MICA CORD bQz Si H2O
12	ILM GARNET (2)FSP WHITE MICA CORD bQz Si H2O	ILM GARNET (2)FSP CORD bQz Si H2O
13	ILM GARNET (2)FSP BIOTITE WHITE MICA bQz H2O	ILM GARNET (2)FSP WHITE MICA bQz H2O
14	ILM GARNET (2)FSP WHITE MICA bQz H2O	ILM GARNET (2)FSP WHITE MICA CORD bQz H2O
15	ILM GARNET (2)FSP WHITE MICA bQz H2O	ILM GARNET (2)FSP WHITE MICA bQz Si H2O
16	ILM GARNET (2)FSP WHITE MICA bQz Si H2O	ILM GARNET (2)FSP bQz Si H2O
17	ILM GARNET (2)FSP BIOTITE WHITE MICA aQz H2O	ILM GARNET (2)FSP WHITE MICA aQz H2O
18	ILM GARNET (2)FSP WHITE MICA aQz H2O	ILM GARNET (2)FSP WHITE MICA bQz H2O
19	ILM GARNET FSP BIOTITE WHITE MICA CORD aQz H2O	ILM GARNET (2)FSP BIOTITE WHITE MICA CORD aQz H2O
20	ILM GARNET FSP BIOTITE WHITE MICA aQz H2O	ILM GARNET FSP BIOTITE WHITE MICA CORD aQz H2O
21	ILM GARNET (2)FSP CORD bQz H2O	ILM GARNET (2)FSP CORD aQz H2O
22	ILM GARNET (2)FSP WHITE MICA CORD aQz H2O	ILM GARNET (2)FSP CORD aQz H2O
23	ILM GARNET (2)FSP BIOTITE WHITE MICA CORD aQz H2O	ILM GARNET (2)FSP WHITE MICA CORD aQz H2O
24	ILM GARNET (2)FSP CORD bQz Si H2O	ILM GARNET (2)FSP CORD bQz H2O
25	ILM GARNET (2)FSP bQz Si H2O	ILM GARNET (2)FSP CORD bQz Si H2O
26	ILM GARNET (2)FSP CORD aQz H2O	ILM GARNET (2)FSP BIOTITE CORD aQz H2O
27	ILM GARNET (2)FSP WHITE MICA CORD bQz H2O	ILM GARNET (2)FSP WHITE MICA CORD aQz H2O
28	ILM GARNET (2)FSP WHITE MICA bQz Si H2O	ILM GARNET (2)FSP WHITE MICA CORD bQz Si H2O
29	ILM GARNET (2)FSP WHITE MICA CORD bQz H2O	ILM GARNET (2)FSP CORD bQz Si H2O
30	ILM GARNET (2)FSP BIOTITE WHITE MICA bQz H2O	ILM GARNET (2)FSP WHITE MICA CORD bQz H2O
31	ILM GARNET (2)FSP BIOTITE WHITE MICA CORD aQz H2O	ILM GARNET (2)FSP CORD aQz H2O
32	ILM GARNET (2)FSP WHITE MICA bQz H2O	ILM GARNET (2)FSP WHITE MICA CORD bQz Si H2O

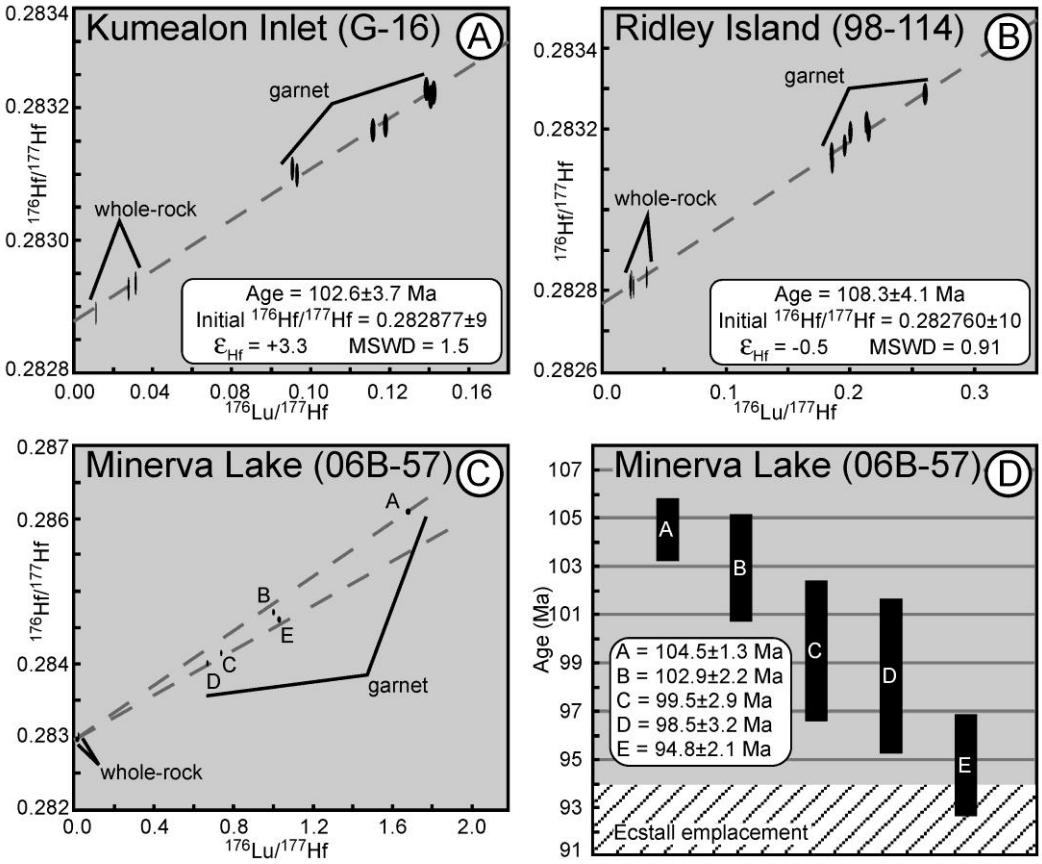

Figure 8. Plots of geochemical data with 2σ error ellipses and boxes. A: The sample from Kumealon Inlet, G-16, produced a robust isochron from seven garnet fractions and three whole-rock fractions. B: The sample from Ridley Island, 98–114, produced a robust isochron from seven garnet and five whole-rock fractions. C: The sample from Minerva Lake, 06B-57, had complex isotope systematics that precluded a single isochron. D: Individual isochrons were produced using an average initial $^{176}Hf/^{177}Hf$ value, estimated from the other samples, and single garnet fractions, and were plotted as a weighted average. The hatched-area indicates the period when the Ecstall was emplaced, constrained from U–Pb zircon ages. These garnet ages show a range in garnet growth from 104.5 to 94.8 Ma. Data used to produce plots in Table 4.

Table 4. Lu-Hf data for analyzed garnet samples in the western metamorphic belt

Sample*	Lu (ppm) †	Hf (ppm) †	$^{176}Lu/^{177}Hf$ §	$^{176}Hf/^{177}Hf$ #	2σ (abs)**
G-16A, Kumealon Inlet					
sav WR	1.25	6.38	0.0278	0.282928	0.000004
bomb WR 1	1.63	7.38	0.0314	0.282937	0.000009
bomb WR 2	1.81	22.4	0.0114	0.282893	0.000003
grt 1	4.27	3.36	0.1807	0.283215	0.000007
grt 2	5.50	4.29	0.1821	0.283221	0.000004
grt 3	3.66	4.59	0.1131	0.283098	0.000004
grt 4	4.11	3.85	0.1514	0.283165	0.000005
grt 5	4.95	4.45	0.1578	0.283172	0.000007
grt 6	3.48	4.46	0.1107	0.283108	0.000006
grt 7	4.00	3.18	0.1784	0.283227	0.000006
98-114A, Ridley Island					
sav WR 1	0.223	1.33	0.0237	0.282827	0.000006
sav WR 2	0.213	1.20	0.0252	0.282812	0.000005
sav WR 3	0.145	0.91	0.0225	0.282818	0.000006
bomb WR 1	0.365	1.44	0.0360	0.282836	0.000007
bomb WR 2	0.530	3.25	0.0231	0.282808	0.000006
grt 1	2.26	1.50	0.2133	0.283216	0.000005
grt 2	1.86	1.43	0.1851	0.283139	0.000008
grt 3	1.66	1.18	0.2000	0.283192	0.000007
grt 4	1.97	1.51	0.1855	0.283116	0.000007
grt 5	2.05	1.48	0.1957	0.283158	0.000004
grt 6	2.05	1.11	0.2604	0.283285	0.000008
grt 7	2.08	1.37	0.2149	0.283194	0.000006
06B-57, Minerva Lake					
sav WR 1	1.88	0.260	0.0052	0.282978	0.000007
sav WR 2	1.69	0.327	0.0088	0.282957	0.000008
bomb WR 1	0.119	3.28	0.0100	0.282999	0.000006
grt 1	2.03	0.288	0.9989	0.284720	0.000006
grt 2	2.40	0.203	1.679	0.286081	0.000006
grt 3	1.69	0.327	0.7349	0.284167	0.000004
grt 4	1.46	0.311	0.6645	0.284023	0.000005
grt 5	1.88	0.260	1.027	0.284618	0.000005
grt 6	1.57	0.920	0.2425	0.283398	0.000012

* Abbreviations: bomb WR, whole rock by bomb digestion; sav WR, whole rock by Tabletop Savillex© digestion; Grt, garnet.

† Lu and Hf concentrations determined by isotope dilution with uncertainties estimated to be better than 0.5%.

§ Uncertainties for $^{176}Lu/^{177}Hf$ for the purpose of regressions and age calculations is estimated to be 0.5%.

$^{176}Hf/^{177}Hf$ ratios were corrected for instrumental mass bias using $^{179}Hf/^{177}Hf = 0.7935$ and normalized relative to $^{176}Hf/^{177}Hf = 0.282160$ for JMC-475.

** Reported errors on $^{176}Hf/^{177}Hf$ represent within-run uncertainty expressed as 2s, standard error. Estimated total uncertainty on individual $^{176}Hf/^{177}Hf$ measurements for the purpose of regressions and age calculations is estimated to be 0.01% for $^{176}Hf/^{177}Hf$ for low concentration samples (e.g., most garnets) and 0.005% for higher concentration samples (> 3ppm).

4.2. Ridley Island

Ridley Island is a small island found to the south of the city of Prince Rupert (Figure 4, Locality "B"). Structurally, the island is to the east of the Grenville Channel shear zone and to the southwest of crustal-scale thrust shear zones found on the Tsimpsian peninsula. The thrust shear zones are diffuse zones of penetrative ductile deformation that accommodated top to the west reverse shear. These produced the inverted metamorphic gradients observed from Prince Rupert north to at least the Alaskan border. The rocks on Ridley Island therefore lay in between the Grenville Channel shear zone and major thrust shear zones to the north. Foliations on Ridley Island strike to the northwest with an average azimuth of 315°, and dip moderately to steeply (~65°) to the northeast. To the north and east of Ridley Island the average foliation strikes to the north to northeast; to the south of the island the foliation strikes northwest–southeast. The curvature of the foliations is reflected in the map pattern of metamorphic isograds (Chardon 2003), which are broadly parallel to foliation (Figure 4). Mineral lineations on Ridley Island are strike-parallel with shallow pitches to the south, similar to those at Kumealon Inlet. The geometry of the isograds and foliation distribution at the map scale indicate the regional structure was folded at some time after regional metamorphism and thrust stacking within the Prince Rupert area.

The western shores of Ridley Island have spectacular kinematic indicators. For instance, asymmetric quartz vein arrays are common (see Figure 8a in Chardon 2003). These quartz veins define asymmetric boudins that are cut by shear bands with a consistent left-lateral shear sense. Garnet tails are asymmetric and indicate left-lateral shear (Figure 5C). Further, inclusions trails in garnet are oblique to the matrix foliation by as much as 45° and have sigmoidal geometry consistent with left-lateral shear. Thus, inclusion trails, quartz veins, and winged porphyroclasts all indicate left-lateral shear across northeast dipping foliations, with shallow lineations on Ridley Island.

We analyzed sample 98–114, collected from the west shore of Ridley Island (Figure 4). The mineral assemblage for this sample is garnet– muscovite–biotite–chlorite–staurolite–plagioclase–quartz, and ilmenite. Garnets are euhedral and ≤ 7 mm in diameter. Very small anhedral chloritoid porphyroblasts occur in one thin section, and chloritoid is abundant in rocks found farther northwest in the Prince Rupert area (Crawford and Hollister 1982). The garnet contains inclusions of quartz and ilmenite, and rarely staurolite. Two textural generations of chlorite are present. The first helps to define the foliation, and is aligned parallel to biotite and muscovite suggesting it was present during deformation. The second generation of chlorite is undeformed and occurs as subhedral grains cutting across the foliation. These chlorites often have ilmenite inclusions. Locally, chlorite is found intergrown with biotite, suggesting growth at the expense of biotite. Staurolite occurs as corroded grains that are surrounded by fine-grained aggregates of muscovite and quartz, distinct from muscovite and quartz in other parts of the thin sections.

These textures suggest the following reaction history. A reaction similar to chloritoid + chlorite + muscovite = biotite + garnet + staurolite + H_2O (Spear and Cheney 1989) is likely responsible for the development of the peak mineral assemblage which includes staurolite, garnet, biotite and chlorite. The corroded staurolite surrounded by fine-grained muscovite and the occurrence of second generation chlorite likely represent the retrograde reaction biotite + staurolite + H_2O = chlorite + muscovite. The textures further suggest that retrogression of staurolite occurred after deformation ended.

Garnets in sample 98–114 are almandine rich and zoned. The analyzed garnet has slightly higher concentrations of Mn and Ca and slightly lower Fe and Mg in the cores than in the rims. Additionally, a subtle increase in Ca and Mn occurs in the X-ray map and line scan shown in Figure 9. The rims show evidence for retrograde

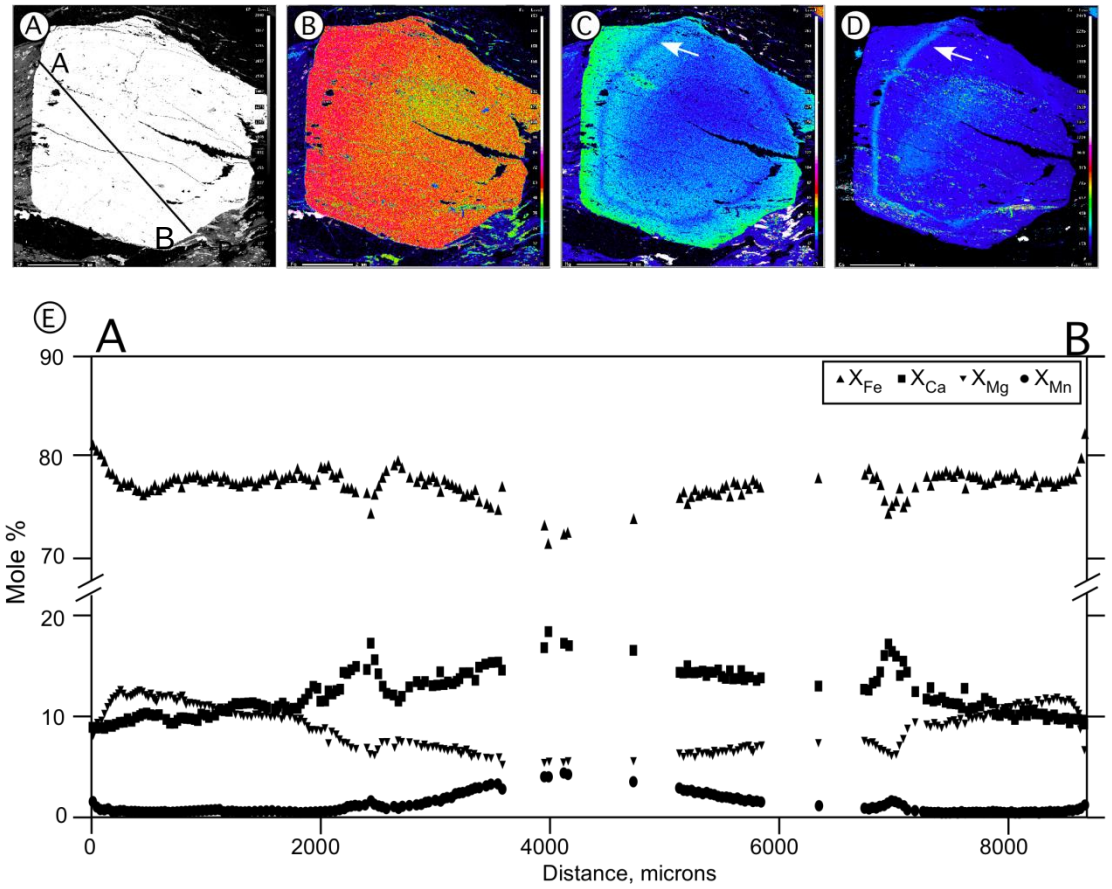

Figure 9. Backscatter electron image, X-ray intensity maps, and compositional line scan collected for sample 98–114. A) Backscatter electron image of garnet. White line marked A–B is location of compositional line scan shown in (E). B) X-ray intensity map for Fe Kα. C) X-ray intensity map for Mg Kα. Note the decrease in Mg indicated by white arrows. D) X-ray intensity map for Ca Kα. Note the increase in Ca indicated by white arrows. In all X-ray maps blues and purples are low concentrations and reds and yellows are higher concentrations. E) Compositional line scan collected by quantitative wavelength dispersive scanning analysis.

diffusional modification of the garnet rim compositions with increases in Fe and Mn and decreases in Mg and Ca. Overall, the zoning pattern is consistent with growth zoning (Hollister 1966). In addition, there are nearly symmetrical positive spikes in Ca and Mn, and corresponding dips in Fe, and Mg, about one quarter to one third in from the edge of the garnets. These spikes and dips suggest that the garnet producing reaction may have changed during growth or that there was a change in the P–T conditions at this point in garnet growth. We have not investigated the cause of these patterns. It is interesting to note that the spike in the zoning profile occurs where inclusions in the garnet change orientation (Figure 9B), suggesting that deformation occurred synchronous with the change in zoning.

Metamorphic P-T conditions were estimated using WinTWQ version 2.10. Garnet compositions were chosen from just inside of the diffusional rims identified in the compositional line scan (Table 5). The same database and mixing models were used for calculations in sample 98-114 as were used for sample G-16D. Additionally, the mixing model of Fuhrman and Lindsey (1988) was used for plagioclase. The resultant P-T estimates is 450 MPa and 523° C based on the intersection of the linearly independent reactions phlogopite + almandine = annite + pyrope and muscovite + grossular + almandine = annite + anorthite (Figure 10).

An isochemical phase diagram was also calculated for sample 98–114 using the Theriak–Domino software and the same database as was used for sample G-16 (Figure 10). Mn was excluded from the phase diagram calculation as it only constituted 0.09% of the bulk rock composition. The garnets in 98–114, however, contain ~2 wt.% MnO suggesting the stability field for the garnet in the natural samples will be expanded relative to the MnO free system used for the phase diagram calculation. The phase diagram calculation reproduces the mineral assemblage of 98–114 with temperatures between 480° and 560° C and pressures from 340 to 500 MPa. The P–T estimates

Table 5. Representative microprobe mineral analyses* for 98-114 from Ridley Island

Weight % Oxides

Oxides	Plagioclase	Garnet Rim	Garnet Core	Biotite	Muscovite	Chlorite	Ilmenite
SiO_2	58.83	37.03	36.52	25.24	46.69	24.64	0.14
TiO_2	0.01	0.04	0.05	0.41	0.30	0.10	50.73
Al_2O_3	25.28	21.64	21.35	55.85	34.99	22.52	0.08
FeO	0.04	36.52	35.92	11.88	1.47	27.80	48.95
MnO	0.03	0.48	0.29	0.03	0.00	0.00	0.10
MgO	0.00	2.37	2.75	1.39	0.90	13.59	0.11
CaO	6.88	3.12	4.12	0.00	0.01	0.09	0.00
Na_2O	7.59	0.04	0.04	0.21	0.88	0.05	0.00
K_2O	0.07	0.02	0.00	0.01	9.48	0.19	0.11
Cr_2O_3	0.00	0.04	0.05	0.00	0.00	0.00	0.01
Cl^-	0.02	0.00	0.00	0.00	0.03	0.00	0.00
F^{2-}	0.00	0.13	0.00	0.00	0.00	0.00	0.00
Ba^-	0.00	0.00	0.09	0.09	0.00	0.07	0.50
Total†	98.73	101.38	101.18	95.11	94.75	89.04	100.70

Ions in Formula§

Element	Plagioclase	Garnet Rim	Garnet Core	Biotite	Muscovite	Chlorite	Ilmenite
Si	2.656	2.952	2.926	1.713	3.109	1.852	0.002
Ti	0.000	0.002	0.003	0.021	0.015	0.005	0.646
Al	1.345	2.034	2.016	4.467	2.745	1.995	0.002
Fe^{2+}	0.002	2.435	2.407	0.674	0.082	1.748	0.693
Mn	0.001	0.033	0.019	0.001	0.000	0.000	0.001
Mg	0.000	0.282	0.328	0.141	0.089	1.522	0.003
Ca	0.333	0.266	0.354	0.000	0.001	0.007	0.000
Na	0.664	0.007	0.006	0.028	0.114	0.008	0.000
K	0.004	0.002	0.000	0.001	0.806	0.019	0.002
Cl	0.002	0.001	0.000	0.000	0.003	0.000	0.000
F	0.000	0.032	0.000	0.000	0.000	0.000	0.000
Ba	0.000	0.000	0.003	0.003	0.000	0.002	0.004
Cr	0.000	0.002	0.003	0.000	0.000	0.000	0.000
Total	5.006	8.048	8.066	7.049	6.965	7.159	1.354

* Representative analyses were chosen for plagioclase, garnet interior and rim, and ilmenite inclusion. Biotite, muscovite and chlorite numbers were produced from averaging multiple analyses.
† Oxide totals corrected for Cl, F, and Ba using the method described in Deer, Howie and Zussmen.
§ Stoichiometric ratios of elements based on 12 oxygen for garnet, 11 for biotite, 11 for muscovite, 8 for plagioclase, 2 for ilmenite, 10 for chlorite.

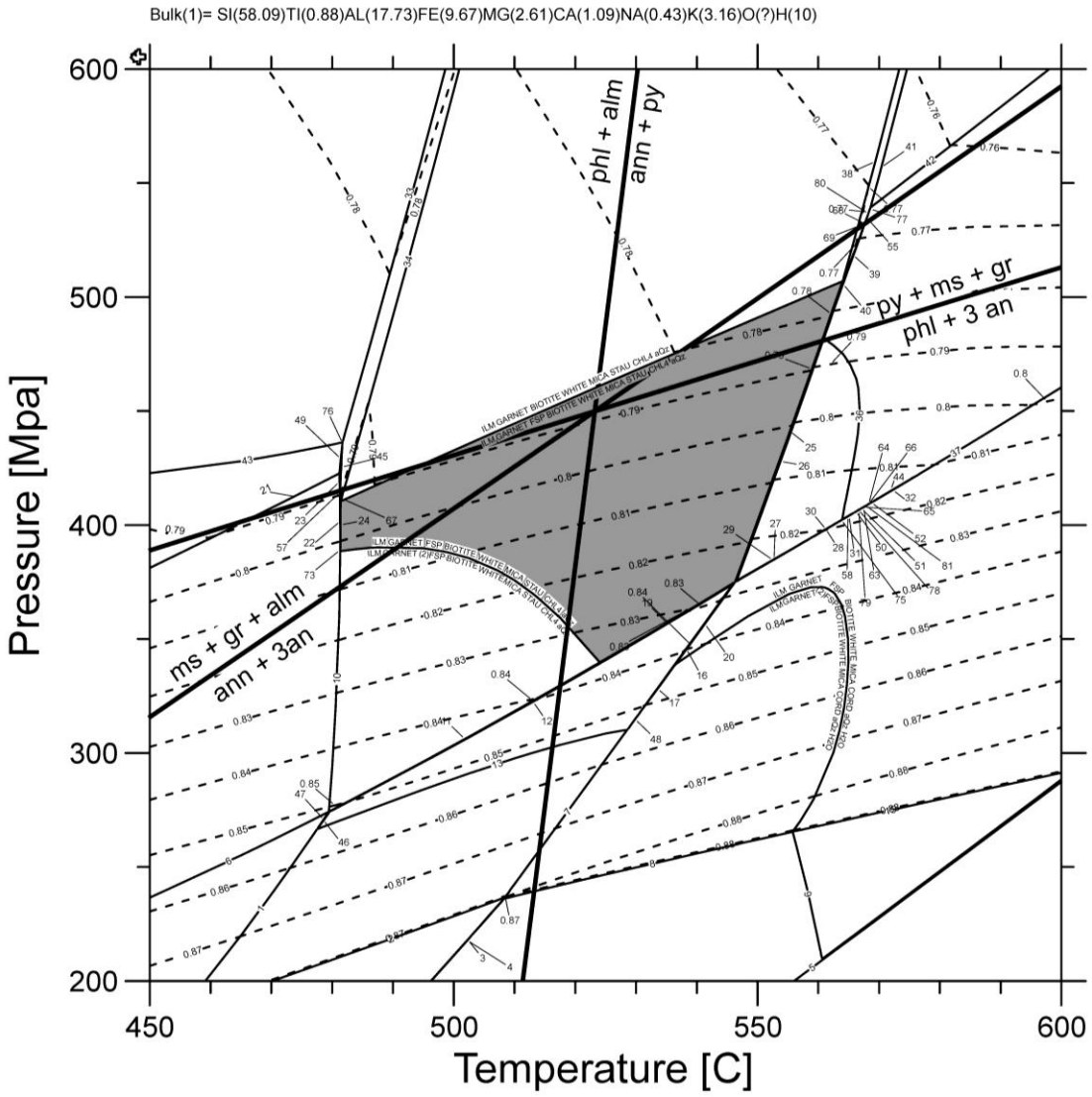

Figure 10. Isochemical phase diagram for sample 98–114 calculated using Theriak–Domino software. Rock bulk chemistry is shown across top of Figure. Gray shaded region is region is estimated stability field for minerals in 98–114. Dashed lines are isopleths of almandine in garnet. Note that garnet in 98–114 has almandine contents near 0.79 in regions exterior to the Ca spike and interior to the rims where Mn and Fe increase (Figure 9). Heavy lines are equilibrium reaction lines for thermobarometers calculated by WinTWQ. Only two of the three thermobarometers shown are linearly independent. Table 2 gives definitions of mineral abbreviations shown on the phase diagram, and a complete list of reactions on the phase diagram is given in Table 6.

Table 6. Changes in mineral assemblages for phase diagram of 98-114

Reaction number	Mineral assemblage, reactants	Mineral assemblage, products
1	ILM GARNET (2)FSP BIOTITE WHITE MICA CORD CTOID aQz	ILM GARNET (2)FSP BIOTITE WHITE MICA CHL4 CORD
2	ILM GARNET (2)FSP BIOTITE WHITE MICA CHL4 CORD aQz	ILM (2)FSP BIOTITE WHITE MICA CHL4 CORD aQz
3	ILM (2)FSP BIOTITE WHITE MICA CHL4 CORD aQz	ILM (2)FSP BIOTITE WHITE MICA CHL4 CORD aQz H2O
4	ILM (2)FSP BIOTITE WHITE MICA CHL4 CORD aQz H2O	ILM (2)FSP BIOTITE WHITE MICA CORD aQz H2O
5	ILM (2)FSP BIOTITE WHITE MICA CORD aQz H2O	ILM (2)FSP BIOTITE CORD aQz H2O
6	ILM GARNET (2)FSP BIOTITE WHITE MICA STAU CTOID aQz	ILM GARNET (2)FSP BIOTITE WHITE MICA CORD CTOID
7	ILM GARNET (2)FSP BIOTITE WHITE MICA CHL4 CORD aQz	ILM GARNET (2)FSP BIOTITE WHITE MICA CORD aQz H2O
8	ILM GARNET (2)FSP BIOTITE WHITE MICA CORD aQz H2O	ILM (2)FSP BIOTITE WHITE MICA CORD aQz H2O
9	ILM FSP BIOTITE WHITE MICA CORD aQz H2O	ILM (2)FSP BIOTITE WHITE MICA CORD aQz H2O
10	ILM GARNET (2)FSP BIOTITE WHITE MICA STAU CTOID aQz	ILM GARNET (2)FSP BIOTITE WHITE MICA STAU CHL4
11	ILM GARNET (2)FSP BIOTITE WHITE MICA STAU CHL4 aQz	ILM GARNET FSP BIOTITE WHITE MICA STAU CHL4 CORD
12	ILM GARNET FSP BIOTITE WHITE MICA STAU CHL4 CORD aQz	ILM GARNET FSP BIOTITE WHITE MICA CHL4 CORD aQz
13	ILM GARNET FSP BIOTITE WHITE MICA CHL4 CORD aQz	ILM GARNET (2)FSP BIOTITE WHITE MICA CHL4 CORD aQz
14	ILM GARNET (2)FSP BIOTITE WHITE MICA CORD aQz H2O	ILM GARNET FSP BIOTITE WHITE MICA CORD aQz H2O
15	ILM GARNET FSP BIOTITE WHITE MICA CORD aQz H2O	ILM FSP BIOTITE WHITE MICA CORD aQz H2O
16	ILM GARNET FSP BIOTITE WHITE MICA CHL4 CORD aQz	ILM GARNET FSP BIOTITE WHITE MICA CHL4 CORD aQz H2O
17	ILM GARNET FSP BIOTITE WHITE MICA CHL4 CORD aQz H2O	ILM GARNET (2)FSP BIOTITE WHITE MICA CORD aQz
18	ILM GARNET (2)FSP BIOTITE WHITE MICA STAU CHL4 aQz	ILM GARNET FSP BIOTITE WHITE MICA STAU CHL4 aQz
19	ILM GARNET FSP BIOTITE WHITE MICA STAU CHL4 aQz	ILM GARNET FSP BIOTITE WHITE MICA STAU CHL4 CORD aQz
20	ILM GARNET FSP BIOTITE WHITE MICA CHL4 CORD aQz H2O	ILM GARNET FSP BIOTITE WHITE MICA CORD aQz H2O
21	ILM GARNET FSP BIOTITE WHITE MICA STAU CTOID aQz	ILM GARNET (2)FSP BIOTITE WHITE MICA STAU CTOID aQz
22	ILM GARNET (2)FSP BIOTITE WHITE MICA STAU CTOID aQz	ILM GARNET FSP BIOTITE WHITE MICA STAU CHL4 CTOID
23	ILM GARNET (2)FSP BIOTITE WHITE MICA STAU CTOID aQz	ILM GARNET FSP BIOTITE WHITE MICA STAU CHL4 CTOID
24	ILM GARNET FSP BIOTITE WHITE MICA STAU CHL4 CTOID aQz	ILM GARNET FSP BIOTITE WHITE MICA STAU CHL4
25	ILM GARNET FSP BIOTITE WHITE MICA STAU CHL4 aQz	ILM GARNET FSP BIOTITE WHITE MICA STAU CHL4 aQz H2O
26	ILM GARNET FSP BIOTITE WHITE MICA STAU CHL4 aQz H2O	ILM GARNET (2)FSP BIOTITE WHITE MICA STAU aQz
27	ILM GARNET (2)FSP BIOTITE WHITE MICA STAU aQz H2O	ILM GARNET FSP BIOTITE WHITE MICA STAU CORD aQz
28	ILM GARNET (2)FSP BIOTITE WHITE MICA STAU aQz H2O	ILM GARNET FSP BIOTITE WHITE MICA STAU CORD aQz
29	ILM GARNET FSP BIOTITE WHITE MICA STAU CORD aQz H2O	ILM GARNET FSP BIOTITE WHITE MICA CORD aQz H2O
30	ILM GARNET FSP BIOTITE WHITE MICA STAU CORD aQz H2O	ILM GARNET FSP BIOTITE WHITE MICA CORD aQz H2O
31	ILM GARNET FSP BIOTITE WHITE MICA STAU CORD aQz H2O	ILM GARNET FSP BIOTITE WHITE MICA CORD aQz H2O
32	ILM GARNET FSP BIOTITE WHITE MICA STAU CORD aQz H2O	ILM GARNET FSP BIOTITE WHITE MICA CORD aQz H2O
33	ILM GARNET BIOTITE WHITE MICA STAU CTOID aQz	ILM GARNET BIOTITE WHITE MICA STAU CHL4 CTOID aQz
34	ILM GARNET BIOTITE WHITE MICA STAU CHL4 CTOID aQz	ILM GARNET BIOTITE WHITE MICA STAU CHL4 aQz
35	ILM GARNET BIOTITE WHITE MICA STAU CHL4 aQz	ILM GARNET FSP BIOTITE WHITE MICA STAU CHL4 aQz
36	ILM GARNET (2)FSP BIOTITE WHITE MICA STAU aQz H2O	ILM GARNET FSP BIOTITE WHITE MICA STAU aQz H2O
37	ILM GARNET FSP BIOTITE WHITE MICA STAU aQz H2O	ILM GARNET FSP BIOTITE WHITE MICA CORD aQz H2O

Table 6 (cont.). Changes in mineral assemblages for phase diagram of 98-114

38	ILM GARNET BIOTITE WHITE MICA STAU CHL4 aQz	ILM GARNET BIOTITE WHITE MICA STAU CHL4 aQz H2O
39	ILM GARNET BIOTITE WHITE MICA STAU CHL4 aQz H2O	ILM GARNET FSP BIOTITE WHITE MICA STAU CHL4 aQz H2O
40	ILM GARNET FSP BIOTITE WHITE MICA STAU CHL4 aQz H2O	ILM GARNET FSP BIOTITE WHITE MICA STAU aQz H2O
41	ILM GARNET BIOTITE WHITE MICA STAU CHL4 aQz H2O	ILM GARNET BIOTITE WHITE MICA STAU aQz H2O
42	ILM GARNET BIOTITE WHITE MICA STAU aQz H2O	ILM GARNET FSP BIOTITE WHITE MICA STAU aQz H2O
43	ILM GARNET BIOTITE WHITE MICA STAU CTOID aQz	ILM GARNET FSP BIOTITE WHITE MICA STAU CTOID aQz
44	ILM GARNET FSP BIOTITE WHITE MICA STAU aQz H2O	ILM GARNET FSP BIOTITE WHITE MICA STAU CORD aQz H2O
45	ILM GARNET FSP BIOTITE WHITE MICA STAU CHL4 CTOID aQz	ILM GARNET BIOTITE WHITE MICA STAU CHL4 CTOID
46	ILM GARNET (2)FSP BIOTITE WHITE MICA CORD CTOID aQz	ILM GARNET FSP BIOTITE WHITE MICA CHL4 CORD CTD
47	ILM GARNET FSP BIOTITE WHITE MICA CHL4 CORD CTOID aQz	ILM GARNET FSP BIOTITE WHITE MICA CHL4 CORD
48	ILM GARNET (2)FSP BIOTITE WHITE MICA CORD aQz H2O	ILM GARNET FSP BIOTITE WHITE MICA CHL4 CORD aQz
49	ILM GARNET FSP BIOTITE WHITE MICA STAU CTOID aQz	ILM GARNET FSP BIOTITE WHITE MICA STAU CHL4 CTOID
50	ILM GARNET FSP BIOTITE WHITE MICA STAU aQz H2O	ILM GARNET FSP BIOTITE WHITE MICA CORD aQz H2O
51	ILM GARNET FSP BIOTITE WHITE MICA STAU aQz H2O	ILM GARNET FSP BIOTITE WHITE MICA CORD aQz H2O
52	ILM GARNET FSP BIOTITE WHITE MICA STAU aQz H2O	ILM GARNET FSP BIOTITE WHITE MICA CORD aQz H2O
53	ILM GARNET (2)FSP BIOTITE WHITE MICA STAU aQz H2O	ILM GARNET FSP BIOTITE WHITE MICA CORD aQz H2O
54	ILM GARNET BIOTITE WHITE MICA STAU CHL4 aQz H2O	ILM GARNET FSP BIOTITE WHITE MICA STAU aQz H2O
55	ILM GARNET BIOTITE WHITE MICA STAU CHL4 aQz H2O	ILM GARNET FSP BIOTITE WHITE MICA STAU aQz H2O
56	ILM GARNET FSP BIOTITE WHITE MICA STAU CHL4 aQz	ILM GARNET FSP BIOTITE WHITE MICA CORD aQz H2O
57	ILM GARNET (2)FSP BIOTITE WHITE MICA STAU CTOID aQz	ILM GARNET BIOTITE WHITE MICA STAU CHL4 CTOID
58	ILM GARNET FSP BIOTITE WHITE MICA STAU CORD aQz H2O	ILM GARNET FSP BIOTITE WHITE MICA STAU aQz H2O
59	ILM GARNET FSP BIOTITE WHITE MICA STAU CHL4 aQz H2O	ILM GARNET FSP BIOTITE WHITE MICA STAU aQz H2O
60	ILM GARNET FSP BIOTITE WHITE MICA STAU CHL4 aQz H2O	ILM GARNET FSP BIOTITE WHITE MICA STAU aQz H2O
61	ILM GARNET BIOTITE WHITE MICA STAU CHL4 aQz H2O	ILM GARNET FSP BIOTITE WHITE MICA STAU CHL4 aQz H2O
62	ILM GARNET BIOTITE WHITE MICA STAU CHL4 aQz H2O	ILM GARNET FSP BIOTITE WHITE MICA STAU CHL4 aQz H2O
63	ILM GARNET FSP BIOTITE WHITE MICA STAU CORD aQz H2O	ILM GARNET FSP BIOTITE WHITE MICA CORD aQz H2O
64	ILM GARNET FSP BIOTITE WHITE MICA STAU CORD aQz H2O	ILM GARNET FSP BIOTITE WHITE MICA CORD aQz H2O
65	ILM GARNET FSP BIOTITE WHITE MICA STAU CORD aQz H2O	ILM GARNET FSP BIOTITE WHITE MICA STAU aQz H2O
66	ILM GARNET FSP BIOTITE WHITE MICA STAU aQz H2O	ILM GARNET FSP BIOTITE WHITE MICA STAU CORD aQz H2O
67	ILM GARNET FSP BIOTITE WHITE MICA STAU CHL4 CTOID aQz	ILM GARNET BIOTITE WHITE MICA STAU CHL4 CTOID
68	ILM GARNET BIOTITE WHITE MICA STAU CHL4 aQz H2O	ILM GARNET FSP BIOTITE WHITE MICA STAU CHL4 aQz H2O
69	ILM GARNET FSP BIOTITE WHITE MICA STAU CHL4 aQz H2O	ILM GARNET FSP BIOTITE WHITE MICA STAU aQz H2O
70	ILM GARNET FSP BIOTITE WHITE MICA CHL4 CORD aQz	ILM GARNET (2)FSP BIOTITE WHITE MICA CORD CTOID aQz
71	ILM (2)FSP BIOTITE WHITE MICA CHL4 CORD aQz H2O	ILM GARNET (2)FSP BIOTITE WHITE MICA CORD aQz H2O
72	ILM GARNET (2)FSP BIOTITE WHITE MICA STAU CHL4 aQz	ILM GARNET FSP BIOTITE WHITE MICA CHL4 CORD CTOID
73	ILM GARNET (2)FSP BIOTITE WHITE MICA STAU CTOID aQz	ILM GARNET FSP BIOTITE WHITE MICA STAU CHL4 aQz

Table 6 (cont.). Changes in mineral assemblages for phase diagram of 98-114

74	ILM GARNET FSP BIOTITE WHITE MICA CHL4 CORD aQz H2O	ILM GARNET FSP BIOTITE WHITE MICA STAU CHL4 CORD
75	ILM GARNET (2)FSP BIOTITE WHITE MICA STAU aQz H2O	ILM GARNET FSP BIOTITE WHITE MICA CORD aQz H2O
76	ILM GARNET FSP BIOTITE WHITE MICA STAU CTOID aQz	ILM GARNET BIOTITE WHITE MICA STAU CHL4 CTOID aQz
77	ILM GARNET BIOTITE WHITE MICA STAU CHL4 aQz H2O	ILM GARNET FSP BIOTITE WHITE MICA STAU aQz H2O
78	ILM GARNET FSP BIOTITE WHITE MICA STAU CORD aQz H2O	ILM GARNET FSP BIOTITE WHITE MICA STAU aQz H2O
79	ILM GARNET FSP BIOTITE WHITE MICA STAU CORD aQz H2O	ILM GARNET FSP BIOTITE WHITE MICA CORD aQz H2O
80	ILM GARNET BIOTITE WHITE MICA STAU CHL4 aQz H2O	ILM GARNET FSP BIOTITE WHITE MICA STAU aQz H2O
81	ILM GARNET FSP BIOTITE WHITE MICA STAU aQz H2O	ILM GARNET FSP BIOTITE WHITE MICA CORD aQz H2O
82	ILM GARNET BIOTITE WHITE MICA STAU CHL4 aQz H2O	ILM GARNET FSP BIOTITE WHITE MICA STAU aQz H2O
83	ILM GARNET FSP BIOTITE WHITE MICA STAU CHL4 aQz H2O	ILM GARNET FSP BIOTITE WHITE MICA STAU aQz H2O
84	ILM GARNET BIOTITE WHITE MICA STAU CHL4 aQz H2O	ILM GARNET FSP BIOTITE WHITE MICA STAU CHL4 aQz H2O

from the phase diagram are in excellent agreement with that obtained using WinTWQ. Together the phase diagram calculations and cation thermobarometry suggest P–T conditions of approximately 450 MPa and 525° C.

Lu–Hf dating of garnet from this sample produced a robust isochron at 108.3 ± 4.1 Ma (2σ; MSWD = 0.91; Figure 8B). This isochron is defined by five whole-rock and seven garnet fractions (Table 4). The $^{176}Lu/^{177}Hf$ for the garnet fractions ranged from 0.18 to 0.26. These ratios are also quite low for garnets and indicate the presence of a Hf-rich component such as zircon or rutile. The isochron defines an initial $^{176}Hf/^{177}Hf$ of 0.282760 ± 10 (ε_{Hf}= -0.5 ± 0.4).

4.3. Minerva Lake

Minerva Lake is located to the northeast of the Ecstall Pluton within the contact aureole of the pluton (Figure 4, Locality "C"). Map scale foliations in the region define folds with an axial surface sub-parallel to the pluton contact and dip moderately towards the center of the pluton. This relationship suggests that fold-development was coeval with the formation of the magmatic foliation in the Ecstall pluton, parallel to the axial planes of the folds. In the outcrop containing the dated sample, the average axial surface strikes 100° and dips 44° S and the magmatic foliation in the pluton strikes 110° and dips 56° S. These orientations are consistent with coeval folding of the host rock foliation and pluton emplacement. Asymmetric tails on garnet porphyroclasts formed during contact metamorphism indicate top-to-the-northeast shear, consistent with local fold vergence. Late-stage pegmatite dikes, that represent the final stages of magmatism during pluton emplacement, cut the pluton and country rocks. The magmatic foliation represents a plane of flattening, with pegmatite dikes occurring at a high angle to the foliation (Figure 5D). These dikes are locally sheared, consistent with reverse, pluton-side-up shear across the contact.

Sample 06B-57 contains an assemblage of quartz, plagioclase, garnet, hornblende and epidote. The rocks are migmatitic with tonalite leucosomes. The presence of magmatic epidote within the leucosomes suggests that migmatization occurred during contact metamorphism around the Ecstall pluton, which is also well known for the occurrence of magmatic epidote (Crawford and Hollister 1982; Zen and Hammarstrom 1984). Allanite present in the cores of epidote grains within the migmatite is consistent with this interpretation (Zen and Hammarstrom 1984; Zen, 1985), and can be observed in samples near the pluton (Figure 5E). The epidote rims on allanite occur as strain shadows sub-parallel to the foliation in the sample, indicating syn-deformational growth. Al in Hbl barometry by Butler et al. (2002) indicates emplacement pressures for the Ecstall Pluton of 750–810 ± 100 MPa. This estimate is similar to estimates by Hollister et al. (1987). Phase equilibria from adjacent rocks predict a pressure of 880 ± 100 MPa, and a temperature of 630° ± 50° C (Crawford and Hollister 1982). Garnets are up to 3.5 cm in diameter, and poikilitic with inclusions of zoesite, chlorite, oxides and calcite. Garnet is concentrated in leucosome layers of migmatites that have a leucotonalite composition (Figure 5F).

Lu–Hf data for sample 06B-57 failed to define a single isochron (Figure 8C). In order to interpret this data, a series of two-point isochrons were produced using all whole-rock fractions and individual garnet fractions. This method allows us to determine the range of possible garnet ages present in this sample, based on the Lu–Hf systematics. The average initial Hf isotopic composition from three whole-rock fractions of 06B-57 was 0.28288 ± 0.00003 (Table 4). Following this approach, we deter- mined a range of ages from 104.5 ± 1.3 to 94.8 ± 2.1 Ma for the five garnet fractions (Figure 8D). The older age is within error of our other two samples in the WMB, while the younger age is consistent with emplacement of the Ecstall Pluton. While various thermal mechanisms could be utilized to explain the younger garnet

age, the only explanation of the older age is that the sample recorded garnet-growing metamorphism at approximately 105 Ma. It is unlikely that the system was completely reopened during pluton emplacement, or else all of the garnet fraction ages would be equivalent to the emplacement of the Ecstall Pluton (<94 Ma). Multiple phases of garnet growth is a likely candidate, with at least two during the main phase of western metamorphic belt growth at ~ 105 Ma, and through contact metamorphism synchronous with pluton emplacement (Getty et al. 1993). Preferential sampling of core fractions could attribute for higher Lu/Hf ratios, and would be consistent with the older age interpretation for this sample.

5. Discussion

Our samples record peak metamorphism and a phase of deformation in the WMB and Grenville Channel shear zone from 108 to 102 Ma. Our new dates constrain the timing of this metamorphism and deformation much more precisely than previously inferred from igneous crystallization ages and argon cooling ages and facilitate comparison of deformation in the Coast Mountains with tectonomagmatic processes along the entire Cordilleran margin during this time (Figures 4 and 11). The closure temperature of garnet for the Lu–Hf isotopic system is thought to be in excess of 700° C, and likely as high as 800° C (Scherer et al. 2000; van Orman et al. 2002; Tirone et al. 2005) and requires high temperatures and long time periods to mobilize elements via diffusion (Dodson 1973). The peak metamorphic temperature for 98–114 is certainly below this range of temperature, suggesting that the date reflects the time of garnet growth in this sample (Scherer et al. 2000). G-16 experienced a higher peak temperature of 720° C, but does not record any later thermal events. The robustness of the isochron and lack of influence by Ecstall emplacement support this date recording prograde garnet growth. Peak metamorphic conditions for this region

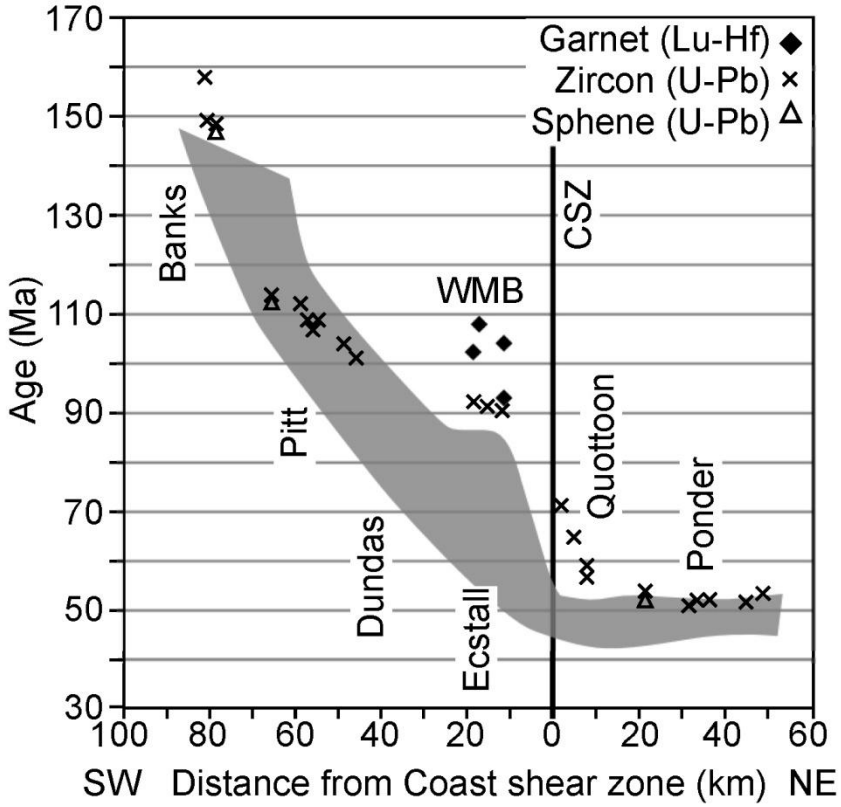

Figure 11. Isotopic ages plotted with respect to the Coast shear zone (0), modified from Butler et al. (2002). U–Pb zircon and titanite data are from Butler et al. (2006), and K–Ar and Ar–Ar hornblende and biotite data are from Butler et al. (2006) and Hollister et al. (2004). The upper boundary of the grayed zone represents the oldest hornblende ages at a given location, and the lower boundary the youngest biotite ages. This should represent the time interval over which the rocks cooled from 500° C to 350° C. Zircon ages are thought to represent crystallization ages, and are marked with "X". The solid diamonds show the Lu–Hf garnet samples dated in this study. Note the substantial gap between the garnet ages and the U/Pb zircon ages and Ar cooling ages. The age data suggest the cooling ages were reset during emplacement of the Ecstall pluton and the garnet ages directly date metamorphism. Also note that the garnet ages are broadly concordant with isotopic ages on Pitt Island suggesting metamorphism and plutonism were widespread at this time.

can now be bracketed as beginning around 108 Ma, and are synchronous with emplacement of the Captain Cove Pluton at 103 Ma (Chardon et al. 1999; Butler et al. 2006). Garnet at Kumealon Inlet and Ridley Island indicate garnet growth during left-lateral shearing deformation, supporting the conclusion that the Lu–Hf ages record the timing of deformation within the Grenville Channel shear zone and thrust stacking in the western metamorphic belt. The robustness of the isochrons for samples at distance from the Ecstall pluton indicate garnet growth related to metamorphism in the WMB must have terminated no later than 100 Ma.

An important observation to be made from the data is the gap between Lu–Hf ages recording fabric development in the WMB and the timing of the emplacement of the Ecstall pluton (Figure 11). The northern end of the Ecstall pluton was emplaced from 91.5 to 90.5 Ma, 10–15 m.y. after metamorphism and deformation in the dated samples. The folding of metamorphic isograds at the head of the Ecstall pluton indicates this pre-existing structure within the fold-and-thrust belt was deformed by the later emplacement of the pluton (Chardon 2003). Our new Lu–Hf ages indicate that regional metamorphism predated emplacement of the Ecstall Pluton. This gap is also recorded by the complex systematics of sample 06B-57 from Minerva Lake, which likely experienced phases of garnet growth at ~105 Ma (during deformation in the WMB) followed by either additional garnet growth and or partial resetting of the Lu–Hf clock during Ecstall emplacement (91.5–90.5 Ma). This multi-phase growth is not observed distal to the pluton, where contact metamorphism did not reach high enough temperatures to disturb the Lu–Hf systematics of earlier grown garnet. Any interpretation of this range in garnet age must attribute an older generation of garnet growth that at ~105 Ma that predates pluton emplacement by at least 10–15 m.y. (Getty et al. 1993).

The left-lateral strike-slip shearing and contraction from 108 to 102 Ma recorded

in our dated samples is consistent with the crustal- scale, left-lateral transpression identified by Chardon et al. (1999), and is consistent with the rest of the Canadian Cordillera and north Cascades. Numerous previous studies have identified contractional deformation (Crawford et al. 1987; Rubin et al. 1990; Evenchick 1991; Gehrels et al. 1992; McClelland et al. 1992; Cook and Crawford 1994; Miller et al. 2000; Driver et al. 2000) and left-lateral transpressional deformation (Avé Lallemant and Oldow 1988; Wyld and Wright 1988; Saleeby and Busby-Spera 1992; Hurlow 1993; Chardon et al. 1999; Evenchick 2001; Schermer et al. 2001) during this event in the Cordillera. This left-lateral transpression is observed as far south as the north Cascades, where the terminal phase of the northwest Cascade system occurs between 100 and 80 Ma (Brown 1987; Brandon et al. 1988).

To the south, the ages of deformation remain consistent but record different kinematics. Structures in the Pacific Northwest Cordillera of Washington and Idaho record right-lateral transpression and boundary-normal convergence between 110 and 75 Ma. The Idaho–Salmon River suture zone has been inferred to be predominately dip slip by some workers (Strayer et al. 1989; Selverstone et al. 1992; McClelland et al. 2000; Wyld and Wright 2001), with a more significant component of dextral transpression by others (Lund and Snee 1988, McClelland et al. 2000). Mylonite lineations at the boundary of the Seven Devils– Wallowa terranes in western Idaho are down-dip and structures are consistent with top-to-the-southwest reverse motion (Strayer et al. 1989). Evidence for right-lateral transpression is apparent on the western margin of the Idaho batholith, adjacent to the western Idaho shear zone and is constrained to be 105 to 90 Ma in age (Giorgis et al. 2008). Discrepancy in the contractional directions observed in the region is not mutually exclusive, as McClelland and Oldow (2007) observe a change in the accommodated convergence from left-lateral, margin-parallel motion in the western Idaho shear zone from 120 to

90 Ma, to a more margin-normal contractional deformation across the Orofino shear zone from 90 to 70 Ma.

Further south, the sense of shear on structures of similar age becomes consistent with right-lateral transpression. For instance, in the Sierra Nevada batholith, the Western Nevada shear zone system records right-lateral transpressional deformation between 115 and 95 Ma (Mattinson and James 1986; Saleeby and Busby-Spera 1992; Pickett and Saleeby 1994; Tikoff and Greene 1997; Wyld and Wright 2001). Regional structures in northern California were also active at this time, recording right-lateral transpression (Lahren et al. 1990; Busby-Spera and Saleeby 1990; Tikoff and de Saint Blanquat 1997). East of the Sierras, coeval contractional deformation is recorded in the Sevier fold and thrust belt (Gillespie and Heller 1995; DeCelles and Currie 1996; DeCelles and Coogan 2006). Wyld and Wright (2001) argue for a single deformational event accommodated from Oregon through the Sierras, along the right-lateral Western Nevada shear zone, connecting contractional deformation in the Idaho–Salmon River suture zone in the north to right-lateral transpression in the south. In Baja California, contraction is observed along the Main Mártir thrust between 115 and 108 Ma, constrained by crosscutting relation- ships with the eastern and western parts of the Peninsular Ranges batholith (Johnston et al. 1999).

These data are consistent with the Cordilleran-scale, boundary- wide contractional deformation during the mid-Cretaceous along the entire North American Cordillera, from the Sierras to Alaska (Hurlow 1993; Monger et al. 1994; Wyld and Wright 2001; Umhoefer 2003). This transpression resulted from oblique convergence along the boundary during the Cretaceous (Engebretson et al. 1985; Oldow et al. 1989; Umhoefer 2003). Transpressional deformation with a large strike-slip component is also widely recognized in the time interval from ∼110 to 90 Ma. From southeast Alaska to the North Cascades, however, transpressional deformation is dominated by

left- lateral strike-slip displacements. Right-lateral strike-slip dominates from the North Cascades to at least as far south as the Peninsular Ranges. This change in the strike-slip component from left-lateral in the north, to right-lateral in the south, appears to be a first-order feature of the kinematics of the North American Cordillera during the mid-Cretaceous (Umhoefer 2003). This change in kinematics requires distinct boundary conditions, indicating that different oceanic plates may have been interacting with the continent in the north and south (Figure 12). Alternatively, if the terranes that compose the western flank of the Coast Mountains are far traveled (e.g., Hollister and Andronicos 1997) and sourced near Baja California, then this kinematic reversal may indicate tectonic escape as suggested by Umhoefer (2003). Finally, because paleomagnetic data give no constraint on longitude, if the terranes are far traveled from the south, the deformation features in the Prince Rupert region may record tectonic processes occurring outboard of the continental margin synchronous with dextral transpression along the American Coast in Baja California, California, Nevada and Idaho. Because plate reconstructions from this period are limited by the Cretaceous Normal Superchron from 124 to 84 Ma (Engebretson et al. 1985), by lack of preservation of oceanic crust, and by possible motion of oceanic hotspots, detailed tectonic studies in the North American Cordillera will likely provide the best tests of these alternative hypotheses.

6. Conclusions

Our results allow for a more detailed and complete picture of the tectonic evolution of the western margin of the Coast plutonic complex during the time period from 110 to 90 Ma. The new Lu–Hf Grt dates show that there is a distinct time gap between the main phase of transpressive deformation from 108 to 102 Ma and emplacement of the high pressure Ecstall pluton at ~90 Ma, one of the largest

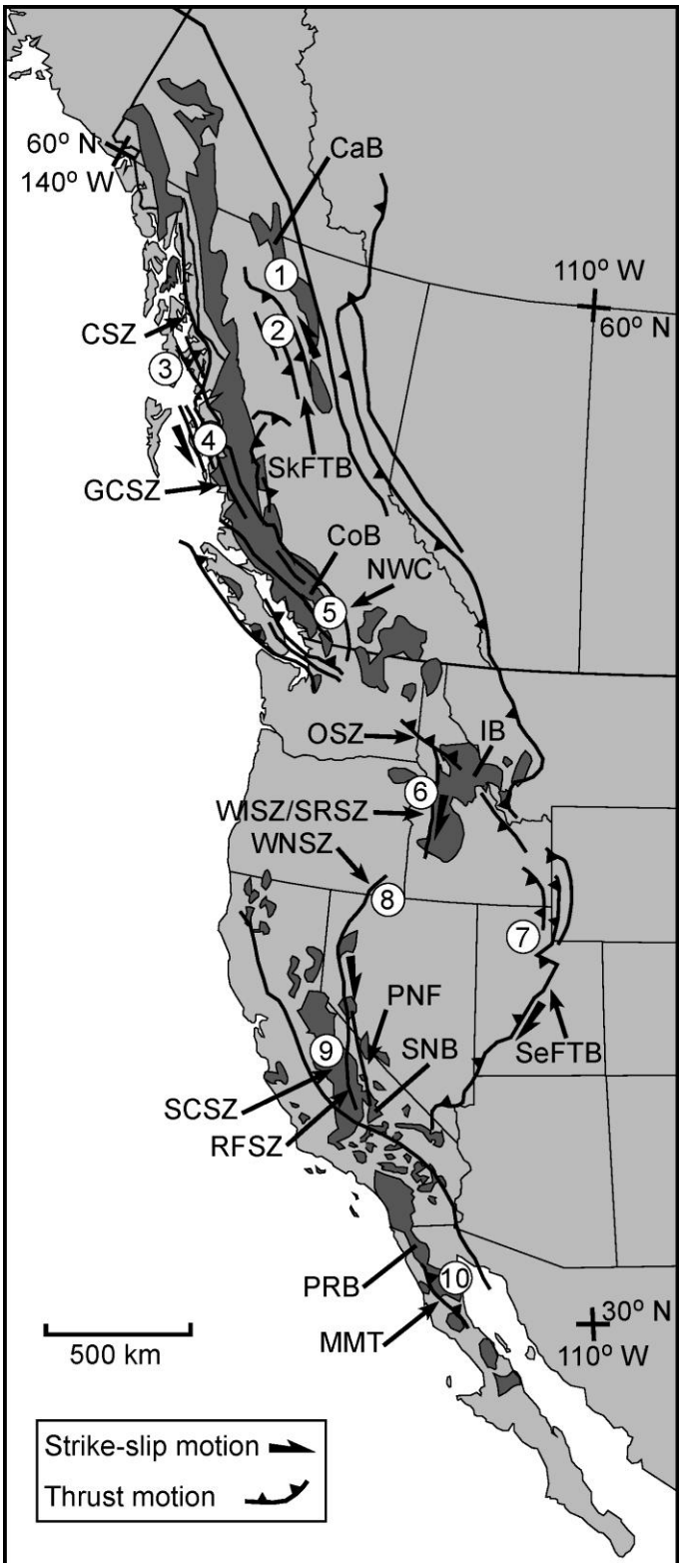

Figure 12. Caption on next page.

Figure 12. Tectonic map showing regional-scale structures in the North American Cordillera, highlighting structures active during 110–90 Ma. Base map and location of igneous bodies modified from Driver et al. (2000). Structures in the Canadian Cordillera record left-lateral transpression, orthogonal convergence in the Pacific northwest, and right-lateral transpression in the Sierra Nevada and Baja California. 1. CaB — Cassiar Batholith (Driver et al. 2000); 2. SkFTB — Skeena fold-and-thrust belt (Evenchick 1991 and Evenchick 2001); 3. SE Alaska (Gehrels et al. 1992 and McClelland et al. 1992); 4. GCSZ — Grenville Channel shear zone (Crawford et al. 1987, Chardon et al. 1999 and Chardon 2003; and this study); 5. NWC — Northwest Cascades (Brandon et al. 1988 and Brown 1987); 6. WISZ — Western Idaho shear zone, OSZ — Orofino shear zone, SRSZ — Salmon River suture zone (McClelland et al. 2000 and Wyld and Wright 2001); 7. SeFTB — Sevier fold-and-thrust belt (Giorgis et al. 2008 and DeCelles and Coogan 2006); 8. WNSZ — Western Nevada shear zone (Wyld and Wright 2001 and Pickett and Saleeby 1994); 9. SCSZ — Sierra Crest shear zone (Wyld and Wright 2001), PNF — Pine Nut Fault and RFSZ — Rosy Finch shear zone (Tikoff and de Saint Blanquat 1997); 10. PRB — Peninsular Ranges Batholith and MMT — Main Mártir thrust (Johnston et al. 1999). CSZ — Coast shear zone; CoB — Coast Batholith; IB — Idaho Batholith; SNB — Sierra Nevada Batholith.

Cretaceous batholiths in the Coast Mountains. Strike-slip shearing and contraction resulted in thickened crust with a suppressed geotherm (Zen and Hammarstrom 1984; Zen 1985). This regional deformation and metamorphism ended by ~102 Ma. Emplacement of the Ecstall pluton 10 m.y. after this event substantially modified the regional structure, producing crustal-scale folding of the thrust belt and of the metamorphic isograds at the northern margin of the pluton. Rather than being synchronous, it is now clear that this is an overprinting relationship between the host units and the pluton. Our dates highlight the need to directly date metamorphic minerals in deep crustal sequences as U/Pb ages of igneous rocks and lower temperature cooling ages may not always directly constrain the timing of amphibolite facies metamorphism.

Major plate-scale transpressional deformation is observed throughout the North American Cordillera from 110 to 90 Ma. The dominance of left-lateral transpression in the Canadian Cordillera, and right-lateral transpression in the U.S. segment of the North American Cordillera, however, appears to be a first-order feature of the kinematics of the orogen. This reversal in kinematics suggests a distinct change in kinematics along the coast of western North America in the Cretaceous if the terranes are not far traveled. Alternatively, if the terranes are far traveled, then the reversal in kinematics may indicate tectonic escape or process occurring off shore of North America during the Cretaceous.

7. Chapter-specific acknowledgements

This work was supported by: the Geological Society of America Student Research Fund to DEW; National Science Foundation grant EAR- 0738827 to CLA; and National Science Foundation grants EAR-0609856 and EAR-0711326 to JDV. We also thank Garret Hart for his assistance in clean laboratory separations and MC-

ICP-MS analyses. Peter Freeman provided invaluable assistance for our work in the Prince Rupert area. Freddie Letts and Vernon Libbe are excellent boat captains without whom we could not have completed this work. Andrew Letts is an excellent pilot for our skiff providing safe landings on a rocky coastline in often-choppy waters. Comments on a draft of the manuscript and discussions with Lincoln S. Hollister were very helpful in clarifying our arguments. Constructive journal reviews by Michael L. Williams and an anonymous reviewer helped us to improve the manuscript.

REFERENCES

Anczkiewicz, R., Platt, J.P., Thrilwall, M.F., Wakabayashi, J., 2004. Franciscan subduction off to a slow start: evidence from high-precision Lu–Hf garnet ages on high-grade blocks. Earth and Planetary Science Letters 225, 147–161.

Andronicos, C.L., Hollister, L.S., Davidson, C., Chardon, D.H., 1999. Kinematics and tectonic significance of transpressive structures within the Coast Plutonic Complex, British Columbia. Journal of Structural Geology 21, 229–243.

Andronicos, C.L., Chardon, D.H., Hollister, L.S., Gehrels, G.E., Woodsworth, G.J., 2003. Strain partitioning in an obliquely convergent orogen, plutonism, and synorogenic collapse: Coast Mountains Batholith, British Columbia, Canada. Tectonics 22, 1012–1035.

Avé Lallemant, H.G., Oldow, J.S., 1988. Early Mesozoic southward migration of Cordilleran transpressional terranes. Tectonics 7, 1057–1088.

Berman, R.G., 1988. Internally-consistent thermodynamic data for minerals in the system Na_2O–K_2O–CaO–MgO–FeO–Fe_2O_3–Al_2O_3–SiO_2–TiO_2–H_2O–CO_2. Journal of Petrology 29, 445–522.

Berman, R.G., 1991. Thermobarometry using multi-equilibrium calculations: a new technique, with petrological applications. Canadian Mineralogist 29, 833–855.

Berman, R.G., 2007. WinTWQ (version 2.3): a software package for performing internally-consistent thermobarometric calculations: Geological Survey of Canada, Open File 5462. 41 p.

Bouvier, A., Vervoort, J.D., Patchett, P.J., 2008. The Lu–Hf and Sm–Nd isotopic composition of CHUR: constraints from unequilibrated chondrites and implications for the bulk composition of terrestrial planets. Earth and Planetary Science Letters 273, 48–57.

Brandon, M.T., Cowan, D.S., Vance, J.A., 1988. The late Cretaceous San Juan thrust system, San Juan Islands, Washington: Geological Society of America Special Paper 221. 81 p.

Brew, D.A., Ford, A.B., 1978. Megalineament in southeastern Alaska marks southwest edge of Coast Range batholithic complex. Canadian Journal of Earth Sciences 15, 1763.

Brown, E.H., 1987. Structural geology and accretionary history of the Northwest Cascades system, Washington and British Columbia. Geological Society of America Bulletin 99, 201–214.

Burton, K.W., O'Nions, R.K., 1991. High-resolution garnet chronometry and the rates of metamorphic processes. Earth and Planetary Science Letters 107, 649–671.

Busby-Spera, C.J., Saleeby, J.B., 1990. Intra-arc strike-slip fault exposed at batholithic levels in the southern Sierra Nevada, California. Geology 18, 255–259.

Butler, R.F., Gehrels, G.E., Baldwin, S.L., Davidson, C., 2002. Paleomagnetism and geochronology of the Ecstall pluton in the Coast Mountains of British Columbia; Evidence for local deformation rather than large-scale transport. Journal of Geophysical Research 107, 3–13. DOI:10.1029/2001JB000270.

Butler, R.F., Gehrels, G.E., Hart, W., Davidson, C., Crawford, M.L., 2006. Paleomagnetism of Late Jurassic to mid-Cretaceous plutons near Prince Rupert, British Columbia. *In:* Haggart, J.W., Enkin, R.J., Monger, J.W.H. (Eds.), Paleogeography of the North American Cordillera: Evidence for and Against Large-scale Displacements: Geological Association of Canada Special Paper, vol. 46, pp. 171–200.

Chardon, D., Andronicos, C.L., Hollister, L.S., 1999. Large-scale transpressive shear zone patterns and displacements within magmatic arcs: the Coast Plutonic Complex, British Columbia. Tectonics 18, 278–292.

Chardon, D., 2003. Strain partitioning and batholith emplacement at the root of a transpressive magmatic arc. Journal of Structural Geology 25, 91–97.

Chatterjee, N.D., Froese, E., 1975. A thermodynamic study of the pseudo-binary join muscovite–paragonite in the system $KAlSi_3O_8$–$NaAlSi_3O_8$–Al_2O_3–SiO_2–H_2O. American Mineralogist 60, 985–993.

Cheng, H., King, R.L., Nakamura, E., Vervoort, J.D., Zhou, Z., 2008. Coupled Lu–Hf and Sm–Nd geochronology constrains garnet growth in ultra-high-pressure eclogites from the Dabie orogen. Journal of Metamorphic Geology 26, 741–758.

Cook, R.D., Crawford, M.L., 1994. Exhumation and tilting of the western metamorphic belt of the Coast orogen in southern southeastern Alaska. Tectonics 13, 528–537.

Cowan, D.S., Brandon, M.R., Garver, J.I., 1997. Geologic tests of hypotheses for large coastwise displacements — a critique illustrated by the Baja British Columbia controversy. American Journal of Science 297, 117–173.

Crawford, M.L., Hollister, L.S., 1982. Contrast of metamorphic and structural histories across the Work channel lineament. Coast Plutonic Complex, British Columbia. Journal of Geophysical Research 87, 3849–3860.

Crawford, M.L., Hollister, L.S., Woodsworth, G.J., 1987. Crustal deformation and regional metamorphism across a terrain boundary, Coast Plutonic Complex, British Columbia. Tectonics 6, 343–361.

Crawford, M.L., Crawford, W.A., Gehrels, G.E., 2000. Terrane assembly and structural relationships in the eastern Prince Rupert quadrangle, British Columbia. *In:* Stowell, H.H., McClelland, W.C. (Eds.), Tectonics of the Coast Mountains, Southeastern Alaska and British Columbia: Geological Society of America, Special Paper 343, 1–21.

DeCelles, P.G., Coogan, J.C., 2006. Regional structure and kinematic history of the

Sevier fold-and-thrust belt, Central Utah. Geological Society of America Bulletin 118 (7–8), 841–864.

DeCelles, P.G., Currie, B.S., 1996. Long-term sediment accumulation in the Middle Jurassic– early Eocene Cordilleran retroarc foreland-basin system. Geology 24, 591–594.

de Capitani, C., Brown, T.H., 1987. The computation of chemical equilibrium in complex systems containing non-ideal solutions. Geochimica et Cosmochimica Acta 51, 2639–2652.

Dodson, M.H., 1973. Closure temperature in cooling geochronological and petrological systems. Contributions to Mineralogy and Petrology 40, 259–264.

Driver, L.A., Creaser, R.A., Chacko, T., Erdmer, P., 2000. Petrogenesis of the Cretaceous Cassiar batholith, Yukon–British Columbia, Canada: implications for magmatism in the North American Cordilleran Interior. Geological Society of America Bulletin 112 (7), 1119–1133.

Ducea, M., 2001. The California arc: thick granite batholiths, eclogitic residues, lithospheric-scale thrusting, and magmatic flare-ups. GSA Today 11 (11), 4–10.

Engebretson, D.C., Cox, A., Gordon, R.G., 1985. Relative motions between oceanic and continental plates in the Pacific basin: Geological Society of America Special Paper 206. 59 p.

Enkin, R.J., 2006. Paleomagnetism and the case for Baja British Columbia. *In:* Haggart, J.W., Enkin, R.J., Monger, J.W.H. (Eds.), Paleogeography of the North American Cordillera; Evidence for and against large-scale displacements: Geological Association of Canada, Special Paper 46, 233–253.

Evenchick, C.A., 1991. Geometry, evolution, and tectonic framework of the Skeena fold belt, north central British Columbia. Tectonics 10 (3), 527–546.

Evenchick, C.A., 2001. Northeast-trending folds in the western Skeena fold belt,

northern Canadian Cordillera: a record of early Cretaceous sinistral plate convergence. Journal of Structural Geology 23, 1123–1140.

Fuhrman, M.L., Lindsey, D.H., 1988. Ternary-feldspar modeling and thermometry. American Mineralogist 73, 201–215.

Gareau, S.A., 1991. The Scotia–Quaal metamorphic belt: a distinct assemblage with pre- early Cretaceous deformational and metamorphic history, Coast Plutonic complex, British Columbia. Canadian Journal of Earth Sciences 28, 870–880.

Gehrels, G.E., McClelland, W.C., Samson, S.D., Patchett, P.J., Brew, D.A., 1991. U–Pb geochronology of Late Cretaceous and early Tertiary plutons in the northern Coast Mountains batholith. Canadian Journal of Earth Science 28, 899–911.

Gehrels, G.E., McClelland, W.C., Samson, S.D., Patchett, P.J., Orchard, M.J., 1992. Geology of the western flank of the Coast Mountains between Cape Fanshaw and Taku Inlet, southeastern Alaska. Tectonics 11, 567–585.

Getty, S.R., Selverstone, J., Wernicke, B.P., Jacobsen, S.B., Aliberti, E., Lux, D.R., 1993. Sm–Nd dating of multiple growth events in arc–continent collision zone, northwestern U.S. Cordillera. Contributions to Mineralogy and Petrology 115, 45–57.

Gillespie, J.M., Heller, P.L., 1995. Beginning of foreland subsidence in the Columbia–Sevier belts, southern Canada and northwest Montana. Geology 23, 723–726.

Giorgis, S., McClelland, W., Fayon, A., Singer, B.S., Tikoff, B., 2008. Timing of deformation and exhumation in the western Idaho shear zone, McCall, Idaho. Geological Society of America Bulletin 120 (9–10), 1119–1133.

Hollister, L.S., 1966. Garnet zoning: an interpretation based on the Rayleigh fractionation model. Science 154, 1647–1651.

Hollister, L.S., Grisson, G.C., Peters, E.K., Stowell, H.H., Sisson, V.B., 1987. Confirmation of the empirical correlation of Al in hornblende with pressure of

solidification of calc-alkaline plutons. American Mineralogist 72 (3–4), 231–239.

Hollister, L.S., Andronicos, C.L., 1997. A candidate for the Baja British Columbia fault system in the Coast Plutonic Complex. GSA Today 7 (11), 1–7.

Hollister, L.S., Hargraves, R.B., James, T.S., Renne, P.R., 2004. The paleomagnetic effects of reheating the Ecstall pluton, British Columbia. Earth and Planetary Science Letters 221-1, 397–407.

Hollister, L.S., Andronicos, C.L., 2006. Formation of new continental crust in western British Columbia during transpression and transtension. Earth and Planetary Science Letters 249, 29–38.

Hurlow, H., 1993. Mid-Cretaceous strike-slip and contractional fault zones in the western Intermontane terrane, Washington, and their relation to the north Cascades–southeastern Coast Belt orogen. Tectonics 12, 1240–1257.

Hutchinson, W.W., 1982. Geology of the Prince Rupert – Skeena Map Area, British Columbia: Geological Survey of Canada, Memoir 394.

Johnston, S.E., Tate, M.C., Fanning, C.M., 1999. New geologic mapping and SHRIMP U–Pb zircon data in the Peninsular Ranges batholith, Baja California, Mexico: evidence for a suture? Geology 27 (8), 743–746.

Klepeis, K.A., Crawford, M.L., Gehrels, G.E., 1998. Structural history of the crustal-scale Coast shear zone north of Portland Canal, southeast Alaska and British Columbia. Journal of Structural Geology 20, 883–904.

Kohn, M.J., 2009. Models of garnet differential geochronology. Geochimica et Cosmochimica Acta 73, 170–182.

Lapen, T.J., Johnson, C.M., Baumgartner, L.P., Mahlen, N.J., Beard, B.L., Amato, Jeffrey, M.A., 2003. Burial rates during prograde metamorphism of an ultra-high-pressure terrane: an example from Lago di Cignana, western Alps, Italy. Earth and Planetary Science Letters 215, 57–72.

Lapen, T.J., Medaris Jr., L.G., Johnson, C.M., Beard, B.L., 2005. Archean to Middle Proterozoic evolution of Baltica subcontinental lithosphere: evidence from combined Sm–Nd and Lu–Hf isotope analyses of the Sandvik ultramafic body, Norway. Contributions to Mineralogy and Petrology 150, 131–145.

Lahren, M.M., Schweickert, R.A., Mattinson, J.M., Walker, J.D., 1990. Evidence of uppermost Proterozoic to Lower Cambrian miogeoclinal rocks and the Mojave–Snow Lake fault: Snow Lake pendant, central Sierra Nevada, California. Tectonics 9, 1585–1608.

Lonsdale, P., 1995. Segmentation and disruption of the East Pacific Rise in the mount of the Gulf of California. Marine Geophysical Research 17, 323–359.

Ludwig, K.R., 2003. IsoPlot/Ex, rev 3.61, a Geochronologic Toolkit for Microsoft Excel: Berkeley Geochronology Center.

Lund, K., Snee, L.W., 1988. Metamorphism, structural development, and age of the continental–island arc juncture in western-central Idaho. *In:* Ernst, W.G. (Ed.), Metamorphism and crustal evolution, western conterminous United States, Rubey Volume VII: Englewood Cliffs. Prentice Hall, New Jersey, 296–331.

Mansfield, M.R., 2004. Thermal and structural evolution of the Grenville Channel shear zone, Coast plutonic complex, British Columbia: M.S. thesis, University of Texas, El Paso.

Mattinson, J.M., James, E.W., 1986. Salinian block U–Pb age and isotopic variations: implications for the origin and emplacement of the Salinian terrane. *In:* Howell, D.G. (Ed.), Tectonostratigraphic terranes of the Circum-Pacific region: Circum-Pacific Council for Energy and Mineral Resources, Earth Sciences Service 1, 215–226.

McClelland, W.C., Gehrels, G.E., Samson, S.D., Patchett, P.J., 1992. Structural and geochronologic relations along the western flank of the Coast Mountains batholith;

Stikine River to Cape Fanshaw, central southeastern Alaska: Journal of Structural Geology 14, 475–489.

McClelland, W.C., Tikoff, B., Manduca, C.A., 2000. Two-phase evolution of accretionary margins; examples from the North American Cordillera. Tectonophysics 326, 37–55.

McClelland, W.C., Oldow, J.S., 2007. Late Cretaceous truncation of the western Idaho shear zone in the central North American Cordillera. Geology 35, 723–726. DOI:10.1130/G23623A.1.

McMullin, D., Berman, R.G., Greenwood, H.J., 1991. Calibration of the SGAM thermobarometer for pelitic rocks using data from phase equilibrium experiments and natural assemblages. Canadian Mineralogist 29, 889–908.

Miller, L.D., Stowell, H.H., Gehrels, G.E., 2000. Progressive deformation associated with mid-Cretaceous to Tertiary contractional tectonism in the Juneau gold belt, Coast Mountains, southeastern Alaska. *In:* Stowell, H.H., McClelland, W.C. (Eds.), Tectonics of the Coast Mountains, Southeastern Alaska and British Columbia: Boulder, Colorado: Geological Society of America Special Paper 343.

Monger, J.W.H., van der Heyden, P., Journeay, J.M., Evenchick, C.A., Majoney, J.B., 1994. Jurassic–Cretaceous basins along the Canadian Coast Belt; their bearing on pre-Mid-Cretaceous sinistral displacements. Geology 22, 175–178.

Morozov, I.B., Smithson, S.B., Hollister, L.S., Diebold, J.B., 1998. Wide-angle seismic imaging across accreted terranes, southeastern Alaska and western British Columbia. Tectonophysics 299, 281–296.

Münker, C., Weyer, S., Scherer, E., Mezger, K., 2001. Separation of high field strength elements (Nb, Ta, Zr, Hf) and Lu from rock samples for MC-ICPMS measurements: G-cubed 2. DOI:10.1029/2001GC000183.

Oldow, J.S., Bally, A.W., Avé Lallemant, H.G., Leeman, W.P., 1989. Phanerozoic

evolution of the North American Cordillera, United States and Canada. *In:* Bally, A.W., Palmer, A.R. (Eds.), Geology of North America — An overview: Boulder, Colorado, Geological Society of America, Geology of North America A, 139–232.

Pickett, D.A., Saleeby, J.B., 1994. Nd, Sr and Pb isotopic characteristics of Cretaceous intrusive rocks from deep levels of the Sierra Nevada batholith, Tehachapi Mountains, California. Contributions in Mineralogy and Petrology 118, 198–205.

Roddick, J.A., 1970. Douglas Channel — Hecate Strait Map Area. British Columbia Geological Survey of Canada, Paper 70-41.

Rubin, C.M., Saleeby, J.B., Cowan, D.S., Brandon, M.T., McGroder, M.F., 1990. Regionally extensive mid-Cretaceous west-vergent thrust system in the northwestern Cordillera: Implications for continent-margin tectonism. Geology 18 (3), 276–280.

Rubin, C.M., Saleeby, J.B., 1992. Tectonic history of the eastern edge of the Alexander Terrane, southeast Alaska. Tectonics 11, 586–602.

Rusmore, M.E., Gehrels, G., Woodsworth, G.J., 2001. Southern continuation of the Coast shear zone and Paleocene strain partitioning in British Columbia–southeast Alaska. GSA Bulletin 113, 961–975.

Saleeby, J.B., Busby-Spera, C., 1992. Early Mesozoic tectonic evolution of the western U.S. Cordillera. *In:* Burchfiel, B.C., Lipman, P.W., Zoback, M.L. (Eds.), The Cordillera orogen, Conterminous United States: Geological Society of America, Geology of North America G-3, 107–168.

Scherer, E.E., Cameron, K.L., Blichert-Toft, J., 2000. Lu–Hf geochronology: Closure temperature relative to the Sm–Nd system and the effects of trace mineral inclusions. Geochimica et Cosmochimica Acta 64, 3413–3432.

Scherer, E.E., Münker, C., Mezger, K., 2001. Calibration of the lutetium–hafnium clock. Science 293, 683–687.

Schermer, E.R., Stephens, K.A., Walker, J.D., 2001. Paleogeographic and tectonic implications of the geology of the Tiefort Mountains, northern Mojave Desert, California. Geological Society of America Bulletin 113, 920–938.

Schmidt, M.W., Poli, S., 2004. Magmatic Epidote: Reviews in Mineralogy and Geochemistry 56, 399–430.

Selverstone, J., Wernicke, B., Aliberti, E., 1992. Intracontinental subduction and hinged uplift along the Salmon River suture zone in west central Idaho. Tectonics 11, 355–372.

Söderlund, U., Patchett, P.J., Vervoort, J.D., Isachsen, C.E., 2004. The 176Lu decay constant determined by Lu–Hf and U–Pb isotope systematics of Precambrian mafic intrusions. Earth and Planetary Science Letters 219, 311–324.

Spear, F.S., Cheney, J.T., 1989. A petrogenetic grid for pelitic schists in the system SiO_2– Al_2O_3–FeO–MgO–K_2O–H_2O. Contributions to Mineralogy and Petrology 101, 149–164.

Stowell, H.H., Hooper, R.J., 1990. Structural development of the western metamorphic belt adjacent to the Coast Plutonic Complex, southeastern Alaska: evidence from Holkham Bay. Tectonics 9, 391–408.

Stowell, H.H., Goldberg, S.A., 1997. Sm–Nd garnet dating of polyphase metamorphism: northern Coast Mountains, southeastern Alaska, USA. Journal of Metamorphic Geology 15, 439–450.

Strayer, L.M., Hyndman, D.W., Sears, J.W., Myers, P.E., 1989. Direction and shear sense during suturing of the Seven Devils–Wallowa terrane against North America in western Idaho. Geology 17, 1025–1028.

Tikoff, B., Greene, D., 1997. Stretching lineations in transpressional shear zones; an example from the Sierra Nevada batholith, California. Journal of Structural Geology 19, 29–39.

Tikoff, B., de Saint Blanquat, M., 1997. Transpressional shearing and strike-slip partitioning in the Late Cretaceous Sierra Nevada magmatic arc, California. Tectonics 16, 442–459.

Tirone, M., Ganguly, J., Dohmen, R., Langenhorst, F., Hervig, R., Becker, H.W., 2005. Rare earth diffusion kinetics in garnet: experimental studies and applications. Geochimica et Cosmochimica Acta 69, 2385–2398.

Tracey, R.J., Robinson, P., Thompson, A.B., 1976. Garnet composition and zoning in the determination of temperature and pressure of metamorphism, central Massachusetts. American Mineralogist 61, 762–775.

Umhoefer, P.J., 2003. A model for the North America Cordillera in the Early Cretaceous: Tectonic escape related to arc collision of the Guerrero terrane and a change in North America plate motion. *In:* Johnston, S.E., Paterson, S.R., Fletcher, J.M., Girty, G.H., Kimbrough, D.L., Martín-Barajas, A. (Eds.), Tectonic evolution of north- western México and the southwestern USA: Geological Society of America Special Paper 374, 117–134.

van der Heyden, P., 1989. U–Pb and K–Ar geochronometry of the Coast Plutonic Complex, 53° N–54° N, and implication for the Insular–Intermontane superterrane boundary, British Columbia: Ph.D. thesis, University of British Columbia.

van Orman, J.A., Grove, T.L., Shimizu, N., Layne, G.D., 2002. Rare earth element diffusion in a natural pyrope single crystal at 2.8 GPa. Contributions to Mineralogy and Petrology 142, 416–424.

Vervoort, J.D., Patchett, P.J., Söderlund, U., Baker, M., 2004. Isotopic composition of Yb and the determination of Lu concentrations and Lu–Hf ratios by isotope dilution using MC- ICPMS. Geochemistry, Geophysics, Geosystems 5. DOI:10.1029/2004GC000721.

Woodsworth, G.J., 1977. Homogenization of zoned garnets from pelitic schists.

Canadian Mineralogist 15, 230–242.

Wyld, S.J., Wright, J.E., 1988. The Devil's Elbow ophiolite remnant and overlying Galice Formation: new constraints on the Middle to Late Jurassic evolution of the Klamath Mountains, California. Geological Society of America Bulletin 100, 29–44.

Wyld, S.J., Wright, J.E., 2001. New evidence for Cretaceous strike-slip faulting in the United States cordillera and implications for terrane-displacement, deformation patterns, and plutonism. American Journal of Science 301, 150–181.

Zen, E.-A., 1985. Implications of magmatic epidote-bearing plutons on crustal evolution in the accreted terranes of the northwestern North America. Geology 13, 266–269. Zen, E.-A., Hammarstrom, J.M., 1984. Magmatic epidote and its petrologic significance. Geology 12, 515–518.

CHAPTER 3

PARTITIONED STRAIN IN THE MIDDLE CRUST OF THE COAST MOUNTAINS, BRITISH COLUMBIA, CONSTRAINED BY GARNET GEOCHRONOLOGY

Abstract

Oblique plate convergence is known to cause partitioning of strain in the brittle upper crust. New data from the central gneiss complex (CGC) of British Columbia supports continuity between the upper and middle crust such that strain partitioning extends into the deeper crust, producing cotemporaneous conjugate shear deformation. The CGC is the exhumed middle crust of a continental magmatic arc. These rocks are intruded by a series of Cretaceous to Eocene plutons. The belt is cut by the Coast shear zone, an 800 km long crustal-scale structure that separates higher pressure rocks of the ductile fold-and-thrust belt around Prince Rupert from the granulite facies gneisses and migmatites that experienced temperatures in excess of 750° C at mid-crustal pressures (5-7 kbar). Dextral transpression along the Coast shear zone is synchronous with structures within the central gneiss complex formed during convergence between the Insular and Intermontane terranes.

Eight Lu-Hf and one Sm-Nd garnet ages constrain syn-deformational metamorphism between 71.9±9.4 to 63.5±3.1 Ma (2σ). The deformation occurred during the initiation of an 18 million year metamorphic event in upper-amphibolite and granulite facies. Metamorphism ended during crustal scale transtension at 52 Ma, when the CGC was rapidly uplifted beneath the Shames River mylonite zone. Significant vertical shortening within the mylonite zone is suggested by gently dipping isotherms and isobars that are recorded by multiple isotopic cooling ages (U-Pb

zircon, Ar-Ar hornblende, Ar-Ar biotite) and the distribution of metamorphic mineral assemblages.

The Lu-Hf system retained information on prograde garnet growth despite metamorphic conditions in the surrounding crust at upper-amphibolite- to granulite-facies conditions for 18 million years. This indicates that the Lu-Hf system in garnet is extremely robust and a useful geochronologic tool for deciphering metamorphic ages despite high temperature thermal histories.

1. Introduction

Transpressive deformation zones result from oblique convergence of tectonic plates (Harland 1971). At all scales, from individual grains to the whole of an orogenic belt, strain may be partitioned. As originally defined by Fitch (1972), strain partitioning involves some fraction of slip parallel to the plate margin to be accommodated along a vertical structure on the continental side of the subduction zone. This is the model most often called upon for displacement of a fore-arc sliver for movement of terranes (e.g. Engebretson 1985; Umhoefer 1985; Hollister and Andronicos 1997; Cowan 1997; Umhoefer 2003; Enkin 2006) It is also possible for strain to be partitioned into conjugate strike slip faults, as can be observed in the San Andreas and Garlock fault systems (Teyssier and Tikoff 1998). The degree of divergence between the relative plate motion and zones of weakness within the deforming crust (i.e. pre-existing structures, lithologic heterogeneities, etc) is responsible for bulk wrench-dominated transpression (e.g. Tapponnier et al. 1982; Davy and Cobbold 1988; Sylvester 1988; Teyssier et al. 1995). It has also been proposed that deformation in the lower crust should occur in single unpartitioned shear zones, where slip parallels the convergence (or divergence) vector (e.g. Trouw et al. 2000). This would occur where there are high temperature metamorphic conditions typical of the lower crust, and materials are softened such that mechanical contrasts are eliminated enhancing the ability to of materials to flow homogenously. Models for strain partitioning frequently call on a vertically detached section, where the crust at one structural level is mechanically decoupled and deforms independently from that at higher or lower levels. Horizontal shear zones are inferred to detach the different structural levels (e.g., Collins and Vernon 1991; Jackson and Cruden 1995; Hajnal et al. 1996; Axen et al. 1998). An alternative explanation is that lithospheric layers are attached along shear zones that parallel the layer boundaries, with the shear zones

acting to transfer strain from one layer to the next, maintaining kinematic compatibility (Teyssier and Tikoff 1998). Both of these mechanisms can result in strain partitioning (Teyssier et al. 2002; Tikoff et al. 2002; Tikoff et al. 2004).

Here we present garnet ages from samples of gneiss within the central gneiss complex, the exhumed middle crust of a continental magmatic arc (Figure 13). Samples were collected in the vicinity of the Skeena River, between the Quottoon and Alistair Lake Plutons. Our new Lu-Hf garnet ages indicate that rocks of the central gneiss complex (CGC) experienced prograde metamorphism into the granulite-facies at 70-65 Ma, synchronous with transpressional deformation. The deformation was partitioned into zones of shallow and steep fabrics that crosscut one another spatially and temporally. We interpret the observed foliation pattern to indicate partitioned wrenching during oblique plate convergence.

Our new Sm-Nd garnet age, combined with previously published U-Pb and Ar-Ar data, show that rocks of the CGC experienced upper-amphibolite to granulite facies metamorphism for at least 18 million years. The end of metamorphism coincided with regionally distributed transtensional deformation and metamorphic core complex exhumation between 51 and 48 Ma (Andronicos et al. 2003).

The central gneiss complex of British Columbia is an excellent example of exposed mid-crustal rocks that have experienced transpressional deformation at the crustal scale. This is the result of an attached crustal section, where surface partitioning continues at depth and is not resolved onto a single oblique shear plane (e.g. Trouw et al. 2000). Our Lu-Hf and Sm-Nd garnet ages effectively resolve the timing of prograde metamorphism, and allow us to directly date the development of deformational fabrics. We then combine our field observations of crosscutting relationships with the age constraints to identify this as a single progressive partitioned

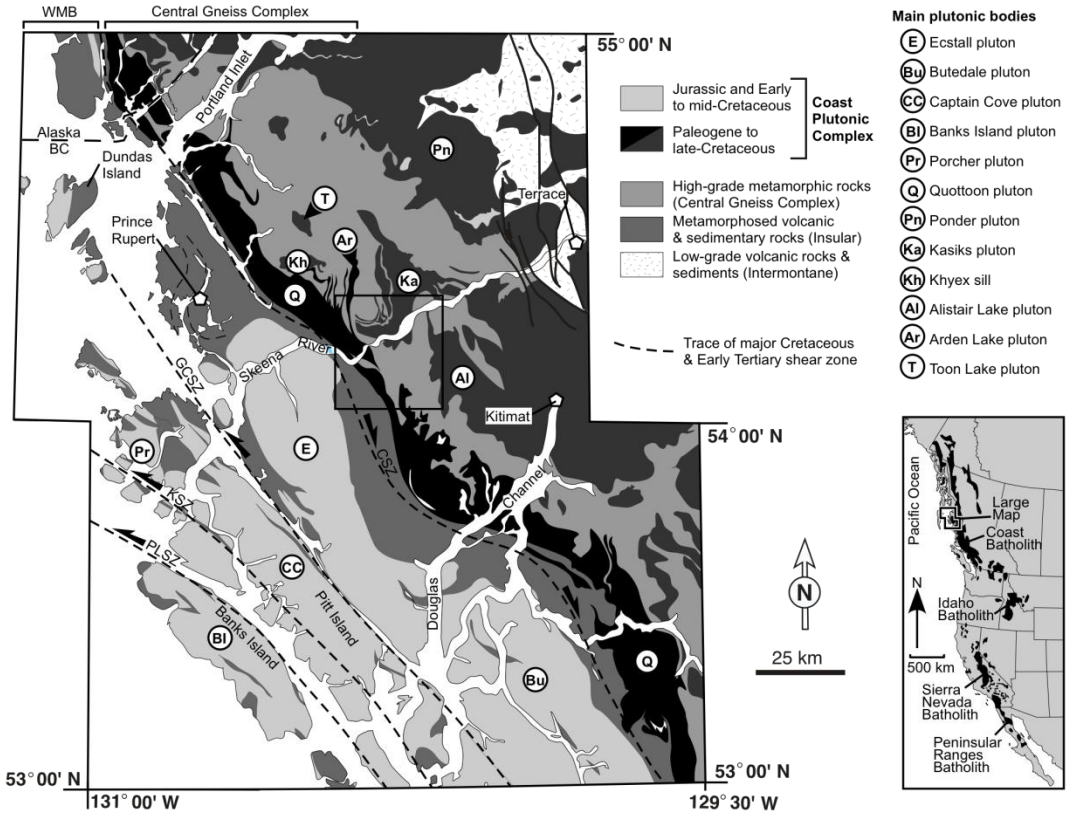

Figure 13. Simplified geologic map of the Coast Mountains between 53° and 55° N latitude, modified from Chardon et al. 1999. CSZ - Coast shear zone. The area of Figures 14, 16 and 17 is marked by a black box towards the center of the Figure. Inset map shows location of field area in the western North America cordillera with Cretaceous batholiths in black. Lithologies, foliations, and structures compiled from: Roddick 1970; Crawford and Hollister 1982; Hutchison 1982; van der Heyden 1989; Gareau 1991; Cook and Crawford 1994; Andronicos et al. 1999; Chardon et al. 1999; Rusmore et al. 2001; Mansfield 2004.

deformation, rather than multiple generations of overprinted deformation which represent distinct orogenic phases.

2. Regional Geology

The central gneiss complex (CGC) is the high-grade metamorphic core of the Coast plutonic complex (Figure 13). The western boundary of the CGC is the Coast shear zone, a crustal-scale structure that is steeply dipping and extends over 800 km from Alaska to southern British Columbia (Stowell and Hopper 1990; McClelland et al. 1992; Ingram and Hutton 1994; Klepeis et al. 1998; Andronicos et al. 1999). The Coast shear zone has a complex polyphase history that includes an early phase of dextral motion, followed by east-side-up reverse dip slip shearing during Quottoon emplacement, concluded by east-side-down normal shearing (Andronicos et al. 1999). Units immediately west of the Coast shear zone are higher pressure (0.8-0.9 GPa) amphibolite facies units, separated from lower pressure-higher temperature units in the east (Crawford et al. 1987).

Within our field area, the Coast shear zone incorporates rocks along the western edge of the Great Tonalite Sill (e.g. Stowell and Hopper 1990; McClelland et al. 1992; Ingram and Hutton 1994; Klepeis et al. 1998), but as defined by Andronicos (1999), also includes the Quottoon pluton and metamorphic rocks on its eastern side.

The central gneiss complex is intruded by a series of plutons that range in age from Jurassic to Mid-Cretaceous (Crawford and Hollister 1982; Crawford et al. 1987; Crawford et al. 2000; Gehrels et al., 2009), with the most voluminous plutonism occurring during the late Cretaceous to Tertiary (Armstrong 1988; van der Heyden 1992; Gehrels et al., 2009). Within our field area, most plutons are 85-52 Ma (Gehrels et al. 1991; Andronicos et al. 1999; Andronicos et al. 2003; Gehrels et al. 2009). The older plutons were emplaced deeper in the crust at pressures of 5-7 kbars, while

younger plutons were emplaced at shallower depths, around 3-5 kbars (Hollister et al. 1987; Crawford et al. 1987).

The Great tonalite sill is Late Cretaceous to Early Tertiary in age (83-57 Ma) (Gehrels et al. 1991; Gehrels et al. 2009). It was assembled as many elongate plutons, with individual bodies less than 20 km thick separated by steep contacts (Brew and Ford 1978; Ingram and Hutton 1994).

The Quottoon pluton is southern-most pluton in the Great Tonalite Sill sequence. The Quottoon intrudes along the Coast shear zone for 200 km in SE Alaska to southeast of Douglas Channel, British Columbia (Andronicos et al. 1999). The pluton has an average thickness of 10 km with a well foliated western margin, and a more weakly foliated core and eastern margin (Andronicos et al. 1999). The Quottoon is composed mostly of a medium-grained hornblende±biotite tonalite (Andronicos et al. 1999). The age of the eastern side of the Quottoon has been determined by Gehrels et al. (1991; 2009) to be 58.6±0.8 Ma from a U-Pb zircon date located along the Skeena River, and Thomas and Sinha (1999) report an age of 55 Ma for the Quottoon within Quottoon Inlet. Thomas and Sinha (1999) provide a comprehensive discussion of the geochemistry and petrology of the Quottoon pluton, and suggest it was derived from melting of garnet amphibolite at high pressure metamorphic conditions, expected in the lower crust of the arc.

Lithologies present in the study area (Figure 14 and 15), and used to define the central gneiss complex, are: paragneiss, orthogneiss, migmatite, luecogneiss, amphibolite and minor calc-silicate (Hutchison 1982; Hollister and Andronicos 2000). The paragneiss is composed of plagioclase, quartz, biotite, with variable amounts of sillimanite, garnet, cordierite and spinel (Andronicos et al. 1999). The orthogneiss and migmatite are composed of plagioclase, quartz, biotite, hornblende, and minor accessory phases, and contain a strong foliation. The amphibolite has a finer grain

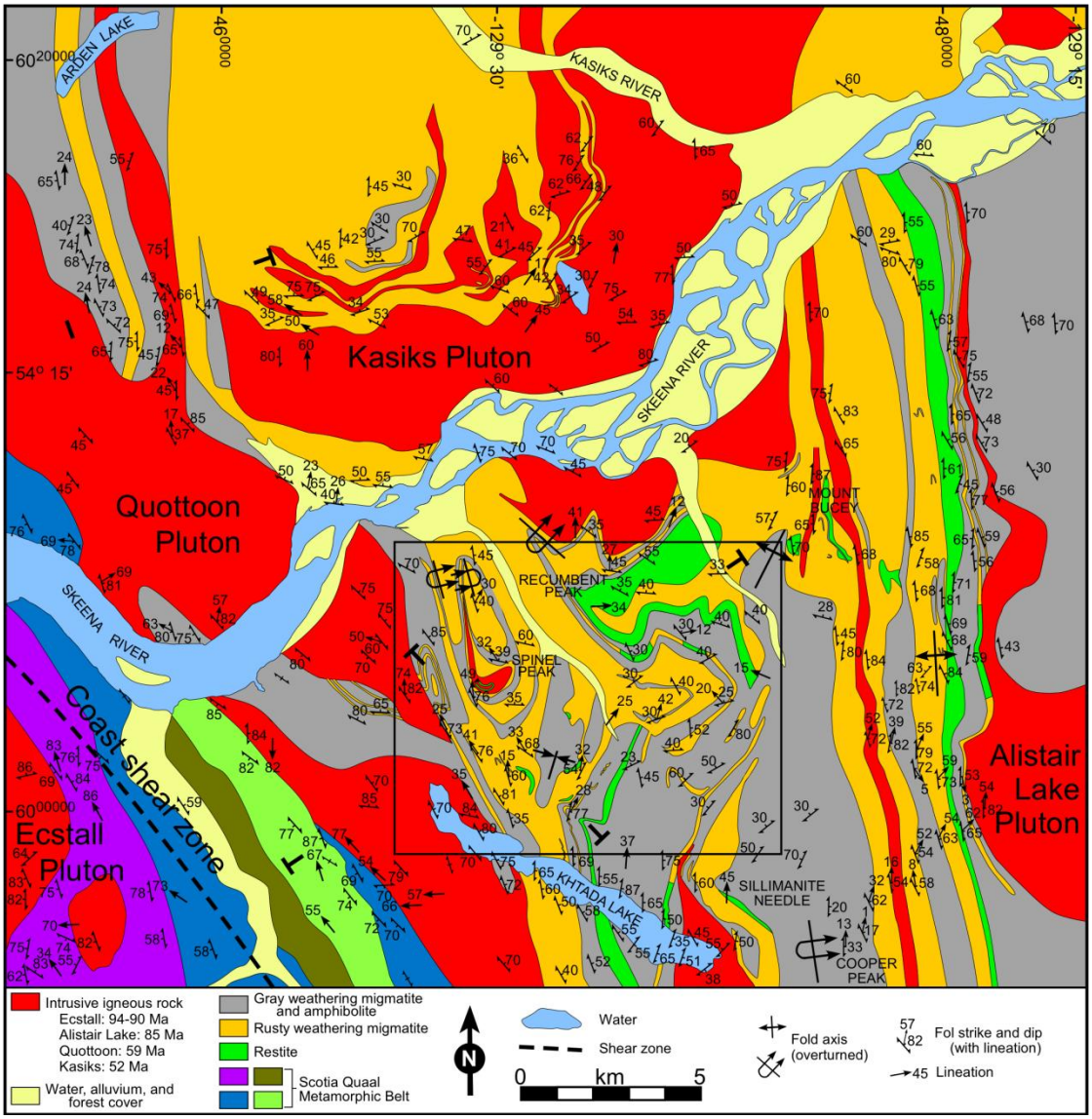

Figure 14. Geologic map of the central gneiss complex in the vicinity of the Skeena River. Outcrop measurement data compiled from: Hutchison, 1982; Kenah and Hollister 1983; Andronicos et al. 1999; Andronicos et al. 2003; this study. Black box around Spinel Peak is location of Figure 15.

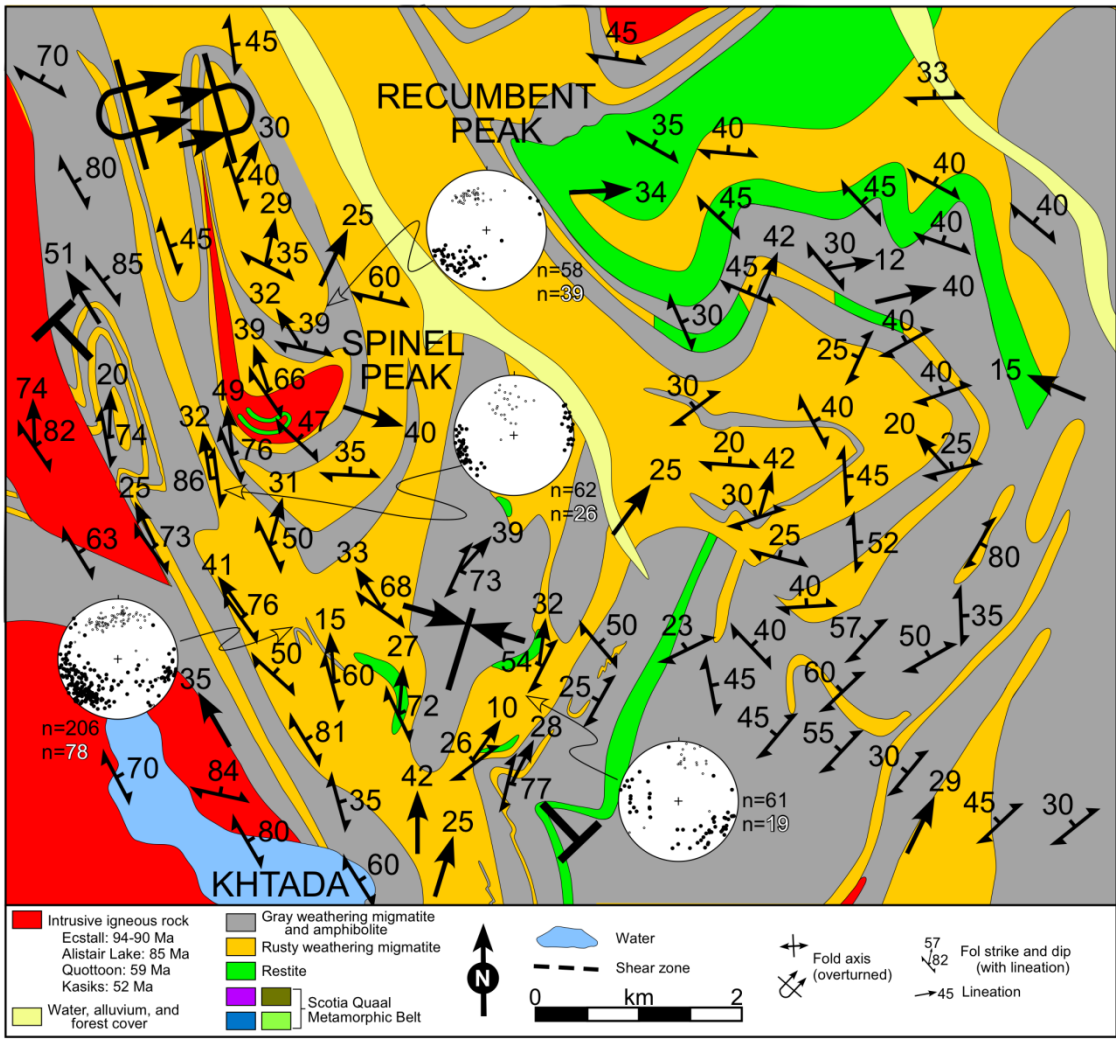

Figure 15. Geologic map of Spinel Peak. Location marked on Figure 14. Outcrop measurement data compiled from: Kenah and Hollister 1983, and this study. In stereonets, closed dots are poles to foliation planes, enumerated in black text. Open dots are lines (lineations and fold axes), numbered in white text.

size, and contains hornblende and biotite with minor amounts of plagioclase, pyroxene and quartz (Andronicos et al. 1999). Occasional small pods of mafic to ultramafic rock ranging from hornblendite to pyroxenite can be observed throughout the field area (Andronicos et al. 1999).

The mapped area is also intruded by the Kasiks sill complex and Alistair Lake Pluton (Figure 14). The Kasiks sill ranges in composition from diorite to tonalite. The sill complex is an assemblage of tabular plutons concordant with country rock foliation and ranging in size from meter- to kilometer-scale (Hutchison 1982; Crawford et al. 1987; Hollister and Andronicos 2000; Andronicos et al., 2003). Emplacement pressures have been estimated from the host metamorphic rocks using aluminum-in-hornblende, and produced pressures between 4 and 5 kbars (Hollister et al. 1987). It was intruded and crystallized between 54 and 52 Ma as determined by U-Pb zircon and sphene ages (Andronicos et al. 2003). The emplacement of the Kasiks sill was synchronous with northwest-directed extensional shearing within the sill complex overlain by northeast directed extensional shearing within the Shames River mylonite zone (Andronicos et al., 2003). This pattern of partitioned deformation is consistent with sub-vertical shorting during crustal extension. This crustal scale extensional deformation is interpreted to have caused uplift, exhumation and cooling that ended by ~48 Ma (Andronicos et al. 2003).

The Alistair Lake pluton is tonalite to granodioritic in composition, and was emplaced at 86±3 Ma (Andronicos et al. 2003; Gehrels et al. 2009). It is categorized as para-autochthonous by Hutchison (1970), as it overlies generally flat-lying to moderately inclined gneisses. The Alistair Lake pluton overlies the country rock gneisses and extends a minimum horizontal distance of 13 km over the gneiss (Hutchinson 1970).

Other important magmatic bodies that do not appear in the map area are the

Ponder Pluton and Khyex sill complex. The Ponder Pluton has been ranges in composition from tonalite to granite (Hutchison 1982; Sisson 1985). Its margins record different emplacement pressures of 3 kbar in the east and 5 kbar in the west (Hill 1984; Sisson 1985; Hollister et al. 1987), consistent with a shallow northeast dip, similar to the Alastair Lake pluton. Thus its base is exposed in the west and its roof is exposed in the east (Andronicos et al. 2003).

The Khyex sill complex is a package of sills and country rocks approximately 10 km thick, dipping 30-45° to the NNE (Crawford et al. 1999). The sills have been dated to 74-63 Ma by U-Pb zircon (Crawford et al. 1999). The Khyex has solid-state and magmatic fabrics that record top down to the north and northwest extension (Klepeis and Crawford 1999; Crawford et al. 1999). The magmatic fabrics indicate that deformation was synchronous with pluton-emplacement, and the deformation likely facilitated pluton emplacement (Klepeis et al. 1998; Crawford et al. 1999; Crawford et al. 2009).

The Central Gneiss Complex has experienced metamorphism ranging from amphibolite to granulite facies (Hollister 1975; Hollister 1982). Temperature estimates of 675-750° C and pressures of 0.6-0.8 GPa were recorded along the west side of the Quottoon during anatexis (Lappin and Hollister 1980). On the eastern side of the Quottoon, within our study area, peak conditions were estimated at >825° C and 0.45 GPa during emplacement of the Quottoon (Kenah and Hollister 1983). Selverstone and Hollister (1980) estimated similar P-T conditions to the east of the study area, reporting 725-775° C and 0.42-0.55 GPa. From these P-T estimates, mineral textures, and fluid inclusion data, a P-T curve was constructed by Hollister (1982) that records a clockwise path for the central gneiss complex. This path begins in the kyanite stability field, increases to peak conditions at 750° C and 0.5 GPa, and decreasing P and T to 550° C and 0.25 GPa (Hollister 1982).

The study area underwent rapid cooling during a major phase of exhumation in the early Eocene (Hollister 1982). This uplift proceeded at a rate of ~2 mm/y; bringing rocks from 35 km depth to 5 km. Sphene, hornblende and biotite geochronology summarized in Andronicos et al. (2003) track this cooling. This uplift was driven by deformation across the Shames River mylonite zone.

3. Analytical Methods

Electron microprobe analyses for thermobarometry were completed at Cornell University on a JEOL 8900 electron microprobe. Qualitative wavelength dispersive scanning (WDS) X-ray maps were collected by moving the stage beneath a fixed beam with a beam current of 100 or 250 ηa and a beam size 5 or 10 mm, depending on the image size. Operating conditions for quantitative WDS analysis were 20 KeV and 20 ηa, using a 2 mm beam for most minerals and a 10 μm beam for micas to prevent alkali loss. P-T calculations for pelitic samples were made using the computer program WinTWQ versions 1 and 2 (Berman 1991 and 2007). Calculations were made using the thermodynamic database of Berman, (1988). P-T calculations for samples containing orthopyroxene were made using the RCLC program (Pattison et al. 2003). Garnet compositions were chosen from the rim (or just inside any diffusional rims) as identified in the compositional line scan. Analyses for other minerals are representative points on matrix grains, except for biotite, which was an average of at least 20 analyses. We have not formally estimated the error on our P-T estimates, but assume a standard error of $\pm 50^{\circ}$ C and ±1 kbar.

Isochemical phase diagrams were made using the Theriak-Domino software version 150508 (http://titan.minpet.unibas.ch/minpet/theriak/theruser.html), based on the Gibbs free energy minimization algorithm of de Capitani and Brown (1987). Phase diagram calculations used both the thermodynamic database of Berman (1988 and

1991) and Holland and Powell (1998). Phase diagrams made using the Berman database are internally consistent with calculations made using WinTWQ. Water was not assumed to be a pure phase, with water fluid pressure assumed equal to $P_{H2O} = 0.7$ P_{Total}. Whole rock chemical analyses were performed by X-ray florescence at Washington State University's GeoAnalytical Lab for most samples, and for sample 09B-06A by glass via EMPA at Cornell. Trace element analyses were calculated by ICP-MS and normalized to chondrite of Sun and McDonough (1989).

All isotopic work was performed in the radiogenic isotope laboratory at Washington State University. Rock samples were ground with a mortar and pestle to sand-sized grains and handpicked into ~250 mg garnet and garnet-free 'whole-rock' fractions under a microscope. Garnet fractions were dissolved in Savillex© beakers on hot plates, while whole-rock fractions were dissolved using Teflon© capsules in steel pressure vessels. Both methods used a 10:1 mixture of concentrated HF and HNO_3 for the primary dissolution. Samples were spiked with mixed $^{176}Lu/^{180}Hf$ tracers for the accurate determination of Lu-Hf ratios necessary for geochronology. Separations of Lu, Hf, Sm and Nd followed established chromatographic techniques and have been described elsewhere (Münker et al. 2001; Vervoort et al. 2004; Cheng et al. 2008). Isotopic ratios of the purified elements were measured on a ThermoFinnigin© Neptune multi-collector inductively coupled plasma-mass spectrometer (MC-ICP-MS). Analytical details including data reduction methods are provided in Vervoort et al. (2004) and Cheng et al. (2008). Garnet Lu-Hf ages were calculated using $\lambda\ ^{176}Lu = 1.867x10^{-11}\ y^{-1}$ (Scherer et al. 2001; Söderlund et al. 2004), and Sm-Nd ages were calculated using $\lambda\ ^{147}Sm = 6.54x10^{-12}\ y^{-1}$ and using Isoplot 3.61 (Ludwig 2003). Initial $^{176}Hf/^{177}Hf$ and ε_{Hf} values were calculated using $^{176}Hf/^{177}Hf = 0.282785$ and $^{176}Lu/^{177}Hf = 0.0336$ for CHUR (Bouvier et al. 2008). Initial $^{143}Nd/^{144}Nd$ and ε_{Nd} values were calculated using $^{143}Nd/^{144}Nd = 0.512638$ and $^{147}Sm/^{144}Nd = 0.1966$ for

CHUR (Bouvier et al. 2007). Five samples were dated using Lu-Hf from the central gneiss complex: GMO from north of the Skeena River adjacent to the Quottoon Pluton; Kwin from Kwinitsa Quarry; 09B-06 from Oden Peak; 09B-15 from Petrologists' Ridge; and 09B-34 from the east ridge of Spinel Peak; and GMO was also dated using Sm-Nd (Figure 16). Samarium concentrations in other samples were insufficient to produce a meaningful isochron and were not analyzed.

4. Deformational Fabrics

The central gneiss complex has experienced a polyphase deformation history related to regional deformation and pluton emplacement. Structural and geologic data from this study and previously published works are summarized in Figure 14 and 15. Local foliation measurements are presented in Figure 14 and 15 and were interpolated to produce the foliation trajectory map show in Figure 16, which includes kinematic indicators from both outcrop and thin section observations.

First-order observations can be made about the study area based on these maps. The southwestern side of the study area is dominated by northwest-striking, steeply dipping foliations with oblique lineations (Fig 14, 15 and 17). In contrast, on the north side around the Kasiks sill foliations are dominated by roughly east-west strikes and moderately dips. Fabrics from the Kasiks sill are at a high angle to the Quottoon pluton. However, they more concordant to the Kasiks sill at the pluton margin. Fabrics on the east side of the map trend north-south, dipping moderately to steeply to the east with oblique lineations.

Previous workers have defined five distinct foliations in the central gneiss complex around the Skeena River. Bedding (S_0) ranges in age from Permian (constrained by fossils in Hill 1985) to Jurassic (Gehrels et al. 2009) in supracrustal rocks. Protolith ages for the luecogneiss older than ca. 140 Ma are indicated by a U-Pb

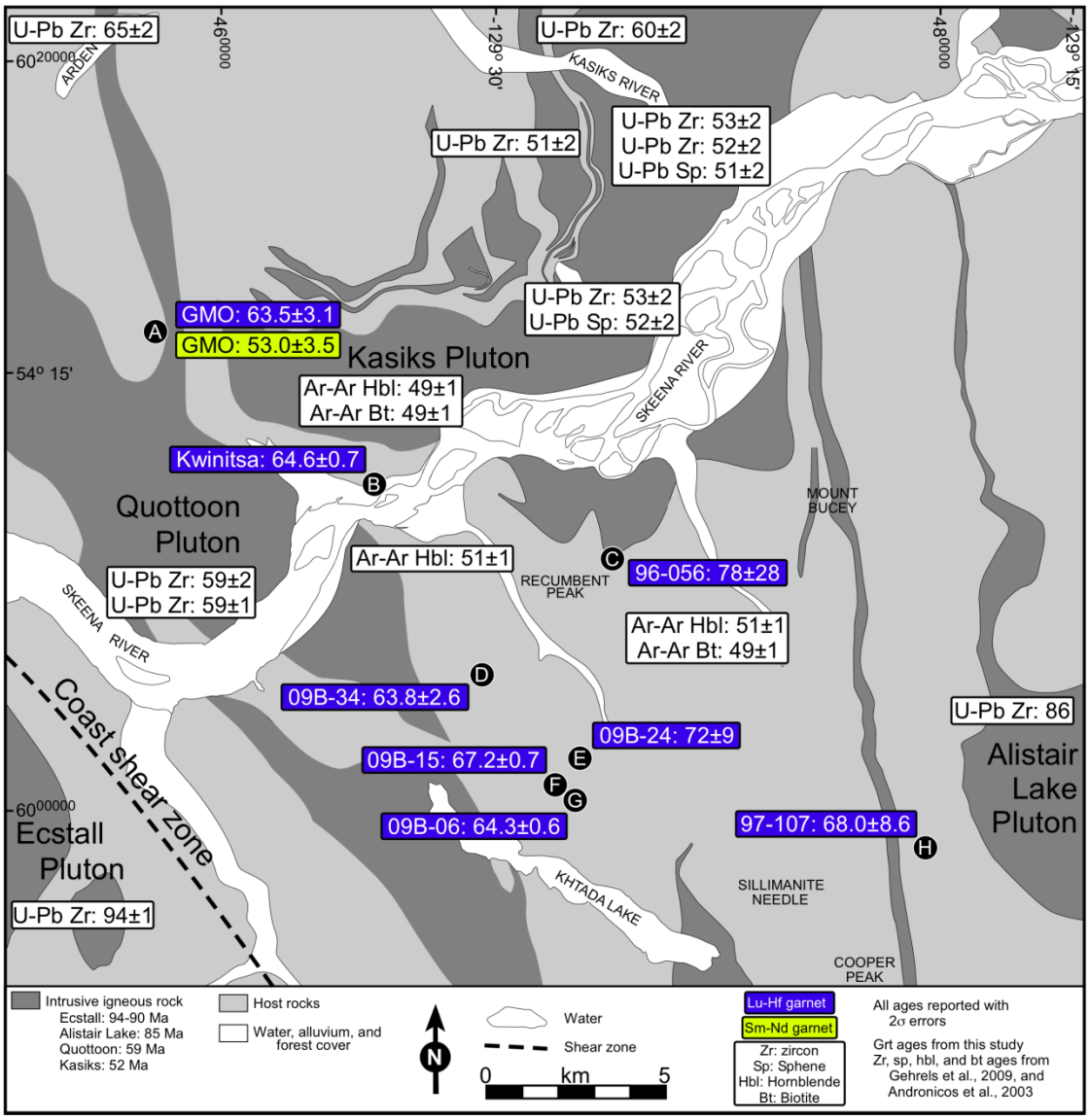

Figure 16. Simplified geologic map of the central gneiss complex, covering the same area as Figure 14. Sample locations marked to black dots with letters, which correspond to the text. U-Pb zircon ages from Gehrels et al. 1991; U-Pb sphene, Ar-Ar hornblende, and Ar-Ar biotite ages from Andronicos et al. 2003; Lu-Hf and Sm-Nd garnet ages from this study.

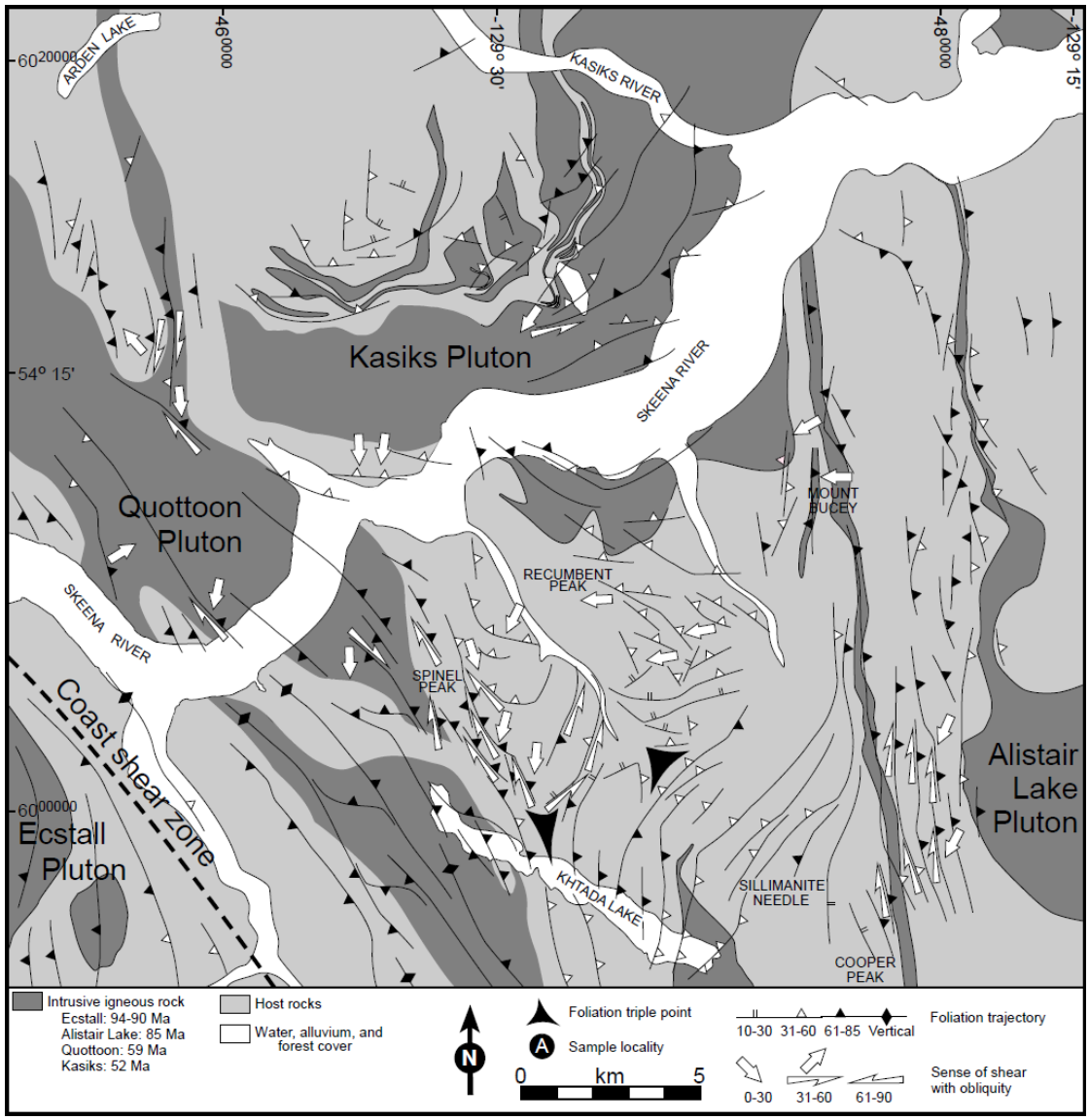

Figure 17. Simplified geologic map of the central gneiss complex, covering the same area as Figure 14. Structural outcrop data extrapolated to form foliation trajectories with representative dip angles. Interpretation of kinematic indicators shown by white arrows, signifying the degree of slip obliquity. Kinematics from Hollister and Andronicos 1997; Andronicos et al. 1999; Andronicos et al. 2003; This study.

zircon date (Hill 1984). Despite penetrative deformation, sequences of distinct lithologies have maintained coherence (Hollister and Andronicos 2000). Map-scale units include: (1) thick, rusty-weathering aluminous metasedimentary units, herein referred to as the rusty-weathering migmatite (RWM); (2) gray-weathering orthogneiss- and paragneiss that consist of variable amounts of plagioclase, quartz, and mafic minerals, herein referred to as the gray-weathering migmatite (GWM); and (3) amphibolite. The rusty color of the weathered metasedimentary rocks is due to the presence of pyrrohotite which oxidizes during weathering. Contacts between the rusty-weathering and gray-weathering units are often sharp and are easily seen in cliff exposures.

Hollister and Andronicos (2000) identify that gray-weathering units have three typical textural presentations with unique protolith interpretations. They interpret:
1) GWM with holocrystalline textures are believed to be intrusive sills; 2) GWM with a single, well-developed foliation are thought to be intrusive rocks that were deformed after solidification; and 3) GWM with refolded folds may represent early sills of intrusive tonalite and/or granodiorite, or may be metamorphosed sulfide-free metaclastic rocks. The amphibolite units are thought to be from high-alumina basalts and may be flows or sills. These can be mapped around map scale fold hinges and are interpreted to be part of the original stratigraphy (S_0).

The earliest identified foliation, S_1, appears to be concordant with stratigraphic layering and parallel to S_0. Oblique inclusion trails in garnets suggest this may be a second-generation fabric, but this is not definitive. This foliation is defined by alternating layers of leucocratic bands, composed predominately of plagioclase and quartz, and mica- or sillimanite-rich layers (Andronicos et al. 1999; Hollister and Andronicos 2000).

The gneissic fabric S_1 was folded into open, asymmetrical to isoclinal regional

nappes that can be observed at Recumbent and Cooper Peaks (Figure 18 A&B) and east to the Alistair Lake pluton (Andronicos et al. 1999). This deformational event is termed F_2, and the resultant axial planes are S_2. Axial planes strike NNW, and dip gently to the NE. Syn-deformational migmatization causes leucosomes to occur along the axial planes of the F_2 folds. This folding incorporated the RWM and GWM, as well as amphibolites and garnet-sillimanite restites (Figure 18 C). The lineation associated with this deformation (L_2) is defined by sillimanite grains that are parallel to the fold hinges in the paragneiss (Figure 18 D). The lineations and fold hinges associated with the L_2 deformation are parallel everywhere within our study area. This deformation resulted from mostly east-west shortening with a possible vertical component. Since these folds have been refolded by later deformational events, it is difficult to interpret their original orientation.

West from the F_2 folds, there is a set of kilometer scale isoclinal folds occurring along the eastern margin of the Quottoon pluton (Andronicos et al. 1999). These fold a differentiated gneissic banding with no associated axial planar cleavage. The folds are crosscut by the Quottoon pluton, giving them a minimum age of 59 Ma. These folds are considered F_3, with an axial plane termed S_3. These are interpreted by Andronicos et al. (1999) as a tightening and reorientation of the S_1 fabric (and L_1) observed on the east ridge of Spinel Peak and south (Figure 19 E&F). These fabrics sweep into parallel with the Quottoon, with varying foliation and lineation. It is possible that these are associated with emplacement of the Quottoon, as the foliation rotated from an east-west orientation to more northwest-southeast trend. Kinematics along the ridge south of Spinel Peak show the same dextral kinematics as are observed within the Quottoon (Figure 19 G).

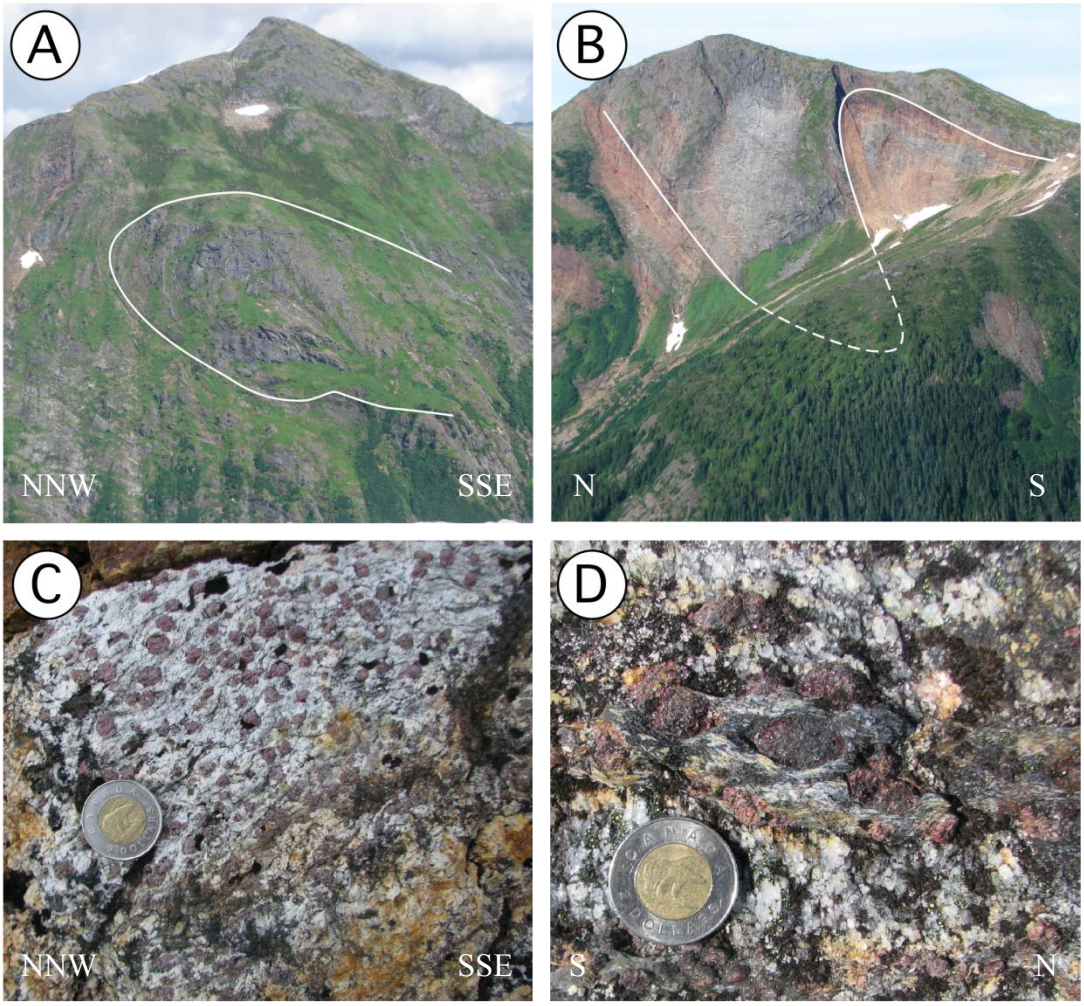

Figure 18. Field photographs from the central gneiss complex. A) Ridge south of Recumbent peak as viewed from Spinel Peak. S_1 layering can be observed (one layer marked in white) folding into an isoclinal fold with a shallow axial plane. B) Mount Bucey as viewed from Spinel Peak. S_1 layering marked by white, folded into northward-verging, tight folds. C) Restite lithology observed along ridge south of Spinel Peak, similar to sample 09B-15. D) Packet of sillimanite defining the lineation around garnet. This sillimanite is a pseudomorph after kyanite.

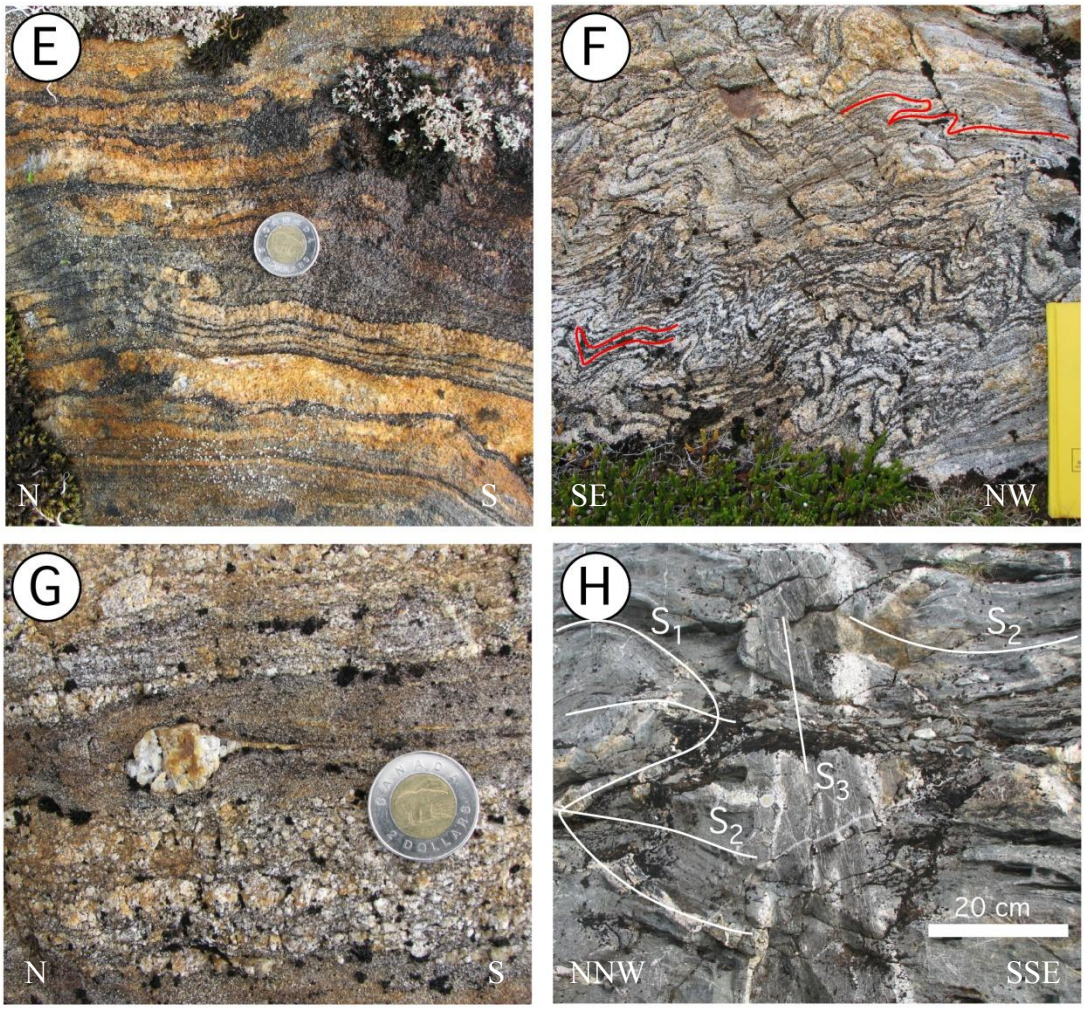

Figure 19. Field photographs from the central gneiss complex. E) S_1 gneissic banding with asymmetrically folded layers. F) Tightly refolded asymmetrical folds south of Spinel Peak. Nose closures marked by red lines. Edge of field notebook is 19 mm long. G) Asymmetrical porphyroclasts within layers indicating right-lateral shear. H) Deformation focused in melt-rich zones. Orientation of S_2 and S_3 indicated on Figure.

The Quottoon pluton has a strong magmatic foliation trending NNW-SSE (local S_1), which parallels a host rock fabric identified as S_3 (Andronicos et al. 1999). Along the pluton margins, there is a complete reorientation of S_1 and S_2 into parallel with the Coast shear zone and Quottoon fabric. This can also be observed on the ridge south of Spinel Peak in the vicinity of sample 09B-15, where the transition from S_2 to S_3 takes place across melt-present zones (Figure 19 H). While the host rock would have an S_2 orientation, the foliation within local melt bands is parallel to S_3, focusing the strain into the melt weakened zones. Continuing down the outcrop, this orientation of S_2 (with an L_2) transitioned to S_3 with a preserved L_2, and finally into a complete transposition of S_3 with L_3. This is possible since the lineation is parallel to both foliations (S_2 and S_3). This suggests that the migmatization of many layers was synchronous with the S_3 foliation.

The final foliation orientation is S_4, formed during emplacement of the Kasiks sill. Magmatic foliations within the Kasiks (local S_0) trend east-west and dip shallowly to the north. Emplacement of the Kasiks caused a tightening of the F_2 generation of folds at Recumbent Peak, with a north-south shortening. Timing of Kasiks emplacement is well constrained by U-Pb zircon and sphene ages within the Kasiks, as well as Ar-Ar hornblende and biotite ages in the host rocks (Andronicos et al. 2003). The Kasiks was emplaced during north-south oriented shortening with a moderately inclined strain field and the initiation of orogenic collapse, and this pre-existing strain field factored into the magmatic foliation orientation.

Exhumation of the orogen is accomplished through top down to the northeast motion along the northwest-southeast trending Shames River mylonite zone (SRMZ). This structure uplifted the middle crust at a rate of 2 mm/y, bringing units from a depth of 35 km to 5 km (Hollister 1982). Andronicos et al. (2003) found that U-Pb sphene, Ar-Ar hornblende and biotite ages were consistent across the width of the

Kasiks. As these represent cooling ages of the samples, this would imply that the width of the Kasiks cooled at the same time, rather than one side having been exhumed before the other. In order to accomplish this, a significant vertical component of shortening must have been present beneath the SRMZ during uplift, at least enough to disguise the exhumation within the error of geochronology.

When three structural domains intersect spatially, it is defined as a foliation triple point. Two foliation triple points are formed from the intersection of S_2 and S_3 domains: (1) adjacent to the Quottoon Pluton at Khtada Lake; and (2) to the south of Recumbent Peak (Figure 17). At these points, we see a reversal of the shear sense. Along the margin of the Quottoon, kinematics indicate dextral top-to-the-south (reverse) shear, while the ridge east of Spinel and south of Recumbent experienced sinistral top-to-the-south (reverse) shear. We interpret these two shear zones form an acute angle, and likely represent conjugate shear zones. If these structures are kinematically related, the sense of shear observed is consistent with north-south oriented shortening, possibly due to Kasiks emplacement (orogenic collapse).

5. Sample descriptions, petrology, and geochronology

Samples are discussed from north to south, including descriptions of the mineralogy, local deformational fabrics, and garnet geochronology. Mineralogies of samples are summarized in Table 7.

5.1 GMO - Head Waters Kwinitsa Creek

Sample GMO (Figure 16 Locality "A") is located at the headwaters of Kwinitsa Creek, seven kilometers north of the Skeena River, 8 km east of the Coast shear zone (CSZ). The outcrop is 500 m from the eastern contact of the Quottoon Pluton, and 3 km west of the Kasiks Sill. Map scale foliations in the vicinity of the outcrop trend

Table 7. Sample mineralogy, in order presented in text

	Grt	Sil	Plag	Qtz	Bt	Ilm	Gph	Cord	Ms	Staur	Spin	And	Opx	Cpx	Hbl
GMO	M	B	M	M	B	B	M		I						
Kwin	M		M	M											
96-056	M	B		M	B	B		M		I	I	I			
09B-34	M		M	M	B	B									
09B-24	M	M			I	B									
09B-15	M	B	M	M	B	B		M							
97-107	M		M	M	B	B									
09B-06A	M		M		B								M	M	M

Grt - Garnet
Sil - Sillimanite
Plag - Plagioclase
Qtz - Quartz
Bt - Biotite
Ilm - Ilmenite
Gph - Graphite
Cord - Cordierite
Ms - Muscovite
Staur - Staurolite
Spin - Spinel (Hercynite)
And - Andalusite
Opx - Orthopyroxene
Cpx - Clinopyroxene
Hbl - Hornblende

M - Mineral occurs in matrix
I - Mineral occurs as inclusion in garnet
B - Mineral occurs in both matrix and as inclusion in garnet

330° and dip steeply to the northeast in the west and change to north-south with a moderate westerly dip in the east. In the vicinity of the outcrop, the average foliation is 000°/45° W, defined by the alignment of sillimanite and biotite. The lineation is also defined by aligned grains of sillimanite, plunging 22° towards 326°.

Kinematic indicators including asymmetrical folds of sillimanite layers and a crenulation cleavage overgrowing sillimanite microlithons are consistent with dextral, top-to-the-west deformation. This sense of shear is consistent with that determined by Andronicos et al. (1999), based on micro-, macro- and mesoscale kinematic analysis of this area. Folded sillimanite and curved inclusions can be observed within garnet grains, while the matrix foliation wraps around the grains. This indicates that the garnets formed after an early fabric (S_1), are syn-tectonic with another fabric (S_2), and pre-date a later fabric (S_3).

Units in the field are migmatite and gneiss. Bands of leucosomes and melanosomes are easily identified at the hand-sample scale. The lithology at GMO is a garnet-sillimanite gneiss, containing garnet + sillimanite + biotite + plagioclase + ilmenite + graphite (Table 7). In thin section, the plagioclase is heavily twinned, but lacks a grain-shape preferred orientation (GSPO). Quartz has occasional undulose extinction. Graphite exists as inclusions in feldspars, surrounded by bulging grain boundaries. Feldspar grain boundaries are pinned by micas and graphite. Grains of biotite and ilmenite occur as inclusions within the garnet with no obvious GSPO.

Ilmenite is present in the matrix, where it has a strong GSPO and helps to define the foliation. Matrix biotite occurs parallel to the foliation with a strong GSPO in high strain zones, and without any GSPO in the strain shadows of the garnet.

A garnet-bearing sample from the outcrop of garnet-sillimanite schist (sample GMO) was analyzed by electron microprobe. Garnet grains are 6-8 mm across and

relatively inclusion-rich, with larger inclusions towards the center of the garnet. The matrix foliation is defined by sillimanite alternating with plagioclase- and quartz-rich domains. Sillimanite also appears as large inclusions near the center of the garnet. WDS X-ray images and quantitative WDS analysis show that the garnet is weakly zoned in Fe, Mg, and Mn. There are slight elevations in Fe concentrations towards grains of biotite (Figure 20). Like Fe, Mg is relatively uniform, but with a slight decrease towards the biotite. The overall uniform mineral composition is consistent with homogenization at high temperature after garnet growth, followed by retrograde exchange near biotite.

In contrast, Ca shows relics of growth zoning within the garnet, with higher concentration near the "northern" margin of the garnet grain (Figure 20). Plagioclase is sodium rich and zoned. Matrix plagioclase increases in Na from core to rim with a matching decrease in Ca. This is consistent with feldspar growth during decreasing pressure (Holdaway 2001). Core compositions of matrix plagioclase are similar to plagioclase that occurs as inclusions inside of the garnet (Table 8).

P-T calculations were made using WinTWQ v. 2 (Table 8). The resultant P-T estimate is 5981 bars and 796° C based on the intersection of the linearly independent reactions: Alm + Phl ⇆ Ann + Py; and Grt + bQz + 2Si ⇆ 3An (Figure 21). An internally consistent phase diagram was constructed using the Berman database in Theriak-Domino. Domino utilized the following mixing models: Ab - ABSAL, CO_2 - CK&J, H_2O - HAAR, Olv - ideal, Spn - ideal and margules, Ilm - ideal, Grt - site mixing and margules, Fsp - external and margules, Bt - ideal, Ms - ideal and margules, St - site mixing and margules, Opx - ideal, Omph - ideal and. margules, Chl - ideal, Crd - ideal, Ctd - ideal, Amph - ideal and margules, H_2O-CO_2 - external. The resultant phase diagram (Figure 21) reproduces the mineral assemblage of the dated sample well and suggests P-T conditions above 680° C and pressures greater than 5 kbar, with

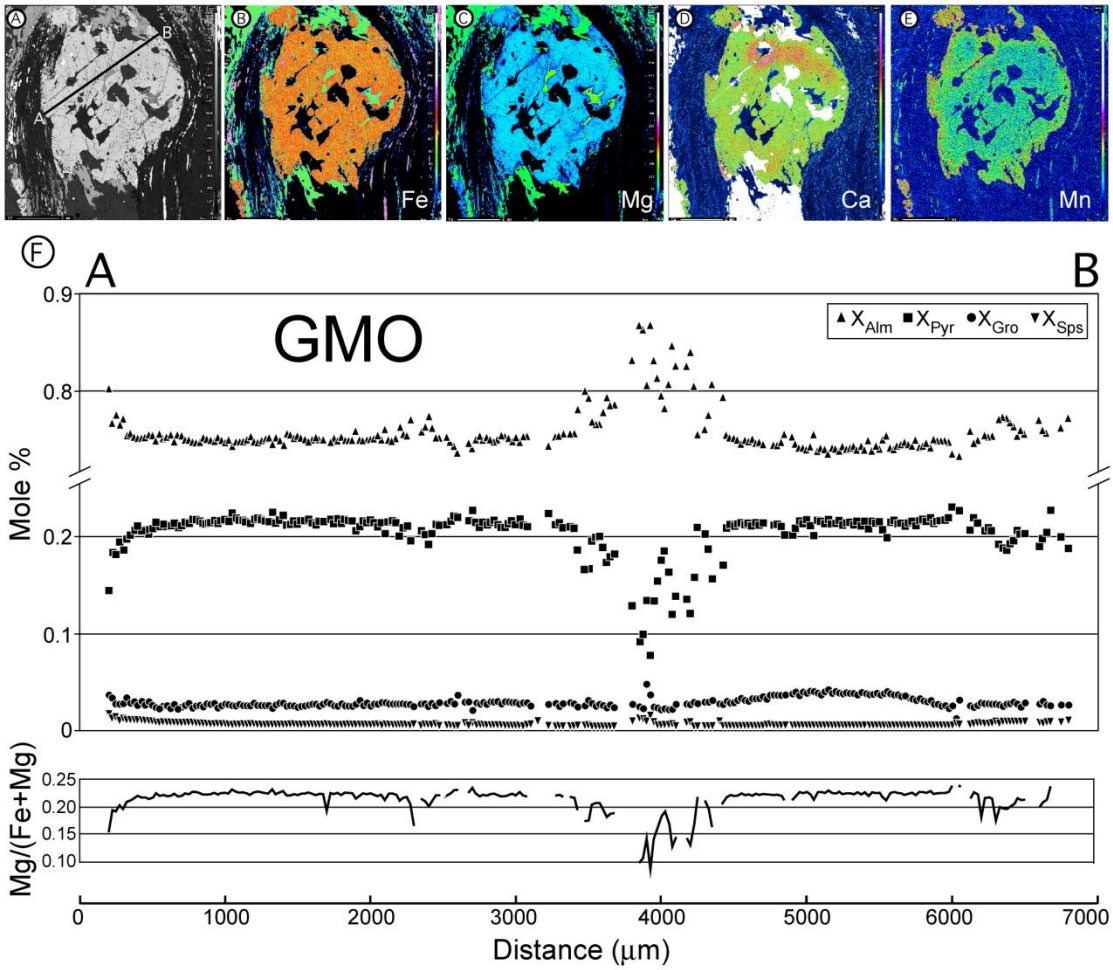

Figure 20. Backscatter electron image, X-ray intensity maps, and compositional line scan collected for sample GMO. A) Backscatter electron image of garnet. Black line marked A-B is location of compositional line scan shown in (F). B) X-ray intensity map for Fe Kα. C) X-ray intensity map for Mg Kα. D) X-ray intensity map for Ca Kα. E) X-ray intensity map for Mn Kα. Color scales have been adjusted to highlight Ca zoning within garnet. D) Compositional line scan collected by quantitative wavelength dispersive scanning analysis. Note compressed vertical scale. Representative analyses of minerals used for thermobarometry calculations reported in Table 8. Large variation is Fe and Mg near center of garnet corresponds to a biotite inclusion adjacent to the scan line.

Table 8. Representative microprobe mineral analyses* for GMO

Weight % Oxides

Oxides	Garnet (Core)	Garnet (Rim)	Plag (Incl)	Plag (Matrix)	Biot (Incl)	Biot (Matrix)	Ilmenite
SiO_2	37.87	37.34	61.76	60.89	34.84	34.40	0.10
TiO_2	0.02	0.04	0.04	0.04	2.31	3.99	51.66
Al_2O_3	21.66	21.40	23.54	23.84	18.85	18.28	0.15
FeO	34.63	36.17	0.05	0.03	20.27	20.96	48.24
MnO	0.28	0.66	0.01	0.01	0.01	0.02	0.37
MgO	5.79	4.96	0.01	0.02	9.18	7.67	0.13
CaO	1.57	0.99	5.36	5.71	0.11	0.01	0.00
Na_2O	0.03	0.01	8.43	8.27	0.25	0.25	0.01
K_2O	0.00	0.00	0.24	0.15	8.87	9.13	0.00
Cr_2O_3	0.00	0.01	0.00	0.00	0.01	0.04	0.02
Cl^-	0.00	0.02	0.00	0.00	0.03	0.05	0.01
F^{2-}	0.00	0.09	0.00	0.00	0.00	0.00	0.00
Ba^-	0.02	0.00	0.00	0.04	0.06	0.39	0.47
Total†	101.86	101.63	99.42	98.98	94.79	95.15	101.12

Ions in Formula§

Element	Garnet (Core)	Garnet (Rim)	Plag (Incl)	Plag (Matrix)	Biot (Incl)	Biot (Matrix)	Ilmenite
Si	2.958	2.948	2.756	2.732	2.919	2.900	0.002
Ti	0.001	0.002	0.001	0.001	0.146	0.253	0.652
Al	1.995	1.991	1.238	1.261	1.862	1.816	0.003
Fe^{2+}	2.262	2.388	0.002	0.001	1.421	1.478	0.677
Mn	0.019	0.044	0.000	0.000	0.001	0.001	0.005
Mg	0.674	0.583	0.000	0.001	1.147	0.964	0.003
Ca	0.131	0.084	0.256	0.275	0.010	0.001	0.000
Na	0.004	0.001	0.729	0.720	0.040	0.041	0.000
K	0.000	0.000	0.014	0.008	0.948	0.982	0.000
Cl	0.000	0.002	0.000	0.000	0.005	0.006	0.000
F	0.000	0.023	0.000	0.000	0.000	0.000	0.000
Ba	0.001	0.000	0.000	0.001	0.002	0.014	0.003
Cr	0.000	0.001	0.000	0.000	0.000	0.002	0.000
Total	8.046	8.067	4.996	5.000	8.501	8.459	1.347

* Representative analyses were chosen for most minerals. Biotite numbers were produced from averaging multiple analyses.
† Oxide totals corrected for Cl, F, and Ba using the method described in Deer, Howie and Zussmen.
§ Stoichiometric ratios of elements based on 12 oxygen for garnet, 11 for biotite, 8 for plagioclase, 2 for ilmenite.

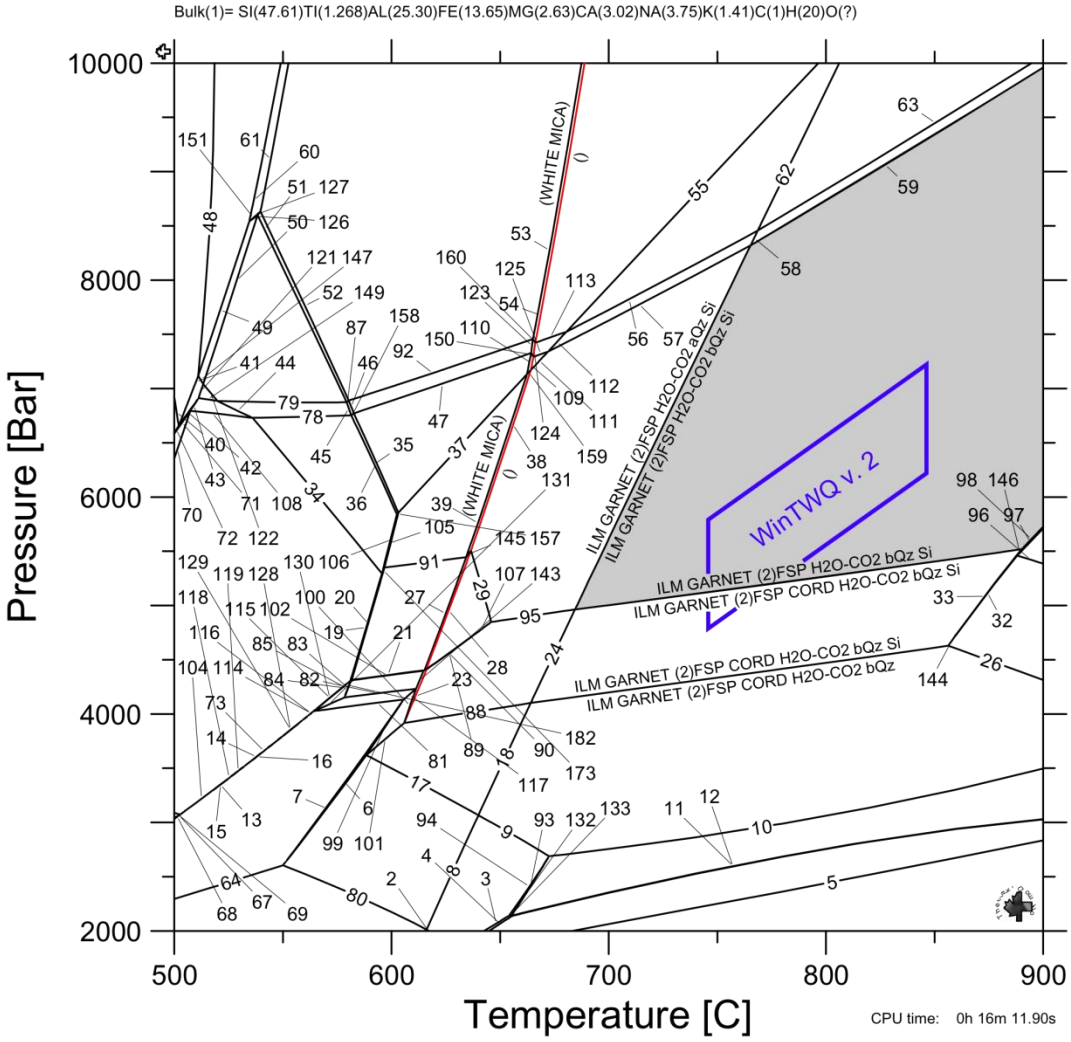

Figure 21. Isochemical phase diagram for sample GMO calculated using Theriak-Domino software. Rock bulk chemistry is shown across top of Figure. Gray shaded region is estimated stability field for minerals in GMO. Blue box shows pressure-temperature estimate calculated by WinTWQ, utilizing microprobe data shown in Table 8. A complete list of reactions on the phase diagram is shown in Table 9.

Table 9. Changes in mineral assemblages for phase diagram of GMO

Reaction number	Mineral assemblage, reactants	Mineral assemblage, products
1	FSP ILM GARNET CHTD CHLR BIO STAU q	FSP ILM GARNET CHTD CHLR BIO STAU q H2O
2	FSP ILM GARNET CHTD CHLR BIO STAU q	FSP ILM GARNET CHTD CHLR BIO STAU q H2O
3	FSP ILM GARNET CHTD CHLR BIO STAU q	FSP ILM GARNET CHTD CHLR BIO STAU q H2O
4	FSP ILM GARNET CHTD CHLR BIO STAU q H2O	FSP ILM GARNET CHLR BIO STAU q H2O
5	FSP ILM GARNET CHTD CHLR BIO STAU q H2O	FSP ILM GARNET CHLR BIO STAU q H2O
6	FSP ILM GARNET CHTD CHLR BIO STAU q H2O	FSP ILM GARNET CHLR BIO STAU q H2O
7	FSP ILM GARNET CHLR BIO STAU q H2O	FSP ILM GARNET BIO STAU CORD q H2O
8	FSP ILM GARNET BIO STAU CORD q H2O	FSP ILM GARNET BIO CORD and q H2O
9	FSP ILM GARNET BIO CORD and q H2O	FSP ILM GARNET BIO CORD TI and q H2O
10	FSP ILM GARNET BIO CORD TI and q H2O	FSP ILM GARNET BIO CORD TI q H2O
11	FSP ILM GARNET BIO CORD TI q H2O	FSP ILM GARNET BIO CORD q H2O
12	FSP ILM GARNET BIO CORD q H2O	FSP ILM GARNET OPX BIO CORD q H2O
13	FSP ILM GARNET OPX BIO CORD q H2O	(2)FSP ILM GARNET OPX BIO CORD q H2O
14	(2)FSP ILM GARNET OPX BIO CORD q H2O	(2)FSP ILM GARNET OPX CORD q H2O
15	(2)FSP ILM GARNET OPX CORD q H2O	(2)FSP ILM OPX CORD q H2O
16	(2)FSP ILM OPX CORD q H2O	(2)FSP ILM OPX CORD LIQtc q H2O
17	(2)FSP ILM OPX CORD LIQtc q H2O	(2)FSP ILM OPX CORD LIQtc H2O
18	(2)FSP ILM OPX CORD LIQtc H2O	(2)FSP ILM OPX CORD SPIN LIQtc H2O
19	(2)FSP ILM OPX CORD SPIN LIQtc H2O	FSP ILM OPX CORD SPIN LIQtc H2O
20	FSP ILM GARNET CHTD CHLR BIO q	FSP ILM GARNET CHTD CHLR BIO STAU q
21	FSP ILM GARNET CHTD CHLR BIO STAU q	FSP ILM GARNET CHLR BIO STAU q H2O
22	FSP ILM GARNET BIO CORD q H2O	(2)FSP ILM GARNET BIO CORD q H2O
23	(2)FSP ILM GARNET BIO CORD q H2O	(2)FSP ILM GARNET BIO CORD LIQtc q H2O
24	(2)FSP ILM GARNET BIO CORD LIQtc q H2O	FSP ILM GARNET BIO CORD LIQtc q H2O
25	FSP ILM GARNET BIO CORD LIQtc q H2O	FSP ILM GARNET OPX BIO CORD LIQtc q H2O
26	FSP ILM GARNET OPX BIO CORD LIQtc q H2O	FSP ILM GARNET OPX CORD LIQtc q H2O
27	FSP ILM GARNET OPX CORD LIQtc q H2O	FSP ILM GARNET OPX CORD LIQtc H2O
28	FSP ILM GARNET OPX CORD LIQtc H2O	FSP ILM GARNET OPX CORD SPIN LIQtc H2O
29	FSP ILM GARNET OPX CORD SPIN LIQtc H2O	FSP ILM OPX CORD SPIN LIQtc H2O
30	FSP ILM GARNET CHTD CHLR BIO q	FSP ILM GARNET CHTD CHLR BIO q H2O
31	FSP ILM GARNET CHTD CHLR BIO q H2O	FSP ILM GARNET CHLR BIO STAU q H2O
32	FSP ILM GARNET CHLR BIO STAU q H2O	FSP ILM GARNET BIO STAU q H2O
33	FSP ILM GARNET BIO STAU q H2O	FSP ILM GARNET CHLR BIO STAU q H2O
34	FSP ILM GARNET BIO STAU q H2O	FSP ILM GARNET BIO and q H2O
35	FSP ILM GARNET BIO STAU q H2O	FSP ILM GARNET BIO and q H2O
36	FSP ILM GARNET BIO and q H2O	FSP ILM GARNET BIO TI and q H2O
37	FSP ILM GARNET BIO TI and q H2O	FSP ILM GARNET BIO CORD TI and q H2O
38	FSP ILM GARNET BIO CORD TI sill q H2O	FSP ILM GARNET BIO CORD TI and q H2O
39	FSP ILM GARNET BIO CORD TI sill q H2O	FSP ILM GARNET BIO CORD TI q H2O
40	FSP ILM GARNET BIO CORD TI q H2O	(2)FSP ILM GARNET BIO CORD TI q H2O
41	(2)FSP ILM GARNET BIO CORD TI q H2O	(2)FSP ILM GARNET BIO CORD q H2O
42	(2)FSP ILM GARNET CORD q H2O	(2)FSP ILM GARNET BIO CORD q H2O
43	(2)FSP ILM GARNET CORD q H2O	(2)FSP ILM GARNET CORD LIQtc q H2O
44	(2)FSP ILM GARNET CORD LIQtc q H2O	FSP ILM GARNET CORD LIQtc q H2O
45	FSP ILM GARNET CORD LIQtc q H2O	FSP ILM GARNET CORD LIQtc H2O
46	FSP ILM GARNET CORD LIQtc H2O	FSP ILM GARNET CORD SPIN LIQtc H2O
47	FSP ILM GARNET CORD SPIN LIQtc H2O	FSP ILM GARNET OPX CORD SPIN LIQtc H2O
48	FSP ILM GARNET CHTD CHLR BIO q H2O	FSP ILM GARNET CHTD CHLR BIO STAU q H2O
49	FSP ILM GARNET CHTD CHLR BIO STAU q H2O	FSP ILM GARNET CHLR BIO STAU q H2O
50	FSP ILM GARNET BIO STAU TI q H2O	FSP ILM GARNET BIO STAU q H2O
51	FSP ILM GARNET BIO STAU q H2O	FSP ILM GARNET BIO STAU TI q H2O
52	FSP ILM GARNET BIO STAU q H2O	FSP ILM GARNET BIO STAU sill q H2O
53	FSP ILM GARNET BIO STAU sill q H2O	FSP ILM GARNET BIO sill q H2O
54	FSP ILM GARNET BIO sill q H2O	FSP ILM GARNET BIO TI sill q H2O
55	FSP ILM GARNET BIO TI sill q H2O	FSP ILM GARNET BIO sill q H2O
56	FSP ILM GARNET BIO TI sill q H2O	FSP ILM GARNET BIO CORD TI sill q H2O
57	FSP ILM GARNET BIO CORD TI sill q H2O	(2)FSP ILM GARNET BIO CORD TI sill q H2O
58	(2)FSP ILM GARNET BIO CORD TI sill q H2O	(2)FSP ILM GARNET CORD TI sill q H2O
59	(2)FSP ILM GARNET CORD TI sill q H2O	(2)FSP ILM GARNET CORD LIQtc TI sill q H2O
60	(2)FSP ILM GARNET CORD LIQtc TI sill q H2O	FSP ILM GARNET CORD LIQtc TI sill q H2O
61	FSP ILM GARNET CORD LIQtc TI sill q H2O	FSP ILM GARNET CORD LIQtc sill q H2O
62	FSP ILM GARNET CORD LIQtc sill q H2O	FSP ILM GARNET CORD LIQtc q H2O
63	FSP ILM GARNET OPX CORD SPIN LIQtc H2O	FSP ILM GARNET OPX SPIN LIQtc H2O
64	FSP ILM GARNET CHTD CHLR BIO STAU q H2O	FSP ILM GARNET CHLR PHNG BIO STAU q H2O
65	FSP ILM GARNET CHLR PHNG BIO STAU q H2O	FSP ILM GARNET CHLR BIO STAU q H2O

Table 9 (cont). Changes in mineral assemblages for phase diagram of GMO

Reaction number	Mineral assemblage, reactants	Mineral assemblage, products
66	FSP ILM GARNET BIO STAU TI q H2O	FSP ILM GARNET BIO STAU TI sill q H2O
67	FSP ILM GARNET BIO STAU TI sill q H2O	FSP ILM GARNET BIO TI sill q H2O
68	FSP ILM GARNET BIO TI sill q H2O	(2)FSP ILM GARNET BIO TI sill q H2O
69	(2)FSP ILM GARNET BIO TI sill q H2O	(2)FSP ILM GARNET TI sill q H2O
70	(2)FSP ILM GARNET TI sill q H2O	(2)FSP ILM GARNET LIQtc TI sill q H2O
71	(2)FSP ILM GARNET LIQtc TI sill q H2O	FSP ILM GARNET LIQtc TI sill q H2O
72	FSP ILM GARNET LIQtc TI sill q H2O	FSP ILM GARNET CORD LIQtc TI sill q H2O
73	FSP ILM GARNET CORD LIQtc sill q H2O	FSP ILM GARNET CORD LIQtc sill H2O
74	FSP ILM GARNET CORD LIQtc sill H2O	FSP ILM GARNET CORD SPIN LIQtc sill H2O
75	FSP ILM GARNET CORD SPIN LIQtc sill H2O	FSP ILM GARNET CORD SPIN LIQtc H2O
76	FSP ILM GARNET SPIN LIQtc H2O	FSP ILM GARNET CORD SPIN LIQtc H2O
77	ILM GARNET CHTD CHLR PHNG BIO zo q H2O	FSP ILM GARNET CHTD CHLR PHNG BIO q H2O
78	FSP ILM GARNET CHTD CHLR PHNG BIO q H2O	FSP ILM GARNET CHLR PHNG BIO STAU q H2O
79	FSP ILM GARNET CHLR PHNG BIO STAU q H2O	FSP ILM GARNET PHNG BIO STAU q H2O
80	FSP ILM GARNET PHNG BIO STAU q H2O	FSP ILM GARNET BIO STAU q H2O
81	FSP ILM GARNET BIO STAU TI q H2O	FSP ILM GARNET BIO STAU TI ky q H2O
82	FSP ILM GARNET BIO STAU TI ky q H2O	FSP ILM GARNET BIO TI ky q H2O
83	FSP ILM GARNET BIO TI ky q H2O	FSP ILM GARNET BIO TI sill q H2O
84	FSP ILM GARNET LIQtc TI sill q H2O	FSP ILM GARNET LIQtc sill q H2O
85	FSP ILM GARNET LIQtc sill q H2O	FSP ILM GARNET LIQtc sill H2O
86	FSP ILM GARNET LIQtc sill H2O	FSP ILM GARNET SPIN LIQtc sill H2O
87	FSP ILM GARNET SPIN LIQtc sill H2O	FSP ILM GARNET SPIN LIQtc H2O
88	ILM GARNET CHTD CHLR PHNG BIO zo q H2O	ILM GARNET CHLR PHNG BIO STAU zo q H2O
89	ILM GARNET CHLR PHNG BIO STAU zo q H2O	ILM GARNET PHNG BIO STAU zo q H2O
90	ILM GARNET PHNG BIO STAU zo q H2O	FSP ILM GARNET PHNG BIO STAU zo q H2O
91	FSP ILM GARNET PHNG BIO STAU zo q H2O	FSP ILM GARNET PHNG BIO STAU q H2O
92	ILM GARNET CHTD PHNG BIO zo q H2O	ILM GARNET CHTD (2)PHNG BIO zo q H2O
93	ILM GARNET CHTD (2)PHNG BIO zo q H2O	ILM GARNET (2)PHNG BIO STAU zo q H2O
94	ILM GARNET (2)PHNG BIO ky zo q H2O	ILM GARNET (2)PHNG BIO STAU zo q H2O
95	ILM GARNET (2)PHNG BIO ky zo q H2O	FSP ILM GARNET (2)PHNG BIO ky q H2O
96	FSP ILM GARNET (2)PHNG BIO ky q H2O	FSP ILM GARNET (2)PHNG BIO TI ky q H2O
97	FSP ILM GARNET (2)PHNG BIO TI ky q H2O	FSP ILM GARNET PHNG BIO TI ky q H2O
98	FSP ILM GARNET PHNG BIO TI ky q H2O	FSP ILM GARNET BIO TI ky q H2O
99	FSP ILM GARNET BIO sill q H2O	FSP ILM GARNET BIO TI sill q H2O
100	FSP ILM GARNET BIO sill q H2O	FSP ILM GARNET BIO TI sill q H2O
101	FSP ILM GARNET BIO sill q H2O	(2)FSP ILM GARNET BIO sill q H2O
102	(2)FSP ILM GARNET BIO sill q H2O	(2)FSP ILM GARNET BIO TI sill q H2O
103	FSP ILM GARNET LIQtc TI sill q H2O	FSP ILM GARNET LIQtc TI sill H2O
104	FSP ILM GARNET LIQtc TI sill H2O	FSP ILM GARNET LIQtc sill H2O
105	ILM GARNET (2)PHNG BIO ky zo q H2O	ILM GARNET (2)PHNG BIO zo q H2O
106	ILM GARNET (2)PHNG BIO zo q H2O	FSP ILM GARNET CHTD BIO STAU q H2O
107	ILM GARNET (2)PHNG BIO zo q H2O	ILM GARNET (2)PHNG BIO q H2O
108	ILM GARNET (2)PHNG BIO q H2O	ILM GARNET (2)PHNG BIO TI q H2O
109	ILM GARNET (2)PHNG BIO TI q H2O	FSP ILM GARNET (2)PHNG BIO TI q H2O
110	FSP ILM GARNET (2)PHNG BIO TI q H2O	FSP ILM GARNET (2)PHNG BIO TI ky q H2O
111	FSP ILM GARNET BIO TI ky q H2O	(2)FSP ILM GARNET BIO TI ky q H2O
112	(2)FSP ILM GARNET BIO TI ky q H2O	(2)FSP ILM GARNET TI ky q H2O
113	(2)FSP ILM GARNET TI ky q H2O	(2)FSP ILM GARNET ky q H2O
114	(2)FSP ILM GARNET TI ky q H2O	(2)FSP ILM GARNET ky q H2O
115	(2)FSP ILM GARNET ky q H2O	(2)FSP ILM GARNET sill q H2O
116	(2)FSP ILM GARNET sill q H2O	(2)FSP ILM GARNET TI sill q H2O
117	ILM GARNET CHTD (2)PHNG BIO zo q H2O	ILM GARNET (2)PHNG BIO zo q H2O
118	FSP ILM GARNET PHNG BIO TI ky q H2O	(2)FSP ILM GARNET PHNG BIO TI ky q H2O
119	(2)FSP ILM GARNET PHNG BIO TI ky q H2O	(2)FSP ILM GARNET BIO TI ky q H2O
120	(2)FSP ILM GARNET TI ky q H2O	(2)FSP ILM GARNET TI sill q H2O
121	FSP ILM GARNET CHTD CHLR PHNG BIO q H2O	FSP ILM GARNET CHTD CHLR BIO q H2O
122	ILM GARNET CHTD PHNG BIO zo q H2O	ILM GARNET CHTD CHLR PHNG BIO zo q H2O
123	FSP ILM GARNET (2)PHNG BIO STAU q H2O	FSP ILM GARNET PHNG BIO STAU q H2O
124	FSP ILM GARNET PHNG BIO STAU q H2O	FSP ILM GARNET (2)PHNG BIO STAU q H2O
125	FSP ILM GARNET (2)PHNG BIO ky q H2O	FSP ILM GARNET (2)PHNG BIO STAU q H2O
126	FSP ILM GARNET BIO and q H2O	FSP ILM GARNET BIO CORD and q H2O
127	FSP ILM GARNET BIO sill q H2O	FSP ILM GARNET BIO and q H2O
128	(2)FSP ILM GARNET BIO CORD TI q H2O	(2)FSP ILM GARNET CORD TI q H2O
129	(2)FSP ILM GARNET CORD TI sill q H2O	(2)FSP ILM GARNET CORD TI q H2O
130	(2)FSP ILM GARNET OPX CORD LIQtc H2O	(2)FSP ILM OPX CORD LIQtc H2O

Table 9 (cont). Changes in mineral assemblages for phase diagram of GMO

Reaction number	Mineral assemblage, reactants	Mineral assemblage, products
131	FSP ILM GARNET OPX CORD LIQtc H2O	(2)FSP ILM GARNET OPX CORD LIQtc H2O
132	FSP ILM GARNET CORD LIQtc H2O	FSP ILM GARNET OPX CORD LIQtc H2O
133	(2)FSP ILM GARNET TI sill q H2O	(2)FSP ILM GARNET CORD TI sill q H2O
134	FSP ILM GARNET LIQtc sill q H2O	FSP ILM GARNET CORD LIQtc sill q H2O
135	FSP ILM GARNET SPIN LIQtc sill H2O	FSP ILM GARNET CORD SPIN LIQtc sill H2O
136	FSP ILM OPX SPIN LIQtc H2O	FSP ILM OPX CORD SPIN LIQtc H2O
137	FSP ILM GARNET OPX SPIN LIQtc H2O	FSP ILM OPX SPIN LIQtc H2O
138	FSP ILM GARNET BIO STAU q H2O	FSP ILM GARNET BIO STAU CORD q H2O
139	FSP ILM GARNET BIO STAU CORD q H2O	FSP ILM GARNET BIO STAU CORD and q H2O
140	FSP ILM GARNET BIO STAU CORD and q H2O	FSP ILM GARNET BIO CORD and q H2O
141	(2)FSP ILM GARNET OPX CORD q H2O	(2)FSP ILM GARNET OPX CORD LIQtc q H2O
142	(2)FSP ILM GARNET OPX CORD LIQtc q H2O	(2)FSP ILM GARNET OPX CORD LIQtc H2O
143	FSP ILM GARNET BIO CORD LIQtc q H2O	FSP ILM GARNET CORD LIQtc q H2O
144	FSP ILM GARNET CORD LIQtc q H2O	FSP ILM GARNET OPX CORD LIQtc q H2O
145	FSP ILM GARNET BIO STAU q H2O	FSP ILM GARNET BIO STAU and q H2O
146	FSP ILM GARNET BIO STAU and q H2O	FSP ILM GARNET BIO and q H2O
147	FSP ILM GARNET BIO TI sill q H2O	FSP ILM GARNET BIO TI and q H2O
148	(2)FSP ILM GARNET BIO CORD TI sill q H2O	(2)FSP ILM GARNET BIO CORD TI q H2O
149	(2)FSP ILM GARNET CORD TI q H2O	(2)FSP ILM GARNET CORD q H2O
150	FSP ILM GARNET CORD LIQtc sill H2O	FSP ILM GARNET CORD LIQtc H2O
151	FSP ILM GARNET (2)PHNG BIO STAU q H2O	FSP ILM GARNET (2)PHNG BIO STAU TI q H2O
152	FSP ILM GARNET (2)PHNG BIO STAU TI q H2O	FSP ILM GARNET PHNG BIO STAU TI q H2O
153	FSP ILM GARNET PHNG BIO STAU TI q H2O	FSP ILM GARNET PHNG BIO STAU TI ky q H2O
154	FSP ILM GARNET PHNG BIO STAU TI ky q H2O	FSP ILM GARNET PHNG BIO TI ky q H2O
155	FSP ILM GARNET PHNG BIO STAU TI q H2O	FSP ILM GARNET BIO STAU TI q H2O
156	(2)FSP ILM GARNET BIO TI sill q H2O	(2)FSP ILM GARNET BIO CORD TI sill q H2O
157	(2)FSP ILM GARNET BIO TI ky q H2O	(2)FSP ILM GARNET BIO TI sill q H2O
158	(2)FSP ILM GARNET BIO sill q H2O	(2)FSP ILM GARNET BIO TI sill q H2O
159	(2)FSP ILM GARNET BIO ky q H2O	(2)FSP ILM GARNET BIO sill q H2O
160	(2)FSP ILM GARNET BIO ky q H2O	(2)FSP ILM GARNET BIO TI ky q H2O
161	FSP ILM GARNET CORD LIQtc sill H2O	FSP ILM GARNET LIQtc sill H2O
162	ILM GARNET CHTD PHNG BIO zo q H2O	ILM GARNET CHTD PHNG BIO STAU zo q H2O
163	ILM GARNET CHTD PHNG BIO STAU zo q H2O	ILM GARNET PHNG BIO STAU zo q H2O
164	ILM GARNET (2)PHNG BIO STAU zo q H2O	ILM GARNET PHNG BIO STAU zo q H2O
165	ILM GARNET (2)PHNG BIO STAU zo q H2O	FSP ILM GARNET (2)PHNG BIO STAU q H2O
166	FSP ILM GARNET PHNG BIO TI ky q H2O	(2)FSP ILM GARNET BIO TI ky q H2O
167	(2)FSP ILM GARNET BIO CORD q H2O	(2)FSP ILM GARNET OPX BIO CORD q H2O
168	(2)FSP ILM GARNET OPX CORD LIQtc H2O	(2)FSP ILM GARNET OPX CORD SPIN LIQtc H2O
169	(2)FSP ILM GARNET OPX CORD SPIN LIQtc H2O	FSP ILM GARNET OPX CORD SPIN LIQtc H2O
170	FSP ILM GARNET CHTD CHLR BIO STAU q H2O	FSP ILM GARNET CHLR BIO STAU q H2O
171	FSP ILM GARNET CHTD CHLR BIO q H2O	FSP ILM GARNET CHTD CHLR BIO STAU q H2O
172	FSP ILM GARNET CHLR PHNG BIO STAU q H2O	FSP ILM GARNET CHTD PHNG (2)BIO STAU q H2O
173	FSP (2)ILM GARNET BIO sill q H2O	FSP ILM GARNET BIO sill q H2O
174	FSP ILM GARNET PHNG BIO STAU q H2O	FSP ILM GARNET PHNG BIO STAU TI q H2O
175	(2)FSP ILM GARNET BIO sill q H2O	(2)FSP ILM GARNET sill q H2O
176	FSP ILM GARNET CORD SPIN LIQtc H2O	FSP ILM GARNET CORD SPIN (3)LIQtc sill H2O
177	ILM GARNET CHLR PHNG BIO STAU zo q H2O	FSP ILM GARNET CHLR PHNG BIO STAU q H2O
178	ILM GARNET CHTD PHNG BIO STAU zo q H2O	ILM GARNET CHLR PHNG BIO STAU zo q H2O
179	ILM GARNET CHTD (2)PHNG BIO zo q H2O	ILM GARNET CHTD PHNG BIO STAU zo q H2O
180	ILM GARNET (2)PHNG BIO STAU zo q H2O	ILM GARNET (2)PHNG BIO zo q H2O
181	ILM GARNET (2)PHNG BIO q H2O	FSP ILM GARNET (2)PHNG BIO q H2O
182	FSP ILM GARNET (2)PHNG BIO q H2O	FSP ILM GARNET (2)PHNG BIO ky q H2O
183	FSP ILM GARNET (2)PHNG BIO TI ky q H2O	FSP ILM GARNET PHNG BIO STAU TI ky q H2O
184	(2)FSP ILM GARNET OPX CORD SPIN LIQtc H2O	(2)FSP ILM OPX CORD SPIN LIQtc H2O
185	FSP ILM GARNET CHTD CHLR BIO q H2O	FSP ILM GARNET CHLR BIO STAU q H2O
186	(2)FSP ILM GARNET CORD LIQtc q H2O	(2)FSP ILM GARNET BIO CORD LIQtc q H2O
187	FSP ILM GARNET BIO STAU q H2O	FSP ILM GARNET BIO STAU and q H2O
188	FSP ILM GARNET BIO STAU and q H2O	FSP ILM GARNET BIO and q H2O
189	FSP ILM GARNET BIO CORD TI sill q H2O	(2)FSP ILM GARNET BIO CORD TI q H2O
190	(2)FSP ILM GARNET CORD LIQtc TI sill q H2O	(2)FSP ILM GARNET CORD LIQtc q H2O
191	FSP ILM GARNET BIO STAU q H2O	FSP ILM GARNET BIO sill q H2O
192	FSP ILM GARNET CHLR BIO STAU q H2O	FSP ILM GARNET CHLR BIO STAU TI q H2O
193	FSP ILM GARNET CHLR BIO STAU TI q H2O	FSP ILM GARNET BIO STAU q H2O
194	(2)FSP ILM GARNET BIO TI sill q H2O	(2)FSP ILM GARNET CORD TI sill q H2O
195	(2)FSP ILM GARNET LIQtc TI sill q H2O	(2)FSP ILM GARNET CORD LIQtc TI sill q H2O

Table 9 (cont). Changes in mineral assemblages for phase diagram of GMO

Reaction number	Mineral assemblage, reactants	Mineral assemblage, products
196	FSP ILM GARNET BIO TI sill q H2O	(2)FSP ILM GARNET BIO TI sill q H2O
197	ILM GARNET PHNG BIO STAU zo q H2O	FSP ILM GARNET (2)PHNG BIO STAU q H2O
198	ILM GARNET (2)PHNG BIO zo q H2O	FSP ILM GARNET (2)PHNG BIO zo q H2O
199	FSP ILM GARNET (2)PHNG BIO zo q H2O	FSP ILM GARNET (2)PHNG BIO ky q H2O
200	FSP ILM GARNET (2)PHNG BIO TI ky q H2O	FSP ILM GARNET (2)PHNG BIO STAU TI q H2O
201	(2)FSP ILM GARNET BIO ky q H2O	(2)FSP ILM GARNET ky q H2O
202	FSP ILM GARNET CHTD CHLR BIO STAU q	FSP ILM GARNET CHLR BIO STAU q H2O
203	FSP ILM GARNET BIO and q H2O	FSP ILM GARNET BIO CORD TI and q H2O
204	(2)FSP ILM GARNET OPX CORD LIQtc q H2O	FSP ILM GARNET OPX BIO CORD LIQtc q H2O
205	FSP ILM GARNET CHTD CHLR BIO q H2O	FSP ILM GARNET CHTD CHLR BIO STAU q H2O
206	FSP ILM GARNET CHTD CHLR BIO q H2O	FSP ILM GARNET CHTD CHLR BIO STAU q H2O
207	FSP ILM GARNET CHTD CHLR BIO STAU q H2O	FSP ILM GARNET CHLR BIO STAU q H2O
208	FSP ILM GARNET CHTD CHLR BIO STAU q H2O	FSP ILM GARNET CHLR BIO STAU q H2O
209	FSP ILM GARNET CHLR BIO STAU q H2O	FSP ILM GARNET BIO STAU TI q H2O
210	FSP ILM GARNET BIO STAU CORD q H2O	FSP ILM GARNET BIO CORD and q H2O
211	FSP ILM GARNET BIO STAU and q H2O	FSP ILM GARNET BIO and q H2O
212	FSP ILM GARNET BIO STAU q H2O	FSP ILM GARNET BIO STAU and q H2O
213	FSP ILM GARNET CORD LIQtc sill H2O	FSP ILM GARNET CORD SPIN LIQtc H2O
214	FSP ILM GARNET BIO STAU TI ky q H2O	FSP ILM GARNET BIO TI sill q H2O
215	ILM GARNET CHTD CHLR PHNG BIO zo q H2O	ILM GARNET CHLR PHNG BIO zo ma q H2O
216	ILM GARNET CHLR PHNG BIO zo ma q H2O	FSP ILM GARNET CHLR PHNG BIO ma q H2O
217	FSP ILM GARNET CHLR PHNG BIO ma q H2O	FSP ILM GARNET CHLR PHNG BIO STAU q H2O
218	FSP ILM GARNET CHLR PHNG BIO ma q H2O	FSP ILM GARNET CHTD CHLR PHNG BIO q H2O
219	ILM GARNET CHLR PHNG BIO STAU zo q H2O	FSP ILM GARNET PHNG BIO STAU q H2O
220	FSP ILM GARNET PHNG BIO STAU TI ky q H2O	FSP ILM GARNET BIO TI ky q H2O
221	ILM GARNET CHTD PHNG BIO zo q H2O	ILM GARNET CHLR PHNG BIO STAU zo q H2O
222	FSP ILM GARNET PHNG BIO STAU zo q H2O	FSP ILM GARNET (2)PHNG BIO STAU q H2O
223	FSP ILM GARNET (2)PHNG BIO q H2O	FSP ILM GARNET (2)PHNG BIO TI q H2O
224	(2)FSP ILM GARNET BIO TI ky q H2O	(2)FSP ILM GARNET ky q H2O
225	FSP ILM GARNET CHTD CHLR BIO q H2O	FSP ILM GARNET CHLR BIO STAU q H2O
226	(2)FSP ILM GARNET OPX CORD LIQtc q H2O	FSP ILM GARNET OPX CORD LIQtc H2O
227	FSP ILM GARNET CHTD CHLR BIO q H2O	FSP ILM GARNET CHLR PHNG BIO STAU q H2O
228	FSP ILM GARNET CHLR BIO STAU TI q H2O	FSP ILM GARNET BIO STAU TI q H2O
229	FSP ILM GARNET PHNG BIO STAU TI q H2O	FSP ILM GARNET BIO STAU TI ky q H2O
230	ILM GARNET CHTD PHNG BIO zo q H2O	ILM GARNET CHTD PHNG BIO STAU zo q H2O
231	ILM GARNET CHTD PHNG BIO STAU zo q H2O	ILM GARNET CHLR PHNG BIO STAU zo q H2O
232	ILM GARNET CHTD (2)PHNG BIO zo q H2O	ILM GARNET PHNG BIO STAU zo q H2O
233	FSP ILM GARNET (2)PHNG BIO q H2O	FSP ILM GARNET (2)PHNG BIO TI ky q H2O
234	FSP ILM GARNET (2)PHNG BIO zo q H2O	FSP ILM GARNET (2)PHNG BIO q H2O
235	ILM GARNET (2)PHNG BIO q H2O	FSP ILM GARNET (2)PHNG BIO TI q H2O
236	(2)FSP ILM GARNET ky q H2O	(2)FSP ILM GARNET TI sill q H2O
237	(2)FSP ILM GARNET ky q H2O	(2)FSP ILM GARNET TI ky q H2O
238	FSP ILM GARNET BIO STAU CORD q H2O	FSP ILM GARNET BIO CORD and q H2O
239	FSP ILM GARNET BIO STAU CORD and q H2O	FSP ILM GARNET BIO CORD and q H2O
240	FSP ILM GARNET BIO STAU CORD q H2O	FSP ILM GARNET BIO STAU CORD and q H2O
241	(2)FSP ILM GARNET BIO TI ky q H2O	(2)FSP ILM GARNET BIO sill q H2O
242	(2)FSP ILM GARNET TI ky q H2O	(2)FSP ILM GARNET ky q H2O
243	FSP ILM GARNET CHTD CHLR BIO STAU q	FSP ILM GARNET CHLR BIO STAU q H2O
244	(2)FSP ILM GARNET OPX BIO CORD q H2O	(2)FSP ILM GARNET OPX CORD LIQtc q H2O
245	(2)FSP ILM GARNET BIO CORD LIQtc q H2O	(2)FSP ILM GARNET OPX BIO CORD q H2O
246	(2)FSP ILM GARNET OPX CORD q H2O	(2)FSP ILM OPX CORD LIQtc q H2O
247	(2)FSP ILM GARNET OPX CORD LIQtc q H2O	(2)FSP ILM OPX CORD LIQtc q H2O
248	(2)FSP ILM GARNET OPX CORD LIQtc H2O	(2)FSP ILM OPX CORD SPIN LIQtc H2O
249	FSP ILM GARNET OPX CORD SPIN LIQtc H2O	FSP ILM OPX CORD SPIN LIQtc H2O
250	(3)FSP ILM OPX CORD SPIN LIQtc H2O	FSP ILM OPX CORD SPIN LIQtc H2O
251	FSP ILM GARNET OPX CORD SPIN LIQtc H2O	(3)FSP ILM OPX CORD SPIN LIQtc H2O
252	FSP ILM GARNET CHTD CHLR BIO STAU q	FSP ILM GARNET CHTD CHLR BIO STAU q H2O
253	FSP ILM GARNET CHTD CHLR BIO STAU q H2O	FSP ILM GARNET CHLR BIO STAU q H2O
254	(2)FSP ILM GARNET BIO CORD LIQtc q H2O	FSP ILM GARNET CORD LIQtc q H2O
255	FSP ILM GARNET BIO CORD LIQtc q H2O	FSP ILM GARNET OPX CORD LIQtc q H2O
256	(2)FSP ILM GARNET OPX CORD LIQtc H2O	FSP ILM GARNET OPX CORD SPIN LIQtc H2O
257	FSP ILM GARNET CORD LIQtc H2O	FSP ILM GARNET OPX CORD SPIN LIQtc H2O
258	FSP ILM GARNET CHLR PHNG BIO STAU q H2O	FSP ILM GARNET BIO STAU q H2O
259	FSP ILM GARNET BIO STAU q H2O	FSP ILM GARNET BIO STAU sill q H2O
260	FSP ILM GARNET BIO STAU sill q H2O	FSP ILM GARNET BIO sill q H2O

Table 9 (cont). Changes in mineral assemblages for phase diagram of GMO

Reaction number	Mineral assemblage, reactants	Mineral assemblage, products
261	FSP ILM GARNET BIO STAU q H2O	FSP ILM GARNET BIO sill q H2O
262	FSP ILM GARNET BIO STAU sill q H2O	FSP ILM GARNET BIO sill q H2O
263	FSP ILM GARNET BIO STAU q H2O	FSP ILM GARNET BIO STAU sill q H2O
264	FSP ILM GARNET PHNG BIO STAU TI ky q H2O	FSP ILM GARNET BIO STAU TI ky q H2O
265	ILM GARNET CHLR PHNG BIO STAU zo q H2O	ILM GARNET CHLR PHNG BIO zo ma q H2O
266	ILM GARNET CHTD PHNG BIO zo q H2O	ILM GARNET CHLR PHNG BIO STAU zo q H2O
267	ILM GARNET CHLR PHNG BIO STAU zo q H2O	FSP ILM GARNET PHNG BIO STAU zo q H2O
268	ILM GARNET (2)PHNG BIO zo q H2O	FSP ILM GARNET (2)PHNG BIO ky q H2O
269	FSP ILM GARNET (2)PHNG BIO ky q H2O	FSP ILM GARNET (2)PHNG BIO STAU TI q H2O
270	FSP ILM GARNET BIO STAU CORD q H2O	FSP ILM GARNET BIO STAU CORD and q H2O
271	FSP ILM GARNET BIO STAU CORD and q H2O	FSP ILM GARNET BIO CORD and q H2O
272	FSP ILM GARNET BIO STAU CORD and q H2O	FSP ILM GARNET BIO and q H2O
273	ILM GARNET PHNG BIO STAU zo q H2O	FSP ILM GARNET (2)PHNG BIO STAU q H2O
274	FSP ILM GARNET PHNG BIO STAU zo q H2O	FSP ILM GARNET (2)PHNG BIO STAU q H2O
275	ILM GARNET PHNG BIO STAU zo q H2O	FSP ILM GARNET PHNG BIO STAU zo q H2O
276	FSP ILM GARNET CHTD CHLR BIO q H2O	FSP ILM GARNET CHLR BIO STAU q H2O

no upper bounds in the plotted area. Inclusions of muscovite inside of the garnet indicate the sample grew garnet as temperature increased past 600° C, and that muscovite was consumed during the reaction, growing K-feldspar in its place. Some garnet growth could be expected from lower temperature reactions such as the staurolite or chloritoid breakdown, but these minerals are absent as inclusions in the garnet. The absence of muscovite in the matrix but present as an inclusion supports that the sample experienced heating without any necessary change in pressure (Figure 21). The main phase of garnet growth occurred during prograde metamorphism during increasing temperature and decreasing pressure. From the phase diagram alone, we know that peak temperature would have been in excess of 675° C, although we lack an upper bound on this temperature. The phase equilibria predict a pressure between 5 and 10 kbars at this temperature range. While the phase diagram predicts that cordierite should form at slightly lower pressure, the sample did not produce cordierite during exhumation. Cordierite growth would have occurred from garnet + qtz breakdown, and all quartz had already been removed from the matrix during prograde metamorphic reactions.

The phase diagram predicts that biotite would have been removed from the mineral assemblage during prograde metamorphism and that muscovite would have broken down to form K-feldspar. Notably biotite is present in the rock, and K-feldspar is absent. Biotite grains have random orientations, and overgrow mats of oriented sillimanite suggesting that it is retrograde, and may have formed by back reaction with K-feldspar.

The trace element pattern for this sample has a very shallow slope, with a La/Yb ratio of 1.92 (Figure 22). The elements La to Nd and Tb-Lu have a linear slopes, with a symmetrical pull-down towards Nd.

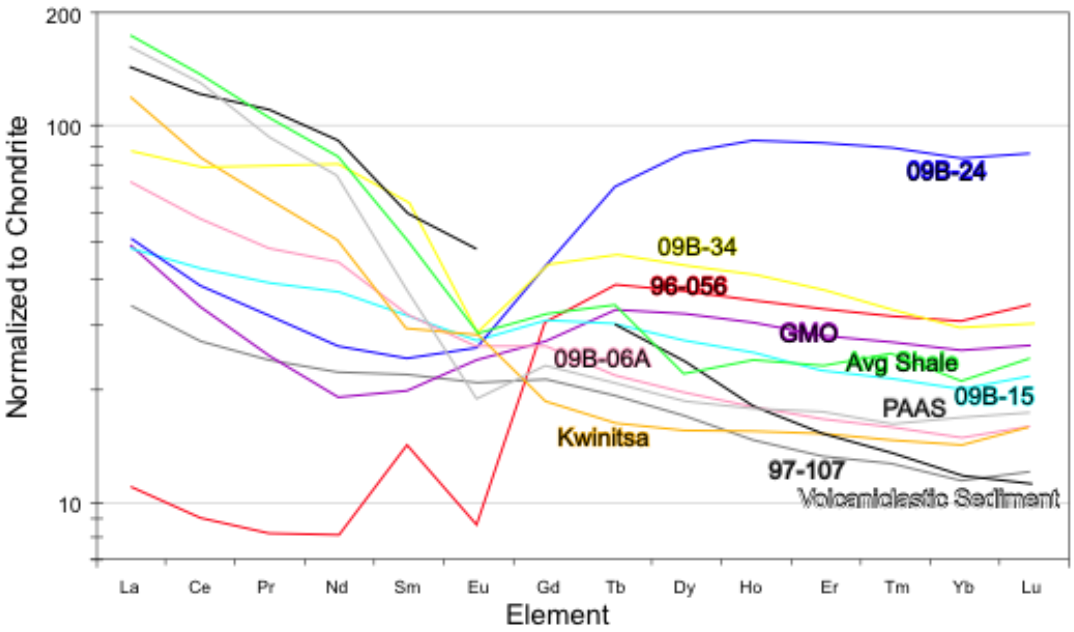

Figure 22. Trace element data normalized to chondrite of Sun and McDonough (1989). Includes average compositions for Average shale, post-Archean Australian Shale (PAAS), and volcaniclastic sediment, also normalized to chondrite. See Table 10 for data and average composition citations.

Table 10. Trace element data for samples from the central gneiss complex.

Raw Data (ppm):

	La	Ce	Pr	Nd	Sm	Eu	Gd	Tb	Dy	Ho	Er	Tm	Yb	Lu
GMO	11.38	19.96	2.29	8.78	3.00	1.35	5.40	1.20	7.95	1.67	4.56	0.67	4.26	0.65
Kwin	27.96	50.27	6.00	22.95	4.40	1.59	3.77	0.60	3.89	0.85	2.48	0.37	2.40	0.40
96-056	2.60	5.55	0.78	3.79	2.16	0.51	6.23	1.41	9.21	1.94	5.35	0.79	5.10	0.85
97-107	7.80	16.17	2.23	10.21	3.29	1.19	4.31	0.71	4.25	0.82	2.16	0.32	1.94	0.30
09B-06	16.67	34.57	4.49	19.95	4.74	1.50	5.31	0.80	4.90	1.00	2.73	0.40	2.50	0.40
09B-15	11.27	25.15	3.57	16.70	4.76	1.54	6.28	1.10	6.82	1.39	3.72	0.54	3.38	0.55
09B-24	11.70	22.92	2.95	12.03	3.63	1.50	8.77	2.56	21.40	5.14	14.80	2.20	13.83	2.13
09B-34	20.19	47.26	7.39	36.51	9.44	1.61	8.80	1.69	10.71	2.25	6.02	0.82	4.90	0.75

Post-Archean Australian Shale (PAAS) of Taylor and McLemmans, 1985 (ppm):

La	Ce	Pr	Nd	Sm	Eu	Gd	Tb	Dy	Ho	Er	Tm	Yb	Lu
38.20	79.59	8.84	33.90	5.55	1.08	4.65	0.78	4.68	0.99	2.84	0.41	2.82	0.44

Average Shale of Piper, 1974 (ppm):

La	Ce	Pr	Nd	Sm	Eu	Gd	Tb	Dy	Ho	Er	Tm	Yb	Lu
41.00	83.00	10.10	38.00	7.50	1.61	6.35	1.23	5.50	1.34	3.75	0.63	3.53	0.61

Volcaniclastic sediment of Castillo, 2009 (ppm):

La	Ce	Pr	Nd	Sm	Eu	Gd	Tb	Dy	Ho	Er	Tm	Yb	Lu
33.81	73.67	10.30	42.22	8.85	2.70		1.12	5.92	1.01	2.48	0.34	1.98	0.29

Chondrite of Sun and McDonough 1989, used for normalization of all data (ppm):

La	Ce	Pr	Nd	Sm	Eu	Gd	Tb	Dy	Ho	Er	Tm	Yb	Lu
0.237	0.612	0.095	0.467	0.153	0.058	0.206	0.037	0.254	0.057	0.166	0.026	0.170	0.025

Lu-Hf dating of garnet from this sample yielded meaningful ratios from one whole rock and three garnet fractions. With all four data points, the sample defines an isochron at 59±17 Ma (2σ error), with an MSWD = 10.3 (Figure 23). One additional garnet point was culled to help reduce the error, and a three point isochron was produced at 63.5±3.1 Ma (2σ error), with an MSWD = 1.9. This isochron was consistent with all data points, with better resolution on the age and a more reasonable MSWD. The low $^{176}Lu/^{177}Hf$ ratios in all of the garnet fractions indicate that significant amounts of fine-grained ilmenite likely still remained in the garnet fractions (Table 11). The initial $^{176}Hf/^{177}Hf$ for the sample GMO was 0.283030±0.000028 with an initial ε_{Hf} = +8.7±1.1.

This sample was also dated using Sm-Nd in garnet, and produced a robust isochron at 53.0±3.5 Ma (2σ error), with an MSWD = 1.3 (Figure 23). This isochron is defined by two whole rock and four garnet fractions. These were the same garnet fractions used for the Lu-Hf dating. The initial $^{143}Nd/^{144}Nd$ for the sample was 0.512810±0.000023 with an initial ε_{Nd} = +3.36±0.45. Data is summarized in Table 12.

5.2 Kwinitsa Quarry

The Kwinitsa sample (Fig. 16, Locality "B") is located immediately north of the Skeena River along the western edge of the Kasiks Sill Complex. Map scale foliations in the vicinity of the outcrop trend east-west with moderate dips to the north. Within the quarry, the average foliation is 096°/55° N, and defined by layers of plagioclase and quartz (leucosome) and biotite rich layers (melanosomes). Garnet occurs in both the leucosome and the melanosome, but is generally more concentrated in the leucosome. The lineation, where present, is defined by streaks of biotite.

The lithology in the quarry is interpreted as paragneiss, containing quartz + feldspar + garnet + biotite + oxides (Table 7). In thin section, bands of plagioclase

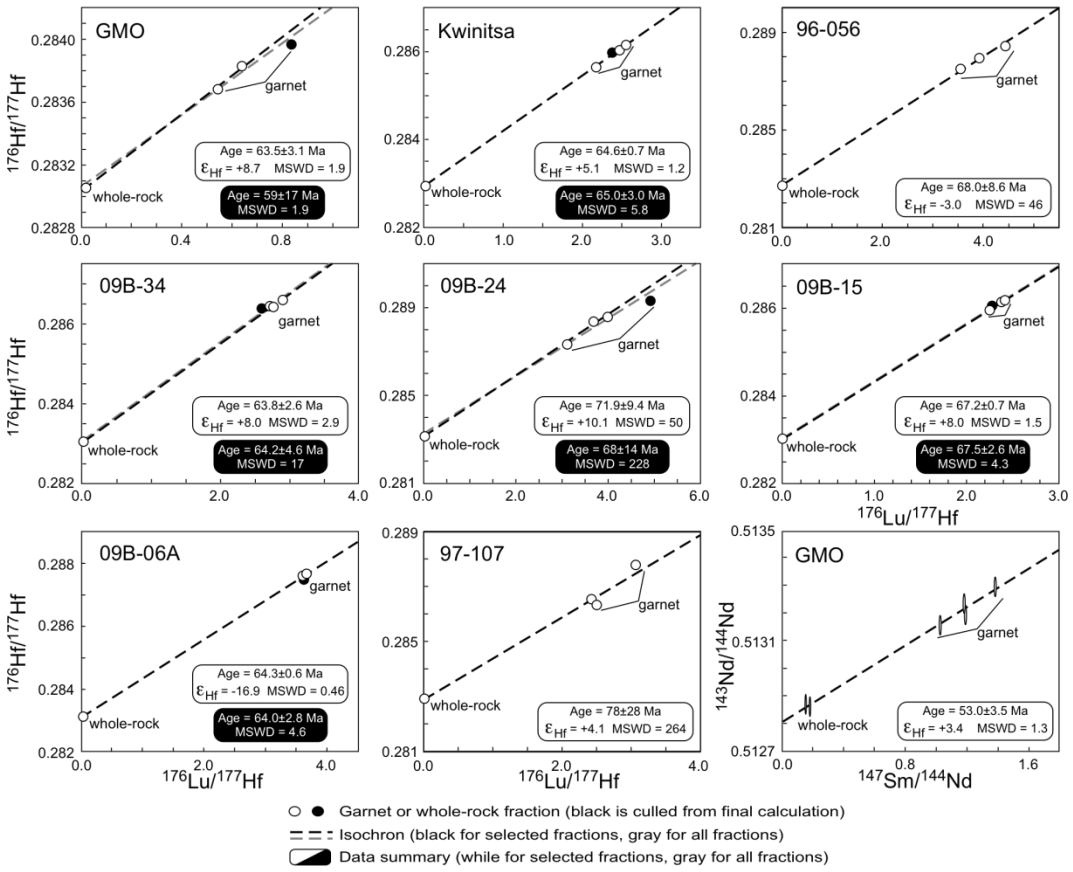

Figure 23. Lu-Hf and Sm-Nd isochrons for all samples. The black summary box for each sample includes all analyzed fractions, while the white summary box is only calculated from the fractions shown in white. See text for explanation of culling criteria. Lu-Hf data is plotted as points, as 2σ error ellipses cannot be observed at this scale. Sm-Nd data is shown as 2σ error ellipses. Data reported in Table 11 (Lu-Hf) and 12 (Sm-Nd).

Table 11. Lu-Hf data for analyzed garnet samples in the central gneiss complex.

Sample*	Lu (ppm) †	Hf (ppm) †	$^{176}Lu/^{177}Hf$ §	$^{176}Hf/^{177}Hf$ #	2σ (abs)**
GMO					
bomb WR	0.64	7.99	0.0114	0.283051	0.000029
grt 1	0.90	0.24	0.5370	0.283682	0.000029
grt 2	0.99	0.22	0.6333	0.283829	0.000030
grt 3 - culled	1.26	0.21	0.8315	0.283966	0.000029
Kwinitsa					
bomb WR	0.15	3.76	0.0055	0.282938	0.000029
grt 1	4.05	0.23	2.4599	0.286010	0.000029
grt 2	4.61	0.26	2.5565	0.286155	0.000029
grt 3	3.47	0.23	2.1791	0.285646	0.000029
grt 4 - culled	4.09	0.24	2.3699	0.285975	0.000029
96-056					
bomb WR	0.04	6.39	0.0008	0.282670	0.000029
grt 1	3.67	0.15	3.5514	0.287497	0.000029
grt 2	3.58	0.13	3.9268	0.287937	0.000031
grt 3	4.16	0.13	4.4373	0.288409	0.000030
09B-34					
bomb WR	0.14	2.41	0.0082	0.283023	0.000029
grt 1	3.14	0.16	2.7507	0.286430	0.000030
grt 2	3.26	0.16	2.9052	0.286579	0.000030
grt 3	3.01	0.16	2.7368	0.286428	0.000031
grt 4 - culled	3.17	0.17	2.6031	0.286367	0.000030
09B-24					
bomb WR	0.14	3.29	0.0058	0.283089	0.000029
grt 1	7.24	0.28	3.6720	0.288343	0.000029
grt 2	6.62	0.30	3.0981	0.287289	0.000029
grt 3	6.39	0.23	3.9678	0.288550	0.000030
grt 4 - culled	6.32	0.18	4.9114	0.289261	0.000030
09B-15					
Bomb WR	0.06	2.90	0.0030	0.283008	0.000029
grt 1	2.15	0.14	2.2552	0.285922	0.000030
grt 2	2.19	0.13	2.4150	0.286156	0.000030
grt 3	2.15	0.13	2.3860	0.286134	0.000030
grt 4 - culled	2.14	0.13	2.2806	0.286038	0.000030
09B-06A					
bomb WR	0.41	2.16	0.0271	0.283109	0.000029
grt 1	2.54	0.10	3.6730	0.287652	0.000032
grt 2	2.68	0.11	3.6188	0.287603	0.000033
grt 3 - culled	2.63	0.10	3.6173	0.287523	0.000030
97-107					
bomb WR	0.04	0.75	0.0069	0.282935	0.000027
grt 1	1.71	0.10	2.4313	0.286501	0.000030
grt 2	1.81	0.10	2.4981	0.286301	0.000032
grt 3	2.08	0.10	3.0668	0.287752	0.000030

* Abbreviations: bomb WR, whole rock by bomb digestion; sav WR, whole rock by Tabletop Savillex© digestion; Grt, garnet.

† Lu and Hf concentrations determined by isotope dilution with uncertainties estimated to be better than 0.5%.

§ Uncertainties for $^{176}Lu/^{177}Hf$ for the purpose of regressions and age calculations are estimated to be 0.5%.

$^{176}Hf/^{177}Hf$ ratios were corrected for instrumental mass bias using $^{179}Hf/^{177}Hf = 0.7935$ and normalized relative to $^{176}Hf/^{177}Hf = 0.282160$ for JMC-475.

** Reported errors on $^{176}Hf/^{177}Hf$ represent within-run uncertainty expressed as 2σ, standard error. Estimated total uncertainty on individual $^{176}Hf/^{177}Hf$ measurements for the purpose of regressions and age calculations is estimated to be 0.01% for $^{176}Hf/^{177}Hf$ for low concentration samples (e.g., most garnets) and 0.005% for higher concentration samples (> 3ppm).

Table 12. Sm-Nd data for analyzed garnet samples in the central gneiss complex.

Sample*	Sm (ppm) †	Nd (ppm) †	$^{147}Sm/^{144}Nd$ §	$^{143}Nd/^{144}Nd$ #	2σ (abs)**
GMO					
bomb WR 1	2.04	8.00	0.1542	0.512869	0.000028
bomb WR 2	2.79	9.34	0.1806	0.512862	0.000029
grt 1	3.73	1.63	1.3809	0.513292	0.000028
grt 2	3.66	1.87	1.1805	0.513234	0.000029
grt 3	3.65	1.86	1.1860	0.513195	0.000030
grt 4	3.75	2.22	1.0207	0.513155	0.000029

* Abbreviations: bomb WR, whole rock by bomb digestion; sav WR, whole rock by Tabletop Savillex© digestion; Grt, garnet.

† Sm and Nd concentrations determined by isotope dilution with uncertainties estimated to be better than 0.5%.

§ Uncertainties for $^{147}Sm/^{144}Nd$ for the purpose of regressions and age calculations are estimated to be 0.5%.

$^{143}Nd/^{144}Nd$ ratios were corrected for instrumental mass bias using $^{142}Nd/^{144}Nd = 1.141880$ and normalized relative to $^{143}Hf/^{144}Hf = 0.512140$ for Ames.

** Reported errors on $^{143}Nd/^{144}Nd$ represent within-run uncertainty expressed as 2σ, standard error. Estimated total uncertainty on individual $^{143}Nd/^{144}Nd$ measurements for the purpose of regressions and age calculations is estimated to be 0.01% for $^{143}Nd/^{144}Nd$ for low concentration samples.

define the foliation. Feldspar has developed well developed subgrain boundaries within larger grains, and displays lobate grain boundaries suggesting recrystallization by grain boundary migration. The presence of garnet in both the leucosome and melanosome suggest garnet growth occurred during partial melting. Inclusion trails inside the garnets occur at a high angle to matrix foliation. The sample lacks asymmetrical kinematic indicators, and lineation is weakly developed within the quarry and was argued by Andronicos et al., (2003) to have been affected by flattening during emplacement of the Kasiks sill. The biotite defined fabric wraps around garnet consistent with garnet being present before the foliation was fully developed.

A garnet-bearing sample from the outcrop was analyzed by electron microprobe. Garnet grains are four to six mm across and mostly euhedral. Fe increases and Mg decreases towards the rim of the garnet and towards biotite inclusions. Plagioclase grains are unzoned, with a thin reaction rind of biotite and quartz around garnet in the analyzed sample.

A phase diagram was constructed using the Berman database in Theriak-Domino. Domino utilized the same mixing models as sample GMO. The resultant phase diagram (Figure 24) reproduces the mineral assemblage of the dated sample well, but it is known that this rock experienced in-situ partial melting (migmatite). The upper bounds of the shaded area is believed to be accurate, as the sample did not grow orthopyroxene, but the temperature constraints are not as constrained as indicated. Still, this gives a minimum guess for temperature of 725°. The lack of orthopyroxene from the sample adds additional constraints to the upper temperature limit of 825°.

The trace element pattern for this sample is steep, with a La/Yb ratio of 8.37 (Figure 22). The sample is enriched in the LREE and depleted in the HREE, consistent with a garnet-bearing source. Figure 22 also includes average curves for shale, PAAS, and volcaniclastic sediment, all normalized to chondrite. The shape of the curve for

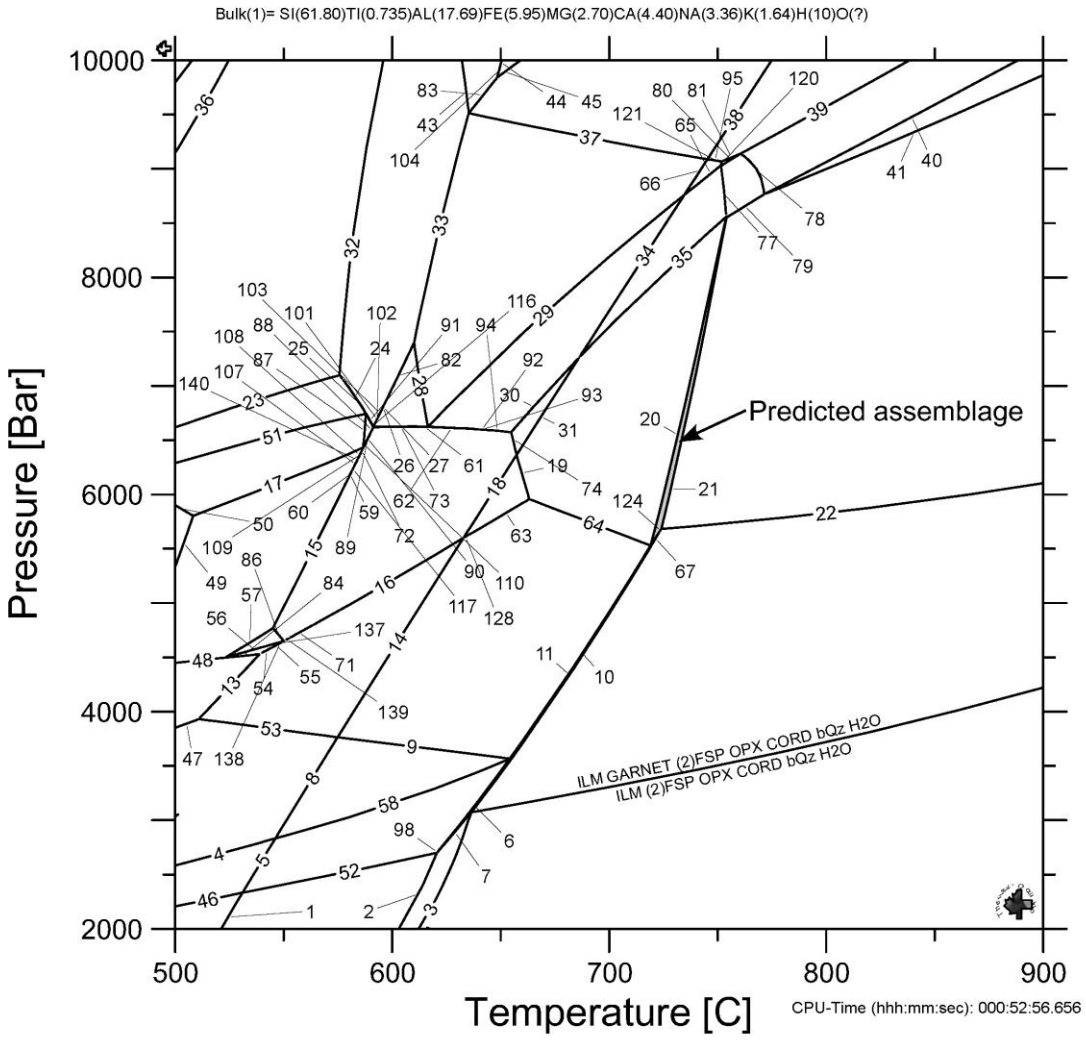

Figure 24. Isochemical phase diagram for sample Kwin calculated using Theriak-Domino software. Rock bulk chemistry is shown across top of Figure. Gray shaded region is estimated stability field for minerals in Kwin. A complete list of reactions on the phase diagram is shown in Table 13.

Table 13. Changes in mineral assemblages for phase diagram of Kwinitsa

Reaction number	Mineral assemblage, reactants	Mineral assemblage, products
1	ILM FSP BIOTITE OPX CORD aQz H2O	ILM FSP BIOTITE OPX CORD bQz H2O
2	ILM FSP BIOTITE OPX CORD bQz H2O	ILM (2)FSP BIOTITE OPX CORD bQz H2O
3	ILM (2)FSP BIOTITE OPX CORD bQz H2O	ILM (2)FSP OPX CORD bQz H2O
4	ILM GARNET FSP BIOTITE CORD aQz H2O	ILM GARNET FSP BIOTITE OPX CORD aQz H2O
5	ILM GARNET FSP BIOTITE OPX CORD aQz H2O	ILM GARNET FSP BIOTITE OPX CORD bQz H2O
6	ILM GARNET FSP BIOTITE OPX CORD bQz H2O	ILM GARNET (2)FSP BIOTITE OPX CORD bQz H2O
7	ILM GARNET (2)FSP BIOTITE OPX CORD bQz H2O	ILM (2)FSP BIOTITE OPX CORD bQz H2O
8	ILM GARNET FSP BIOTITE CORD aQz H2O	ILM GARNET FSP BIOTITE CORD bQz H2O
9	ILM GARNET (2)FSP BIOTITE CORD bQz H2O	ILM GARNET FSP BIOTITE CORD bQz H2O
10	ILM GARNET (2)FSP BIOTITE CORD bQz H2O	ILM GARNET (2)FSP BIOTITE OPX CORD bQz H2O
11	ILM GARNET (2)FSP BIOTITE OPX CORD bQz H2O	ILM GARNET (2)FSP OPX CORD bQz H2O
12	ILM GARNET (2)FSP OPX CORD bQz H2O	ILM (2)FSP OPX CORD bQz H2O
13	ILM GARNET FSP BIOTITE WHITE MICA CORD aQz H2O	ILM GARNET (2)FSP BIOTITE CORD aQz H2O
14	ILM GARNET (2)FSP BIOTITE CORD aQz H2O	ILM GARNET (2)FSP BIOTITE CORD bQz H2O
15	ILM GARNET FSP BIOTITE WHITE MICA aQz Si H2O	ILM GARNET (2)FSP BIOTITE aQz Si H2O
16	ILM GARNET (2)FSP BIOTITE aQz Si H2O	ILM GARNET (2)FSP BIOTITE CORD aQz H2O
17	ILM GARNET FSP BIOTITE WHITE MICA aQz H2O	ILM GARNET FSP BIOTITE WHITE MICA aQz Si H2O
18	ILM GARNET (2)FSP BIOTITE aQz Si H2O	ILM GARNET (2)FSP BIOTITE bQz Si H2O
19	ILM GARNET (2)FSP BIOTITE bQz Si H2O	ILM GARNET (2)FSP BIOTITE bQz H2O
20	ILM GARNET (2)FSP BIOTITE bQz H2O	ILM GARNET (2)FSP BIOTITE OPX bQz H2O
21	ILM GARNET (2)FSP BIOTITE OPX bQz H2O	ILM GARNET (2)FSP OPX bQz H2O
22	ILM GARNET (2)FSP OPX bQz H2O	ILM GARNET (2)FSP OPX CORD bQz H2O
23	GARNET FSP BIOTITE WHITE MICA Rt aQz H2O	ILM GARNET FSP BIOTITE WHITE MICA Rt aQz H2O
24	ILM GARNET FSP BIOTITE WHITE MICA Rt aQz H2O	ILM GARNET (2)FSP BIOTITE WHITE MICA Rt aQz H2O
25	ILM GARNET (2)FSP BIOTITE WHITE MICA Rt aQz H2O	GARNET (2)FSP BIOTITE WHITE MICA Rt aQz H2O
26	GARNET (2)FSP BIOTITE WHITE MICA Rt aQz H2O	GARNET (2)FSP BIOTITE WHITE MICA Rt aQz Si H2O
27	GARNET (2)FSP BIOTITE WHITE MICA Rt aQz Si H2O	GARNET (2)FSP BIOTITE Rt aQz Si H2O
28	GARNET (2)FSP BIOTITE Rt aQz Si H2O	GARNET (2)FSP BIOTITE Rt aQz H2O
29	GARNET (2)FSP BIOTITE Rt aQz H2O	ILM GARNET (2)FSP BIOTITE Rt aQz H2O
30	ILM GARNET (2)FSP BIOTITE Rt aQz H2O	ILM GARNET (2)FSP BIOTITE aQz H2O
31	ILM GARNET (2)FSP BIOTITE aQz H2O	ILM GARNET (2)FSP BIOTITE bQz H2O
32	GARNET FSP BIOTITE WHITE MICA Rt aQz H2O	GARNET (2)FSP BIOTITE WHITE MICA Rt aQz H2O
33	GARNET (2)FSP BIOTITE WHITE MICA Rt aQz H2O	GARNET (2)FSP BIOTITE Rt aQz H2O
34	ILM GARNET (2)FSP BIOTITE Rt aQz H2O	ILM GARNET (2)FSP BIOTITE Rt bQz H2O
35	ILM GARNET (2)FSP BIOTITE Rt bQz H2O	ILM GARNET (2)FSP BIOTITE bQz H2O
36	GARNET FSP BIOTITE WHITE MICA AMPHx Rt aQz H2O	GARNET FSP BIOTITE WHITE MICA Rt aQz H2O
37	GARNET (2)FSP BIOTITE Rt aQz H2O	GARNET (2)FSP Rt aQz H2O
38	GARNET (2)FSP Rt aQz H2O	GARNET (2)FSP Rt bQz H2O
39	GARNET (2)FSP Rt bQz H2O	ILM GARNET (2)FSP Rt bQz H2O
40	ILM GARNET (2)FSP Rt bQz H2O	ILM GARNET (2)FSP bQz H2O
41	ILM GARNET (2)FSP bQz H2O	ILM GARNET (2)FSP OPX bQz H2O
42	GARNET FSP WHITE MICA AMPHx Rt aQz H2O	GARNET FSP BIOTITE WHITE MICA AMPHx Rt aQz H2O
43	GARNET (2)FSP BIOTITE WHITE MICA Rt aQz H2O	GARNET (2)FSP WHITE MICA Rt aQz H2O
44	GARNET (2)FSP WHITE MICA Rt aQz H2O	GARNET (2)FSP Rt aQz Ky H2O
45	GARNET (2)FSP Rt aQz Ky H2O	GARNET (2)FSP Rt aQz H2O
46	ILM GARNET FSP BIOTITE OPX CORD aQz H2O	ILM FSP BIOTITE OPX CORD aQz H2O
47	ILM GARNET FSP BIOTITE WHITE MICA CORD aQz H2O	ILM GARNET FSP BIOTITE CORD aQz H2O
48	ILM GARNET FSP BIOTITE WHITE MICA aQz Si H2O	ILM GARNET FSP BIOTITE WHITE MICA CORD aQz H2O
49	ILM GARNET FSP BIOTITE WHITE MICA STAU aQz H2O	ILM GARNET FSP BIOTITE WHITE MICA aQz Si H2O
50	ILM GARNET FSP BIOTITE WHITE MICA aQz H2O	ILM GARNET FSP BIOTITE WHITE MICA STAU aQz H2O
51	ILM GARNET FSP BIOTITE WHITE MICA Rt aQz H2O	ILM GARNET FSP BIOTITE WHITE MICA aQz H2O
52	ILM GARNET FSP BIOTITE OPX CORD bQz H2O	ILM FSP BIOTITE OPX CORD bQz H2O
53	ILM GARNET (2)FSP BIOTITE CORD aQz H2O	ILM GARNET FSP BIOTITE CORD aQz H2O
54	ILM GARNET FSP BIOTITE CORD aQz Si H2O	ILM GARNET (2)FSP BIOTITE CORD aQz H2O
55	ILM GARNET (2)FSP BIOTITE CORD aQz H2O	ILM GARNET FSP BIOTITE CORD aQz Si H2O
56	ILM GARNET FSP BIOTITE CORD aQz Si H2O	ILM GARNET FSP BIOTITE aQz Si H2O
57	ILM GARNET FSP BIOTITE aQz Si H2O	ILM GARNET FSP BIOTITE WHITE MICA aQz Si H2O
58	ILM GARNET FSP BIOTITE CORD bQz H2O	ILM GARNET FSP BIOTITE OPX CORD bQz H2O

Table 13 (cont). Changes in mineral assemblages for phase diagram of Kwinitsa

Reaction number	Mineral assemblage, reactants	Mineral assemblage, products
59	ILM GARNET (2)FSP BIOTITE WHITE MICA aQz Si H2O	ILM GARNET (2)FSP BIOTITE aQz Si H2O
60	ILM GARNET FSP BIOTITE WHITE MICA aQz Si H2O	ILM GARNET (2)FSP BIOTITE WHITE MICA aQz Si H2O
61	ILM GARNET (2)FSP BIOTITE Rt aQz Si H2O	ILM GARNET (2)FSP BIOTITE aQz Si H2O
62	ILM GARNET (2)FSP BIOTITE Rt aQz H2O	ILM GARNET (2)FSP BIOTITE Rt aQz Si H2O
63	ILM GARNET (2)FSP BIOTITE bQz Si H2O	ILM GARNET (2)FSP BIOTITE CORD bQz H2O
64	ILM GARNET (2)FSP BIOTITE bQz H2O	ILM GARNET (2)FSP BIOTITE CORD bQz H2O
65	ILM GARNET (2)FSP BIOTITE Rt bQz H2O	GARNET (2)FSP BIOTITE Rt bQz H2O
66	GARNET (2)FSP BIOTITE Rt bQz H2O	GARNET (2)FSP BIOTITE Rt aQz H2O
67	ILM GARNET (2)FSP BIOTITE OPX bQz H2O	ILM GARNET (2)FSP BIOTITE OPX CORD bQz H2O
68	ILM GARNET (2)FSP BIOTITE aQz Si H2O	ILM GARNET (2)FSP BIOTITE CORD bQz H2O
69	ILM GARNET (2)FSP BIOTITE aQz Si H2O	ILM GARNET (2)FSP BIOTITE CORD aQz Si H2O
70	ILM GARNET (2)FSP BIOTITE CORD aQz Si H2O	ILM GARNET (2)FSP BIOTITE CORD aQz H2O
71	ILM GARNET (2)FSP BIOTITE aQz Si H2O	ILM GARNET (2)FSP BIOTITE CORD aQz H2O
72	ILM GARNET FSP BIOTITE WHITE MICA aQz Si H2O	ILM GARNET (2)FSP BIOTITE aQz Si H2O
73	GARNET (2)FSP BIOTITE Rt aQz Si H2O	ILM GARNET (2)FSP BIOTITE Rt aQz Si H2O
74	ILM GARNET (2)FSP BIOTITE aQz Si H2O	ILM GARNET (2)FSP BIOTITE aQz H2O
75	ILM GARNET (2)FSP BIOTITE Rt aQz H2O	ILM GARNET (2)FSP BIOTITE aQz Si H2O
76	ILM GARNET (2)FSP BIOTITE Rt aQz H2O	ILM GARNET (2)FSP BIOTITE aQz Si H2O
77	ILM GARNET (2)FSP BIOTITE Rt bQz H2O	ILM GARNET (2)FSP OPX Rt bQz H2O
78	ILM GARNET (2)FSP OPX Rt bQz H2O	ILM GARNET (2)FSP Rt bQz H2O
79	ILM GARNET (2)FSP OPX Rt bQz H2O	ILM GARNET (2)FSP OPX bQz H2O
80	GARNET (2)FSP OPX Rt bQz H2O	ILM GARNET (2)FSP OPX Rt bQz H2O
81	GARNET (2)FSP Rt bQz H2O	GARNET (2)FSP OPX Rt bQz H2O
82	GARNET (2)FSP BIOTITE WHITE MICA Rt aQz H2O	GARNET (2)FSP BIOTITE Rt aQz Si H2O
83	GARNET (2)FSP WHITE MICA Rt aQz H2O	GARNET (2)FSP Rt aQz H2O
84	ILM GARNET FSP BIOTITE CORD aQz Si H2O	ILM GARNET FSP BIOTITE WHITE MICA CORD aQz H2O
85	ILM GARNET FSP BIOTITE aQz Si H2O	ILM GARNET (2)FSP BIOTITE CORD aQz H2O
86	ILM GARNET FSP BIOTITE aQz Si H2O	ILM GARNET (2)FSP BIOTITE aQz Si H2O
87	ILM GARNET FSP BIOTITE WHITE MICA aQz H2O	ILM GARNET (2)FSP BIOTITE WHITE MICA aQz H2O
88	ILM GARNET (2)FSP BIOTITE WHITE MICA aQz H2O	ILM GARNET (2)FSP BIOTITE aQz Si H2O
89	ILM GARNET (2)FSP BIOTITE WHITE MICA aQz Si H2O	ILM GARNET (2)FSP BIOTITE aQz Si H2O
90	ILM GARNET (2)FSP BIOTITE WHITE MICA aQz H2O	ILM GARNET (2)FSP BIOTITE WHITE MICA aQz Si H2O
91	ILM GARNET (2)FSP BIOTITE WHITE MICA aQz H2O	ILM GARNET (2)FSP BIOTITE WHITE MICA Rt aQz H2O
92	ILM GARNET (2)FSP BIOTITE Rt aQz Si H2O	ILM GARNET (2)FSP BIOTITE aQz Si H2O
93	ILM GARNET (2)FSP BIOTITE Rt aQz H2O	ILM GARNET (2)FSP BIOTITE Rt aQz Si H2O
94	ILM GARNET (2)FSP BIOTITE Rt aQz H2O	ILM GARNET (2)FSP BIOTITE aQz Si H2O
95	GARNET (2)FSP Rt bQz H2O	GARNET (2)FSP BIOTITE Rt bQz H2O
96	GARNET (2)FSP WHITE MICA Rt aQz Ky H2O	GARNET (2)FSP Rt aQz Ky H2O
97	GARNET (2)FSP WHITE MICA Rt aQz H2O	GARNET (2)FSP WHITE MICA Rt aQz Ky H2O
98	ILM GARNET FSP BIOTITE OPX CORD bQz H2O	ILM (2)FSP BIOTITE OPX CORD bQz H2O
99	ILM GARNET (2)FSP BIOTITE CORD bQz Si H2O	ILM GARNET (2)FSP BIOTITE CORD bQz H2O
100	ILM GARNET (2)FSP BIOTITE CORD bQz Si H2O	ILM GARNET (2)FSP BIOTITE bQz Si H2O
101	GARNET (2)FSP BIOTITE WHITE MICA Rt aQz H2O	GARNET (2)FSP BIOTITE WHITE MICA Rt aQz Si H2O
102	GARNET (2)FSP BIOTITE WHITE MICA Rt aQz Si H2O	GARNET (2)FSP BIOTITE Rt aQz Si H2O
103	GARNET (2)FSP BIOTITE WHITE MICA Rt aQz H2O	GARNET (2)FSP BIOTITE Rt aQz Si H2O
104	GARNET (2)FSP WHITE MICA Rt aQz H2O	GARNET (2)FSP Rt aQz Ky H2O
105	ILM GARNET (2)FSP BIOTITE CORD aQz Si H2O	ILM GARNET (2)FSP BIOTITE CORD aQz H2O
106	ILM GARNET FSP BIOTITE CORD aQz Si H2O	ILM GARNET (2)FSP BIOTITE CORD aQz Si H2O
107	ILM GARNET FSP BIOTITE WHITE MICA aQz Si H2O	ILM GARNET (2)FSP BIOTITE aQz Si H2O
108	ILM GARNET (2)FSP BIOTITE WHITE MICA aQz Si H2O	ILM GARNET (2)FSP BIOTITE aQz Si H2O
109	ILM GARNET (2)FSP BIOTITE WHITE MICA aQz Si H2O	ILM GARNET FSP BIOTITE WHITE MICA aQz Si H2O
110	ILM GARNET (2)FSP BIOTITE WHITE MICA aQz H2O	ILM GARNET (2)FSP BIOTITE aQz Si H2O
111	ILM GARNET FSP BIOTITE WHITE MICA Rt aQz H2O	GARNET (2)FSP BIOTITE WHITE MICA Rt aQz H2O
112	ILM GARNET FSP BIOTITE WHITE MICA Rt aQz H2O	ILM GARNET (2)FSP BIOTITE WHITE MICA Rt aQz H2O
113	ILM GARNET (2)FSP BIOTITE WHITE MICA Rt aQz H2O	ILM GARNET FSP BIOTITE WHITE MICA Rt aQz H2O
114	ILM GARNET (2)FSP BIOTITE WHITE MICA Rt aQz H2O	GARNET (2)FSP BIOTITE WHITE MICA Rt aQz H2O
115	GARNET (2)FSP BIOTITE WHITE MICA Rt aQz H2O	ILM GARNET (2)FSP BIOTITE WHITE MICA Rt aQz H2O
116	GARNET (2)FSP BIOTITE WHITE MICA Rt aQz H2O	GARNET (2)FSP BIOTITE Rt aQz Si H2O

Table 13 (cont). Changes in mineral assemblages for phase diagram of Kwinitsa

Reaction number	Mineral assemblage, reactants	Mineral assemblage, products
117	ILM GARNET FSP BIOTITE WHITE MICA aQz Si H2O	ILM GARNET (2)FSP BIOTITE aQz Si H2O
118	ILM GARNET (2)FSP BIOTITE WHITE MICA aQz Si H2O	ILM GARNET (2)FSP BIOTITE aQz Si H2O
119	ILM GARNET FSP BIOTITE WHITE MICA aQz Si H2O	ILM GARNET (2)FSP BIOTITE WHITE MICA aQz Si H2O
120	GARNET (2)FSP BIOTITE Rt bQz H2O	GARNET (2)FSP BIOTITE OPX Rt bQz H2O
121	GARNET (2)FSP BIOTITE OPX Rt bQz H2O	GARNET (2)FSP OPX Rt bQz H2O
122	ILM GARNET (2)FSP BIOTITE CORD aQz Si H2O	ILM GARNET (2)FSP BIOTITE CORD aQz H2O
123	ILM GARNET (2)FSP BIOTITE aQz Si H2O	ILM GARNET (2)FSP BIOTITE CORD aQz Si H2O
124	ILM GARNET (2)FSP BIOTITE OPX bQz H2O	ILM GARNET (2)FSP OPX CORD bQz H2O
125	ILM GARNET FSP BIOTITE WHITE MICA aQz Si H2O	ILM GARNET (2)FSP BIOTITE aQz Si H2O
126	ILM GARNET (2)FSP BIOTITE WHITE MICA aQz Si H2O	ILM GARNET (2)FSP BIOTITE aQz Si H2O
127	ILM GARNET FSP BIOTITE WHITE MICA aQz Si H2O	ILM GARNET (2)FSP BIOTITE WHITE MICA aQz Si H2O
128	ILM GARNET (2)FSP BIOTITE bQz Si H2O	ILM GARNET (2)FSP BIOTITE CORD bQz H2O
129	ILM GARNET (2)FSP BIOTITE Rt bQz H2O	ILM GARNET (2)FSP BIOTITE OPX Rt bQz H2O
130	ILM GARNET (2)FSP BIOTITE OPX Rt bQz H2O	ILM GARNET (2)FSP OPX Rt bQz H2O
131	ILM GARNET FSP BIOTITE WHITE MICA Rt aQz H2O	GARNET (2)FSP BIOTITE WHITE MICA Rt aQz H2O
132	ILM GARNET (2)FSP BIOTITE WHITE MICA aQz Si H2O	ILM GARNET (2)FSP BIOTITE aQz Si H2O
133	ILM GARNET (2)FSP BIOTITE WHITE MICA aQz H2O	ILM GARNET (2)FSP BIOTITE WHITE MICA aQz Si H2O
134	ILM GARNET (2)FSP BIOTITE aQz Si H2O	ILM GARNET (2)FSP BIOTITE Rt aQz Si H2O
135	ILM GARNET (2)FSP BIOTITE Rt aQz Si H2O	ILM GARNET (2)FSP BIOTITE Rt aQz H2O
136	ILM GARNET (2)FSP BIOTITE bQz H2O	ILM GARNET (2)FSP BIOTITE Rt aQz H2O
137	ILM GARNET (2)FSP BIOTITE CORD aQz Si H2O	ILM GARNET FSP BIOTITE CORD aQz Si H2O
138	ILM GARNET (2)FSP BIOTITE CORD aQz Si H2O	ILM GARNET (2)FSP BIOTITE CORD aQz H2O
139	ILM GARNET (2)FSP BIOTITE aQz Si H2O	ILM GARNET (2)FSP BIOTITE CORD aQz H2O
140	ILM GARNET FSP BIOTITE WHITE MICA aQz Si H2O	ILM GARNET (2)FSP BIOTITE aQz Si H2O
141	ILM GARNET (2)FSP BIOTITE WHITE MICA aQz Si H2O	ILM GARNET (2)FSP BIOTITE aQz Si H2O
142	ILM GARNET FSP BIOTITE WHITE MICA aQz Si H2O	ILM GARNET (2)FSP BIOTITE WHITE MICA aQz Si H2O
143	ILM GARNET (2)FSP BIOTITE CORD aQz Si H2O	ILM GARNET FSP BIOTITE CORD aQz Si H2O
144	ILM GARNET (2)FSP BIOTITE CORD aQz Si H2O	ILM GARNET (2)FSP BIOTITE CORD aQz H2O
145	ILM GARNET FSP BIOTITE CORD aQz Si H2O	ILM GARNET (2)FSP BIOTITE CORD aQz H2O
146	ILM GARNET (2)FSP BIOTITE WHITE MICA aQz H2O	ILM GARNET (2)FSP BIOTITE aQz Si H2O
147	ILM GARNET (2)FSP BIOTITE WHITE MICA aQz Si H2O	ILM GARNET (2)FSP BIOTITE aQz Si H2O
148	ILM GARNET (2)FSP BIOTITE WHITE MICA aQz H2O	ILM GARNET (2)FSP BIOTITE WHITE MICA aQz Si H2O
149	ILM GARNET (2)FSP BIOTITE Rt bQz H2O	ILM GARNET (2)FSP OPX Rt bQz H2O
150	ILM GARNET (2)FSP BIOTITE Rt aQz H2O	ILM GARNET (2)FSP BIOTITE aQz Si H2O
151	GARNET (2)FSP BIOTITE WHITE MICA Rt aQz H2O	GARNET (2)FSP Rt aQz H2O
152	ILM GARNET FSP BIOTITE CORD aQz Si H2O	ILM GARNET (2)FSP BIOTITE CORD aQz H2O
153	ILM GARNET (2)FSP BIOTITE Rt aQz Si H2O	ILM GARNET (2)FSP BIOTITE aQz Si H2O
154	ILM GARNET (2)FSP BIOTITE Rt aQz H2O	ILM GARNET (2)FSP BIOTITE Rt aQz Si H2O
155	GARNET (2)FSP BIOTITE Rt bQz H2O	GARNET (2)FSP OPX Rt bQz H2O
156	ILM GARNET (2)FSP BIOTITE CORD aQz Si H2O	ILM GARNET (2)FSP BIOTITE CORD aQz H2O
157	ILM GARNET (2)FSP BIOTITE aQz Si H2O	ILM GARNET (2)FSP BIOTITE CORD aQz Si H2O
158	ILM GARNET FSP BIOTITE WHITE MICA Rt aQz H2O	GARNET (2)FSP BIOTITE WHITE MICA Rt aQz H2O

the Kwinitsa data very closely matches these, and indicates that it likely has a medisedimentary protolith.

Lu-Hf dating of garnet from this sample yielded meaningful ratios from one whole rock and four garnet fractions. With all five data points, the sample defines an isochron at 65.0±3.0 Ma (2σ error), with an MSWD = 5.8 (Figure 24). One garnet point was culled to help reduce the error, and a four point isochron was produced at 64.6±0.7 Ma (2σ error), with an MSWD = 1.2. This isochron was consistent with all data points, with better resolution on the age and a more reasonable MSWD. The $^{176}Lu/^{177}Hf$ for the garnet fractions ranged from 2.179 to 2.556 (Table 11). The isochron defines an initial $^{176}Hf/^{177}Hf$ of 0.28293±0.00003 (ε_{Hf} = +5.13±1.06).

5.3 Recumbent Peak (96-056)

The Recumbent Peak sample (Figure 16, Locality "C") is located 3 km south of the Skeena River, 5.5 km northeast of Spinel Peak. Isoclinal nappes have an axial planar cleavage that strikes northwest-southeast, dipping moderately to the northeast (Fig 18A). Around the outcrop, the average foliation is 126°/50° NE, defined by the alignment of sillimanite. The lineation is defined by biotite and sillimanite, and is plunging 34° to 082°. Kinematics from garnet porphyroclast tails indicate top to the northeast (normal) motion, down dip. The fabric has been reoriented a full 90°.. Inclusion trails are perpendicular between the core and rim of garnets, which could be interpreted as multiple phases of garnet growth are syntectonic, overgrowing the fabrics as they develop.

The lithology on Recumbent Peak is restitic gneiss (Table 7). In thin section, the foliation is defined by sillimanite, with cordierite rimming the garnet. The foliation deflects around garnet. Layers of quartz show subgrain development, with minor amounts of lobate structures along the grain boundaries that would accompany

migration. Inclusion trails in garnet occur at a high angle to the matrix foliation, and are parallel between garnets.

A garnet-bearing sample from the outcrop was analyzed by electron microprobe. Garnet grains are six mm in the direction of foliation, and four mm across the foliation (Figure 25). The matrix foliation is defined by sillimanite. Cordierite is seen replacing sillimanite along the garnet rims, suggesting a reaction such as garnet + biotite + sillimanite ⇆ cordierite + hercynite (inclusions) + ilmenite + K-feldspar + water, while above the staurolite breakdown curve, which occurs from decreasing pressure (Hollister 1982). This is supported by the lack of cordierite where those three reactants do not come in contact with one another. Fe elevations and Mg decreases only occurs adjacent to the cordierite, and is not observed distal to the cordierite. This zoning is a result of garnet breaking down to cordierite, as Mg is partitioned into cordierite, and Fe remains in the garnet. The layering of sillimanite and cordierite suggests that a foliation was present prior to the formation of cordierite, indicating that deformation occurred prior to cordierite growth. Garnets have inclusions of sillimanite, staurolite, spinel, quartz, and plagioclase. Inclusions of andalusite and quartz can be found inside of staurolite in some garnets. Inclusion trails within the garnet occur at a high angle to the matrix foliation.

P-T calculations were made using WinTWQ v. 1 and microprobe data (Table 14). For the garnet rim adjacent to cordierite, the resultant P-T is 4.9 kbars and 674° C based on the intersection 4Si + 5bQz + 2Py ⇆ 3Crd; 3bQz + 2Py + 6An ⇆ 3Crd + 2Gr; 2Si + bQz + Gr ⇆ 3An; and 3Crd + 5Gr + 6Si ⇆ 3Py + 15An (Figure 26).

A phase diagram was constructed using the Holland and Powell database in Theriak-Domino. Domino utilized the following mixing models: Ab - ABSAL, H_2O -

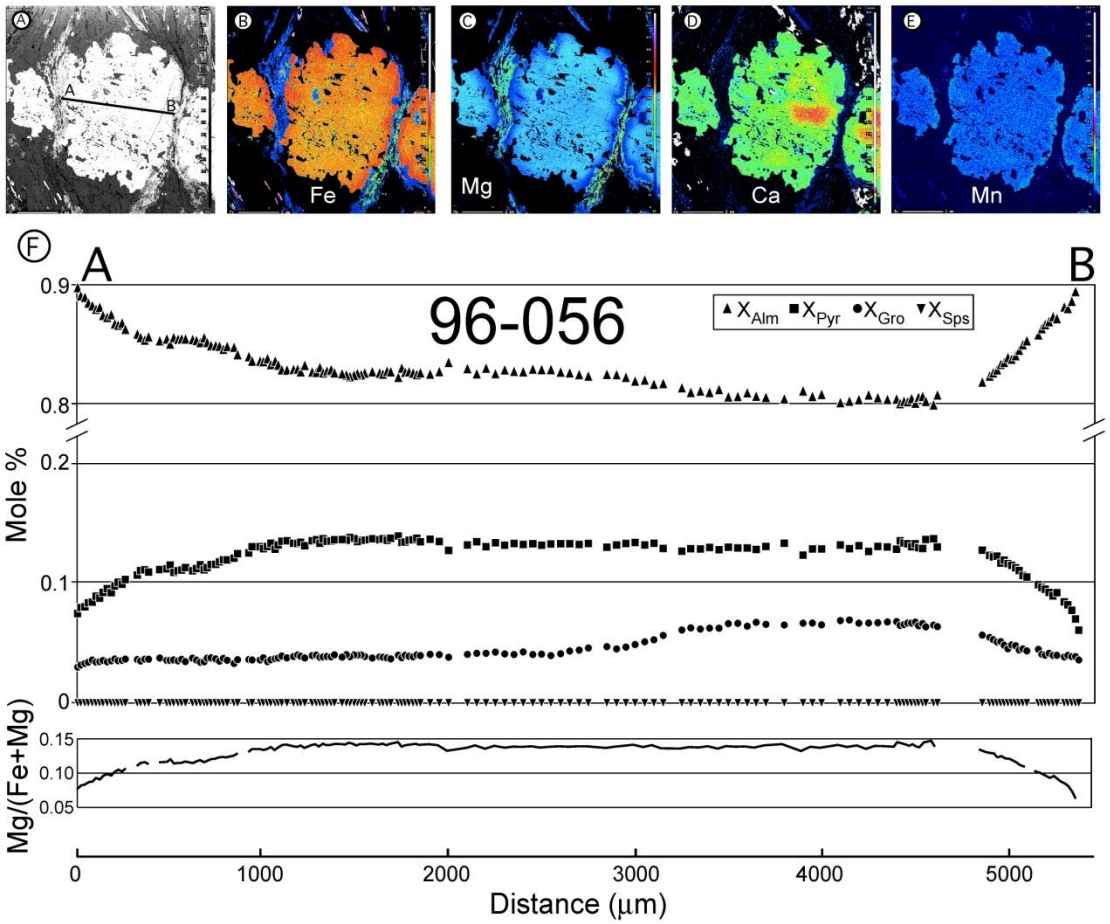

Figure 25. Backscatter electron image, X-ray intensity maps, and compositional line scan collected for sample 96-056. A) Backscatter electron image of garnet. Black line marked A-B is location of compositional line scan shown in (D). B) X-ray intensity map for Fe Kα. Color scale adjusted to highlight zoning in garnet. C) X-ray intensity map for Ca Kα. Color scale adjusted to highlight zoning in garnet. D) Compositional line scan collected by quantitative wavelength dispersive scanning analysis. Note compressed vertical scale. Representative analyses of minerals used for thermobarometry calculations reported in Table 14.

Table 14. Representative microprobe mineral analyses* for 96-056

Weight % Oxides

Oxides	Garnet (Crd Rim)	Garnet (Qtz Rim)	Garnet (Core)	Plag (Incl)	Plag (Matrix)	Cord	Biot (Matrix)	Staur	Spn	Ilmenite
SiO_2	37.06	38.27	37.96	56.71	58.77	48.13	41.33	26.31	0.04	0.02
TiO_2	0.00	0.00	0.00	0.02	0.00	0.00	0.00	0.00	0.00	51.72
Al_2O_3	21.53	22.18	21.98	26.28	25.58	32.75	30.01	57.37	60.68	0.05
FeO	37.73	34.07	34.64	0.31	0.05	10.08	13.49	13.84	25.72	46.76
MnO	0.00	0.01	0.01	0.00	0.00	0.00	0.00	0.00	0.01	0.24
MgO	3.37	5.65	5.50	0.10	0.00	7.44	5.27	1.92	5.85	0.41
CaO	1.34	1.68	1.69	8.28	7.47	0.00	0.14	0.00	0.00	0.00
Na_2O	0.00	0.00	0.00	6.86	7.57	0.18	0.39	0.04	0.30	0.00
K_2O	0.00	0.00	0.00	0.24	0.21	0.00	4.51	0.08	0.00	0.00
Cr_2O_3	0.03	0.00	0.00	0.00	0.00	0.00	0.02	0.03	0.01	
Cl^-	0.00	0.00	0.01	0.01	0.00	0.00	0.03	0.01	0.00	
F^{2-}	0.00	0.00	0.00	0.00	0.00	0.00	0.00	0.00	0.00	
Ba^-	0.00	0.00	0.00	0.01	0.02	0.09	0.26	0.01	0.00	
Total†	101.05	101.86	101.78	98.82	99.66	98.66	95.43	99.61	92.61	99.19
	37.06	38.27	37.96	56.71	58.77	48.13	41.33	26.31	0.04	0.02

Ions in Formula§

Element	Garnet (Crd Rim)	Garnet (Qtz Rim)	Garnet (Core)	Plag (Incl)	Plag (Matrix)	Cord	Biot (Matrix)	Staur	Spn	Ilmenite
Si	2.960	2.973	2.962	2.578	2.637	4.983	3.132	3.745	0.001	0.000
Ti	0.000	0.000	0.000	0.001	0.000	0.000	0.000	0.000	0.000	0.660
Al	2.027	2.031	2.021	1.408	1.353	3.996	2.680	9.624	2.074	0.001
Fe^{2+}	2.521	2.214	2.261	0.012	0.002	0.873	0.855	1.647	0.624	0.664
Mn	0.000	0.001	0.001	0.000	0.000	0.000	0.000	0.000	0.000	0.003
Mg	0.401	0.654	0.640	0.007	0.000	1.147	0.595	0.408	0.253	0.010
Ca	0.115	0.140	0.141	0.403	0.359	0.000	0.011	0.000	0.000	0.000
Na	0.000	0.000	0.000	0.605	0.658	0.037	0.058	0.011	0.017	0.000
K	0.000	0.000	0.000	0.014	0.012	0.000	0.436	0.014	0.000	0.000
Cl	0.001	0.000	0.001	0.001	0.000	0.000	0.004	0.002	0.000	
F	0.000	0.000	0.000	0.000	0.000	0.000	0.000	0.000	0.000	
Ba	0.000	0.000	0.000	0.000	0.000	0.004	0.009	0.001	0.000	
Cr	0.002	0.000	0.000	0.000	0.000	0.000	0.001	0.003	0.000	
Total	8.026	8.012	8.028	5.028	5.022	11.040	7.781	15.455	2.970	1.339

* Representative analyses were chosen for most minerals. Biotite numbers were produced from averaging multiple analyses.
† Oxide totals corrected for Cl, F, and Ba using the method described in Deer, Howie and Zussmen.
§ Stoichiometric ratios of elements based on 12 oxygen for garnet, 8 for plagioclase, 18 for cordierite, 11 for biotite, 24 for staurolite, 4 for spinel (hercynite), 2 for ilmenite.

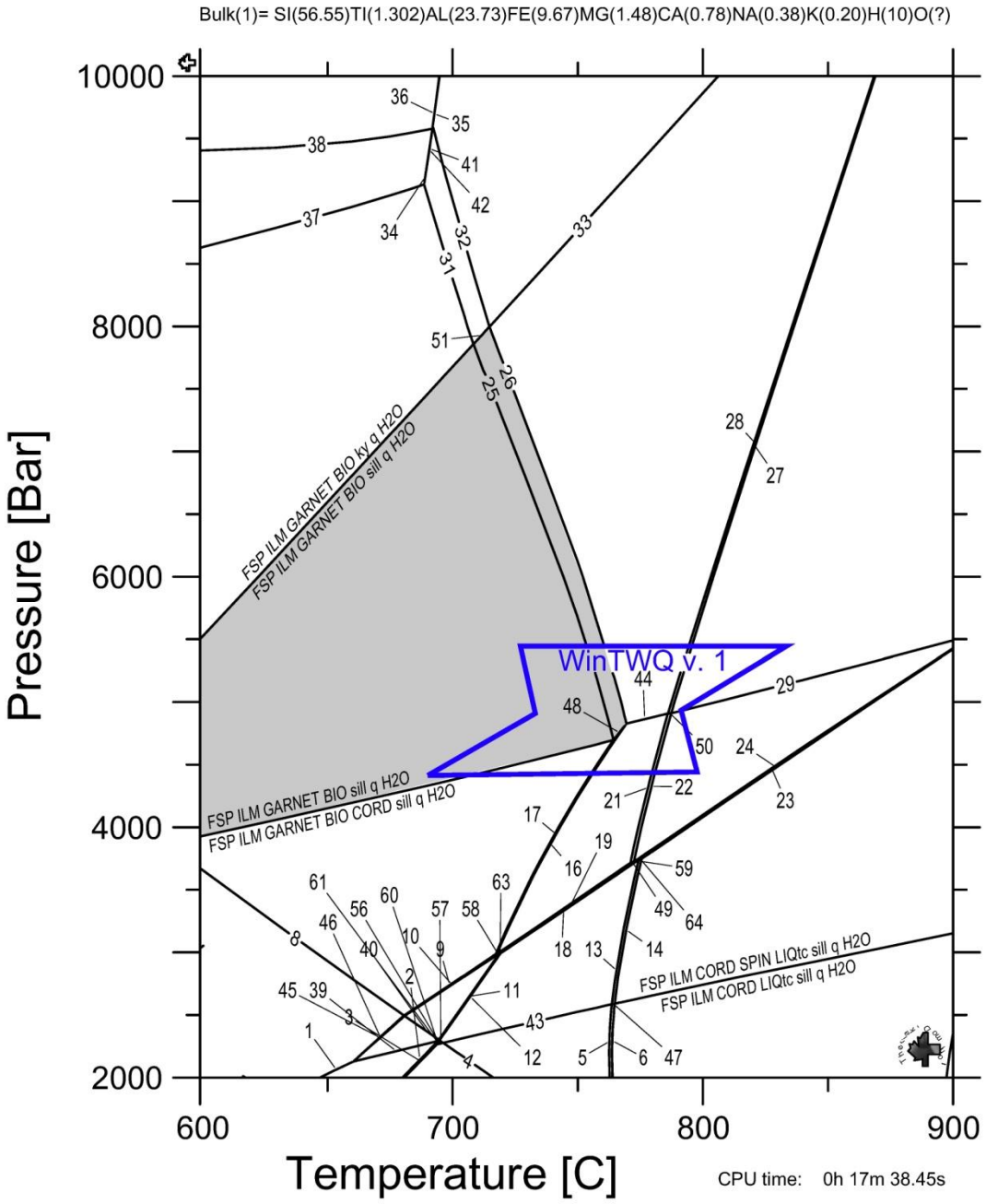

Figure 26. Isochemical phase diagram for sample 96-056 calculated using Theriak-Domino software. Rock bulk chemistry is shown across top of Figure. Gray shaded region is estimated stability field for minerals in 96-056. Blue box shows pressure-temperature estimate calculated by WinTWQ, utilizing microprobe data shown in Table 14. A complete list of reactions on the phase diagram is shown in Table 15.

Table 15. Changes in mineral assemblages for phase diagram of 96-056

Reaction number	Mineral assemblage, reactants	Mineral assemblage, products
1	ILM (2)FSP CORD aQz And H2O	ILM (2)FSP CORD aQz Si H2O
2	ILM (2)FSP CORD aQz Si H2O	ILM (2)FSP CORD bQz Si H2O
3	ILM GARNET FSP WHITE MICA CORD aQz Si H2O	ILM GARNET (2)FSP WHITE MICA CORD aQz Si H2O
4	ILM GARNET (2)FSP WHITE MICA CORD aQz Si H2O	ILM GARNET (2)FSP CORD aQz Si H2O
5	ILM GARNET (2)FSP CORD aQz Si H2O	ILM GARNET (2)FSP CORD bQz Si H2O
6	ILM GARNET (2)FSP CORD bQz Si H2O	SPIN ILM GARNET (2)FSP CORD bQz Si H2O
7	SPIN ILM GARNET (2)FSP CORD bQz Si H2O	SPIN ILM (2)FSP CORD bQz Si H2O
8	ILM GARNET FSP WHITE MICA STAU aQz Si H2O	ILM GARNET FSP WHITE MICA aQz Si H2O
9	ILM GARNET FSP WHITE MICA aQz Si H2O	ILM GARNET (2)FSP WHITE MICA aQz Si H2O
10	ILM GARNET (2)FSP WHITE MICA aQz Si H2O	ILM GARNET (2)FSP aQz Si H2O
11	ILM GARNET (2)FSP aQz Si H2O	ILM GARNET (2)FSP bQz Si H2O
12	ILM GARNET (2)FSP bQz Si H2O	ILM GARNET (2)FSP CORD bQz Si H2O
13	SPIN ILM GARNET (2)FSP CORD bQz Si H2O	SPIN ILM GARNET (2)FSP bQz Si H2O
14	SPIN ILM GARNET (2)FSP bQz Si H2O	SPIN ILM (2)FSP bQz Si H2O
15	ILM GARNET FSP WHITE MICA STAU aQz H2O	ILM GARNET FSP WHITE MICA STAU aQz Ky H2O
16	ILM GARNET FSP WHITE MICA STAU aQz Ky H2O	ILM GARNET FSP WHITE MICA STAU aQz Si H2O
17	ILM GARNET FSP WHITE MICA STAU aQz Ky H2O	ILM GARNET FSP WHITE MICA aQz Ky H2O
18	ILM GARNET FSP WHITE MICA aQz Ky H2O	ILM GARNET FSP WHITE MICA aQz Si H2O
19	ILM GARNET FSP WHITE MICA aQz Ky H2O	ILM GARNET (2)FSP WHITE MICA aQz Ky H2O
20	ILM GARNET (2)FSP WHITE MICA aQz Ky H2O	ILM GARNET (2)FSP aQz Ky H2O
21	ILM GARNET (2)FSP aQz Ky H2O	ILM GARNET (2)FSP aQz Si H2O
22	GARNET FSP WHITE MICA Rt aQz Ky H2O	GARNET (2)FSP WHITE MICA Rt aQz Ky H2O
23	GARNET (2)FSP WHITE MICA Rt aQz Ky H2O	GARNET (2)FSP Rt aQz Ky H2O
24	GARNET (2)FSP Rt aQz Ky H2O	ILM GARNET (2)FSP Rt aQz Ky H2O
25	ILM GARNET (2)FSP Rt aQz Ky H2O	ILM GARNET (2)FSP Rt aQz Si H2O
26	ILM GARNET (2)FSP Rt aQz Si H2O	ILM GARNET (2)FSP aQz Si H2O
27	GARNET (2)FSP Rt aQz Ky H2O	GARNET (2)FSP Rt aQz Si H2O
28	GARNET (2)FSP Rt aQz Si H2O	GARNET (2)FSP Rt bQz Si H2O
29	GARNET (2)FSP Rt bQz Si H2O	ILM GARNET (2)FSP Rt bQz Si H2O
30	ILM GARNET (2)FSP Rt bQz Si H2O	ILM GARNET (2)FSP bQz Si H2O
31	ILM GARNET (2)FSP CORD aQz Si H2O	ILM (2)FSP CORD aQz Si H2O
32	ILM GARNET FSP WHITE MICA CORD aQz Si H2O	ILM GARNET (2)FSP CORD aQz Si H2O
33	ILM GARNET FSP BIOTITE WHITE MICA aQz Si H2O	ILM GARNET FSP WHITE MICA CORD aQz Si H2O
34	ILM GARNET FSP WHITE MICA aQz Si H2O	ILM GARNET FSP BIOTITE WHITE MICA aQz Si H2O
35	ILM GARNET FSP WHITE MICA STAU aQz H2O	ILM GARNET FSP WHITE MICA STAU aQz Si H2O
36	ILM GARNET FSP WHITE MICA Rt aQz Ky H2O	ILM GARNET FSP WHITE MICA aQz Ky H2O
37	GARNET FSP WHITE MICA Rt aQz Ky H2O	ILM GARNET FSP WHITE MICA Rt aQz Ky H2O
38	ILM GARNET (2)FSP CORD aQz Si H2O	ILM GARNET (2)FSP BIOTITE aQz Si H2O
39	ILM GARNET (2)FSP BIOTITE aQz Si H2O	ILM GARNET (2)FSP BIOTITE WHITE MICA aQz Si H2O
40	ILM GARNET (2)FSP BIOTITE WHITE MICA aQz Si H2O	ILM GARNET FSP BIOTITE WHITE MICA aQz Si H2O
41	ILM GARNET (2)FSP CORD bQz Si H2O	ILM (2)FSP CORD bQz Si H2O
42	ILM GARNET (2)FSP aQz Si H2O	ILM GARNET (2)FSP CORD aQz Si H2O
43	ILM GARNET (2)FSP Rt aQz Ky H2O	ILM GARNET (2)FSP aQz Ky H2O
44	GARNET (2)FSP Rt aQz Si H2O	ILM GARNET (2)FSP Rt aQz Si H2O
45	ILM GARNET (2)FSP Rt aQz Si H2O	ILM GARNET (2)FSP Rt bQz Si H2O
46	SPIN ILM (2)FSP CORD bQz Si H2O	ILM (2)FSP CORD bQz Si H2O
47	SPIN ILM (2)FSP bQz Si H2O	SPIN ILM (2)FSP CORD bQz Si H2O
48	ILM GARNET (2)FSP bQz Si H2O	SPIN ILM GARNET (2)FSP bQz Si H2O
49	ILM GARNET FSP WHITE MICA Rt aQz Ky H2O	ILM GARNET (2)FSP Rt aQz Ky H2O
50	ILM GARNET (2)FSP WHITE MICA Rt aQz Ky H2O	ILM GARNET (2)FSP Rt aQz Ky H2O
51	ILM GARNET (2)FSP WHITE MICA Rt aQz Ky H2O	ILM GARNET FSP WHITE MICA Rt aQz Ky H2O
52	ILM GARNET (2)FSP Rt aQz Ky H2O	ILM GARNET (2)FSP aQz Si H2O
53	ILM GARNET (2)FSP CORD bQz Si H2O	SPIN ILM (2)FSP CORD bQz Si H2O
54	SPIN ILM GARNET (2)FSP CORD bQz Si H2O	SPIN ILM (2)FSP bQz Si H2O
55	ILM GARNET (2)FSP aQz Si H2O	ILM GARNET (2)FSP BIOTITE aQz Si H2O
56	ILM GARNET FSP WHITE MICA Rt aQz Ky H2O	ILM GARNET (2)FSP Rt aQz Ky H2O
57	ILM GARNET (2)FSP BIOTITE aQz Si H2O	ILM GARNET (2)FSP BIOTITE CORD aQz Si H2O
58	ILM GARNET (2)FSP BIOTITE CORD aQz Si H2O	ILM GARNET (2)FSP CORD aQz Si H2O
59	ILM GARNET (2)FSP BIOTITE aQz Si H2O	ILM GARNET (2)FSP CORD aQz Si H2O
60	ILM GARNET (2)FSP WHITE MICA aQz Si H2O	ILM GARNET (2)FSP BIOTITE WHITE MICA aQz Si H2O
61	ILM GARNET (2)FSP WHITE MICA aQz Ky H2O	ILM GARNET (2)FSP Rt aQz Ky H2O
62	ILM GARNET (2)FSP WHITE MICA aQz Si H2O	ILM GARNET (2)FSP BIOTITE aQz Si H2O
63	ILM GARNET FSP WHITE MICA Rt aQz Ky H2O	ILM GARNET (2)FSP Rt aQz Ky H2O
64	ILM GARNET (2)FSP WHITE MICA Rt aQz Ky H2O	ILM GARNET (2)FSP Rt aQz Ky H2O
65	ILM GARNET FSP WHITE MICA Rt aQz Ky H2O	ILM GARNET (2)FSP WHITE MICA Rt aQz Ky H2O
66	GARNET (2)FSP Rt aQz Ky H2O	ILM GARNET (2)FSP Rt aQz Si H2O
67	ILM GARNET (2)FSP BIOTITE aQz Si H2O	ILM GARNET (2)FSP BIOTITE CORD aQz Si H2O
68	ILM GARNET (2)FSP BIOTITE CORD aQz Si H2O	ILM GARNET (2)FSP CORD aQz Si H2O
69	ILM GARNET FSP WHITE MICA aQz Ky H2O	ILM GARNET (2)FSP Rt aQz Ky H2O
70	ILM GARNET FSP WHITE MICA Rt aQz Ky H2O	GARNET (2)FSP Rt aQz Ky H2O

HHP98, Olv - ideal, Spn - site mixing and margules, Ilm - site mixing and margules, Grt - site mixing and margules, Fsp - ideal and margules, Bt - site mixing and margules, Ms - site mixing and margules, St - ideal and margules, Opx - site mixing and margules, Omph - site mixing and margules, Chl - site mixing and margules, Crd - site mixing, Ctd - ideal and margules, Amph - site mixing and margules. The resultant phase diagram reproduces the mineral assemblage of the dated sample well (Figure 26). It suggests P-T conditions below 775° C and pressures between 3.5 and 8 kbar. This serves as a minimum constraint, as the rock experienced partial melting at temperatures above the felsic solidus. Inclusions of staurolite within garnet supports staurolite + quartz + muscovite ⇆ garnet + alumnosilicate + biotite as a possible garnet growing reaction with increasing temperature and pressure. Staurolite is converted to spinel at temperatures in excess of 750° C, which provides an additional constraint that the sample was closer to the upper end of Domino's predicted P-T window. Exhumation of the sample to pressures below 4 kbar would facilitate the growth of cordierite at the expense of garnet. The correlation between the phase diagram and the P-T calculated by WinTWQ is not perfect, but the overlap adds strength to the interpretation.

The sample from Recumbent Peak is depleted in the LREE and enriched in the HREE (Fig. 22). The trace element pattern is flat from La to Nd, then slopes up to Tb with a small Eu anomaly before flattening again through Lu. This pattern is characteristic of a garnet bearing restite where the the HREE are partitioned strongly into garnet with forms a residual phase. This trace element pattern confirms that the mineral assemblage of this sample is generated by the extraction of partial melt leaving a residual aluminous rich mineralogy.

5.4 East Ridge Tonalite (09B-34)

The East Ridge Tonalite (Figure 16, Locality "D") is located on the eastern flank of Spinel Peak, south of the Skeena River. The East Ridge consists of half kilometer-scale, overturned isoclinal folds. S_2 axial planes generally trend northwest-southeast, but are refolded about S_3 fabrics, which have a northeast-southwest trending axial planes that dip steeply to the northeast. Around the outcrop, the average foliation is 134°/66° NE, defined by the alignment of biotite. The lineation is defined by biotite, and trends 335°, plunging 35°. Isoclinal folds are preserved in inclusion trails of the garnet. Axial planes of isoclinal folds are parallel to subparallel to the matrix foliation. The inclusion of folded layers within garnet demonstrates that garnet growth was post-folding (S_{1+N}), but deflection of fabrics around the garnet indicate that some deformation occurred post metamorphism. The rusty- and gray-weathering migmatites that serve as the host rock for the East Ridge Tonalite have developed a C-S fabric consistent with dextral shear. Other kinematic indicators include passively folded asymmetrical layers, boudined and folded dikes, and sigma clasts, which are all consistent with dextral shear.

The lithologies on the ridge include an orthogneiss with tonalite protolith and the rusty-weathering migmatite. In thin section, quartz and feldspar contain subgrains. This subgrain development can also be observed in quartz inclusions within garnet.

The trace element pattern for this sample has a negative slope, with a La/Yb ratio of 2.96 (Figure 22). The sample is enriched in the HREE and depleted in the LREE, consistent with melt originating from a garnet-bearing source. The sample has a similar chemical profile to a pelite or volcaniclastic sediment, which likely was the source for melt in the East Ridge "Tonalite". The sample has an Eu anomaly consistent with plagioclase fractionation that occurs during melt generation.

Lu-Hf dating of garnet from this sample yielded meaningful ratios from one

whole rock and four garnet fractions. With all five data points, the sample defines an isochron at 64.2±4.6 Ma (2σ error), with an MSWD = 17 (Figure 23). One garnet point was culled to help reduce the error and MSWD, and a four point isochron was produced at 63.8±2.6 Ma (2σ error), with an MSWD = 2.9. This isochron was consistent with all data points, with better resolution on the age and a more reasonable MSWD. The $^{176}Lu/^{177}Hf$ for the garnet fractions ranged from 2.603 to 2.905 (Table 11). The isochron defines an initial $^{176}Hf/^{177}Hf$ of 0.28301±0.000012 (ε_{Hf} = +8.0±4.3).

5.5 Sample 09B-24

The Oden Ridge sample (Figure 16, Locality "D") is located 1.25 km northeast of Oden Peak. The ridge follows a northeast-trending foliation, with localized left-lateral shear zones. Fabrics dip gently to moderately to the northwest. Around the outcrop, the average foliation is 027°/54° NW, defined by the alignment of biotite. The average lineation is defined by biotite, trends 020° and plunges 22°. Kinematic indicators such as asymmetrical folds, boudins, and shear zones are consistent with oblique left-lateral and reverse deformation. Garnet growth is syn-deformational, as it truncates and includes preexisting fabrics and curved inclusion trails, but also displays minerals deflected around the garnets.

The rock is a paragneiss with a sedimentary protolith (Table 7). In thin section, feldspars contain inclusions of sillimanite. These needles are aligned, and are concentrated near the center of grains. Outside of the feldspar, these sillimanite needles define tight to isoclinal folds. These isoclinal folds are overgrown by garnet. Feldspar grains experienced subgrain development with clear grain boundaries internal to larger grains, and random extinction indicating a component of subgrain rotation. Inclusions are much smaller in garnet than in the matrix.

The sample from Oden Ridge is enriched in the HREE and depleted in the

LREE (Figure 22). The trace element pattern decreases from La to Sm, slopes up to a maximum at Ho, then generally flattens through Lu. This is the opposite of a terrestrial sediment, and is another example of a restite, where melt has been extracted and the sample represents what remained (Miller and Mittlefehldt 1982).

Lu-Hf dating of garnet from this sample yielded meaningful ratios from one whole rock and four garnet fractions. With all five data points, the sample defines an isochron at 68±14 Ma (2σ error), with an MSWD = 228 (Figure 23). One garnet point was culled to help clean the error, and a four point isochron was produced at 71.9±9.4 Ma (2σ error), with an MSWD = 50. This isochron was consistent with all data points, with better resolution on the age and a more reasonable MSWD. The $^{176}Lu/^{177}Hf$ for the garnet fractions ranged from 3.098 to 3.978 (Table 11). The isochron defines an initial $^{176}Hf/^{177}Hf$ of 0.28307±0.000057 (ε_{Hf} = +10.1).

5.6 Petrologists' Ridge (09B-15)

The Petrologists' Ridge sample (Figure 16, Locality "F") is located 3.5 km southeast of Spinel Peak, approximately a third of the way between Spinel and Sillimanite Needle. The foliation trends northwest along the ridge, dipping steeply to the northeast. This sample comes from the hinge of a kilometer-scale synform of inter-layered rusty- and gray-weathering migmatite. Around the outcrop, the average foliation is 155°/72° NE, defined by the alignment of sillimanite. The lineation is defined by sillimanite, plunging 27° towards 005°. Kinematic indicators such as sigma clasts and the development of C-S fabrics within the sample are consistent with top to the southwest reverse deformation. Garnet inclusion trails are curved, are consistent with each other in orientation within the scale of the thin section, and are consistent with syn-deformational garnet growth.

The lithology present here is the gray-weathering migmatite. In thin section,

quartz is in ribbons with subgrain development. Feldspars are recrystallized and embayed, and have subgrain development and kink bands. Garnets have a clear rim, which could indicate a change in the garnet growing reaction.

A garnet-bearing sample from the outcrop was analyzed by electron microprobe (Table 7). Garnet grains are euhedral, 5 mm across and very inclusion rich. The garnets have a clear, inclusion-free rim about 0.5 mm wide. The matrix foliation is defined by cordierite and sillimanite. WDS X-ray images and quantitative WDS analysis show that garnets have increasing iron and decreasing magnesium towards the rims, with uniform concentrations of calcium and manganese (Figure 27). Garnet inclusions define a foliation that is parallel to the matrix foliation. Isoclinal fold hinges are recorded in the inclusion trails, indicating garnet growth post-dated initial folding.

P-T calculations made using WinTWQ v. 2 and microprobe data (Table 16). The estimated P-T is 6854 bars and 798° C from Gr + bQz + 2Si ⇆ 3An; and Alm + Phl ⇆ Py + Ann (Figure 28).

Lu-Hf dating of garnet from this sample yielded meaningful ratios from one whole rock and three garnet fractions. With all four data points, the sample defines an isochron at 68.0±8.6 Ma (2σ error), with an MSWD = 46 (Figure 23). The $^{176}Lu/^{177}Hf$ for the garnet fractions ranged from 3.551 to 4.44 (Table 11). The isochron defines an initial $^{176}Hf/^{177}Hf$ of 0.28270±0.00058 (ε_{Hf} = -3.0).

A phase diagram was constructed using the Holland and Powell database in Theriak-Domino (Figure 28). This calculation utilized the same mixing models as sample 96-056. The phase diagram reproduces the mineral assemblage of the dated sample at temperatures between 600° and 800° C and pressures between 4 and 9 kbars. This is slightly cooler than the P-T estimate by WinTWQ, which could be a result of different databases, or that the observed mineral assemblage is not the peak

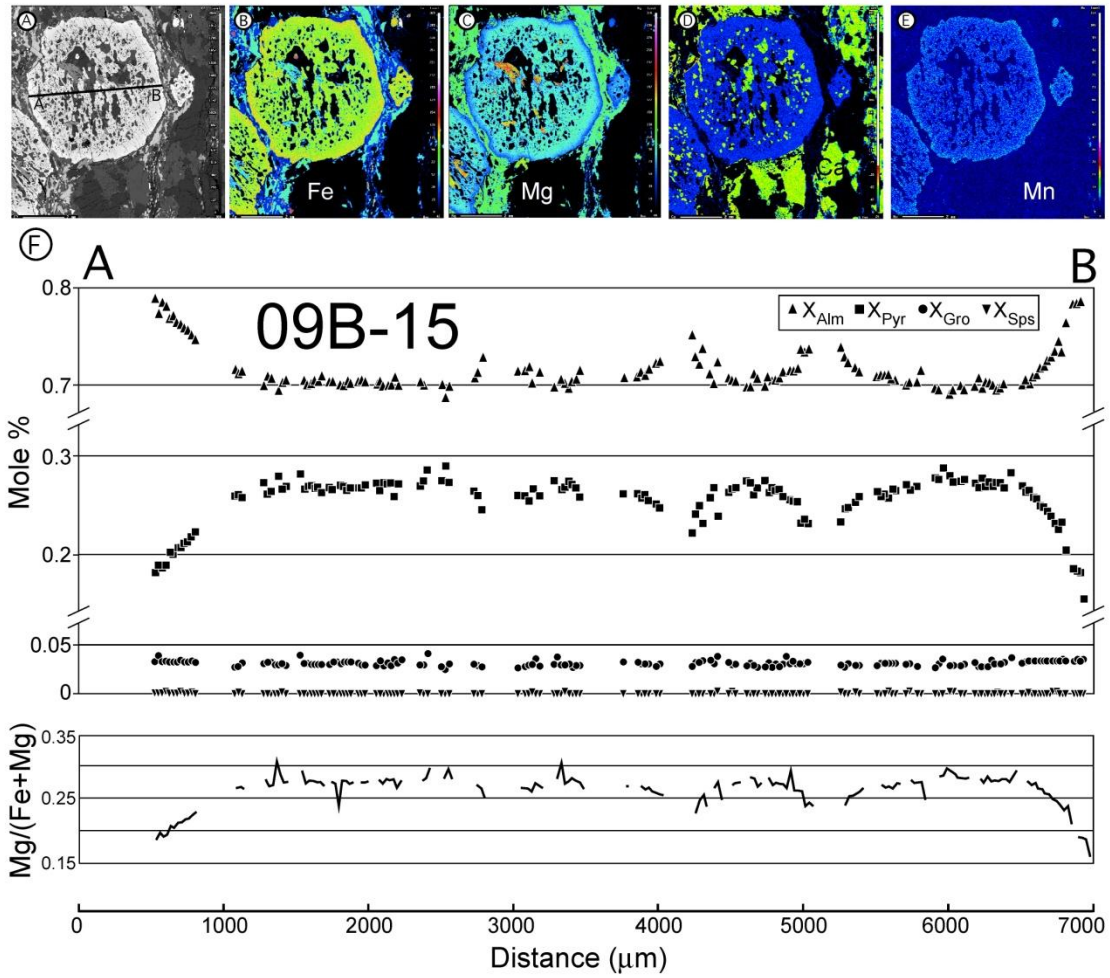

Figure 27. Backscatter electron image, X-ray intensity maps, and compositional line scan collected for sample 09B-15. A) Backscatter electron image of garnet. Black line marked A-B is location of compositional line scan shown in (D). B) X-ray intensity map for Fe Kα. Color scale adjusted to highlight zoning in garnet. C) X-ray intensity map for Mg Kα. D) Compositional line scan collected by quantitative wavelength dispersive scanning analysis. Note compressed vertical scale. Representative analyses of minerals used for thermobarometry calculations reported in Table 16.

Table 16. Representative microprobe mineral analyses* for 09B-15

Weight % Oxides

Oxides	Garnet (Core)	Garnet (Rim)	Plag (Incl)	Plag (Matrix)	Cord	Biot (Matrix)	Ilmenite
SiO_2	37.38	38.18	58.34	57.95	49.05	34.09	0.09
TiO_2	0.00	0.02	0.00	0.00	0.03	4.97	51.77
Al_2O_3	22.15	22.51	25.59	25.68	33.27	17.74	0.02
FeO	32.09	34.64	0.16	0.00	8.44	20.76	47.58
MnO	0.41	0.64	0.00	0.00	0.02	0.02	0.17
MgO	7.00	4.55	0.01	0.00	8.11	7.65	0.50
CaO	1.35	1.61	7.90	7.93	0.00	0.00	0.00
Na_2O	0.03	0.03	7.15	6.99	0.07	0.11	0.04
K_2O	0.00	0.00	0.17	0.56	0.00	9.20	0.01
Cr_2O_3	0.02	0.00	0.04	0.00	0.01	0.06	0.03
Cl^-	0.02	0.00	0.00	0.00	0.00	0.04	0.01
F^{2-}	0.00	0.13	0.00	0.00	0.00	0.00	0.00
Ba^-	0.02	0.00	0.02	0.00	0.00	0.67	0.45
Total†	100.45	102.26	99.38	99.11	98.99	95.25	100.62

Ions in Formula§

Element	Garnet (Core)	Garnet (Rim)	Plag (Incl)	Plag (Matrix)	Cord	Biot (Matrix)	Ilmenite
Si	2.931	2.967	2.628	2.620	5.010	2.880	0.002
Ti	0.000	0.001	0.000	0.000	0.002	0.316	0.655
Al	2.047	2.061	1.358	1.368	4.006	1.767	0.000
Fe^{2+}	2.105	2.251	0.006	0.000	0.721	1.467	0.669
Mn	0.027	0.042	0.000	0.000	0.002	0.001	0.002
Mg	0.818	0.527	0.001	0.000	1.236	0.963	0.012
Ca	0.113	0.134	0.381	0.384	0.000	0.000	0.000
Na	0.004	0.004	0.624	0.613	0.013	0.018	0.001
K	0.000	0.000	0.010	0.032	0.000	0.991	0.000
Cl	0.003	0.000	0.000	0.000	0.000	0.006	0.000
F	0.000	0.031	0.000	0.000	0.000	0.000	0.000
Ba	0.001	0.000	0.000	0.000	0.000	0.025	0.003
Cr	0.001	0.000	0.002	0.000	0.000	0.004	0.000
Total	8.049	8.019	5.010	5.018	10.991	8.438	1.346

* Representative analyses were chosen for most minerals. Biotite numbers were produced from averaging multiple analyses.
† Oxide totals corrected for Cl, F, and Ba using the method described in Deer, Howie and Zussmen.
§ Stoichiometric ratios of elements based on 12 oxygen for garnet, 11 for biotite, 8 for plagioclase, 2 for ilmenite, 18 for cordierite.

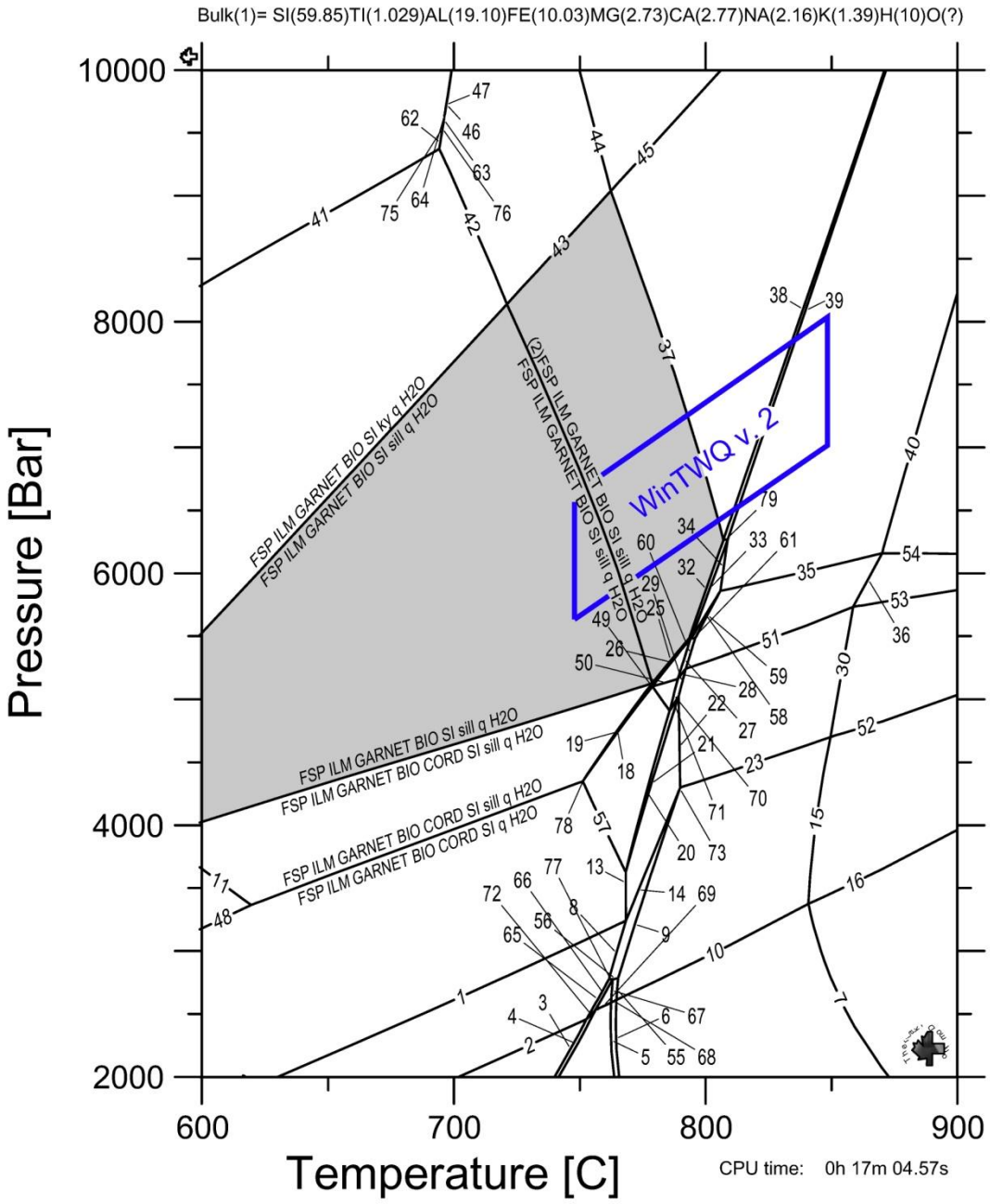

Figure 28. Isochemical phase diagram for sample 09B-15 calculated using Theriak-Domino software. Rock bulk chemistry is shown across top of Figure. Gray shaded region is estimated stability field for minerals in 09B-15. Blue box shows pressure-temperature estimate calculated by WinTWQ, utilizing microprobe data shown in Table 16. A complete list of reactions on the phase diagram is shown in Table 17.

Table 17. Changes in mineral assemblages for phase diagram of 09B-15

Reaction number	Mineral assemblage, reactants	Mineral assemblage, products
1	ILM GARNET FSP BIOTITE CORD aQz H2O	ILM GARNET FSP BIOTITE CORD bQz H2O
2	ILM GARNET FSP BIOTITE CORD bQz H2O	ILM GARNET FSP BIOTITE OPX CORD bQz H2O
3	ILM GARNET FSP BIOTITE OPX CORD bQz H2O	OLIVINEi ILM GARNET FSP BIOTITE OPX CORD bQz H2O
4	ILM GARNET FSP BIOTITE OPX CORD bQz H2O	OLIVINEi ILM GARNET FSP BIOTITE OPX CORD bQz H2O
5	OLIVINEi ILM GARNET FSP BIOTITE OPX CORD bQz H2O	OLIVINEi ILM GARNET FSP BIOTITE CORD bQz H2O
6	OLIVINEi ILM GARNET FSP BIOTITE OPX CORD bQz H2O	OLIVINEi ILM GARNET FSP BIOTITE CORD bQz H2O
7	OLIVINEi ILM GARNET FSP BIOTITE CORD bQz H2O	OLIVINEi ILM GARNET (2)FSP BIOTITE CORD bQz H2O
8	OLIVINEi ILM GARNET (2)FSP BIOTITE CORD bQz H2O	OLIVINEi ILM (2)FSP BIOTITE CORD bQz H2O
9	OLIVINEi ILM (2)FSP BIOTITE CORD bQz H2O	OLIVINEi ILM (2)FSP OPX CORD bQz H2O
10	OLIVINEi ILM (2)FSP OPX CORD bQz H2O	OLIVINEi ILM (2)FSP CORD bQz H2O
11	ILM GARNET (2)FSP BIOTITE CORD aQz H2O	ILM GARNET FSP BIOTITE CORD aQz H2O
12	ILM GARNET (2)FSP BIOTITE CORD aQz H2O	ILM GARNET (2)FSP BIOTITE CORD bQz H2O
13	ILM GARNET (2)FSP BIOTITE CORD bQz H2O	ILM GARNET (2)FSP BIOTITE OPX CORD bQz H2O
14	ILM GARNET (2)FSP BIOTITE OPX CORD bQz H2O	ILM GARNET (2)FSP OPX CORD bQz H2O
15	ILM GARNET (2)FSP OPX CORD bQz H2O	OLIVINEi ILM GARNET (2)FSP OPX CORD bQz H2O
16	OLIVINEi ILM GARNET (2)FSP OPX CORD bQz H2O	OLIVINEi ILM (2)FSP OPX CORD bQz H2O
17	ILM GARNET FSP BIOTITE WHITE MICA CORD aQz H2O	ILM GARNET (2)FSP BIOTITE WHITE MICA CORD aQz H2O
18	ILM GARNET (2)FSP BIOTITE WHITE MICA CORD aQz H2O	ILM GARNET (2)FSP BIOTITE CORD aQz H2O
19	ILM GARNET (2)FSP CORD aQz H2O	ILM GARNET (2)FSP BIOTITE CORD aQz H2O
20	ILM GARNET (2)FSP CORD aQz H2O	ILM GARNET (2)FSP CORD bQz H2O
21	ILM GARNET (2)FSP CORD bQz H2O	ILM GARNET (2)FSP OPX CORD bQz H2O
22	ILM GARNET FSP BIOTITE WHITE MICA aQz Si H2O	ILM GARNET (2)FSP BIOTITE WHITE MICA aQz Si H2O
23	ILM GARNET FSP BIOTITE WHITE MICA aQz Si H2O	ILM GARNET (2)FSP BIOTITE WHITE MICA aQz Si H2O
24	ILM GARNET FSP BIOTITE WHITE MICA aQz Si H2O	ILM GARNET (2)FSP BIOTITE WHITE MICA aQz Si H2O
25	ILM GARNET (2)FSP BIOTITE WHITE MICA aQz Si H2O	ILM GARNET (2)FSP BIOTITE aQz Si H2O
26	ILM GARNET (2)FSP BIOTITE WHITE MICA aQz Si H2O	ILM GARNET (2)FSP BIOTITE aQz Si H2O
27	ILM GARNET (2)FSP BIOTITE WHITE MICA aQz Si H2O	ILM GARNET (2)FSP BIOTITE aQz Si H2O
28	ILM GARNET (2)FSP BIOTITE aQz Si H2O	ILM GARNET (2)FSP BIOTITE CORD aQz Si H2O
29	ILM GARNET (2)FSP BIOTITE CORD aQz Si H2O	ILM GARNET (2)FSP CORD aQz Si H2O
30	ILM GARNET (2)FSP CORD aQz Si H2O	ILM GARNET (2)FSP CORD bQz Si H2O
31	ILM GARNET (2)FSP CORD bQz Si H2O	ILM GARNET (2)FSP CORD bQz H2O
32	ILM GARNET FSP BIOTITE WHITE MICA STAU aQz H2O	ILM GARNET FSP BIOTITE WHITE MICA STAU aQz Si H2O
33	ILM GARNET FSP BIOTITE WHITE MICA STAU aQz Si H2O	ILM GARNET FSP BIOTITE WHITE MICA aQz Si H2O
34	ILM GARNET (2)FSP BIOTITE aQz Si H2O	ILM GARNET (2)FSP aQz Si H2O
35	ILM GARNET (2)FSP aQz Si H2O	ILM GARNET (2)FSP bQz Si H2O
36	ILM GARNET (2)FSP bQz Si H2O	ILM GARNET (2)FSP CORD bQz Si H2O
37	GARNET FSP WHITE MICA Rt aQz Ky H2O	GARNET FSP BIOTITE WHITE MICA Rt aQz Ky H2O
38	GARNET FSP WHITE MICA Rt aQz Ky H2O	GARNET FSP WHITE MICA Rt aQz Si H2O
39	GARNET FSP WHITE MICA Rt aQz Si H2O	ILM GARNET FSP WHITE MICA Rt aQz Si H2O
40	ILM GARNET FSP WHITE MICA Rt aQz Si H2O	GARNET (2)FSP WHITE MICA Rt aQz Si H2O
41	GARNET (2)FSP WHITE MICA Rt aQz Si H2O	GARNET (2)FSP Rt aQz Si H2O
42	GARNET (2)FSP Rt aQz Si H2O	ILM GARNET (2)FSP Rt aQz Si H2O
43	ILM GARNET (2)FSP Rt aQz Si H2O	ILM GARNET (2)FSP aQz Si H2O
44	GARNET FSP WHITE MICA Rt aQz Ky H2O	GARNET (2)FSP WHITE MICA Rt aQz Ky H2O
45	GARNET (2)FSP WHITE MICA Rt aQz Ky H2O	GARNET (2)FSP Rt aQz Ky H2O
46	GARNET (2)FSP Rt aQz Ky H2O	GARNET (2)FSP Rt aQz Si H2O
47	GARNET (2)FSP Rt aQz Si H2O	GARNET (2)FSP Rt bQz Si H2O
48	GARNET (2)FSP Rt bQz Si H2O	ILM GARNET (2)FSP Rt bQz Si H2O
49	ILM GARNET (2)FSP Rt bQz Si H2O	ILM GARNET (2)FSP bQz Si H2O
50	ILM GARNET FSP BIOTITE WHITE MICA aQz Si H2O	ILM GARNET FSP BIOTITE WHITE MICA CORD aQz H2O
51	ILM GARNET FSP BIOTITE WHITE MICA STAU Rt aQz H2O	ILM GARNET FSP BIOTITE WHITE MICA STAU aQz H2O
52	GARNET FSP BIOTITE WHITE MICA STAU Rt aQz H2O	ILM GARNET FSP BIOTITE WHITE MICA STAU Rt aQz H2O
53	GARNET FSP BIOTITE WHITE MICA STAU Rt aQz Ky H2O	GARNET FSP BIOTITE WHITE MICA STAU Rt aQz H2O
54	GARNET FSP BIOTITE WHITE MICA Rt aQz Ky H2O	GARNET FSP BIOTITE WHITE MICA STAU Rt aQz Ky H2O
55	ILM GARNET (2)FSP BIOTITE CORD aQz Si H2O	ILM GARNET (2)FSP BIOTITE CORD aQz H2O

Table 17 (cont.). Changes in mineral assemblages for phase diagram of 09B-15

Reaction number	Mineral assemblage, reactants	Mineral assemblage, products
56	ILM GARNET (2)FSP BIOTITE CORD aQz Si H2O	ILM GARNET (2)FSP BIOTITE CORD aQz H2O
57	ILM GARNET (2)FSP BIOTITE aQz Si H2O	ILM GARNET (2)FSP BIOTITE CORD aQz Si H2O
58	ILM GARNET (2)FSP BIOTITE aQz Si H2O	ILM GARNET (2)FSP BIOTITE CORD aQz Si H2O
59	ILM GARNET (2)FSP BIOTITE aQz Si H2O	ILM GARNET (2)FSP BIOTITE CORD aQz Si H2O
60	ILM GARNET (2)FSP BIOTITE aQz Si H2O	ILM GARNET (2)FSP BIOTITE CORD aQz Si H2O
61	ILM GARNET FSP BIOTITE WHITE MICA Rt aQz Si H2O	ILM GARNET FSP BIOTITE WHITE MICA aQz Si H2O
62	GARNET FSP BIOTITE WHITE MICA Rt aQz Si H2O	ILM GARNET FSP BIOTITE WHITE MICA Rt aQz Si H2O
63	GARNET FSP WHITE MICA Rt aQz Si H2O	GARNET FSP BIOTITE WHITE MICA Rt aQz Si H2O
64	ILM GARNET FSP BIOTITE OPX CORD bQz H2O	OLIVINEi ILM GARNET FSP BIOTITE CORD bQz H2O
65	ILM GARNET (2)FSP BIOTITE CORD bQz H2O	ILM GARNET FSP BIOTITE CORD bQz H2O
66	ILM GARNET (2)FSP CORD aQz Si H2O	ILM GARNET (2)FSP CORD aQz H2O
67	ILM GARNET (2)FSP BIOTITE aQz Si H2O	ILM GARNET (2)FSP CORD aQz Si H2O
68	ILM GARNET FSP WHITE MICA Rt aQz Si H2O	ILM GARNET FSP BIOTITE WHITE MICA Rt aQz Si H2O
69	ILM GARNET (2)FSP CORD bQz H2O	ILM GARNET (2)FSP BIOTITE CORD bQz H2O
70	ILM GARNET (2)FSP BIOTITE aQz Si H2O	ILM GARNET (2)FSP CORD aQz Si H2O
71	ILM GARNET (2)FSP BIOTITE aQz Si H2O	ILM GARNET (2)FSP CORD aQz Si H2O
72	SPIN ILM GARNET (2)FSP CORD bQz H2O	ILM GARNET (2)FSP CORD bQz H2O
73	SPIN ILM GARNET (2)FSP CORD bQz H2O	SPIN ILM GARNET (2)FSP CORD bQz Si H2O
74	SPIN ILM GARNET (2)FSP CORD bQz Si H2O	ILM GARNET (2)FSP CORD bQz Si H2O
75	ILM GARNET FSP BIOTITE OPX CORD bQz H2O	ILM GARNET (2)FSP BIOTITE OPX CORD bQz H2O
76	ILM GARNET FSP BIOTITE WHITE MICA aQz Si H2O	ILM GARNET (2)FSP BIOTITE aQz Si H2O
77	ILM GARNET FSP BIOTITE WHITE MICA aQz Si H2O	ILM GARNET (2)FSP BIOTITE aQz Si H2O
78	ILM GARNET FSP BIOTITE WHITE MICA aQz Si H2O	ILM GARNET (2)FSP BIOTITE aQz Si H2O
79	ILM GARNET FSP BIOTITE WHITE MICA aQz Si H2O	ILM GARNET (2)FSP BIOTITE aQz Si H2O
80	ILM GARNET FSP BIOTITE WHITE MICA aQz Si H2O	ILM GARNET (2)FSP BIOTITE aQz Si H2O
81	ILM GARNET (2)FSP BIOTITE CORD aQz Si H2O	ILM GARNET (2)FSP CORD aQz Si H2O
82	GARNET FSP BIOTITE WHITE MICA Rt aQz Ky H2O	GARNET FSP BIOTITE WHITE MICA Rt aQz Si H2O
83	ILM GARNET FSP BIOTITE WHITE MICA aQz Ky H2O	ILM GARNET FSP BIOTITE WHITE MICA aQz Si H2O
84	ILM GARNET FSP BIOTITE WHITE MICA Rt aQz Ky H2O	ILM GARNET FSP BIOTITE WHITE MICA aQz Ky H2O
85	GARNET FSP BIOTITE WHITE MICA Rt aQz Ky H2O	ILM GARNET FSP BIOTITE WHITE MICA Rt aQz Ky H2O
86	GARNET FSP WHITE MICA Rt aQz Si H2O	GARNET (2)FSP WHITE MICA Rt aQz Si H2O
87	ILM GARNET FSP BIOTITE OPX CORD bQz H2O	OLIVINEi ILM GARNET FSP BIOTITE OPX CORD bQz H2O
88	OLIVINEi ILM GARNET FSP BIOTITE OPX CORD bQz H2O	OLIVINEi ILM GARNET FSP BIOTITE CORD bQz H2O
89	OLIVINEi ILM GARNET (2)FSP BIOTITE CORD bQz H2O	ILM GARNET (2)FSP BIOTITE OPX CORD bQz H2O
90	ILM GARNET FSP BIOTITE WHITE MICA aQz Si H2O	ILM GARNET (2)FSP BIOTITE aQz Si H2O
91	ILM GARNET (2)FSP BIOTITE WHITE MICA aQz Si H2O	ILM GARNET (2)FSP BIOTITE aQz Si H2O
92	ILM GARNET FSP BIOTITE WHITE MICA aQz Si H2O	ILM GARNET (2)FSP BIOTITE WHITE MICA aQz Si H2O
93	ILM GARNET (2)FSP BIOTITE aQz Si H2O	ILM GARNET (2)FSP BIOTITE CORD aQz Si H2O
94	ILM GARNET (2)FSP BIOTITE CORD aQz Si H2O	ILM GARNET (2)FSP CORD aQz Si H2O
95	ILM GARNET (2)FSP BIOTITE aQz Si H2O	ILM GARNET (2)FSP CORD aQz Si H2O
96	ILM GARNET (2)FSP BIOTITE aQz Si H2O	ILM GARNET (2)FSP CORD aQz Si H2O
97	ILM GARNET (2)FSP BIOTITE aQz Si H2O	ILM GARNET (2)FSP CORD aQz Si H2O
98	SPIN ILM GARNET (2)FSP CORD bQz H2O	ILM GARNET (2)FSP CORD bQz Si H2O
99	ILM GARNET FSP BIOTITE WHITE MICA STAU aQz H2O	ILM GARNET FSP BIOTITE WHITE MICA STAU aQz Ky H2O
100	ILM GARNET FSP BIOTITE WHITE MICA aQz Ky H2O	ILM GARNET FSP BIOTITE WHITE MICA STAU aQz Ky H2O
101	ILM GARNET (2)FSP Rt aQz Si H2O	ILM GARNET (2)FSP Rt bQz Si H2O
102	ILM GARNET (2)FSP BIOTITE aQz Si H2O	ILM GARNET (2)FSP BIOTITE CORD aQz Si H2O
103	ILM GARNET (2)FSP BIOTITE CORD aQz Si H2O	ILM GARNET (2)FSP CORD aQz Si H2O
104	ILM GARNET FSP BIOTITE OPX CORD bQz H2O	OLIVINEi ILM GARNET FSP BIOTITE CORD bQz H2O
105	OLIVINEi ILM (2)FSP BIOTITE CORD bQz H2O	OLIVINEi ILM (2)FSP BIOTITE OPX CORD bQz H2O
106	OLIVINEi ILM (2)FSP BIOTITE OPX CORD bQz H2O	OLIVINEi ILM (2)FSP OPX CORD bQz H2O
107	ILM GARNET (2)FSP BIOTITE CORD bQz H2O	ILM GARNET (2)FSP OPX CORD bQz H2O
108	ILM GARNET (2)FSP BIOTITE CORD bQz H2O	ILM GARNET (2)FSP OPX CORD bQz H2O
109	ILM GARNET (2)FSP BIOTITE WHITE MICA aQz Si H2O	ILM GARNET (2)FSP BIOTITE aQz Si H2O
110	ILM GARNET FSP BIOTITE WHITE MICA aQz Si H2O	ILM GARNET (2)FSP BIOTITE WHITE MICA aQz Si H2O
111	ILM GARNET FSP WHITE MICA Rt aQz Si H2O	ILM GARNET (2)FSP WHITE MICA Rt aQz Si H2O
112	ILM GARNET (2)FSP WHITE MICA Rt aQz Si H2O	ILM GARNET (2)FSP Rt aQz Si H2O
113	ILM GARNET (2)FSP BIOTITE Rt aQz Si H2O	ILM GARNET (2)FSP BIOTITE aQz Si H2O
114	ILM GARNET (2)FSP Rt aQz Si H2O	ILM GARNET (2)FSP BIOTITE Rt aQz Si H2O
115	ILM GARNET (2)FSP aQz Si H2O	ILM GARNET (2)FSP CORD aQz Si H2O
116	ILM GARNET FSP BIOTITE WHITE MICA STAU Rt aQz H2O	ILM GARNET FSP BIOTITE WHITE MICA Rt aQz Ky H2O

Table 17 (cont.). Changes in mineral assemblages for phase diagram of 09B-15

Reaction number	Mineral assemblage, reactants	Mineral assemblage, products
117	ILM GARNET (2)FSP BIOTITE aQz Si H2O	ILM GARNET (2)FSP BIOTITE CORD aQz H2O
118	ILM GARNET (2)FSP Rt aQz Si H2O	ILM GARNET (2)FSP BIOTITE aQz Si H2O
119	GARNET FSP BIOTITE WHITE MICA Rt aQz Ky H2O	ILM GARNET FSP BIOTITE WHITE MICA Rt aQz Si H2O
120	ILM GARNET FSP BIOTITE WHITE MICA aQz Si H2O	ILM GARNET (2)FSP BIOTITE WHITE MICA aQz Si H2O
121	ILM GARNET (2)FSP BIOTITE WHITE MICA aQz Si H2O	ILM GARNET (2)FSP BIOTITE aQz Si H2O
122	ILM GARNET (2)FSP BIOTITE aQz Si H2O	ILM GARNET (2)FSP BIOTITE CORD aQz Si H2O
123	ILM GARNET (2)FSP BIOTITE CORD aQz Si H2O	ILM GARNET (2)FSP CORD aQz Si H2O
124	ILM GARNET FSP BIOTITE WHITE MICA aQz Si H2O	ILM GARNET (2)FSP BIOTITE aQz Si H2O
125	ILM GARNET (2)FSP BIOTITE CORD aQz Si H2O	ILM GARNET (2)FSP BIOTITE CORD aQz H2O
126	ILM GARNET FSP BIOTITE WHITE MICA aQz Si H2O	ILM GARNET (2)FSP BIOTITE aQz Si H2O
127	GARNET FSP WHITE MICA Rt aQz Ky H2O	GARNET (2)FSP WHITE MICA Rt aQz Si H2O
128	GARNET FSP WHITE MICA Rt aQz Si H2O	ILM GARNET FSP BIOTITE WHITE MICA Rt aQz Si H2O
129	ILM GARNET FSP BIOTITE WHITE MICA STAU Rt aQz H2O	ILM GARNET FSP BIOTITE WHITE MICA STAU aQz Ky H2
130	ILM GARNET FSP BIOTITE WHITE MICA Rt aQz Ky H2O	ILM GARNET FSP BIOTITE WHITE MICA Rt aQz Si H2O
131	SPIN ILM GARNET (2)FSP CORD bQz Si H2O	ILM GARNET (2)FSP CORD bQz Si H2O
132	SPIN ILM GARNET (2)FSP CORD bQz H2O	SPIN ILM GARNET (2)FSP CORD bQz Si H2O
133	ILM GARNET (2)FSP CORD bQz Si H2O	SPIN ILM GARNET (2)FSP CORD bQz H2O
134	ILM GARNET (2)FSP BIOTITE WHITE MICA aQz Si H2O	ILM GARNET (2)FSP BIOTITE aQz Si H2O
135	ILM GARNET FSP BIOTITE WHITE MICA aQz Si H2O	ILM GARNET (2)FSP BIOTITE WHITE MICA aQz Si H2O
136	ILM GARNET (2)FSP BIOTITE CORD bQz H2O	ILM GARNET (2)FSP BIOTITE OPX CORD bQz H2O
137	ILM GARNET (2)FSP BIOTITE OPX CORD bQz H2O	ILM GARNET (2)FSP OPX CORD bQz H2O
138	ILM GARNET FSP BIOTITE OPX CORD bQz H2O	OLIVINEi ILM GARNET FSP BIOTITE CORD bQz H2O
139	ILM GARNET (2)FSP OPX CORD bQz H2O	OLIVINEi ILM GARNET (2)FSP BIOTITE CORD bQz H2O
140	ILM GARNET (2)FSP BIOTITE aQz Si H2O	ILM GARNET (2)FSP CORD aQz Si H2O
141	ILM GARNET (2)FSP BIOTITE aQz Si H2O	ILM GARNET (2)FSP BIOTITE CORD aQz H2O
142	ILM GARNET (2)FSP BIOTITE WHITE MICA aQz Si H2O	ILM GARNET (2)FSP BIOTITE Rt aQz Si H2O
143	ILM GARNET FSP BIOTITE WHITE MICA STAU aQz Ky H2O	ILM GARNET FSP BIOTITE WHITE MICA STAU aQz Si H2
144	ILM GARNET (2)FSP WHITE MICA Rt aQz Si H2O	GARNET (2)FSP Rt aQz Si H2O
145	GARNET (2)FSP WHITE MICA Rt aQz Si H2O	GARNET (2)FSP Rt aQz Si H2O
146	ILM GARNET (2)FSP WHITE MICA Rt aQz Si H2O	GARNET (2)FSP WHITE MICA Rt aQz Si H2O
147	GARNET (2)FSP WHITE MICA Rt aQz Ky H2O	GARNET (2)FSP WHITE MICA Rt aQz Si H2O
148	GARNET FSP BIOTITE WHITE MICA STAU Rt aQz Ky H2O	ILM GARNET FSP BIOTITE WHITE MICA Rt aQz Ky H2O
149	ILM GARNET FSP BIOTITE WHITE MICA Rt aQz Ky H2O	ILM GARNET FSP BIOTITE WHITE MICA aQz Si H2O
150	SPIN ILM GARNET (2)FSP CORD bQz Si H2O	ILM GARNET (2)FSP CORD bQz Si H2O
151	SPIN ILM GARNET (2)FSP CORD bQz H2O	SPIN ILM GARNET (2)FSP CORD bQz Si H2O
152	ILM GARNET (2)FSP CORD bQz Si H2O	SPIN ILM GARNET (2)FSP CORD bQz H2O
153	ILM GARNET (2)FSP BIOTITE WHITE MICA aQz Si H2O	ILM GARNET (2)FSP BIOTITE aQz Si H2O
154	ILM GARNET FSP BIOTITE WHITE MICA aQz Si H2O	ILM GARNET (2)FSP BIOTITE WHITE MICA aQz Si H2O
155	ILM GARNET FSP BIOTITE WHITE MICA aQz Si H2O	ILM GARNET (2)FSP BIOTITE aQz Si H2O
156	ILM GARNET (2)FSP BIOTITE WHITE MICA aQz Si H2O	ILM GARNET (2)FSP BIOTITE aQz Si H2O
157	ILM GARNET FSP BIOTITE WHITE MICA aQz Si H2O	ILM GARNET (2)FSP BIOTITE WHITE MICA aQz Si H2O
158	ILM GARNET FSP BIOTITE WHITE MICA Rt aQz Ky H2O	ILM GARNET FSP BIOTITE WHITE MICA STAU aQz Ky H2O
159	ILM GARNET (2)FSP BIOTITE aQz Si H2O	ILM GARNET (2)FSP BIOTITE CORD aQz Si H2O
160	ILM GARNET (2)FSP BIOTITE CORD aQz Si H2O	ILM GARNET (2)FSP CORD aQz Si H2O
161	SPIN ILM GARNET (2)FSP CORD bQz Si H2O	ILM GARNET (2)FSP CORD bQz Si H2O
162	SPIN ILM GARNET (2)FSP CORD bQz H2O	SPIN ILM GARNET (2)FSP CORD bQz Si H2O
163	ILM GARNET (2)FSP CORD bQz Si H2O	SPIN ILM GARNET (2)FSP CORD bQz H2O

assemblage. With a pelitic protolith, we would not expect temperatures in excess of 800° C without the production of osmulite, saphrene or orthopyroxene, so the WinTWQ result is probably at the upper end of our expected results. The growth of cordierite occurred during cooling and decompression, from the breakdown of garnet and quartz. Cordierite forms parallel to the foliation in place of quartz, and does not form in the bands of plagioclase.

The trace element pattern for this sample has a very shallow slope, with a La/Yb ratio of 2.39 (Figure 22). Other than a small Eu anomaly, the elements have a linear slope. In order to produce this pattern, this sample likely did not experience any melt removal, nor did it form from a garnet-rich source as a melt.

Lu-Hf dating of garnet from this sample yielded meaningful ratios from one whole rock and four garnet fractions. With all five data points, the sample defines an isochron at 67.5±2.6 Ma (2σ error), with an MSWD = 4.3 (Figure 23). One garnet point was culled to help reduce the error and MSWD, and a four point isochron was produced at 67.2±0.7 Ma (2σ error), with an MSWD = 1.5. This isochron was consistent with all data points, with better resolution on the age and a more reasonable MSWD. The $^{176}Lu/^{177}Hf$ for the garnet fractions ranged from 2.255 to 2.415 (Table 11). The isochron defines an initial $^{176}Hf/^{177}Hf$ of 0.28300±0.000028 (ε_{Hf} = +8.0±4.3).

5.7 Sample 09B-06

Sample 09B-06 (Figure 16, Locality "G") is located 4.5 km southeast of Spinel Peak. Map scale foliations in the vicinity of the outcrop trend north to northeast, dipping steeply to the east. The gneissic layering is folded into asymmetrical outcrop-scale folds verging to the southeast. The average foliation at the outcrop is oriented 194°/77° E, and is defined by the alignment of biotite and segregation of felsic

(plagioclase) and mafic layers. The lineation is defined by biotite, trends towards 027°, and plunges 28°. Kinematic indicators such as asymmetrical tails of biotite around garnet are consistent with left-lateral deformation. As these deflect around garnet grains, prograde metamorphism must have been pre- to syn-deformational.

The lithology is a mafic granulite (Table 7). In thin section, quartz exhibits undulatory extinction. The thin section matrix is primarily an aggregate of embayed quartz and plagioclase grains 0.5 mm in size. Occasional pods of ribbon quartz can be observed. Garnets have symplectic reaction rinds where the garnet has broken down to plagioclase, biotite and anthophyllite.

A garnet-bearing sample from the outcrop was analyzed by electron microprobe. Garnet grains are 4 mm across with irregular grain boundaries (Figure 29). WDS X-ray images and quantitative WDS analysis show that Fe decreases towards the rim of the garnet, with a minor increase in calcium. Along the garnet grain boundary is a symplectic intergrowth of anthophyllite + plagioclase, following the reaction garnet + quartz + clinopyroxene + H_2O ⇆ plagioclase (anthophyllite + anorthite) + oxide. Plagioclase compositions change from higher sodium in the matrix to higher calcium in the reaction rind. The matrix foliation is defined by biotite, although it is a minor component of the matrix. Oxides are very large within the garnet, and significantly smaller in the matrix. Ilmenite is concentrated at the reaction rind, suggesting growth during decompression.

P-T conditions were estimated using the RCLC. This program was utilized because it assesses temperature by combining experimental constraints on P-T stability of granulite-facies minerals with a garnet-orthopyroxene thermobarometry scheme (Pattison et al. 2003). The program takes advantage of a mafic samples refractory mineral assemblage, and applies a correction for retrograde Fe-Mg exchange between garnet and orthopyroxene that accounts for lower P-T conditions.

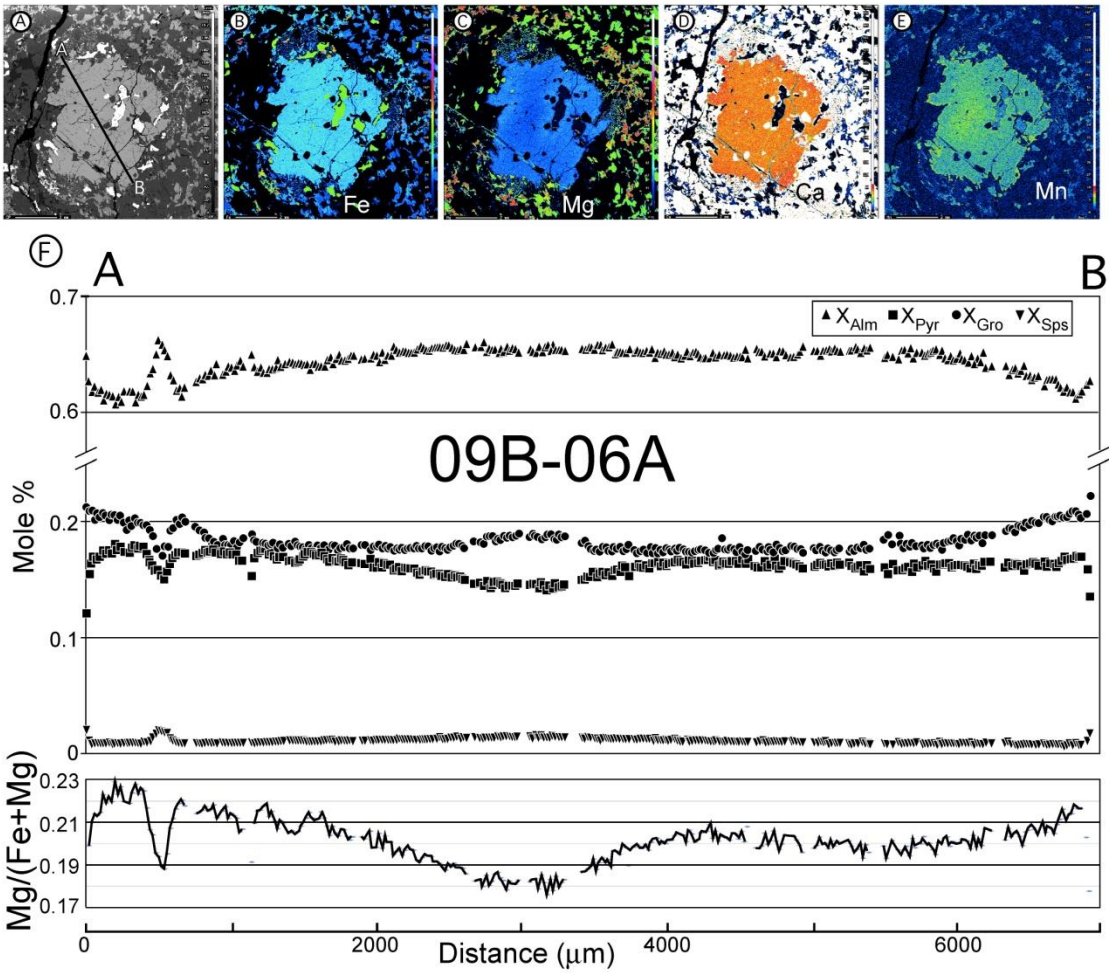

Figure 29. Backscatter electron image, X-ray intensity maps, and compositional line scan collected for sample 09B-06A. A) Backscatter electron image of garnet. Black line marked A-B is location of compositional line scan shown in (D). B) X-ray intensity map for Fe Kα. C) X-ray intensity map for Mg Kα. D) Compositional line scan collected by quantitative wavelength dispersive scanning analysis. Note compressed vertical scale. Representative analyses of minerals used for thermobarometry calculations reported in Table 18.

RCLC produced a P-T estimate of 9200 bars and 783° C (Figure 30). This was consistent the temperature calculation from WinTWQ v. 1, which estimated 736° C from 3Di + Alm ⇆ 3Hd + Py; and 828° C from 3En + 2Alm ⇆ 2Fsl + 2Py (Table 18).

The sample from Oden Peak is slightly enriched in the LREE and depleted in the HREE, with a La/Yb ratio of 4.78 (Figure 22). LREE enrichment can be observed in mafic volcanic rocks such as hotspots and flood basalts, which would serve as the protolith (White 2009).

Another sample with smaller garnets was collected from the same outcrop for geochronology. Lu-Hf dating of garnet yielded meaningful ratios from one whole rock and three garnet fractions. With all four data points, the sample defines an isochron at 64.0±2.8 Ma (2σ error), with an MSWD = 4.6 (Figure 23). One garnet point was culled to help reduce the error, and a three point isochron was produced at 64.3±0.6 Ma (2σ error), with an MSWD = 0.46. This isochron was consistent with all data points, with better resolution on the age and a more reasonable MSWD. The $^{176}Lu/^{177}Hf$ for the garnet fractions ranged from 3.617 to 3.673 (Table 11). The isochron defines an initial $^{176}Hf/^{177}Hf$ of 0.28307±0.000028 (ε_{Hf} = -16.9±6.0).

5.8 Cooper Peak (97-107)

The Cooper Peak sample (Figure 16, Locality "H") is located on the ridge extending to the northeast of Cooper Peak, 2 km west of the Alistair Lake Pluton in the southeast corner of the study area. Map scale foliations trend north-south, with moderate to steep dips to the east. Around the outcrop, the average foliation is 160°/54° NE, defined by the alignment of biotite. The lineation is defined by biotite, with an orientation of 52°/030°.

The sample is a biotite gneiss (Table 7). In thin section, quartz and feldspar are embayed with lobate grain boundaries, consistent with grain boundary migration.

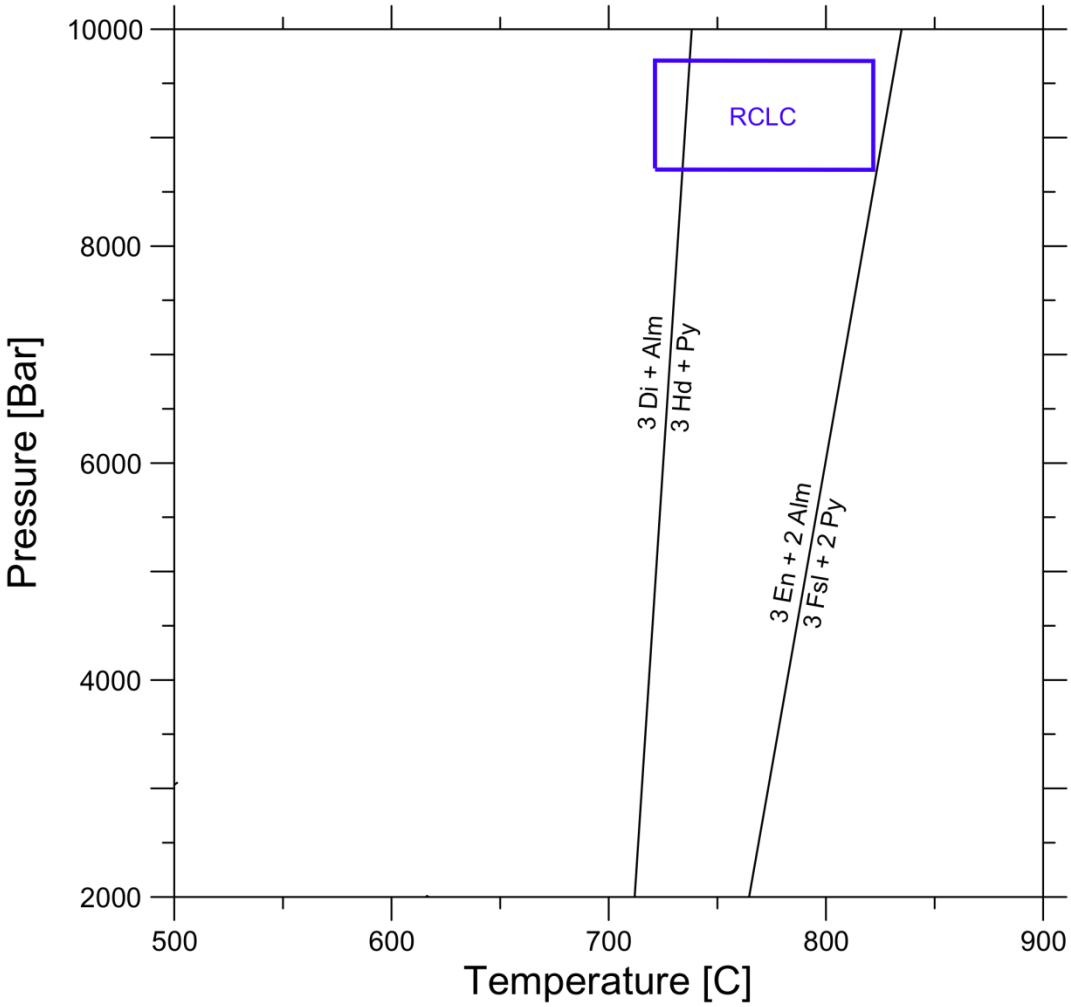

Figure 30. Pressure-temperature estimates for sample 09B-06A. Isochemical phase diagrams did not predict the mineral assemblage for this sample, and were discarded. The blue box shows pressure-temperature estimate calculated by RCLC, utilizing microprobe data shown in Table 18. Reaction lines for thermometry were calculated by WinTWQ v. 2.

Table 18. Representative microprobe mineral analyses* for 09B-06A

Weight % Oxides

Oxides	Garnet (Core)	Garnet (Rim)	Plag (Incl)	Plag (Matrix)	Anth	Ca Plag	Opx	Cpx	Biot (Matrix)	Ilmenite
SiO_2	38.46	38.85	58.25	57.79	49.12	45.60	49.83	44.07	36.16	0.05
TiO_2	0.02	0.08	0.00	0.00	0.00	0.00	0.07	1.47	0.00	48.14
Al_2O_3	21.32	21.42	25.35	25.25	1.39	33.34	1.38	12.37	15.73	0.06
FeO	30.34	28.51	0.13	0.08	33.40	0.43	33.00	19.43	23.29	49.84
MnO	0.68	0.45	0.00	0.05	0.02	0.00	0.38	0.09	0.00	0.26
MgO	3.94	4.46	0.01	0.00	14.04	0.00	14.67	8.84	9.63	0.54
CaO	6.45	7.61	7.82	7.83	0.49	17.75	0.35	11.42	0.02	0.00
Na_2O	0.00	0.00	7.17	6.81	0.03	1.59	0.03	0.78	0.23	0.00
K_2O	0.00	0.00	0.17	0.46	0.00	0.02	0.00	0.95	8.88	0.00
Cr_2O_3			0.00	0.00	0.00	0.05			0.06	
Cl^-			0.01	0.05	0.00	0.01			0.10	
F^{2-}			0.00	0.00	0.00	0.00			0.00	
Ba^-			0.06	0.10	0.00	0.00			1.06	
Total†	101.21	101.37	98.96	98.39	98.50	98.80	99.70	99.44	95.09	98.89

Ions in Formula§

Element	Garnet (Core)	Garnet (Rim)	Plag (Incl)	Plag (Matrix)	Anth	Ca Plag	Opx	Cpx	Biot (Matrix)	Ilmenite
Si	3.009	3.013	2.634	2.632	7.197	2.132	1.962	1.702	3.093	0.001
Ti	0.001	0.005	0.000	0.000	0.000	0.000	0.002	0.043	0.000	0.628
Al	1.965	1.959	1.351	1.355	0.240	1.836	0.064	0.563	1.586	0.001
Fe^{2+}	1.985	1.849	0.005	0.003	4.093	0.017	1.087	0.628	1.666	0.723
Mn	0.045	0.030	0.000	0.002	0.002	0.000	0.013	0.003	0.000	0.004
Mg	0.460	0.516	0.000	0.000	3.068	0.000	0.861	0.509	1.228	0.014
Ca	0.541	0.632	0.379	0.382	0.077	0.889	0.015	0.473	0.002	0.000
Na	0.000	0.000	0.629	0.601	0.010	0.144	0.002	0.059	0.039	0.000
K	0.000	0.000	0.010	0.026	0.000	0.001	0.000	0.047	0.969	0.000
Cl			0.001	0.003	0.000	0.001			0.014	
F			0.000	0.000	0.000	0.000			0.000	
Ba			0.001	0.002	0.000	0.000			0.040	
Cr			0.000	0.000	0.000	0.002			0.004	
Total	8.007	8.003	5.010	5.007	14.688	5.022	4.005	4.026	8.642	1.371

* Representative analyses were chosen for most minerals. Biotite numbers were produced from averaging multiple analyses.
† Oxide totals corrected for Cl, F, and Ba using the method described in Deer, Howie and Zussmen.
§ Stoichiometric ratios of elements based on 12 oxygen for garnet, 22 for anthophyllite, 6 for pyroxene, 11 for biotite, 8 for plagioclase, 2 for ilmenite.

Undulatory extinction is present in feldspar, with subgrain boundaries observable in thin section. Plagioclase and quartz are primarily polygonal, with no observable grain-shape preferred orientation (GPSO). Biotite weakly defines a foliation, although it is in low modal abundance in the thin section. Garnet cross-cuts grains of biotite and is likely syn- to post-deformational.

The trace element pattern for this sample has a very shallow slope, with a La/Yb ratio of 2.88 (Figure 22). The pattern is also extremely consistent, with no Eu enrichment or anomaly.

Lu-Hf dating of garnet from this sample yielded ratios from one whole rock and three garnet fractions. With all four data points, the sample defines an isochron at 78±28 Ma (2σ error), with an MSWD = 264 (Figure 23). The $^{176}Lu/^{177}Hf$ for the garnet fractions ranged from 2.431 to 3.067 (Table 11). The isochron defines an initial $^{176}Hf/^{177}Hf$ of 0.2829±0.0013 (ε_{Hf} = +4.1).

6. Discussion

6.1 Thermobarometry

The central gneiss complex experienced a clockwise P-T path (Figure 31) that recorded: crustal thickening during prograde metamorphism, peak temperatures of 750° - 800° C, rapid decompression and uplift of 2 mm/yr, and finally, isobaric cooling (Hollister 1982; Kenah and Hollister 1983). The thermobarometry of samples from the central gneiss complex nicely agrees with this previously published data.

Early phases of garnet growth occurred from the breakdown of staurolite (Hollister 1982), and was syn-deformational during amphibolite grade metamorphism of 4500 kbars and 520°C (Figure 31). The data collected by electron microprobe (09B-06A, 09B-15, GMO, 96-056) had a narrow range in temperature from 750° to 825° C,

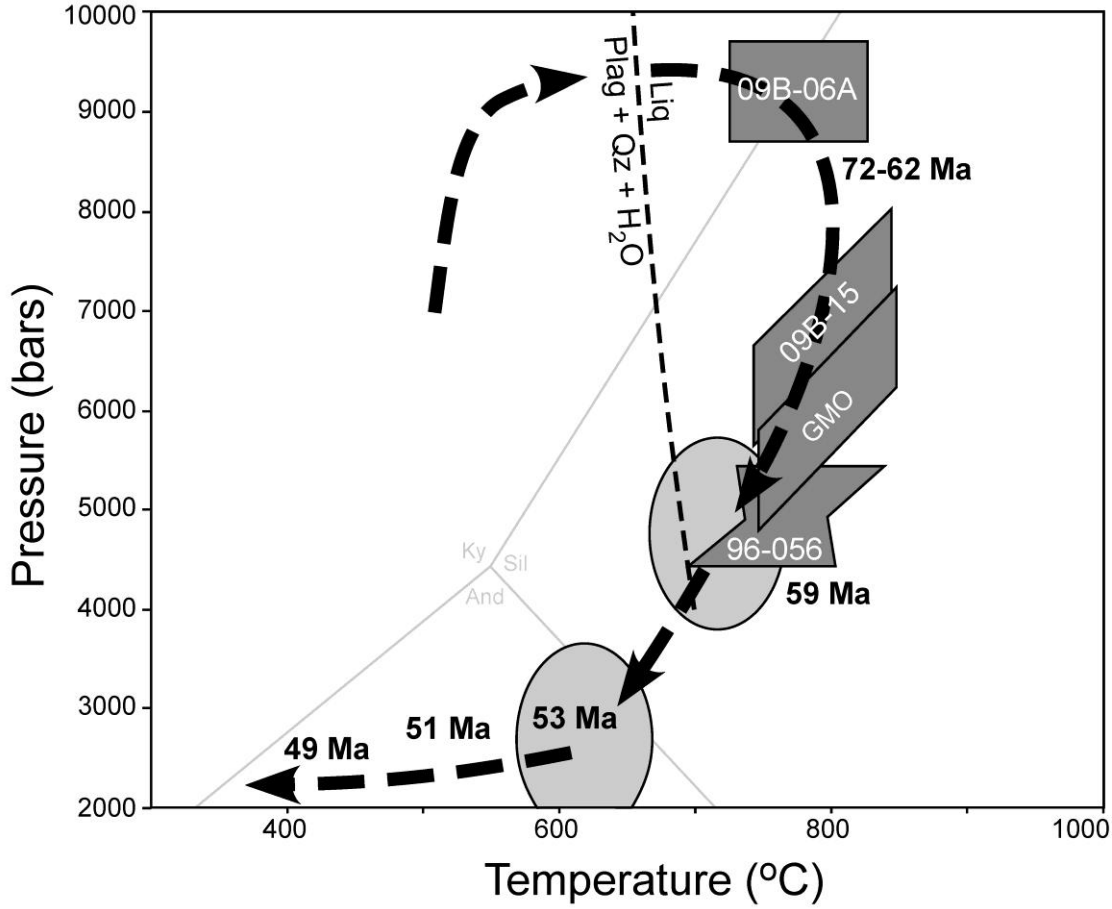

Figure 31. Pressure-Temperature-time path for samples of the central gneiss complex. Alumnosilicate triple point shown for reference. Light gray ovals are P-T estimates from Hollister (1982), Kenah and Hollister (1983) and Andronicos et al. (2003). Dark gray polygons are P-T estimates from WinTWQ, RCLC, and this study. Heavy dashed arrows indicate clockwise path experienced by samples. Bold ages are from various isotopic systems, see text for explanation.

with a wider range in pressure from approximately 5 to 9 kbars (Figure 31). The higher pressure calculated in 09B-06A is likely the most accurate, as it is the only sample corrected for retrograde diffusion in a mafic bulk composition (Pattison et al. 2003). Other samples are in disequilibrium with their peak assemblage, growing cordierite and other low-pressure assemblages during retrograde metamorphism. This high pressure has been previously suspected in the region based on the presence of kyanite (Hollister 1982), but this is the first documented case for pressures >9 kbars in the Coast Mountains. Other high-pressure assemblages have been observed further south in the Cascade crystalline complex, as high as 12 kbars (Miller and Paterson, 2001; Miller et al, 2009).

The breakdown of staurolite to garnet (str + qtz + bt ⇆ grt + AS + ms) is believed to be the dominant garnet-growing reaction, with no observed evidence for chloritoid breakdown. Additional garnet growth occurred at higher P-T conditions, such as bt + sil ⇆ grt + liq.

Previous P-T work in Quottoon host rocks estimated its emplacement at 4.8 kbars and 725° C (Kenah and Hollister 1983), which is comparable to the P-T estimates for our samples at Recumbent Peak and the headwaters of Kwinitsa Creek. Decompression and uplift of the samples (Figure 31) is well documented by Hollister (1982), Kenah and Hollister (1983), and Andronicos (2003). Samples from this study support previous interpretations of the exhumation path. GMO experienced retrograde metamorphism that caused late biotite growth at the expense of K-feldspar; samples 96-056 and 09B-15 grew cordierite from garnet breakdown (garnet + biotite + sillimanite ⇆ cordierite + hercynite + ilmenite + K-feldspar + water) while still at high temperatures; and 09B-06A formed symplectic reaction rinds where the garnet has broken down to plagioclase, biotite and anthophyllite from the reaction garnet + quartz + clinopyroxene + H_2O ⇆ plagioclase (anthophyllite + anorthite) + oxide.

6.2 Geochronology

Prograde, garnet-growing metamorphism occurred in the central gneiss complex around 65 Ma (Figure 32). When all samples are plotted as a weighted average, an overlap occurs at 65 Ma. These samples came from distinct positions within the central gneiss complex, were sourced from different protoliths, and had different initial Hf ratios, so the overlap implies that widespread heating and magmatism occurred at this time. All samples do fall within error of 65-66 Ma when all fractions are considered, and near 65 Ma when samples are cleaned to improve precision. This constrains the main phase of garnet growth to this time period in the late Cretaceous, early Paleogene.

Ages were projected onto a cross section across the central gneiss complex, and plotted with respect to the Coast shear zone (Figure 33). Interpretation of isotopic ages differs by system and mineral. Lu-Hf has a very high closure temperature, and is interpreted as recording the timing of prograde garnet growth when samples remain below 800° C. Zircon ages record the timing of crystallization of zircon from the melt, which is a function of zircon saturation. U-Pb sphene, Sm-Nd garnet, Ar-Ar hornblende, and Ar-Ar biotite all have lower closure temperatures than the peak conditions of the central gneiss complex (Figure 33). Therefore, the date produced by each of these minerals represents when the system cooled past the closure temperature for that mineral. Isotherms were constructed by connecting similar connecting ages across the metamorphic complex. For Ar-Ar hornblende and biotite, these isochrons are also isotherms, as the temperature must have been the same for all samples when the system closed.

Samples presented in this paper date prograde garnet growth between 72-63 Ma (Figure 23, 33). The metamorphic reactions we are dating occur with increases in temperatures while decompressing from pressures above 8 kbar (Figure 31). Our P-T

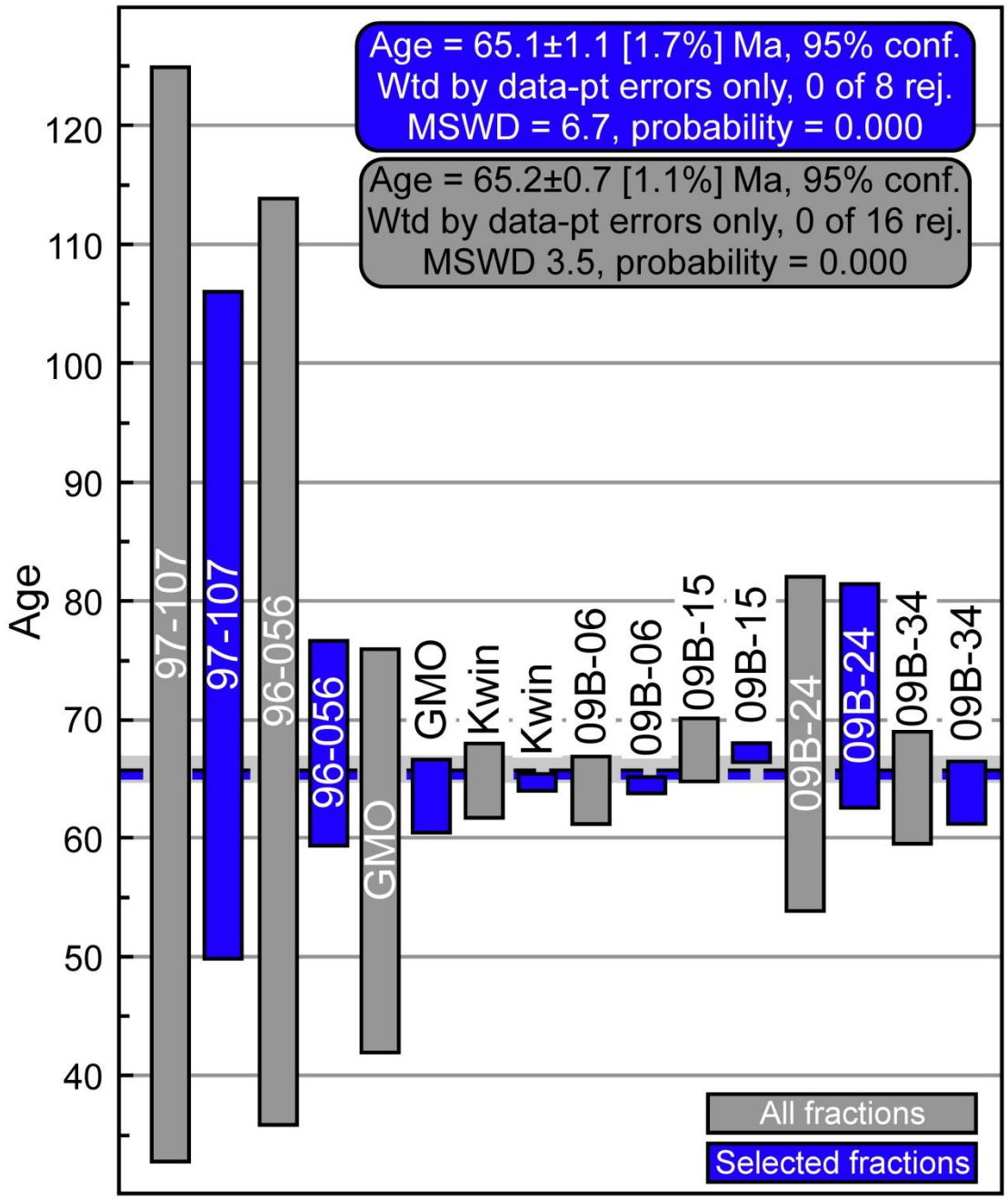

Figure 32. Lu-Hf garnet ages for each sample, plotting all fractions in gray and selected fractions in blue. Average age of metamorphism reported for each population. Horizontal gray line is overlap of samples when all fraction are considered.

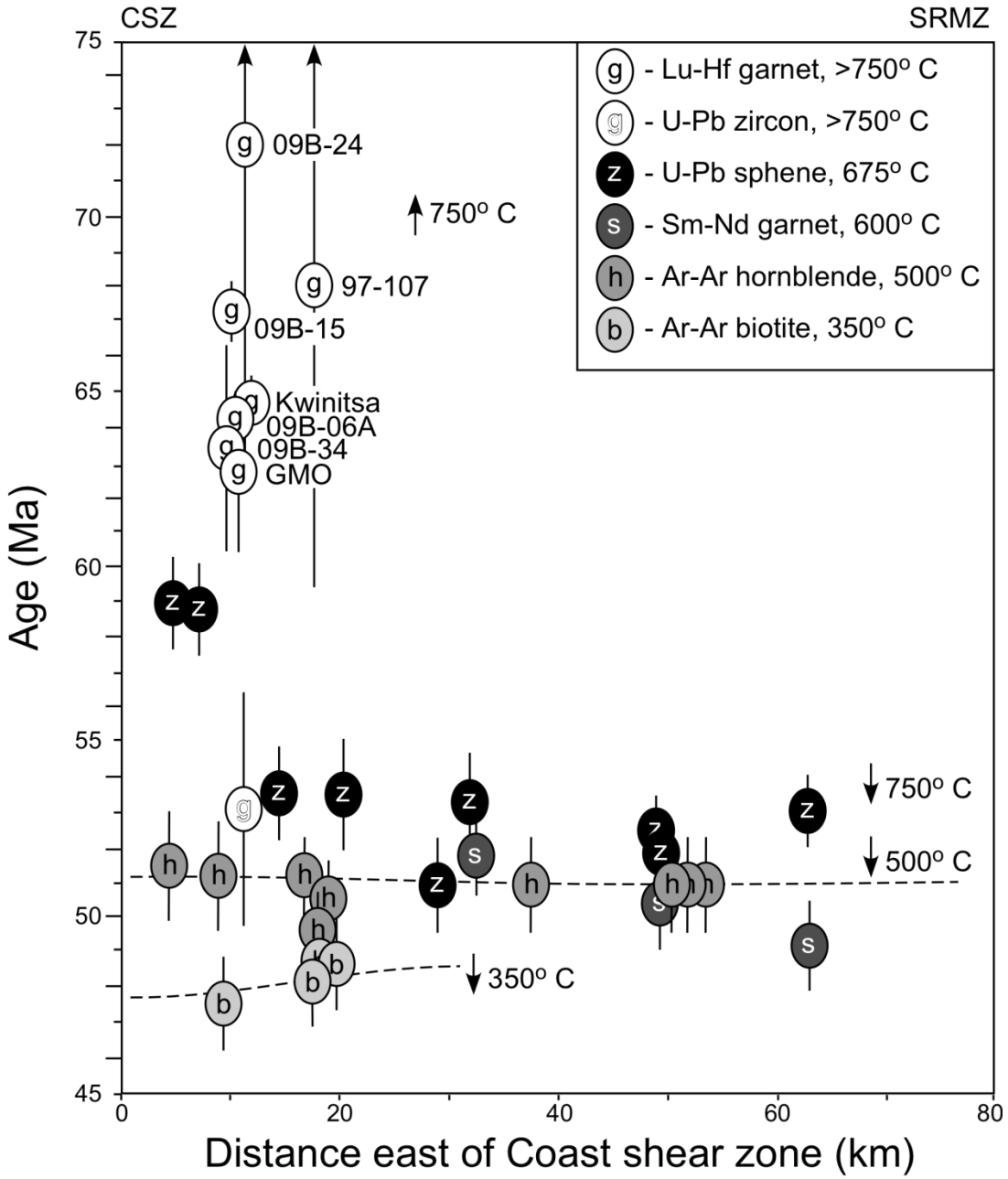

Figure 33. Sample ages plotted relative to distance from the Coast shear zone, modified from Andronicos et al. (2003). The right side of the diagram loosely corresponds to the Shames River mylonite zone. The isotopic system reported in marked by a letter within the oval, with 2σ error bars shown. Isotopic system closure temperatures are summarized in the upper right of the diagram. Dashed lines are interpreted as isotherms, explained in the text. Ages compiled from: Gehrels et al. 1991; Hollister 1993; Andronicos et al. 2003; this study.

work has indicated that temperatures were in excess of 750° C, and that the system was entering upper-amphibolite to granulite metamorphic conditions. Zircon dates at 59 Ma are from the Quottoon Pluton in the west of the field area (Figure 31). These zircon ages overlap within error of samples GMO and 09B-34, which are the two samples closest to the Quottoon (Figure 16). This could be a result of thermal perturbation of the Lu-Hf system during Quottoon emplacement, or prolonged garnet growth during emplacement-related contact metamorphism.

The next set of ages is the U-Pb zircon ages at 53 Ma (Fig. 33). This is the crystallization age of the Kasiks sill, which trends parallel to the section chosen for this plot and was emplaced at the same time in both the east and west of the central gneiss complex (Andronicos et al. 2003). The Sm-Nd garnet date coincides with Kasiks emplacement, and represents when the system cooled below 600° C (Fig. 31). While it is likely the system was reopened during Quottoon emplacement at 59 Ma, it must have been reset during Kasiks emplacement. The thermal effect of the Kasiks pluton emplacement was not recorded by the Lu-Hf system due to its very high closure temperature. Andronicos et al. (2003) report Ar-Ar hornblende samples across the whole CGC define a flat isotherm at 51 Ma, marking the point when units cooled below 500° C, followed by the Ar-Ar biotite isotherm at 48 Ma, units cooled below 350° C (Fig. 31). Hornblende and biotite ages came from the same samples, and the stacked hornblende and biotite ages at 20 km east of the Coast shear zone are due to changes in elevation, with the highest elevations producing the oldest age. Cooling below 500° C marks the end of amphibolite-grade metamorphism, which initiated more than 20 million years prior.

The close spacing of isotherms supports the conclusions of Hollister (1982) and Andronicos et al. (2003) that emplacement of the Kasiks was followed by the rapid uplift and subsequently cooling, of the CGC. Many of our samples at higher

elevations recorded this change in P-T conditions by either growing cordierite (09B-15; 96-056) or decompression rims of anthophyllite (09B-06A). Samples at lower elevations (i.e. Kwinitsa) did not generate cordierite, due to their position lower in the section (and at higher pressure). Since the isotherms are flat across the CGC, the presence of horizontal isograds implies that isobars across the central gneiss complex are similarly flat (or else we would see variation in metamorphic minerals/grade across the belt). These flat isotherms are the result of uniform cooling across the metamorphic belt during exhumation. Andronicos et al. (2003) also reports that the isograd for orthopyroxene is planar, dipping 30° to the northeast, parallel to the Shames River mylonite zone (SRMZ).

6.3 Deformational history

Within the central gneiss complex, we find the development of different domains of moderate to steep fabrics that overlap in time. Gneissic layering of the rusty- and gray-weathering migmatites (S_1) is interpreted as forming prior to main garnet growth (>70 Ma), as inclusion trails in garnets occur at a high angle to the foliation. Evidence of the F_2 folding can be observed in inclusion trails of garnets, indicating that F_2 also developed prior to most garnet growth at 70 Ma. Some garnet growth could have occurred during these deformations, and now is recorded by complex ages at 96-056, 97-107, and 09B-24.

Inclusion trails of folded layers indicate that garnet growth post-dated the development of the S_2 foliation, but curvature of the foliation around garnets at localities 09B-15, 96-056, and GMO, support that garnet growth pre-dated the development of S_3. These samples produced ages of 67-63 Ma, which is within error of Quottoon emplacement. Transition of the S_2 to S_3 fabric also takes place during this period. These fabrics are best recorded along the ridge south of Spinel Peak, where the

transposition of fabrics can be observed at the outcrop scale (Figure 19H). Inclusions in garnet include tight- to isoclinal folds, and asymmetric kinematic indicators that are consistent with F_3 folding along the margin of the Quottoon. Field relationships would suggest that sample 09B-15 is deformed by a fabric that is younger than S_2, but the calculated Lu-Hf age is older than samples within S_3. Therefore, these fabrics must have developed at the same time, and represent a partitioning of the strain between different domains. The age of the magmatic fabric (S_0) within the Quottoon is well constrained at 59 Ma by U-Pb zircon dates. This parallels the host rock S_3, since emplacement followed crustal heterogeneities developed during previous deformation.

The deformation observed within the central gneiss complex occurs at the same time as east-side-up, southwest-directed, ductile shearing along the Coast shear zone (Klepeis et al. 1998; Crawford et al. 1998; Andronicos et al. 1999; McClelland and Mattinson 2000; Andronicos et al. 2003; Crawford et al. 2009). Fabrics observed in the Quottoon and regions to the east suggest synchronous development of southwest-dipping and dextral shear (Andronicos et al. 1999). The new observations and data reported from the central gneiss complex are kinematically consistent with dextral transpression along the Coast shear zone, and date this deformation at 70-65 Ma. This is compatible with models for orogen-parallel displacement of the Insular and Intermontane Superterranes during this time, as proposed by Irving et al. (1996) and Hollister and Andronicos (1997).

At the end of convergence, normal motion on the Shames River mylonite zone (SRMZ) has been accepted for driving exhumation of the central gneiss complex. Models presented by other workers that indicate the CGC experienced significant tilting of $>30^{\circ}$ (e.g. Butler et al. 2001) or incremental exhumation beneath a low-angle normal fault. Such models would predict that ages in the west would be noticeably older than those in the east. In order to produce the observed patterns of horizontal

isotherms across the CGC, vertical shortening must have been a more significant factor than horizontal extension. Had the central gneiss complex been sequentially exhumed from beneath the SRMZ, western ages would be older than those in the east, and the isotherms would be tilted.

6.4 Regional context

The timing of metamorphism and deformation within the central gneiss complex of British Columbia coincides with southwest-northeast contraction and dextral transpression of the Cascade crystalline core between 73-57 Ma (Misch, 1988; Miller and Bowring, 1990; McGroder, 1991; Miller et al, 2006). Mid-Cretaceous burial of the crystalline core is also attributed to intra-arc shortening resulting from final eastward suturing of the Insular and Intermontane superterranes, increased plate coupling (Brandon et al, 1988; Whitney and McGroder, 1989; Evans and Davidson, 1999), and/or to pluton-derived magma loading (Brown and Walker, 1993). Zircon U-Pb analyses from leucosomes in migmatites of the Skagit Gneiss Complex indicate at least two pulses of migmatization (69-63 Ma and 54-51 Ma), which are younger to the east (Gordon, 2009). Multiple leucosomes and melanosomes yielded monazite U-Pb dates of ca. 69 and 49-46 Ma, implying that the Skagit Gneiss Complex remained hot until the middle Eocene (Gordon, 2009). Thermobarometric data indicate that the Skagit Gneiss Complex experienced near-isothermal decompression from 8-10 kbar to 3-4 kbar at temperatures of 725-600º C in the Late Cretaceous and/or early Tertiary (Whitney, 1992).

7. Conclusions

Rocks of the central gneiss complex experienced upper-amphibolite to granulite facies metamorphic conditions for approximately 20 million years between

72 and 52 Ma. This metamorphism was not associated with a single plutonic suite, but seems to span multiple generations of melt injection. This deformation and metamorphism is consistent with structures in the Cascade crystalline core, and is interpreted as resulting from suturing of the Insular and Intermontane Superterranes. Deformation in the CGC does not overlap prograde metamorphism in western metamorphic belt, with a clear separation between WMB deformation at 105 Ma (Wolf et al. 2010) and CGC deformation at 70 Ma.

Metamorphism ended during rapid uplift of the entire central gneiss complex. The whole belt experienced this uplift at the same time, as the orogenic core was uplifted vertically as a cohesive block, and is recorded by the flat isotherms from multiple isotopic systems. Field relationships within the central gneiss complex record a transposition of different structural domains that are chronologically coeval. Based on Lu-Hf garnet ages, these fabrics must have developed at the same time, and represent partitioning of strain in the middle crust. Partitioning of strain onto conjugate dipping fabrics can be observed in the upper crust at the San Andreas and Garlock faults (Teyssier and Tikoff, 1998), as well as at mid-crustal levels. This evidence for partitioning of a transpressive strain in the middle crust support at minimum a partial attachment between the upper and middle crust, crossing the brittle-ductile transition (Teyssier et al. 2002; Tikoff et al. 2002). Other isotopic systems record a rapid, vertical exhumation of the central gneiss complex with minimal horizontal variation. This indicates that the footwall beneath the Shames River mylonite zone experienced significant vertical shortening to accomplish uplift, rather than incremental horizontal motion or tilting.

The convergence direction required for the Cretaceous-Paleocene contraction is not compatible with the extension and collapse of the orogen at 52 Ma. This change has been credited to a shift in relative plate motions between the Kula and North

American plates, from west southwest-east northeast before 57 Ma, to south southwest-north northeast after 54 Ma (Lonsdale 1988; Andronicos et al. 2003).

8. Chapter-specific acknowledgements

This work was supported by: Cornell University Student Travel Grants to David E. Wolf; National Science Foundation grant EAR-0738827 to Chris L. Andronicos; and National Science Foundation grants EAR-0609856 and EAR-0711326 to Jeff D. Vervoort. We also thank Ashley Tefft and Garret Hart for their assistance in clean laboratory separations and MC-ICP-MS analyses. Field transportation was provided by Canadian Helicopters, who could be counted on to deliver us safely and remember where they left us.

REFERENCES

Andronicos, C.L., Hollister, L.S., Davidson, C., Chardon, D.H., 1999. Kinematics and tectonic significance of transpressive structures within the Coast Plutonic Complex, British Columbia. Journal of Structural Geology 21, 229–243.

Andronicos, C.L., Chardon, D.H., Hollister, L.S., Gehrels, G.E., Woodsworth, G.J., 2003. Strain partitioning in an obliquely convergent orogen, plutonism, and synorogenic collapse: Coast Mountains Batholith, British Columbia, Canada. Tectonics 22, 1012–1035.

Armstrong, R.L., and Runkle, D., 1979, Rb-Sr geochronometry of the Ecstall, Kitkatla, and Quottoon plutons and their country rocks, Prince Rupert region, Coast Plutonic Complex, British Columbia: Canadian Journal of Earth Sciences 16, 387-399.

Armstrong, R.L., 1988. Mesozoic and Early Cenozoic magmatic evolution of the Canadian Cordillera. Geological Society of America Special Paper 218, 55-91.

Arth, J.G., Barker, F., and Stern, T.W., 1988. Coast batholith and Taku plutons near Ketchikan, Alaska; petrography, geochronology, geochemistry, and isotopic character: American Journal of Science 288-A, 461–489.

Axen, G.J., Selverstone, J., Byrne, T., and Fletcher, J.M. 1998. If the strong crust leads, will the weak crust follow? GSA Today 8, 1-8.

Berman, R.G., 1988. Internally-consistent thermodynamic data for minerals in the system Na_2O–K_2O–CaO–MgO–FeO–Fe_2O_3–Al_2O_3–SiO_2–TiO_2–H_2O–CO_2. Journal of Petrology 29, 445–522.

Berman, R.G., 1991. Thermobarometry using multi-equilibrium calculations: a new technique, with petrological applications. Canadian Mineralogist 29, 833–855.

Berman, R.G., 2007. WinTWQ (version 2.3): a software package for performing internally-consistent thermobarometric calculations: Geological Survey of Canada,

Open File 5462. 41 p.

Bouvier A., Blichert-Toft J., Moynier F., Vervoort J.D., and Albarède F., 2007. Pb-Pb dating constraints on the accretion and cooling history of chondrites. Geochimica et Cosmochimica Acta 71, 1583-1604.

Bouvier, A., Vervoort, J.D., Patchett, P.J., 2008. The Lu–Hf and Sm–Nd isotopic composition of CHUR: constraints from unequilibrated chondrites and implications for the bulk composition of terrestrial planets. Earth and Planetary Science Letters 273, 48–57.

Brandon, M.T., Cowan, D.S., and Vance, J.A., 1988, The Late Cretaceous San Juan thrust system, San Juan Islands, Washington: A case history of terrane accretion in the western Cordillera: Geological Society of America Special Paper 221, 88 p.

Brew, D.A., Ford, A.B., 1978. Megalineament in southeastern Alaska marks southwest edge of Coast Range batholithic complex. Canadian Journal of Earth Sciences 15, 1763.

Brown, E.H., and Walker, N.W., 1993. A magma-loading model for Barrovian metamorphism in the southeast Coast Plutonic Complex, British Columbia and Washington: Geological Society of America Bulletin 105, 479-500.

Butler, R.F., Gehrels, G.E., Crawford, M.L., and Crawford, W.A., 2001. Paleomagnetism of the Quottoon plutonic complex in the Coast Mountains of British Columbia and southeastern Alaska: evidence for tilting during uplift: Canadian Journal of Earth Sciences 38, 1367–1384, DOI: 10.1139/cjes-38-9-1367.

Chardon, D., Andronicos, C.L., Hollister, L.S., 1999. Large-scale transpressive shear zone patterns and displacements within magmatic arcs: the Coast Plutonic Complex, British Columbia. Tectonics 18, 278–292.

Cheng, H., King, R.L., Nakamura, E., Vervoort, J.D., Zhou, Z., 2008. Coupled Lu–Hf and Sm–Nd geochronology constrains garnet growth in ultra-high-pressure

eclogites from the Dabie orogen. Journal of Metamorphic Geology 26, 741–758.

Collins, W.J. and Vernon, R.H. 1991. Orogeny associated with anticlockwise P-T-t paths: evidence from low-P, high-T metamorphic terranes in the Arunta Inlier, central Australia. Geology 19, 835-838.

Cook, R.D., Crawford, M.L., 1994. Exhumation and tilting of the western metamorphic belt of the Coast orogen in southern southeastern Alaska. Tectonics 13, 528–537.

Crawford, M.L., Hollister, L.S., 1982. Contrast of metamorphic and structural histories across the Work channel lineament. Coast Plutonic Complex, British Columbia. Journal of Geophysical Research 87, 3849–3860.

Crawford, M.L., Hollister, L.S., Woodsworth, G.J., 1987. Crustal deformation and regional metamorphism across a terrain boundary, Coast Plutonic Complex, British Columbia. Tectonics 6, 343–361.

Crawford, M. L., K. A. Klepeis, G. Gehrels, and C. Isachsen, 1999. Batholith emplacement at mid-crustal levels and its exhumation within an obliquely convergent margin: The influence of granite emplacement on tectonics, Tectonophysics, 312, 57–78.

Crawford, M.L., Crawford, W.A., Gehrels, G.E., 2000. Terrane assembly and structural relationships in the eastern Prince Rupert quadrangle, British Columbia. *In:* Stowell, H.H., McClelland, W.C. (Eds.), Tectonics of the Coast Mountains, Southeastern Alaska and British Columbia: Geological Society of America, Special Paper 343, 1–21.

Crawford, M. L., K. A. Klepeis, G. Gehrels, and J. Lindline, 2009. Mid-Cretaceous–Recent crustal evolution in the central Coast orogen, British Columbia and southeastern Alaska: The Geological Society of America Special Paper 456, 97-124.

Davy, P. and Cobbold, P. 1988. Indentation tectonics in nature and experiment, 1. Experiments scaled for gravity. Bulletin of the Geological Institute, University of Uppsala, New Series, 14, 129-141.

de Capitani, C., Brown, T.H., 1987. The computation of chemical equilibrium in complex systems containing non-ideal solutions. Geochimica et Cosmochimica Acta 51, 2639–2652.

Douglas, B.J., 1983. Structural and stratigraphic analysis of a meta-sedimentary inlier within the Coast Plutonic Complex, British Columbia, Canada. Ph.D. thesis, Princeton University, Princeton, N.J.

Douglas, B. J., 1986. Deformational history of an outlier of metasedimentary rocks, Coast Plutonic Complex, British Columbia, Canada, Can. J. Earth Sci., 23, 813–826.

Engebretson, D.C., Cox, A., Gordon, R.G., 1985. Relative motions between oceanic and continental plates in the Pacific basin: Geological Society of America Special Paper 206. 59 pp.

Enkin, R.J., 2006. Paleomagnetism and the case for Baja British Columbia. *In:* Haggart, J.W., Enkin, R.J., Monger, J.W.H. (Eds.), Paleogeography of the North American Cordillera; Evidence for and against large-scale displacements: Geological Association of Canada, Special Paper 46, 233–253.

Evans, B.W., and Davidson, G.F., 1999. Kinetic control of metamorphic imprint during synplutonic loading of batholiths: An example from Mt. Stuart, Washington: Geology 27, 129-139.

Fitch, T.J., 1972. Plate convergence, transcurrent faults, and internal deformation adjacent to South- east Asia and the Western Pacific. Journal of Geophysical Research 77, 4432-4460.

Gareau, S.A., 1991. The Scotia–Quaal metamorphic belt: a distinct assemblage with

pre- early Cretaceous deformational and metamorphic history, Coast Plutonic complex, British Columbia. Canadian Journal of Earth Sciences 28, 870–880.

Gareau, S. A., G. J. Woodsworth, and M. Rickli, 1997. Regional geology of the northeastern quadrant of Terrace map area, west-central British Columbia, Current Research 1997-A, 47–55, Geological Survey of Canada, Ottawa.

Gehrels, G.E., McClelland, W.C., Samson, S.D., Patchett, P.J., Brew, D.A., 1991. U–Pb geochronology of Late Cretaceous and early Tertiary plutons in the northern Coast Mountains batholith. Canadian Journal of Earth Science 28, 899–911.

Gehrels, G., Rusmore, M., Woodsworth, G., Crawford, M., Andronicos, C., Hollister, L., Patchett, J., Ducea, M., Butler, R., Klepeis, K., Davidson, C., Friedman, R., Haggart, J., Mahoney, B. Crawford, W., Pearson, D., and Girardi, J., 2009. U-Th-Pb geochronology of the Coast Mountains batholith in north-coastal British Columbia: Constraints on age and tectonic evolution. Geological Society of America Bulletin 121, 1341-1361, DOI: 10.1130/B26404.1.

Gordon, S.M., 2009. Timescales of migmatization, metamorphism, and deformation in a collapsed orogenic plateau [Ph.D. thesis]: Minneapolis, Minnesota, University of Minnesota, 379 p.

Hajnal, Z., Lucas, S.B., White, D.J., Lewry, J., Bezdan, S., Stauffer, M.R. and Thomas, M.D. 1996. Seismic reflection images of strike-slip faults and linked detachments in the Trans-Hudson Orogen, Tectonics 15, 427-439.

Harland, W.B., 1971. Tectonic transpression in Caledonian Spitzbergen. Geological Magazine 108, 793-802.

Heah, T. S. T., 1991, Mesozoic ductile shear and Paleogene extension along the eastern margin of the central gneiss complex, Coast belt, Shames River area, near Terrace, British Columbia, M.S. thesis, 155 pp., University of British Columbia, Vancouver, British Columbia.

Hill, M. L., 1984. Geology of the Redcap Mountain area, Coast Plutonic Complex, British Columbia, Ph.D. thesis, 216 p., Princeton Univ., Princeton, N. J..

Hill, M.L., Woodsworth, G.J., and van der Heyden, P., 1985. The Coast Plutonic Complex near Terrace, B.C.; a metamorphosed western extension of Stikinia: Geological Society of America Abstracts with Programs 17 (6), 362.

Holdaway, M.J., 2001. Recalibration of the GASP geobarometer in light of recent garnet and plagioclase activity models and versions of the garnet–biotite geothermometer. American Mineralogist 86, 1117–1129.

Holland T.J.B. and Powell R., 1998. An internally consistent thermodynamic data set for phases of petrological interest. Journal of Metamorphic Geology 16, 309-343.

Hollister, L.S., 1975. Granulite facies metamorphism in the Coast Range crystalline belt. Canadian Journal of Earth Sciences 12, 1953-1955.

Hollister, L.S., 1982. Metamorphic evidence for rapid (2 mm/yr) uplift of a portion of the central gneiss complex, Coast Mountains, B.C. Canadian Mineralogist 20, 319-332.

Hollister, L.S., Grisson, G.C., Peters, E.K., Stowell, H.H., Sisson, V.B., 1987. Confirmation of the empirical correlation of Al in hornblende with pressure of solidification of calc-alkaline plutons. American Mineralogist 72 (3–4), 231–239.

Hollister, L. S., 1993. The role of melt in the uplift and exhumation of orogenic belts, in Chemical Geology, 108, 31–48.

Hollister, L.S., and Andronicos, C.L., 1997. A candidate for the Baja British Columbia fault system in the Coast Plutonic Complex. GSA Today 7 (11), 1–7.

Hollister, L. S., and C. L. Andronicos, 2000. The central gneiss complex, Coast Orogen, British Columbia, Special Papers of the Geological Society of America 343, 45–59.

Hutchison, W.W., 1970. Metamorphic framework and plutonic styles in the Prince

Rupert region of the central Coast Mountains, British Colombia. Canadian Journal of Earth Sciences 7, 376- 405.

Hutchison, W. W., 1982. Geology of the Prince Rupert-Skeena map area, British Columbia, Geological Survey of Canada, Ottawa, Ontario.

Ingram, G.M., Hutton, D.H.W., 1994. The Great Tonalite Sill: Emplacement into a contractional shear zone and implications for Late Cretaceous to early Eocene tectonics in southwest Alaska and British Columbia. Geological Society of America Bulletin 106, 715-728.

Irving, E., Wynne, P.J., Thorkelson, D.J., and Schiarizza, P., 1996. Large (1000 to 4000 km) northward movements of tectonic domains in the northern Cordillera, 83 to 45 Ma. Journal of Geophysical Research 106, 901-916.

Jackson, S. and Cruden, A.R. 1995. Formation of the Abitibi greenstone belt by arc-trench migration. Geology, 23, 471-474.

Kenah, C., Hollister, L.S., 1983. Anatexis in the central gneiss complex, British Columbia. *In:* Athreton, M.P., Gribble, C.D. (Eds.), Migmatites, Melting and Metamorphism, 142-162.

Klepeis, K.A., Crawford, M.L., Gehrels, G.E., 1998. Structural history of the crustal-scale Coast shear zone north of Portland Canal, southeast Alaska and British Columbia. Journal of Structural Geology 20, 883–904.

Klepeis, K. A., and M. L. Crawford, 1999. High-temperature arc-parallel normal faulting and transtension at the roots of an obliquely convergent orogen, Geology 27, 7–10.

Lappin, A.R., Hollister, L.S., 1980. Partial melting in the central gneiss complex near Prince Rupert, British Columbia. American Journal of Science 280, 518-545.

Lonsdale, P., 1988. Paleogene history of the Kula plate: Offshore evidence and onshore implications, Geological Society of America Bulletin 100, 733-754.

Ludwig, K.R., 2003. IsoPlot/Ex, rev 3.61, a Geochronologic Toolkit for Microsoft Excel: Berkeley Geochronology Center.

Mansfield, M.R., 2004. Thermal and structural evolution of the Grenville Channel shear zone, Coast plutonic complex, British Columbia: M.S. thesis, University of Texas, El Paso.

McClelland, W.C., Gehrels, G.E., Samson, S.D., Patchett, P.J., 1992. Structural and geochronologic relations along the western flank of the Coast Mountains batholith; Stikine River to Cape Fanshaw, central southeastern Alaska: Journal of Structural Geology 14, 475–489.

McClelland, W.C., and Mattinson, J.M., 2000, Cretaceous-Tertiary evolution of the western Coast Mountains, central southeastern Alaska, *In:* Stowell, H.H., McClelland, W.C. (Eds.), Tectonics of the Coast Mountains, Southeastern Alaska and British Columbia: Geological Society of America, Special Paper 343, 159-182.

McGroder, M.F., 1991. Reconciliation of two-sided thrusting, burial metamorphism, and diachronous uplift in the Cascades of Washington and British Columbia: Geological Society of America Bulletin 103, 189-209.

Miller, C.F., and Mittlefehldt, D.W., 1982. Depletion of light rare-earth elements in felsic magmas: Geology 10 (3), 129-133; DOI: 10.1130/0091-7613(1982)10.

Miller, R.B., and Bowring, S.A., 1990. Structure and chronology of the Oval Peak batholith and adjacent rocks: Implications for the Ross Lake fault zone, North Cascades, Washington: Geological Society of America Bulletin 102, 1361-1377.

Miller, R.B., and Paterson, S.R., 2001. Influence of lithological heterogeneity, mechanical anisotropy, and magmatism on the rheology of an arc, North Cascades, Washington: Tectonophysics 342, 351-370.

Miller, R.B., Paterson, S.R., Lebit, H.A., Alsleben, H., and Luneberg, C., 2006.

Significance of composite lineations in the mid- to deep crust: A case study from the North Cascades, Washington: Journal of Structural Geology 28, 302-322.

Miller, R.B., Paterson, S.R., and Matzel, J.P., 2009. Plutonism at different crustal levels: Insights from the 5–40 km (paleodepth) North Cascades crustal section, Washington, *In:* Miller, R.B., and Snoke, A.W. (Eds.), Crustal cross sections from the western North American Cordillera and elsewhere: Implications for tectonic and petrologic processes: Geological Society of America Special Paper 456, 125-149, DOI:10.1130/2009.2456(05).

Misch, P., 1966. Tectonic evolution of the Northern Cascades of Washington State: A west-Cordilleran case history, *In:* Gunning, H.C. (Ed.), Symposium on the tectonic history and mineral deposits of the western Cordillera in British Columbia and neighboring parts of United States: Canadian Institute of Mining and Metallurgy, Special Volume 8, 101-148.

Misch, P., 1988. Tectonic and metamorphic evolution of the North Cascades: An overview, *In:* Ernst, W.G. (Ed.), Metamorphism and crustal evolution of the western United States: Rubey Volume 7, Upper Saddle River, New Jersey, Prentice Hall, 179-195.

Münker, C., Weyer, S., Scherer, E., Mezger, K., 2001. Separation of high field strength elements (Nb, Ta, Zr, Hf) and Lu from rock samples for MC-ICPMS measurements: G-cubed 2. DOI:10.1029/2001GC000183.

Pattison, D.R.M., Chacko, T., Farquhar, J., and McFarlane, C.R.M., 2003. Temperatures of granulite-facies metamorphism: Constraints from experimental phase equilibria and thermobarometry corrected for retrograde exchange. Journal of Petrology 44 (5), 867-900.

Roddick, J.A., 1970. Douglas Channel — Hecate Strait Map Area. British Columbia Geological Survey of Canada, Paper 70-41.

Rusmore, M.E., Gehrels, G., Woodsworth, G.J., 2001. Southern continuation of the Coast shear zone and Paleocene strain partitioning in British Columbia–southeast Alaska. GSA Bulletin 113, 961–975.

Scherer, E.E., Münker, C., Mezger, K., 2001. Calibration of the lutetium–hafnium clock. Science 293, 683–687.

Selverstone, J., Hollister, L.S., 1980. Cordierite-bearing granulites from the Coast Ranges, British Columbia: P-T conditions of metamorphism. Canadian Mineralogist 18, 119-129.

Sisson, V., 1985. Contact metamorphism associated with the Ponder pluton, Coast Plutonic Complex, British Columbia, Ph.D. thesis, 345 p., Princeton Univ., Princeton, N. J..

Smith, J.G., and Diggles, M.F., 1981. Potassium-argon determinations in the Ketchikan and Prince Rupert quadrangles, southeastern Alaska: U.S. Geological Survey Open-File Report 78-73N, 16 p.

Söderlund, U., Patchett, P.J., Vervoort, J.D., Isachsen, C.E., 2004. The ^{176}Lu decay constant determined by Lu–Hf and U–Pb isotope systematics of Precambrian mafic intrusions. Earth and Planetary Science Letters 219, 311–324.

Stonge, M.R., 1981. “Normal” and “inverted” metamorphic isograds and their relation to syntectonic Proterozoic batholiths in the Wopmay Orogen, Northwest Territories, Canada. Tectonophysics 76, 295-316.

Stowell, H.H., Hopper, R.J., 1990. Structural development of the western metamorphic belt adjacent to the Coast Plutonic Complex, southeastern Alaska: Evidence from Holkham Bay. Tectonics 9, 391-407.

Sun, S.-S., and McDonough, W.F., 1989. Chemical and isotopic systematics of oceanic basalts: implications for mantle composition and processes. *In:* Saunders, A.D., Norry, M.J. (Eds.), Magmatism in the Ocean Basins. Geological Society of

London, 313-345.

Sylvester, A.G., 1988, Strike-slip faults; Geological Society of America Bulletin 100, 1666-1703.

Tapponnier, P., Peltzer, G., La Dain, A.Y., Armijo, R. and Cobbold, P. 1982. Propagating extrusion tectonics in Asia: New insights from simple experiments with plasticene. Geology 10, 611-616.

Teyssier, C., Tikoff, B. and Markley, M. 1995. Oblique plate motion and continental tectonics. Geology 23, 447-450.

Teyssier, C. and Tikoff, B. 1998. Strike-slip partitioned transpression of the San Andreas fault system: a lithospheric scale approach. *In:* Holdsworth, R.E., Strachan, R.A. and Dewey, J.F. (Eds.), Continental Transpression and Transtension Tectonics. Geological Society, London, Special Publications 135, 143–158.

Teyssier, C., Tikoff, B., and Weber, J., 2002. Attachment between brittle and ductile crust at wrenching plate boundaries. *In:* Bertottig, Schulmann, K., and Cloetingh, S. (Eds.) Continental Collision and the Tecton-Sedimentary Evolution of Forelands. European Geophysical Society, Special Publications 1, 57-73.

Thomas, J.B., and Sinha, A.K., 1999. Field, geochemical, and isotopic evidence for magma mixing and assimilation and fractional crystallization processes in the Quottoon Igneous Complex, northwestern British Columbia and southeastern Alaska: Canadian Journal of Earth Sciences 36, 819–831.

Tikoff, B., Teyssier, C., and Waters, C., 2002. Clutch tectonics and the partial attachment of lithospheric layers. *In:* Bertotti, G., Schulmann, K. and Cloetnch, S. (Eds.) Continental Collision and the Tecton-sedimentary evolution of Forelands. European Geophysical Society, Special Publications 1, 119-144.

Tikoff, B., Russo, R., Teyssier, C. and Tommasi, A., 2004. Mantle-driven deformation

of orogenic zones and clutch tectonics. Geological Society, London, Special Publications 227, 41-64. DOI:10.1144/GSL.SP.2004.227.01.03.

Trouw, R.A.J., Passchier, C.W., Valeriano, C.M., Simões, L.S.A., Paciullo, F.V.P., and Ribeiro, A., 2000. Deformational evolution of a Cretaceous subduction complex: Elephant Island, South Shetland Islands, Antarctica. Tectonophysics 319 (2), 93-110. DOI:10.1016/S0040-1951(00)00021-4.

Umhoefer, P.J., 2003. A model for the North America Cordillera in the Early Cretaceous: Tectonic escape related to arc collision of the Guerrero terrane and a change in North America plate motion. *In:* Johnston, S.E., Paterson, S.R., Fletcher, J.M., Girty, G.H., Kimbrough, D.L., Martín-Barajas, A. (Eds.), Tectonic evolution of north- western México and the southwestern USA: Geological Society of America Special Paper 374, 117–134.

van der Heyden, P., 1989. U–Pb and K–Ar geochronometry of the Coast Plutonic Complex, 53° N–54° N, and implication for the Insular–Intermontane superterrane boundary, British Columbia: Ph.D. thesis, University of British Columbia.

van der Heyden, P., 1992. A Middle Jurassic to Early Tertiary Andean-Sierran arc model for the Coast Belt of British Columbia. Tectonics 11, 82-97.

Vervoort, J.D., Patchett, P.J., Söderlund, U., Baker, M., 2004. Isotopic composition of Yb and the determination of Lu concentrations and Lu–Hf ratios by isotope dilution using MC- ICPMS. Geochemistry, Geophysics, Geosystems 5. DOI:10.1029/2004GC000721.

White, W.M., 2009. Chapter 7: Trace elements in igneous processes, *from*: Geochemistry, An Online Textbook. Accessed July 2009. http://www.geo.cornell.edu/geology/classes/geo455/Chapters.HTML.

Whitney, D.L., and McGroder, M.F., 1989. Cretaceous crustal section through the proposed Insular-Intermontane suture, North Cascades, Washington: Geology 17,

555-558.

Whitney, D.L., 1992. High-pressure metamorphism in the Western Cordillera of North America: an example from the Skagit Gneiss, North Cascades, Washington, USA: Journal of Metamorphic Geology 10, 71-85.

Woodsworth, G.J., Loveridge, W.D., Parrish, R.R., Sullivan, R.W., 1983. Uranium-lead dates from the central gneiss complex and Ecstall pluton, Prince Rupert map area, British Columbia. Canadian Journal of Earth Sciences 20, 1475-1483.

Wolf, D.E., Andronicos, C.L., Vervoort, J.D., Mansfield, M.R., Chardon, D., 2010. Application of Lu-Hf garnet dating to unravel the relationships between deformation, metamorphism and plutonism: An example from the Prince Rupert area, British Columbia. Tectonophysics 485, 62-77. DOI: 10.1016/j.tecto.2009.11.020.